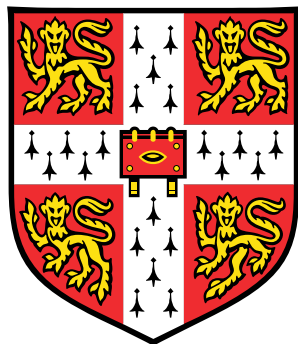


Normalisation and Clustering Methods Applied to Association Studies in Type 1 Diabetes



Nikolas Pontikos
University of Cambridge

This dissertation is submitted for the degree of
Doctor of Philosophy

Pour ma petite Maman chérie, à qui je dois tout ...

Pour Mamie qui s'e

Αφιερωμένο στους: Ήλια, Σοφία, Στέφανο και Ναταλία ...

Zu meinem unerschrockenen Bruder, Theo ...

Til min åndelige far, Constantine ...

To Laurent Cullinan ...

Declaration

This thesis is submitted as part requirement for the PhD Degree in “Medical Genetics” at Cambridge University. It is the result of my own work and includes nothing which is the outcome of work done in collaboration except where explicitly stated. It is not substantially the same as any that I have submitted, or, is being concurrently submitted for a degree or diploma or other qualification at the University of Cambridge or any other University or similar institution. I further state that no substantial part of my dissertation has already been submitted, or, is being concurrently submitted for any such degree, diploma or other qualification at the University of Cambridge or any other University of similar institution. It does not exceed the prescribed word limit for the relevant Degree Committee. It contains less than 60,000 words and less than 150 figures. The report may be freely copied and distributed provided the source is explicitly acknowledged.

Nikolas Pontikos

June 2015

Acknowledgements

I am very grateful for having been offered the great opportunity to undertake this PhD and to learn so much about statistics, genetics, and science in general. I am certain that these three years of intellectual development have truly reshaped the way I think and see the world and will undoubtedly bear great positive influence on my future life.

First and foremost, my eternal gratitude to my Mother for having devoted so much time to my upbringing and to have kindled my enthusiasm for science and adventure from a very young age. Although she is sadly no longer among us, she is the reason why I decided to dedicate my computer science and programming skills to scientific and medical research.

Secondly, I wish to thank all the great people I have had the privilege to know and work with during this academic adventure. In particular, my super-hero supervisor, Chris Wallace, for her efficiency, advice, support, and encouragement when I was feeling down, and her pragmatism, guidance, and helping me channel my enthusiasm productively when it was overflowing. I would also like to thank my advisor, Anna Petrunkina Harrison, for providing much encouragement and support, and putting me in touch with the right people in flow cytometry. John Todd's intense presence and input have been incredibly valuable and I would like to thank him for his relentless drive, insight, experience and his pushing me to publish. I wish to also acknowledge the Medical Research Council, Doctoral Training Grant (C006148), for funding my research.

Having no formal training in statistics, I was privileged enough to be surrounded

by smart people throughout my PhD from whom I have learned a great deal. Notably, Xin Yang, Hui Guo, Nick Cooper, Marina Evangelou, Mary Fortune, James Liley and Arcadio Rubio Garcia spring to mind, with whom I have had many interesting lunchtime conversations. Mary Fortune's mathematical prowess is only rivalled by her baking skills. Xin Yang also makes delicious chinese buns, a skill that will no doubt continue to serve her well.

I also learned a much about biology thanks to discussions with Marcin Pekalski, Tony Cutler, Xaqin Dopico Castro, Ricardo Fereirra and Charlie Bell. They were also very important in making me feel welcome to the lab (perhaps even a little too welcome at times). I wish them all the best in their future endeavours and I am sure science or some other strange force will bring us back together.

The first chapter, I owe in great part to my second supervisor Anna Petunkina-Harrison for the introduction to flow cytometry and putting me in touch with the flow cytometry community. I should also mention that my first year examiner, Lorenz Wernisch, gave me some very constructive feedback on my first year report and food for thought.

The second chapter of my thesis would not have been possible without the previous work and extensive email communications with Vincent Plagnol, Calliope Dendrou and Linda Wicker. Notably, I would like to give special thanks to Vincent for offering me the opportunity of continuing to do what I love at University College London for the next two years. I am sure we will do some great work together.

The third chapter was enabled by Tony Cutler's data set, but also benefitted greatly from Marcin Pekalski's and Charlie Bell's detailed knowledge of immune cell types and flow cytometric artefacts.

The fourth chapter, which led to a publication in BMC Genomics, was a continuation of the important work done by Helen Schuilenberg, Debbie Smyth, James Traherne

and Jyothi Jayaraman, among others, on characterising KIR copy number variation. This body of work is also proof to the testimony of the kind of great work resulting from between lab collaborations. The success of this project rested primarily on the supervision of Chris Wallace, to whom I am very grateful for the time and effort invested in the publication. I also received very meticulous feedback from John Todd and Jo Howson which greatly facilitated the submission procees.

The fifth and final chapter was greatly aided by discussions and proof-reading from Chris Wallace and Mary Fortune.

However, no PhD would be complete without a little bit of extra-curricular adventures which surely should be the object of another thesis. My thanks to my team mates Sriyal Mendis and Gary Low for helping me out on my autorickshaw Indian chapter. Their driving skills kept me alive and unscathed during our 4000km autorickshaw adventure across India, in spite of my unfortunate cowllision in Ongole.

Thanks to Ben Silva-Weatherley, Steve Sawiak, and the rest of the team at RNA Crossfit for making sure I did not completely neglect my health through the daily PhD grind. I'd like to think I tried to stay true to the humanist ideal of a healthy mind in a healthy body “mens sana in corpore sano”. foreign language always in italic characters

I would also like to thank all the friends, both professionals and students, I have made during these five fun years at Cambridge, first at the European Bioinformatics Institute, then at the University and Addenbrookes. Notably, my good friends, Shawn O'Donell and Pallawi Sinha, who have often fed me and generally been very supportive and patient with my poor time-keeping (something this thesis is a testament to). Thanks also to all housemates of 386 Cherry Hinton Road, past and present, my home of five years. Thank you Cambridge for being such a friendly, unique, quirky and curious place, one which I have grown very fond of.

Lastly and most importantly, my everlasting gratitude to my Father and my Brother,

inspirations in their own right, for their unconditional love, incessant support and for listening.

Abstract

Genetic association studies have discovered many variants which influence type 1 diabetes (T1D) risk and further correlate with quantitative cell-type specific phenotypes. However, disease associated differences can be small, and large numbers of samples are required to overcome the heterogeneity that exists between humans. Novel high-throughput biotechnologies measure large number of samples but technical or within-batch variation, may undermine reproducibility of measurements.

In my thesis, I analyse two types of these datasets, central to the study of T1D. The first is generated by flow cytometry, a biotechnology utilising light scatter and fluorescently stained markers to discriminate different cell types. Unfortunately, flow cytometry can be prone to batch effects since blood samples are often collected, prepared and analysed at different times and by different operators. I consider several normalisation techniques to address these issues, using external or within sample controls. The main objective of flow cytometry data analysis is that of identifying different cell types. While this is essentially a clustering problem, currently the most widely applied method is a manual approach which can be inefficient and biased. I investigate ways this process can be automated by fitting mixture models to emulate the manual process. I show that, in the absence of manual gates, data-driven approaches can be applied to detect new cell subsets, not targeted by manual gating, that respond to IL-2 in an in-vitro stimulation experiment.

The second type of dataset is generated by qPCR and genotyping arrays, which

are applied to DNA from T1D cases and controls to determine whether copy number variation in two Killer Immunoglobulin-like Receptors (KIRs) genes associates with T1D. I apply normalisation to correct for batch effects between qPCR plates and clustering using mixture models to identify copy number groups. Supervised clustering is then used to correlate qPCR copy number with SNP data, allowing for association testing in a twenty-fold larger sample size than ever previously considered for KIR genes.

Finally, I conclude with what I have learned from applying these methods and how these may be further developed, with special attention to flow cytometry where these remain under utilised. In particular, I discuss how normalisation and clustering relate, and how prior knowledge, when available, can be incorporated into the clustering process.

Contents

Contributors	xxiv
Genes	xxviii
SNPs	xxix
Proteins	xxx
1 Introduction	1
1.1 Motivation	1
1.2 Biology of type 1 diabetes	3
1.2.1 Aetiology and diagnosis	4
1.2.2 Genetics of type 1 diabetes	5
1.2.3 The immune cell mechanisms	6
1.3 Studying the immune system with flow cytometry	7
1.4 Normalisation	16
1.5 Manual clustering	18
1.6 Automatic methods for identifying clusters	18
1.6.1 Model-based methods	19
1.6.2 Model-free methods	21
1.6.3 Estimating the optimal number of clusters from the data	26
2 The influence of gating on reproducibility and association testing in flow cytometry	29

2.1	Background	29
2.2	Univariate gating of bead data	36
2.3	Univariate gating on CD25: defining a CD25 ⁺ threshold on naive cells	40
2.4	Univariate gating on CD45RA: fitting two-component mixtures on non-regulatory T cells	44
2.4.1	Using the mixing proportions of the mixture model	44
2.4.2	Emulating manual gating by picking a threshold	47
2.5	Association tests	53
2.6	Discussion	57
3	Methods to assess cell response to ex-vivo stimulation in flow cytometry	60
3.1	Background	61
3.2	Preliminary analysis by Tony Cutler	66
3.3	Reproducibility of pSTAT5 response within an individual	73
3.3.1	Normalisation approaches	73
3.3.2	Repeatability	75
3.3.3	Association of pSTAT5 response with type 1 diabetes	78
3.4	Response in the whole sample	78
3.4.1	SPADE: spanning-tree progression analysis of density-normalized events	81
3.4.2	RPART: recursive partitioning on core markers	92
3.4.3	PLSR: partial least squares regression	102
3.4.4	CART: binary recursive partitioning using regression tree on pSTAT5108	
3.4.5	MMPART: identification of low-dose sensitive cells by recursive application of a two component mixture model on pSTAT5	112
3.5	Discussion	119

3.5.1	Association of pSTAT5 with T1D	119
3.5.2	Methods for identifying dose-responsive cell populations	120
3.6	Dose responsive populations identified	127
3.6.1	Are these cells present in other samples?	132
3.6.2	Conclusion	136
4	KIR3DL1/KIR3DS1 copy number variation in type 1 diabetes	137
4.1	Background	138
4.1.1	Killer immunoglobulin receptors and their interaction with human leukocyte antigen molecules	138
4.1.2	<i>KIR3DL1</i> and <i>KIR3DS1</i> : two strong candidates for T1D association	139
4.2	Samples and genotyping assays	142
4.2.1	Samples	142
4.2.2	HLA and SNP Genotyping	142
4.2.3	qPCR experimental protocol	143
4.3	Data Analysis	144
4.3.1	Quality control and normalisation of qPCR data	144
4.3.2	Bivariate clustering: copy number calling in qPCR data	146
4.3.3	k-nearest neighbour (KNN) classification: copy number imputation into the SNP data	151
4.4	Association testing of <i>KIR3DL1/KIR3DS1</i> copy number with T1D . . .	157
4.5	Discussion	162
4.5.1	Previous association studies of KIR genes with T1D	162
4.5.2	My approach	167
4.5.3	Future work	168
5	Discussion	172

5.1	Challenges in automation of flow gating	172
5.1.1	Performance: compute time and memory usage	173
5.1.2	Consistency	174
5.1.3	Accuracy	174
5.1.4	Interpretability	175
5.1.5	Choice of transformation	175
5.1.6	Visualisation of higher dimensional datasets	176
5.1.7	Ascertaining the number of clusters	177
5.1.8	Within sample noise	178
5.1.9	Between sample noise	180
5.1.10	Small number of samples	182
5.2	Moving from manual gating to automatic gating	184
5.2.1	Agreeing on standards	184
5.2.2	Extending manual analysis	186
5.3	Conclusion	188
Appendix A Flow markers		191
Appendix B		193

List of Figures

1.1	Flow cytometer diagram.	9
1.2	Leaking of signal from FITC fluorochrome into PE detector.	10
1.3	The same data encoded in FCS 2.0 (a) and FCS 3.0 (b).	12
1.4	Log transform inflates the variance around zero.	13
1.5	Effect of different values of w parameter of the Logicle transformation on the data distribution.	14
1.6	Normalisation by peak alignment.	17
1.7	Effect of shrinking variance in a two component Gaussian Mixture Model (GMM), with means fixed at 0 and 2, on the decision boundary.	22
1.8	Variance ratio criterion used to estimate the number of clusters with K-means.	28
2.1	Number of samples analysed per day.	33
2.2	Effect of time on CD25 MFI in memory cells.	33
2.3	Manual gating strategy followed by Dendrou et al (2009b).	34
2.4	Linear regression of bead APC MEF against the APC MFI as defined in Table 2.5.	38
2.5	Comparison of bead population MFI using manual and <code>flowBeads</code> gating.	38

2.6	Bead normalisation partially corrects for long term time effect in CD25 MFI of the memory cell population.	39
2.7	Position of the CD25 ⁺ gate over duration of experiment.	41
2.8	Mean square difference (MSD) of the position of the manual gate with that of <code>beads.thresh</code>	42
2.9	Agreement with manual of percentage of CD25 ⁺ naive cell phenotype.	42
2.10	Repeatability of percentage of naive CD25 ⁺ with manual (black) and <code>beads.thresh</code> (red).	43
2.11	Agreement with manual of the percent memory cell phenotype obtained with <code>mm</code> (a) and <code>spmm</code> (b).	46
2.12	Repeatability of the percent memory cell phenotype with manual (black), <code>mm</code> (red) and <code>spmm</code> (blue).	46
2.13	Example on individual d of the two approaches, <code>pct.thresh</code> (a and c) and <code>post.thresh</code> (b and d), of selecting a threshold.	48
2.14	Mean square difference (MSD) of the position of the manual gate with that of <code>pct.thresh</code> (a) and <code>post.thresh</code> (b).	49
2.15	Samples for which the 99 maximum posterior probability is not reached.	50
2.16	Agreement of memory CD25 MEF (a and b) and percentage of memory cells (c and d), obtained from <code>pct.thresh</code> and <code>post.thresh</code> with manual.	51
2.17	Influence of threshold for <code>pct.thresh</code> and <code>post.thresh</code> on distribution of memory CD25 MEF and percent memory cell phenotypes.	52

2.18	Repeatability of the memory cells phenotypes, CD25 MEF (a) and percentage (b), obtained from manual gating (black), pct.thresh (red) and post.thresh (blue).	52
2.19	Effect of rs2104286 on percent memory gated by manual (black), post.thresh (green) and pct.thresh (red).	56
3.1	Schematic of major IL-2 signaling pathway.	62
3.2	Number of cases and controls analysed per day in the 95 samples.	65
3.3	Gates applied across doses.	67
3.4	pSTAT5 distribution in the manually gated cell subsets from Figure 3.3.	68
3.5	pSTAT5 distribution in an individual on visit one (black) and visit two (red).	69
3.6	The percentage of pSTAT5 ⁺ cells increases with proleukin dose in memory Teffs.	70
3.7	The percentage of pSTAT5 ⁺ cells increases with proleukin dose in memory Tregs.	70
3.8	The percentage of pSTAT5 ⁺ cells increases with proleukin dose in naive Teffs.	71
3.9	The percentage of pSTAT5 ⁺ cells increases with proleukin dose in naive Tregs.	71
3.10	Repeatability of pSTAT5 ⁺ in six individuals in the four cell subsets.	72
3.11	Association test of percent pSTAT5 ⁺ in the four cell subsets.	72
3.12	Variation in pSTAT5 MFI is not captured by variation in bead MFI.	74

3.13 pSTAT5 intensity across the three proleukin doses, before (a) and after (b) per-cell baseline pSTAT5 subtraction in the un- gated sample.	75
3.14 Repeatability of pSTAT5 MFI measured as Pearson correlation squared (r^2) per dose per cell type.	76
3.15 Repeatability of the percent of pSTAT5 ⁺ as Pearson correlation squared (r^2) per dose per cell type.	77
3.16 Manually gated lymphocyte subsets projected on all core mark- ers.	79
3.17 Example of density-dependent downsampling on bivariate 50,0000 point dataset on CD45RA and CD25.	82
3.18 Lymphocytes: Minimum Spanning Tree (MST) generated by applying Spanning-tree Progression of Density-normalised Events (SPADE).	85
3.19 Lymphocytes: (a) Mapping of cell subsets defined by manual gates onto the MST obtained in Figure 3.18. (b) A manually identified subset of cells, SPADE.1 (purple).	86
3.20 Lymphocytes core markers: SPADE.1.	87
3.21 Lymphocytes pSTAT5 MFI dose-response: SPADE.1	87
3.22 Non-lymphocytes: pSTAT5 MFI coloured MST generated by applying SPADE on cells which fall outside of the lymphocyte gate.	88
3.23 Non-lymphocytes: SPADE.1b (purple), SPADE.2b (pink) and SPADE.3b (blue) mapped back to forward and side scatter coordinates.	89
3.24 Non-lymphocytes core markers: SPADE.1.	91
3.25 Non-lymphocytes pSTAT5 MFI dose-response: SPADE.1.	91

3.26 Sample recursively partitioned into 128 bins on side and forward scatter.	93
3.27 Each sample is recursively partitioned using 128 bins.	94
3.28 pSTAT5 response in sample recursively partitioned into 128 bins on side and forward scatter.	95
3.29 Lymphocytes: MST built using the 1024 bins obtained from recursive partitioning on the lymphocytes core markers.	97
3.30 Lymphocytes core markers: RPART.1 and RPART.2.	98
3.31 Lymphocytes pSTAT5 MFI dose-response: RPART.1 and RPART.2.	98
3.32 Non-lymphocytes: MST built on the 1024 bins obtained from RPART on non-lymphocytes.	100
3.33 Non-lymphocytes: RPART.1 (purple) does not belong to the lymphocytes population (black).	100
3.34 Non-lymphocytes core markers: RPART.1.	101
3.35 Non-lymphocytes dose-response: RPART.1.	101
3.36 Lymphocytes: First two components of Partial Least Squares (PLS) projection using pSTAT5 as response.	103
3.37 Lymphocytes core markers: PLSR.1.	104
3.38 Lymphocytes pSTAT5 MFI dose response: PLSR.1, PLSR.2 and PLSR.3.	105
3.39 Non-lymphocytes: First two components of PLS projection using pSTAT5 as response.	106
3.40 Non-lymphocytes core markers: PLSR.1 and PLSR.2.	107
3.41 Non-lymphocytes dose-response: PLSR.1, PLSR.2, PLSR.3, PLSR.4, PLSR.4 and PLSR.5.	107

3.42 CART of 1000 unit response against side and forward scatter identifies three subsets.	110
3.43 Lymphocytes: Recursive partitioning tree obtained for the pSTAT5 at 0.1 units (a), 10 units (b) and 1000 units (c) in the lymphocytes which do not belong to any manually identified cell subset.	111
3.44 Non-lymphocytes: Recursive partitioning tree obtained for the pSTAT5 at 0.1 units (a), 10 units (b) and 1000 units (c) in the non-lymphocyte cells.	112
3.45 Lymphocytes: Recursive partitioning of pSTAT5 response into low (red) and high (green) subsets.	114
3.46 Lymphocytes core markers: MMPART.1, MMPART.2 and MMPART.3.	115
3.47 Lymphocytes pSTAT5 MFI dose-response: MMPART.1, MMPART.2 and MMPART.3.	115
3.48 Non-lymphocytes: recursive partitioning of pSTAT5 response into low (red) and high (green) subsets.	117
3.49 Non-lymphocytes core markers: MMPART.1 and MMPART.2.	118
3.50 Non-lymphocytes pSTAT5 MFI dose-response: MMPART.1 and MMPART.2.	118
3.51 The progression of the marker MFI along the horizontal coordinate of the MST nodes in lymphocytes (a) and non-lymphocytes (b).	122
3.52 Lymphocytes: Partition tree obtained in two different samples from running CART on all core markers against pSTAT5 response at 1000 units.	126

3.53 Lymphocytes core markers: SPADE.1, RPART.1, RPART.2 and PLSR.1.	129
3.54 Lymphocytes pSTAT5 MFI dose-response: SPADE.1, RPART.1, RPART.2 and PLSR.1.	129
3.55 Non-lymphocytes core markers: SPADE.1, RPART.1, PLSR.1, MMPART.1 and MMPART.2.	131
3.56 Non-lymphocytes pSTAT5 MFI dose-response: SPADE.1, RPART.1, PLSR.1, MMPART.1 and MMPART.2.	131
3.57 Lymphocytes: CD56 ^{hi} cells within single batch show increased pSTAT5 MFI at 10 units.	133
3.58 Lymphocytes: CD56 ^{hi} cells at 10 units in four additional samples.	133
3.59 Non-lymphocytes: pSTAT5 MFI on side and forward scatter within a single batch.	135
3.60 New non-lymphocyte subset on core markers after doublet exclusion.	135
4.1 <i>KIR3DS1</i> and <i>KIR3DL1</i> ΔCt values for cases (red) and controls (blue) per qPCR plate.	146
4.2 Copy number calling of <i>KIR3DL1</i> / <i>KIR3DS1</i> from qPCR ΔCt.	148
4.3 Post-QC cases (red) and controls (blue) are plotted separately for each qPCR plate.	149
4.4 Repeatability of qPCR assay.	150
4.5 Overlay of ImmunoChip and qPCR samples for R and θ at SNP rs592645.	151
4.6 Signal plots of ImmunoChip SNPs which fall in the <i>KIR3DL1</i> region.	153

4.7	Leave-one-out crossvalidation error rate for k-nearest neighbour (KNN) prediction	155
4.8	Error rate of k-nearest neighbour (KNN) prediction from R and θ of SNP rs592645 in random subset of samples.	156
4.9	Flow chart summarising the key steps involved in the KNN imputation of <i>KIR3DL1/KIR3DS1</i> copy number in SNP data (R and θ signal) from qPCR copy number predictions obtained from GMM clustering.	171
B.1	Association test of pSTAT5 MFI with T1D.	194
B.2	Association test of pSTAT5 MFI, after nearest-neighbour normalisation, with T1D.	194
B.3	Association test of percent pSTAT5 ⁺ with T1D.	195
B.4	Association test of percent pSTAT5 ⁺ , after nearest-neighbour normalisation, with T1D.	195

List of Tables

1.1	Spillover matrix of the fluorochromes used by Dendrou <i>et al</i> italique (2009b) obtained using single colour beads.	11
2.1	Number of days till second visit for recalled individuals.	31
2.2	Distribution of subjects in study, by genotype, age and sex. . .	31
2.3	The fluorochrome-antibody panels with six markers used in the IL2RA dataset.	31
2.4	Repeatability and significance of effects of percentage of naive CD25 ⁺ CD25 MEF and percentage of memory cell phenotypes. .	33
2.5	FluoroSpheres from DakoCytomation.	37
2.6	Genotype, age and sex effect sizes on percentage of CD25 ⁺ cells.	54
2.7	Memory CD25 MEF effect sizes.	54
2.8	Memory percentage effect sizes.	55
3.1	Ten individuals recalled between 98 and 168 days later to assess stability of the cell phenotypes.	63
3.2	Proleukin stimulation assay antibody-fluorochrome panels. . .	64
3.3	Lymphocytes: Cell phenotypes of identified subsets.	128
3.4	Non-lymphocytes: Cell phenotypes.	130
4.1	Grouping of HLA alleles by HLA-Bw4 epitope.	141

4.2 Classification of subjects in study by HLA epitope (as defined in Table 4.1).	142
4.3 The qPCR probes and primers.	144
4.4 ImmunoChip SNPs which fall in <i>KIR3DL1</i>	154
4.5 Association test of <i>KIR3DS1-KIR3DL1</i> copy number with T1D.	159
4.6 Association test of <i>KIR3DS1-KIR3DL1</i> copy number with T1D, conditional on HLA-Bw4.	160
4.7 Case-only χ^2 test for interaction between <i>KIR3DS1-KIR3DL1</i> copy number and HLA-Bw4, across the ten multiply imputed qPCR and SNP datasets.	161
4.8 Proportion of cases to controls in all known Killer Immunoglobulin-like Receptor (KIR) studies in T1D.	164
4.9 Case-control ratio in all known KIR studies in T1D.	165

Contributors

Calliope Dendrou.....40

Charlie Bell.....96, 128

Deborah Smyth 143

James Traherne 168

Linda Wicker.....47

Marcin Pekalski 80, 130

Tony Cutler 63, 66, 67, 73, 119, 130, 188

Abbreviations

1958BC British 1958 Birth Cohort	142
AIC Akaike Information Criterion	27
AML Acute Myeloid Leukemia	92
ANN Approximate-Nearest-Neighbour	74, 108, 135, 173
ANOVA ANalysis Of VAriance	27, 157
BIC Bayesian Information Criterion	27
CART Classification And Regression Tree.....	108–110, 113, 123
CN Copy Number	171
D-GAP Diabetes - Genes, Autoimmunity and Prevention	63
EM Expectation Maximisation.....	21, 44, 57, 147, 186
FCS Flow Cytometry Standard	11, 184
FlowCAP Flow Cytometry Critical Assessment of Population Identification Methods	
18	
GMM Gaussian Mixture Model.....	19, 20, 22, 23, 27, 113, 114, 116, 117, 171, 180

GRID Genetic Resource Investigating Diabetes	142
GWAS Genome-Wide Association Study	2, 5, 139
HIP Human Immunology Project	15
HLA Human Leukocyte Antigen	5, 138, 162
HWE Hardy-Weinberg Equilibrium	163, 169
IL-2 interleukin-2	4
ITIM Immune Tyrosine-based Inhibitory Motif	138
KIR Killer Immunoglobulin-like Receptor	138, 139, 164, 165
KNN k-nearest neighbour	151, 152, 155, 174
LD Linkage Disequilibrium	167, 169
LOO leave-one-out	179
LOOCV leave-one-out cross-validation	152, 171
MARS Multivariate Adaptive Regression Splines	124
MDS multidimensional scaling	81, 123
MEF Molecules of Equivalent Fluorochrome	35, 36
MFI Mean Fluorescence Intensity	35, 36, 66, 85, 181, 183
MISE Mean Integrated Square Error	59
ML Maximum Likelihood	176

MSD Mean Square Difference	58
MST Minimum Spanning Tree .	82–86, 88, 89, 92, 96, 97, 102, 108, 111, 121–123, 132
NK Natural Killer	84, 138
PBMC Peripheral Blood Mononuclear Cells.....	78, 120, 136, 182
PCA Principal Component Analysis.....	81, 102, 142, 180
PLS Partial Least Squares	102–107, 123
PRIM Patient Rule Induction Method	124
qPCR quantitative Polymerase Chain Reaction.....	2, 3, 143, 144
RF Random Forests.....	125, 169, 175
SNP Single Nucleotide Polymorphism	2, 3, 5, 29, 139, 162
SPADE Spanning-tree Progression of Density-normalised Events...	81–83, 85, 88, 92, 108, 121, 177
T1D Type 1 Diabetes	3–5, 61, 64, 69, 127, 138, 162, 165, 172
Teff effector T cell	75
Treg regulatory T cell.....	61, 75
viSNE visual Stochastic Neighbour Embedding	177, 180

Genes

<i>CTLA4</i>	5	<i>KIR3DS1</i> ..	137, 139, 140, 143–161, 167,
<i>FOXP3</i>	61		168, 171, 178
<i>HLA-A</i>	141	<i>PTPN2</i>	61, 69
<i>HLA-B</i>	141	<i>PTPN22</i>	5
<i>HLA-DQ2</i>	166	<i>STAT6</i>	143, 144
<i>HLA-DQ8</i>	166		
<i>HLA-DQB1</i>	6		
<i>HLA-DRB1</i>	6		
<i>IFIH1</i>	5		
<i>IL2RA</i>	5–7, 29, 30, 61, 69		
<i>INS</i>	5		
<i>KIR2DL1</i>	166		
<i>KIR2DL2</i>	162, 163, 166		
<i>KIR2DL3</i>	166, 167		
<i>KIR2DL4</i>	168		
<i>KIR2DL4*005</i>	168		
<i>KIR2DL5</i>	162, 167		
<i>KIR2DS1</i>	167		
<i>KIR2DS2</i>	162, 166		
<i>KIR2DS4</i>	167		
<i>KIR2DS5</i>	167		
<i>KIR3DL1</i> ..	137, 139, 140, 143–161, 167,		
	168, 171, 178		

SNPs

- rs11594656 30, 54, 55
rs12722495 30, 32, 33, 54, 55, 61, 69
rs1893217 61
rs2104286 30, 32, 33, 53–56
rs2756923..... 162, 163
rs45450798 69
rs478582..... 69
rs592645..... 152–156, 167, 168, 171

Proteins

CD122.....	62, 78
CD127.....	30, 32
CD132.....	62, 80
CD16	127
CD25 ..	29, 30, 32, 33, 39–43, 54, 57, 61,
	62, 66, 78, 183
CD4	30, 61
CD45RA.....	32, 35, 47, 51, 57, 183
CD8.....	30
FOXP3.....	32
IL-2	29, 61
IL2RA.....	62, 191
IL2RB.....	62
IL2RG	62
KIR3DL1	140

Chapter 1

Introduction

Il n'y a pas de citadelle inattaquable, il
n'y a que de

1.1 Motivation

Over the last twenty years, the size and dimensionality of biological datasets has increased at a tremendous rate, giving rise to very large data matrices. There is growing interest in developing computational methods for identifying patterns or trends within these datasets. However, the analysis of such large datasets is not without difficulties for both practical and theoretical reasons. One of the major challenges is dealing with noise due to differences in instrument configuration, experimental protocol or method of analysis. This complicates the extraction and comparison of biologically useful information across datasets. Another challenge is identifying rare subsets and outliers. Rare subsets may be biologically significant whereas outliers tend to be noisy samples which can skew association statistics. Throughout my thesis I will investigate how to address these issues using normalisation and clustering techniques. In particular, I will focus on normalisation and clustering of cell-level parameters, acquired with flow cytometry,

as well as genetic data, acquired from quantitative Polymerase Chain Reaction (qPCR) and Single Nucleotide Polymorphism (SNP) arrays. SNP arrays have been at the core of Genome-Wide Association Study (GWAS) over the last ten years. They concurrently probe several hundred thousand of SNPs within an individual and the technology has been parallelised so that a single experiment can assay thousands of individuals. Each SNP probe is fluorescently labelled so that at a given genomic locus, the intensity values can be clustered across individuals, after normalisation. Genotypes at a given locus can be called by individual, depending on the cluster in the pooled dataset to which the individual is assigned. Common genotypes form larger clusters whereas rarer genotypes form smaller clusters. An equally influential technology which has brought cell biology into the sphere of “big biology”, is flow cytometry, a high-throughput technique for measuring up to twenty cell parameters in millions of cells. In flow cytometry, clustering is performed to group similar cell measurements to identify cell types within a sample. Typically, the relative size of these clusters and their means are of biological interest and are compared between samples after normalisation. While clustering applied to SNP calling can be fully automated, clustering in flow cytometry is still reliant on manual inspection. One reason is that clustering of cell types is more uncertain than clustering of genotypes because the number of cell types is unknown and cells are often in intermediate states between cell types. In genetics, in the absence of copy number variation, the expected number of clusters at a given locus is typically known since there are only a finite number of possible genotypes at a SNP.

The choice of normalisation and clustering methods can have an important impact on reproducibility and association statistics (Plagnol et al, 2007). The influence of clustering on reproducibility and association testing will be the focus of Chapter 2, where I revisit a large, long-running flow cytometry experiment designed to measure genotype-phenotype correlation in hundreds of individuals. The cell type clustering was

initially conducted manually by drawing gates to delineate populations of cells. I assess the influence of clustering method on association testing, when part of the gating is replaced by computational thresholding and clustering methods.

In Chapter 3, I analyse another flow cytometry dataset, this time an *ex vivo* stimulation dataset, primarily generated to assess whether there are differences in stimulation response in certain cell types, between type 1 diabetics and matched controls. I will once more consider normalisation for the purpose of improving the reproducibility of the cell phenotypes and hence the power of association testing. Furthermore, I apply computational methods to discover new clusters not identified by manual gating which are responsive to stimulation.

In Chapter 4, I apply normalisation and clustering to genetic copy number genotyping of qPCR and SNP array data where no prior manual analysis has been done. Instead, I use prior information in terms of population frequencies obtained from previous studies to guide the clustering of qPCR data. The clusters applied in qPCR are used to identify the SNP patterns which are predictive of copy number, using supervised clustering.

Finally, I will conclude with what I have learned about normalisation and clustering in general, and the specifics of their application to these datasets. I will discuss how these methods could be further applied and refined, especially with respect to flow cytometry, where they are not yet as commonly used as in genetics.

1.2 Biology of type 1 diabetes

Since all the datasets I have analysed in my thesis relate to Type 1 Diabetes (T1D), I will first give some background on what we know about the disease and the technologies we are using to gain new insight.

1.2.1 Aetiology and diagnosis

T1D (OMIM:222100), also known as insulin dependent diabetes mellitus (diabetes - διαβήτης, a passer through, and mellitus - μέλι, honey), is a disease reported as early as 1500 BC (Poretsky, 2010). It holds its name from the characteristic symptom of excessive discharge of high-glucose urine (glycosuria or hyperglycemia-induced osmotic diuresis polyuria). It has since been established that this symptom is the consequence of persistently high levels of glucose (hyperglycemia) in the blood due to an insufficiency in insulin, the hormone responsible for glucose regulation. Long term high-glucose levels lead to dehydration, drowsiness, cardio-vascular complications, increased chances of morbidity and death. If left untreated T1D is a debilitating and life-threatening disease. From post-mortem analysis of pancreatic samples and animal models, it is widely accepted that the cause of the insulin deficiency in T1D is an autoimmune reaction in which insulin and insulin-producing β -cells of the pancreatic islets are progressively destroyed primarily through auto-reactive T cells (Todd, 2010).

In the last 50 years, the number of cases of T1D worldwide has increased and is predicted to continue increasing in the next decade, affecting mainly children under the age of 5 (Patterson et al, 2009). The World Health Organization reported that in August 2011 around 34 million people worldwide were diagnosed with T1D. At present there is no cure for T1D. The only existing treatment is the regular subcutaneous injection of exogenous insulin. Pre-symptomatic detection of T1D relies on testing for presence of auto-antibodies against insulin and its precursors. Early detection of T1D allows a better understanding of how the disease progresses and how we can develop therapies to delay its onset, reduce the symptoms and hopefully in the future, cure the disease. One such therapy currently undergoing clinical trials in our lab attempts to restore immune tolerance to pancreatic β -cells with low-dose interleukin-2 (IL-2), in newly diagnosed T1D patients (<http://www.clinical-trials-type1-diabetes.com/>).

1.2.2 Genetics of type 1 diabetes

Patterns of familial clustering suggest that a portion of T1D risk is inherited. A measure of heritability used by geneticists is the sibling recurrence risk λ_s , which is defined as the ratio of the probability that a sibling of an affected individual has the disease to the probability of a random individual in the population having the disease. For T1D, λ_s has been estimated to be close to 15 (Risch, 1987), although Clayton (2009) suggested that this might be an overestimate and that λ_s is more likely to lie between 5 and 8.9.

Regardless of the exact estimate of λ_s , some genetic predisposition to T1D is indisputable and researchers have long been interested in identifying likely causal variants in our genetic code that could lead to some insights into the mechanism of the disease. Linkage studies based on the recombination of multiallelic genetic markers in families affected by T1D first mapped a genetic risk factor to the Human Leukocyte Antigen (HLA) region on chromosome 6 (Singal and Blajchman, 1973; Cudworth and Woodrow, 1974; Nerup et al, 1974). As insulin is a target of the autoimmune response in T1D, the insulin gene (*INS*), on chromosome 11, was tested as a strong candidate region and was also found to associate with the disease (Bell et al, 1984; Permutt et al, 1984). In 1994, Davies et al, using a linkage map of 290 marker loci in 96 sibling pairs, confirmed the association with the HLA and insulin gene regions, and further reported a number of new chromosome regions showing some evidence of linkage to T1D. The study confirmed that T1D is a polygenic disease and that, there were unlikely to exist other loci with as strong an effect as HLA.

More recently, GWAS using high density SNP arrays have confirmed strong association of T1D within the HLA (chromosome 6p21) and *INS* (chromosome 11p15) loci, and reported 50 other loci, including regions near *CTLA4* (chromosome 2q33), *PTPN22* (chromosome 1p13), *IL2RA* (chromosome 10p15) and *IFIH1* (chromosome 2q24) (Smyth et al, 2006; Nejentsev et al, 2007; Wellcome Trust Case Control Consortium, 2007; Bar-

rett et al, 2009). Within the HLA region, the strongest effect comes from the HLA class II loci, *HLA-DRB1* and *HLA-DQB1*, but, there is evidence for additional independent effects from the HLA class I loci, involving HLA-A and HLA-B alleles (Nejentsev et al, 2007; Howson et al, 2009). A comprehensive and updated list of all T1D associated loci found so far is maintained on the T1DBase website (www.t1dbase.org).

1.2.3 The immune cell mechanisms

Many of the reported T1D-associated genetic variants are located in proximity to genes and regions with known immune function such as HLA and *IL2RA*, which code for receptors found at the surface of immune cells.

Immune cells are white blood cells formally known as leukocytes, that function in the lymph nodes and other lymphoid tissues but can also be found at lower concentrations in the peripheral blood as they circulate throughout the body. They include lymphocytes, monocytes and granulocytes, and within these subsets, there exists a huge diversity in terms of size, gene expression and function. It is this diversity that enables the versatility of the immune system in neutralising all kinds of pathogens. The first line of defence, innate immunity, is mediated by the recognition of a limited set of conserved pathogenic epitopes. This leads to the rapid recruitment of myeloid cells (mainly dendritic cells, macrophages and monocytes) and an inflammatory response. If this mechanism is not sufficient to clear the pathogen, then antigen presenting cells can recruit T lymphocytes, also known as T cells, which can be clonally expanded and lead to an adaptive response. After having undergone central selection in the thymus, T cells in the peripheral blood have an affinity for foreign antigens but are tolerant to self. Initially these cells are in a naive state (naive T cells) until presented with an antigen, at which point they mainly differentiate into effector T cells, capable of mounting an immediate response, but also into longer-lived memory T cells, capable of mounting a stronger and faster response

in the future thus resulting in long lasting immunity against this pathogen (acquired immunity). In order to moderate the scale of the immune response and preserve self-tolerance, some T cells also have a regulatory function on the immune response mediated by small signalling molecules known as cytokines. These regulatory T cells are important in preventing autoimmunity and hence are the object of thorough study in T1D. Hence adaptive immunity is antigen specific and depends on the generation of high-affinity T cell receptors which leads to immunological memory. The whole process takes much longer (approximately 7 days), but some residual memory persists after the pathogen is cleared, which makes secondary reactions much more efficient.

Some insight into the aetiology of T1D may be gained by seeing how T1D-associated genetic variants correlate with quantitative cell phenotypes such as, ratios of different cell types or mean expression of surface proteins. For example, Dendrou et al (2009b) showed that protective T1D risk variants in proximity of the protein coding gene *IL2RA*, correlate with increased mean expression of CD25 on the surface of memory T cells. CD4⁺ memory cells with higher CD25 levels are likely more responsive to IL-2 and TCR-mediated activation, which in turn leads to increased production of IL-2, suggesting a mechanism by which self-tolerance may be boosted.

1.3 Studying the immune system with flow cytometry

The established method for measuring immune cell phenotypes is flow cytometry. By labelling cells with fluorescent probes conjugated to antibodies, it is possible to distinguish a wealth of distinct cell subsets which concomitantly express specific molecules. Flow cytometry allows us to identify and quantify different types of cells, through individual cell measurements.

The flow cytometer Fluorescence intensity is measured accurately using photosensitive detectors, normally a photomultiplier tube (PMT), which turn light into an analogue (current or voltage) or digital (photon counting) electronic signal which is translated into a digital number indicating the intensity of the fluorescence (Shapiro, 2003; Snow, 2004). For a fluorochrome to emit fluorescent light, it needs to have absorbed high energy light of a given wavelength from an illumination source, usually from a laser, which it can then release at a lower energy, longer wavelength, resulting in a so-called Stokes shift. The wavelength spectrum at which a given fluorochrome most efficiently absorbs and emits light and Stokes shift are known and depend on the physico-chemical properties of that molecule. To enable optical illumination, separation and collection of various fluorochromes with different emission and excitation spectra, a flow cytometer is usually equipped with several lasers which emit at different wavelengths and specially configured optical mirrors, filters and photosensitive detectors which are sensitive to light at distinct frequency ranges (Shapiro, 2003).

Sample staining When staining a sample, fluorochromes are conjugated with antibodies with an affinity for the target polypeptide we wish to quantify. The target can be external, such as a cell receptor, or internal, such as a transcription factor or a cytokine. If the target is internal, the cells have to undergo permeabilisation that can deteriorate the general quality of the staining. Fluorochromes should be selected to minimise overlapping of their emission spectra. Spectral overlap, also known as spillover, leads to a convoluted signal reaching the detectors. Antibodies are also a potential source of noise, since both primary and secondary antibodies may bind to more than one target. Antibodies differing in the variable chain, known as isotypes, or non-immune sera, can be used to control non-specific staining and/or reduce non-specific binding by blocking secondary targets.

Running a sample on the flow cytometer Once a solution of fluorescently labeled cells is fed to the flow cytometer, the sample is delivered to the flow cell after hydrodynamic focusing (Figure 1.1). In the flow cell, the cells are filed up individually so

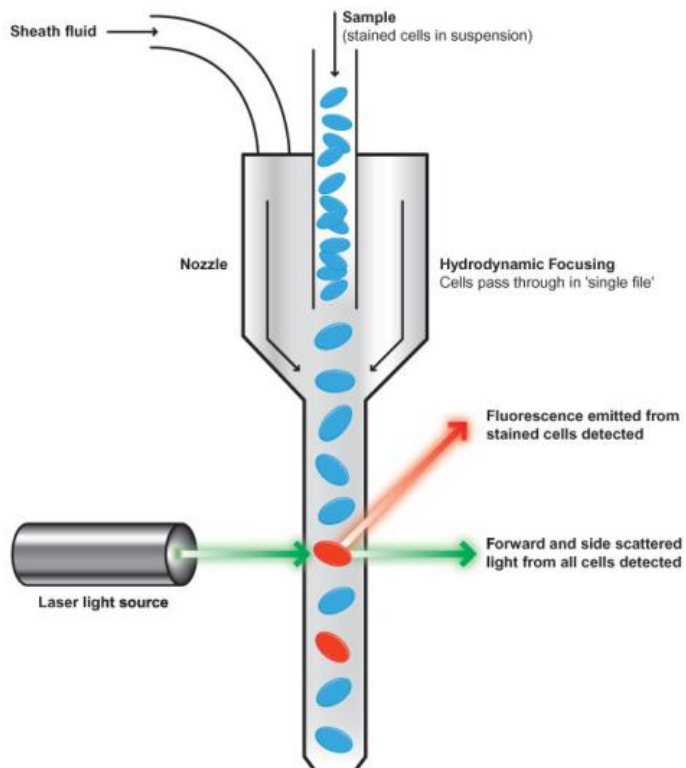


Figure 1.1. Flow cytometer diagram. Source www.abcam.com

they cross a laser beam one by one (Shapiro, 2003). As a cell crosses the laser beam some light is scattered and some is absorbed. The detected scattered light is used to provide an estimate of the size and granularity of the cell. Light scattered in the forward direction (diffracted light) is correlated with the size of the cell, whereas light scattered sideways (refracted light) is correlated with the complexity of the cellular structure. The absorbed light is later emitted as heat and fluorescent light. The intensity of the scattered and fluorescently emitted light measured by the detector thus provides quantitative information about the correlates of size and granularity, and the presence of

certain fluorescently-marked molecules for each cell. When examining leukocytes using only the physical properties provided by the scattered light intensity, it is possible to distinguish lymphocytes from monocytes and more granular neutrophils. Combining this information with the fluorescent intensities it is possible to further distinguish between different types of lymphocytes which have in common certain cellular receptors or transcription factors.

Fluorescent crosstalk As we delve deeper into the lymphocyte subsets more fluorochromes are needed to further distinguish between different classes (Perfetto et al, 2004). However when adding more and more fluorochromes, overlap of emission spectra becomes unavoidable (Roederer, 2001). This implies that the intensity signal measured in one detector is in fact a mixture of signals from other fluorochromes which spillover across detectors (Figure 1.2). The deconvolution of this signal is a process known as compensation. The matrix solution is known as the spillover matrix and is usually a

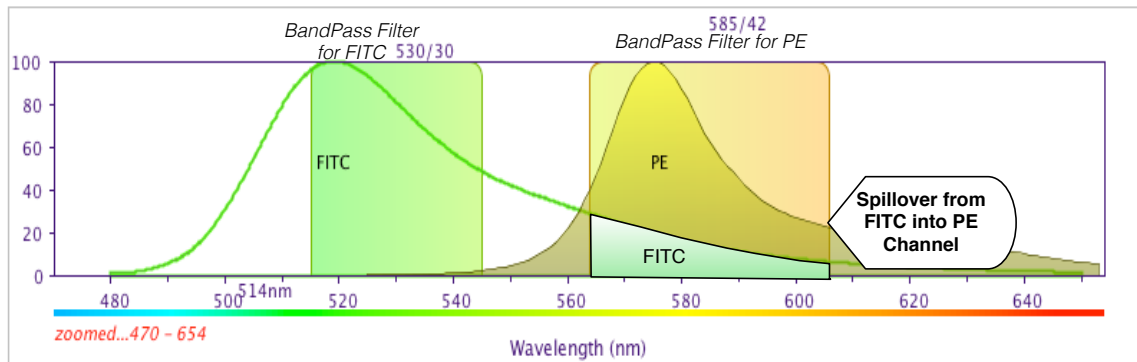


Figure 1.2. Leaking of signal from FITC fluorochrome into PE detector.
Created using: http://www.bdbiosciences.com/research/multicolor/spectrum_viewer/

square matrix with as many rows as there are fluorochromes and columns as there are detectors. To calculate the spillover matrix, single coloured beads are used. The pairwise contribution of a fluorochrome to a non-specific channel is then summarised as a compensation matrix (Table 1.1). By subtracting the spillover values from the mixed

intensity one can then recover the original intensity. This compensation step is usually performed after all the data from an experiment has been collected before commencing analysis.

Signal \ Detector	PMT 1	PMT 2	PMT 3	PMT 4	PMT 5	PMT 6
Signal						
Alexa-488	1	0	0	0.16	0	0
PE-Cy7	0	1	0	0.1	0.2	0
APC	0	0	1	0	0.3	0
PE	0.2	0.1	0	1	0	0
Alexa-700	0	0.1	0.2	0	1	0
Pacific Blue	0	0	0	0	0	1

Table 1.1. Spillover matrix of the fluorochromes used by Dendrou et al (2009b) obtained using single colour beads. Each entry is the percentage of the emitted fluorochrome signal (row) picked up by a detector (column). The rows represent the fluorochromes and the columns are the PMT detectors. Each detector is tuned to capture the intensity of a single fluorochrome (diagonal entries). Spillover occurs when certain fluorochromes are detectable by more than one detector (non-zero terms off the diagonal). Notice that there is an appreciable spillover (30 %) of APC into PMT 5, the detector meant for Alexa-700.

Compensation to account for fluorescence crosstalk is just one of the intricacies of flow data. Other intricacies are data format and the choice of the data transformation, which can both have an important impact on the analysis.

Flow cytometry data format The data format determines the range and the precision of the data stored. The objective of the Flow Cytometry Standard (FCS) is to define a unified file format for flow data that allows files created by one type of acquisition hardware and software to be analyzed by any other type. The first FCS format for data files was FCS 1.0 (Murphy and Chused, 1984). The standard was later updated in 1990 as FCS 2.0 (Dean et al, 1990) and again in 1997 as FCS 3.0 (Seamer et al, 1997). FCS 2.0 and FCS 3.0 are the current two main competing standards. FCS 2.0 is a logarithmically compressed format which does not allow negative intensities. Instead

negative values reported by the instrument are arbitrarily assigned the minimum value. This leads to what is described as the log artefact: a pile-up of intensities on the axes for low intensity values. FCS 2.0 data are integers in the range 1 to 10000 (4 decades). FCS 3.0 on the other hand is closer to the raw data, covers a greater range and allows for negative values. FCS 3.0 leaves more flexibility to the choice of transform. FCS 3.0 are floating point numbers in the range -211 to 262143 (8 decades) FCS 2.0 requires practically no post processing except for a log transform. FCS 3.0 requires more careful thought as it leaves to us the compensation and the choice of a suitable transformation. For low intensity fluorescence, FCS 3.0 is the preferred format as the truncation at zero of intensity values for FCS 2.0 can lead to loss of information (Figure 1.3).

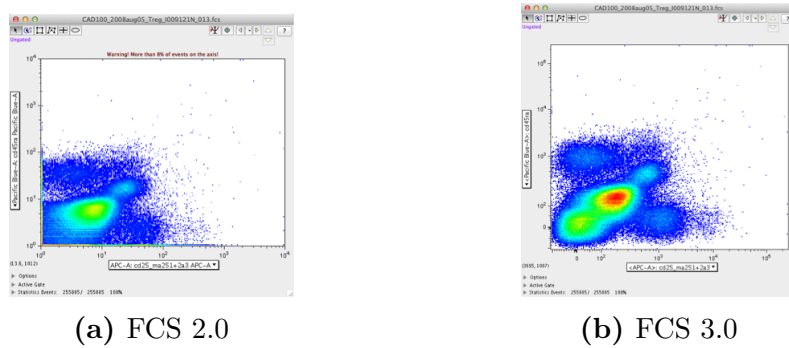


Figure 1.3. The same data encoded in FCS 2.0 (a) and FCS 3.0 (b). In FCS 2.0 (a), truncation at zero leads to loss of low intensity clusters as compared to FCS 3.0 (b).

Data transformation for display and analysis As fluorescence intensity tends to scale multiplicatively, intensity data needs to be linearised for the purpose of visualisation and clustering. Clustering algorithms based on variance (average distance to the mean) perform poorly on skewed data, and in general humans are more comfortable dealing with data on a linear scale. Given FCS 2.0 data is strictly positive, a simple \log_{10} transform is usually applied to linearise the data. As FCS 3.0 allows for negative values a different transform is required. Transforms that are closer to linear near zero are

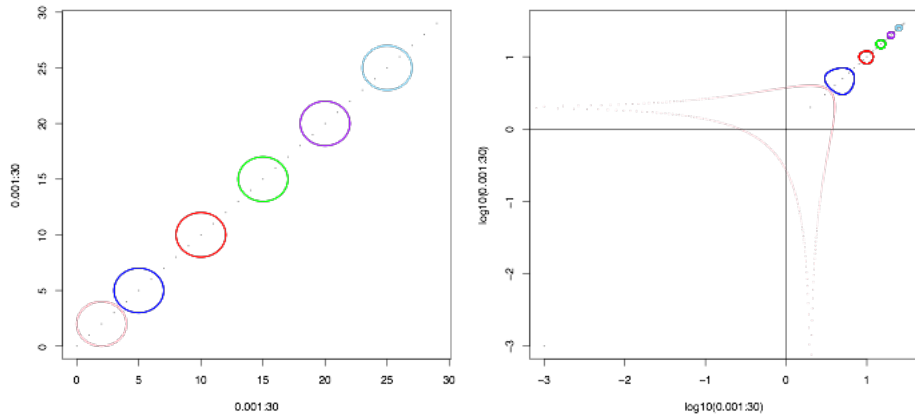


Figure 1.4. Log transform inflates the variance around zero. Depicted on the left are circles of equal diameter viewed on a linear scale. These circles represent spherical two-dimensional Gaussian distributions of equal covariance. When a logarithm transform is applied, the shape of the circles are distorted and they no longer have the same area.

preferred, since the logarithmic transform is distorting (Figure 1.4) for low intensity values (Durbin et al, 2002; Herzenberg et al, 2006). Some appropriate transformations for FCS 3.0 are the Generalized Arcsinh, the Logicle transform, the LinLog and the Generalized BoxCox (Bagwell, 2005; Parks et al, 2006; Finak et al, 2010b). Given the data, parameters for these transformations can be estimated using maximum likelihood assuming a multivariate Gaussian distribution of the data (Finak et al, 2010b). However, as illustrated by Herzenberg et al (2006), care needs to be taken as the transforms can introduce spurious peaks in the intensity distribution around zero. The Logicle transform as defined by Parks et al (2006), is the most widely used transform for FCS 3.0 data and is the one I used in this thesis. It takes as input the w parameter which influences the linearization width around zero in asymptotic decades. The influence of the w parameter on the shape of the transformed intensity distribution is illustrated in Figure 1.5.

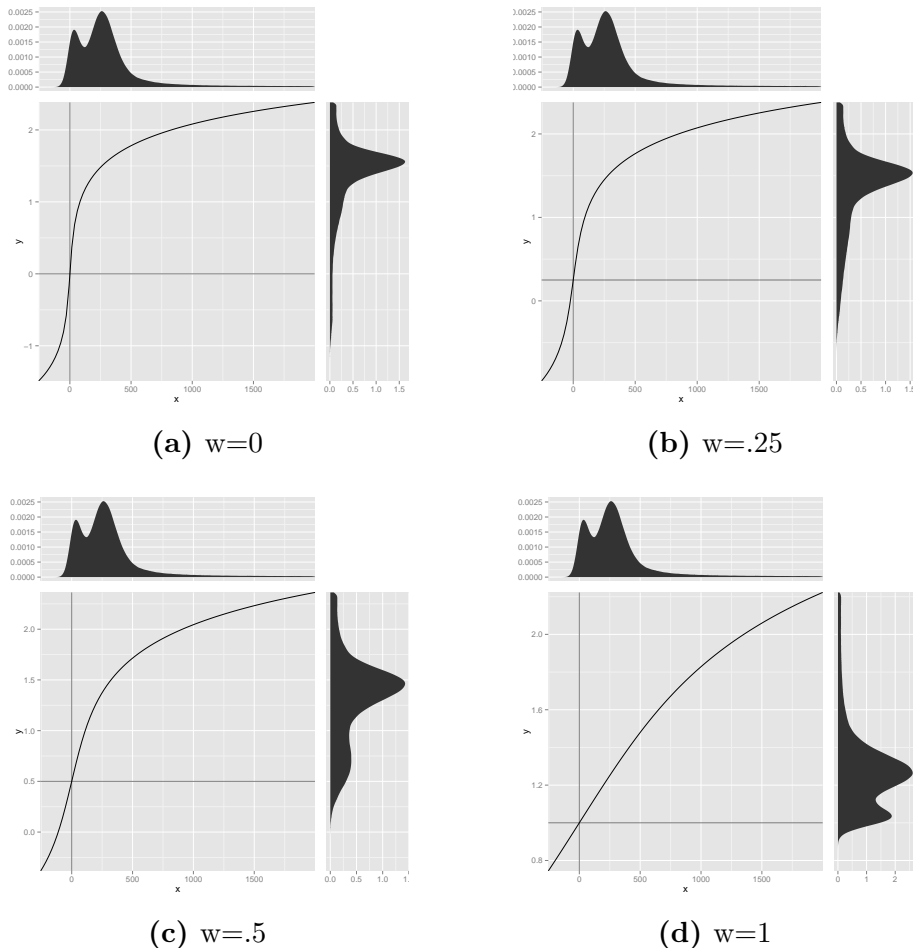


Figure 1.5. Effect of different values of w parameter of the Logicle transformation on the data distribution. The Logicle transform maps the data distribution defined on x to the data distribution defined on y . The transform approximates a linear transform near zero and a log transform elsewhere. The w parameter maps the zero of the transform to w .

Noise in flow cytometry Beside these data format and transformation intricacies, there are many sources of noise in flow cytometry that complicate sample comparison and impact reproducibility:

- **Sample processing and storage conditions noise.** Certain surface markers are more fragile than others and may be shed when cells are frozen for storage. Also certain chemical treatments like permeabilisation can affect the quality of the staining.
- **Noise associated with the staining of the sample.** The qualitative and quantitative choices for selecting antibodies and fluorochromes influence the quality of the staining. Antibodies have a tendency to be sticky and can bind to other targets in an erratic manner leading to spurious signal. The level of non-specific binding can be assessed with isotype control antibodies.
- **Noise linked to the instrument.** The reliability of the lasers and detectors may decrease with time. Fluorescent beads can be used to detect and correct these variations.
- **Noise due to the flow operator.** Sometimes the operator might decide to not collect all the events and may apply a cutoff on the side and forward scatter.

All these sources of noise contribute to different patterns of staining and concentrations of debris which may lead to spurious cell populations or skew the analysis, complicating the analysis across samples and laboratories. Some of these issues are being addressed by the Human Immunology Project (HIP) consortium standardisation efforts (Maecker et al, 2012), which aims to enhance reproducibility of flow analysis results across laboratories, through the use of lyoplates, and agreement on experimental protocols and instrument configurations. However, data analysis techniques such as normalisation are still necessary to deal with residual noise.

1.4 Normalisation

The purpose of normalisation is to remove unwanted experimental variation to make data comparable even when the samples are collected on different days, processed with different protocols or instrumental configurations. Nonetheless, distinguishing between unwanted and biological variation necessitates some prior knowledge about the datasets, either in the form of global distributional assumptions or in the form of local features which exist in a predictable relationship across samples. In microarray gene expression datasets, for example, one distributional assumption is that the majority of genes are not differentially expressed between similar samples, hence the expected log ratio of gene expression in two samples should be centered on zero (Smyth and Speed, 2003; Bolstad et al, 2003). It is also possible to use reference points to normalise across samples by using local features of the distribution or objects with known properties, such as beads in flow cytometry or reference probes in microarrays. In microarray, since the number of data points is constant and the distributions are unimodal across samples, normalisation methods like quantile normalisation perform well (Bolstad et al, 2003). However, in flow cytometry, this type of normalisation is not appropriate because samples contain different number of events and the distributions are typically multimodal, as commonly found in datasets containing mixtures of groups. While in theory, the locations of these modes or peaks of the density function should remain fairly stable across samples provided experimental parameters are kept constant, in practise there is often variation attributed to factors that are beyond our control such as long-term instrument decalibration. On the other hand, the height of the peaks, the relative frequencies of the cell populations, are expected to change since they are sensitive to sampling variation. These observations motivate a normalisation method which aligns the peaks of the distributions so that cell populations are centered in a similar location across samples even when their relative proportions change. The implementation of this normalisation method then depends

on the technique used to identify and match the peaks across samples. One method of identifying peaks of the density function is with a sliding window approach. The sliding window records the point with the highest density estimate in the current window and returns a list of highest density points of which the top K may be chosen. This is one of the approaches implemented in the R BioConductor package **flowStats** (Hahne et al, 2013). Figure 1.6 illustrates this method on real flow data where two common groups stand out and are reasonably well separated. Unfortunately, peaks are not always consistently identifiable across samples. In these cases, it may be preferable to only identify the most distinguishable subset of peaks, those representative of the most common groups, in order to do the alignment.

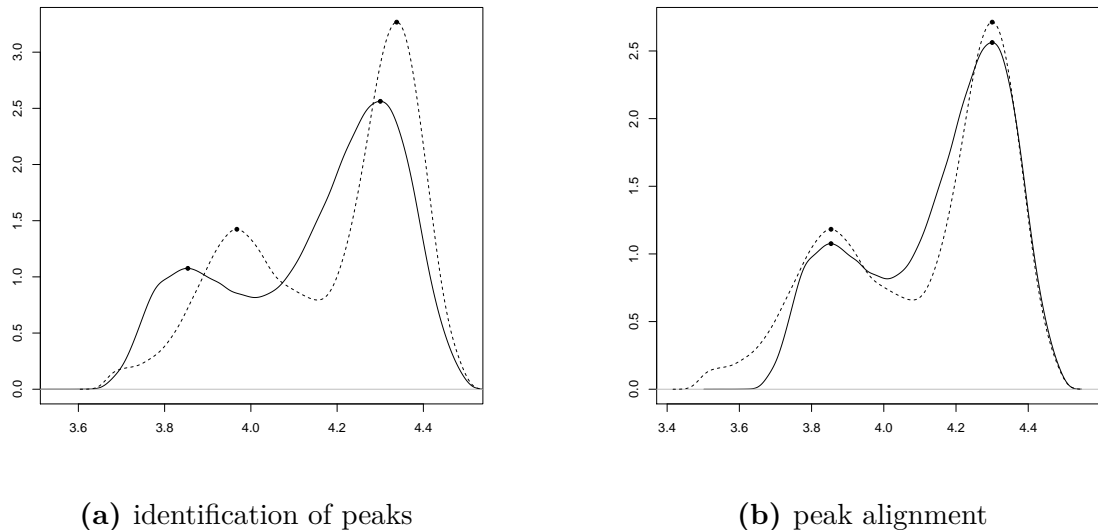


Figure 1.6. Normalisation by peak alignment. Distributions of the same marker in two different flow cytometry samples. The two peaks of each distribution are identified in (a) using a sliding window of size 40 on the density function and aligned in (b) using a linear transform.

1.5 Manual clustering

Once the data has been made comparable thanks to normalisation, the next task is to identify clusters, which in the case of flow cytometry are groups of cells that share some similar properties, that can be matched across samples.

Given a one, two or three dimensional projection of the data, clusters may be visually identifiable. In flow cytometry data, this approach, known as manual gating, is a step-by-step method where we consider and plot one or two channels at a time and delineate a region, called a gate, such that cells which lie outside the gate are filtered out. The result is that a population is defined as an intersection of multiple one or two-dimensional gates.

However, manual gating suffers from a number of drawbacks. Firstly, manual gating introduces technical variation since the position and ordering of the gates on the same data can differ between gaters (Maecker et al, 2010). It suffers from strong bias as it tends to force data to fit a model (the gater's expectation). Also as only the pairwise correlation can be assessed, identification of higher-dimensional clusters may be compromised. Finally, manual gating is not practical when an exhaustive enumeration of all identifiable cell populations is required (Siebert et al, 2010; Aghaeepour et al, 2012) especially as the number of cellular markers increases. For this, unsupervised computational methods, which do not rely on visualisation, are needed.

1.6 Automatic methods for identifying clusters

Unsupervised flow data analysis methods have been reviewed by Bashashati and Brinkman (2009), Lugli et al (2010), and, more recently, by Aghaeepour et al (2013). They are benchmarked annually by the Flow Cytometry Critical Assessment of Population Identification Methods (FlowCAP) group and broadly fall in two camps: unsupervised meth-

ods which have have unlabelled data and supervised methods which require manual training by giving approximate starting gates.

Clustering methods which make explicit assumptions about the shapes of populations are model-based or parametric. Methods which do not, are said to be model-free or non-parametric, although the latter can be limiting cases of parametric models. Here I will mostly focus on unsupervised methods where training data is not provided.

1.6.1 Model-based methods

Model-based methods stipulate that flow data can be explained by a mixture of multivariate distributions where each distribution is representative of a different type of cell. A useful property of these methods is that they can assign a probability of population membership to each cell which can be exploited in downstream statistical analysis to account for uncertainty in the clustering. The first and simplest of these methods applied to flow cytometry data (Chan et al, 2008), assumed cell populations could be represented by a Gaussian Mixture Model (GMM) of K multivariate Gaussians:

$$p(x_i) = \sum_{k=1}^K \tau_k \frac{1}{\sqrt{(2\pi)^2 |\Sigma_k|}} e^{-\frac{1}{2}(\mathbf{x}_i - \boldsymbol{\mu}_k)^T \boldsymbol{\Sigma}_k^{-1} (\mathbf{x}_i - \boldsymbol{\mu}_k)}; \quad \sum_{k=1}^K \tau_k = 1$$

where x_i are the coordinates of the i^{th} cell in a data set of size N . The parameters, $\boldsymbol{\mu}_k$, $\boldsymbol{\Sigma}_k$ and τ_k , correspond to the cluster mean, covariance and weight, respectively, and k indexes the clusters from 1 to K . Assuming the data are identically and independently distributed, we can attempt to estimate the parameter θ , representing the sets of (μ, Σ, τ) , which maximises the joint probability, or likelihood function, of observing the data given the model:

$$\mathcal{L}(\theta | X) = \prod_{i=1}^N p(x_i | \theta).$$

As products of small numbers are hard to deal with analytically and are numerically unstable, this is more commonly done by maximising the logarithm of the likelihood:

$$\ln \mathcal{L}(\theta|X) = \sum_{i=1}^N \ln p(x_i|\theta).$$

In order to find a global optimum of the likelihood function, algorithms proceed in an iterative fashion to explore the parameter space. The stopping criterion is reached upon convergence of the likelihood function or equivalently of the parameter updates. However local optimums in the likelihood function can also lead to convergence. There are also regions of the parameter space which need to be avoided. For example, the likelihood function can be made arbitrarily large if the variance of one of the clusters is allowed to shrink to zero. To safeguard from these situations, some guidance can be provided by picking sensible starting conditions or by setting hard boundaries on the parameter space. Another softer approach is to weight parameter updates with a distribution. This approach is also called regularisation. Regularisation can be achieved using a prior probability density function on the parameters as implemented in the R package **mclust** (Chris Fraley and Scrucca, 2012) and the R BioConductor package **flowClust** (Lo et al, 2009).

When K is unknown, one drawback of the GMM is that it tends to overestimate the number of multivariate Gaussians which best models the data since outliers which are in the tails of the distributions are explained by new low mixture distributions. To account for this, Flowclust replaces Gaussians by t-distributions which have more weight in the tails (Lo et al, 2008). Even so, t-distributions are symmetric and so cannot model skewed populations, commonly found in stimulation experiments or, more generally, when cells are in a transitional state from one cell type to another. Pyne et al (2009) addressed this issue with FLAME (Flow Analysis with Automated Multivariate Estimation) by employing skewed t-distributions instead. Yet a remaining issue is that

these distributions are convex by nature and so a concave population which can arise in transitional cell populations undergoing progressive change on more than one marker may only be represented by the merging of several convex populations. This merging step can be accomplished using FlowMerge (Finak et al, 2009). By adding more parameters to these distributions we can make model-based methods more flexible, but this comes at the price of reducing the degrees of freedom and having to estimate more parameters which can be computationally expensive and risks overfitting. For certain parameters such as mean and covariance, closed-form solutions exist or can efficiently be estimated with an Expectation Maximisation (EM) algorithm (Dempster et al, 1977), but others, such as the skewness factor and degrees of freedom of the t-distributions, may need to be estimated numerically using computationally expensive iterative methods.

1.6.2 Model-free methods

Model-free methods state no explicit assumptions about the shape of populations but instead attempt to minimise some loss function such as the total within-cluster sum of squares. These methods are sometimes qualified as non-parametric because there are no explicit parameters to the model, although the parameter estimation is usually implicit. They typically use local estimates of density or distance to identify clusters of points. Perhaps the oldest and most popular of the model-free methods, due to its simplicity and speed, is the K-means algorithm (MacQueen, 1967). K-means attempts to minimise the total within-cluster sum of squares as its objective function:

$$SS_w = \sum_{k=1}^K \sum_{\mathbf{x}_i \in S_k} (\mathbf{x}_i - \boldsymbol{\mu}_k)^2; \quad \boldsymbol{\mu}_k = E(x_i | x_i \in S_k) \quad (1.1)$$

where each point, x_i , is assigned to exactly one of the clusters S_1, S_2, \dots, S_k .

The algorithm starts by picking K random points which are initial guesses as to where the cluster means lie. Then for each iteration:

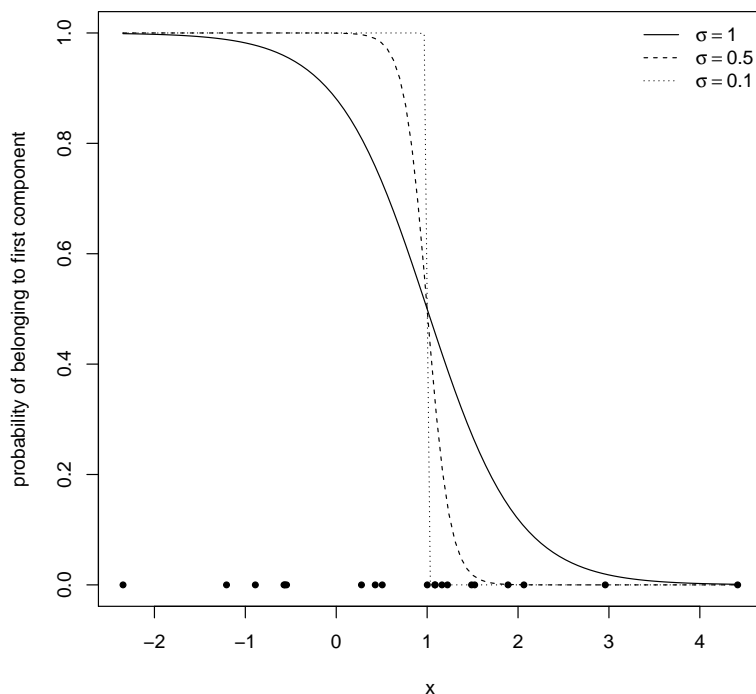


Figure 1.7. Effect of shrinking variance in a two component GMM, with means fixed at 0 and 2, on the decision boundary. In this two component univariate GMM, the y axis represents the posterior probability of being assigned to the first component and the x axis represent the value of the data points. As the variance of the two Gaussian components shrinks, the soft decision boundary approaches the hard K-means decision boundary, so that we go from a soft probabilistic assignment to a hard binary assignment.

- Each point x_i is assigned to the cluster S_k of the closest current cluster mean μ_k .
- Based on this new cluster assignment, the new cluster mean of each cluster is computed.

The algorithm terminates when no cluster mean changes, or equivalently when the cluster assignment does not change.

However, it can be shown that certain so called non-parametric methods turn out to be limiting cases of parametric methods. For example K-means, is a limiting case of spherical GMMs when the covariance tends to zero because maximising the log-likelihood of a multivariate Gaussian is asymptotically equivalent to minimising the residual sum of squares (Figure 1.7).

There are numerous model-free clustering methods which rely on density estimation:

- Density Based Merging (DBM) uses a region growing density approach so that points of high density are linked (Walther et al, 2009).
- Flow Clustering without K (FLOCK) relies on grid based density estimation in higher dimensions (Qian et al, 2010).
- Misty Mountain takes decreasing cross sections of the two-dimensional density histogram so that clusters are progressively merged as the threshold decreases (Sugár and Sealfon, 2010).
- CurvHDR (negative Curvature and High Density Region) identifies regions of significant curvature in the multivariate density function, by using a bandwidth rather than the number of bins, but cannot be applied beyond four dimensions (Naumann et al, 2010).

All these density based approaches require the number of bins or the bandwidth to be specified by the user or estimated from the data according to some heuristic. Care needs to be taken when selecting an appropriate bin or bandwidth to avoid under or

over smoothing of the data. For example, smaller numbers of bins or equivalently larger bandwidths, lead to overestimation of the density in low density regions and underestimation in high density regions. However, as the number of dimensions increases, data tend to become sparser and density based clustering becomes inefficient because the lower bound on the density estimation error increases with the dimensionality. Therefore in high-dimensional settings, distance based clustering becomes more appropriate and fast methods like K-means, which do not rely on the computation of the entire distance matrix, are popular. For example, flowMeans is an extension to K-means for flow cytometry (Aghaeepour et al, 2010). Unfortunately, K-means is known to be very sensitive to starting conditions and is also not robust to outliers, so small changes in the data can lead to very different clustering solutions. These shortcomings are addressed by a related but slower algorithm: K-medoids. Instead of using the cluster means, K-medoids updates the cluster medoids. The medoid is defined as the point of the cluster which minimises the overall distance to all other points belonging to that cluster. The objective function of K-medoids is therefore:

$$\sum_{k=1}^K \sum_{\mathbf{x}_i \in S_k} (\mathbf{x}_i - \mathbf{M}_k)^2; \quad \mathbf{M}_k = \text{Medoid}(x_i | x_i \in S_k)$$

Since the medoids can only be points of the dataset, the complete distance matrix need only be calculated once at the onset. The algorithm starts by picking K starting points which belong to the set of data points. These represent the initial guess as to where the cluster medoids lie. Then for each iteration:

- Each point x_i is assigned to the cluster S_k of the current closest cluster medoid M_k .
- Based on this new cluster assignment, the new cluster medoid of each cluster is selected.

The algorithm terminates when no cluster medoid changes. The algorithm is reasonably

fast but can be slower for larger datasets due to the first step of calculating the complete distance matrix. For sufficiently large N , the size of the distance matrix may be prohibitive and too large for memory. Therefore this version of the algorithm may not scale with large N as well as K-means. This performance issue can be ameliorated by clustering subsets of the data and combining the results. Points which were not selected in the subsampling can be assigned to the closest cluster. This is the approach implemented by the R function `clara` (Clustering Large Application) in the R package `cluster` (Maechler et al, 2014).

If subsampling is used only once to reduce the number of datapoints then caution is required, since uniform downsampling runs the risk of discarding smaller clusters. One workaround is to account for local density so that most of the downsampling occurs in regions of high-density, thus conserving low density regions. Once the downsampling has sufficiently reduced the number of points so that distance matrix may be computed, methods such as, spectral clustering which uses spectral graph theory to determine where to partition the network as implemented in Sampling followed by Spectral Clustering (SAMSpectral, Zare et al (2010)) or more conventional hierarchical clustering as done by Spanning-tree Progression Analysis of Density-normalized Events (SPADE, Qiu et al (2011)), may be applied.

The advantage of these non-parametric methods is that they are usually fast and flexible and often provide some heuristics for estimating the parameters. Unfortunately, this seeming flexibility can come at the price of poor interpretability or generalisation to other datasets since there is no explicit model and the parameters tend to be dataset specific. Furthermore, these parameters do not necessarily have an intuitive interpretation or any biological relevance, which makes setting their value hard to justify.

1.6.3 Estimating the optimal number of clusters from the data

The methods described above normally require the expected number of clusters as an input parameter. Although there are many suggested heuristics, estimating an optimal number of clusters from the data remains an open problem in machine learning and statistics.

Generally these methods seek to maximise utility by reaching a compromise between model complexity, number of parameters in the model, and accuracy, in supervised clustering, or some other metric like variance explained, in unsupervised clustering.

One way of estimating the expected number of clusters, is to find modes in the data: regions of significantly high density (Duong et al, 2008; Jing et al, 2009). An alternative brute force approach is to cluster for increasing numbers of clusters and to pick the cluster value which optimises some criterion, such as the Gap statistic (Tibshirani et al, 2001) or the variance-ratio criterion (Calinski and Harabasz, 1974). These clustering metrics are usually derived from the ratio of the between-cluster sum-of-squares (variance explained by the model) to the within-cluster sum-of-squares (remaining variance). For example, the variance-ratio criterion as defined by Calinski and Harabasz (1974), for k clusters defined on a dataset of size n :

$$\text{VRC} = \frac{SS_b/(k-1)}{SS_w/(n-k)}$$

where SS_w is the total within-sum-of-squares (Equation (1.1)) and SS_b , the total between-sum-of-squares, is defined as:

$$SS_b = SS_t - SS_w$$

where SS_t is the total sum-of-squares:

$$SS_t = \sum_{i=1}^n (\mathbf{x}_i - \boldsymbol{\mu})^2; \quad \boldsymbol{\mu} = E(x_i)$$

Calinski and Harabasz note that the variance-ratio criterion relates to the ANalysis Of VAriance (ANOVA) F-test. Figure 1.8 illustrates that the performance of this metric in predicting the number of clusters is very much dependent on the inherent noise in the data.

In model-based methods, another approach is to maximise the Akaike Information Criterion (AIC) or the Bayesian Information Criterion (BIC), which are both functions of the log likelihood penalised by the number of clusters and free parameters. The BIC is used by the R package `mclust` (Chris Fraley and Scrucca, 2012) to find the optimal number of parameters when fitting a GMM.

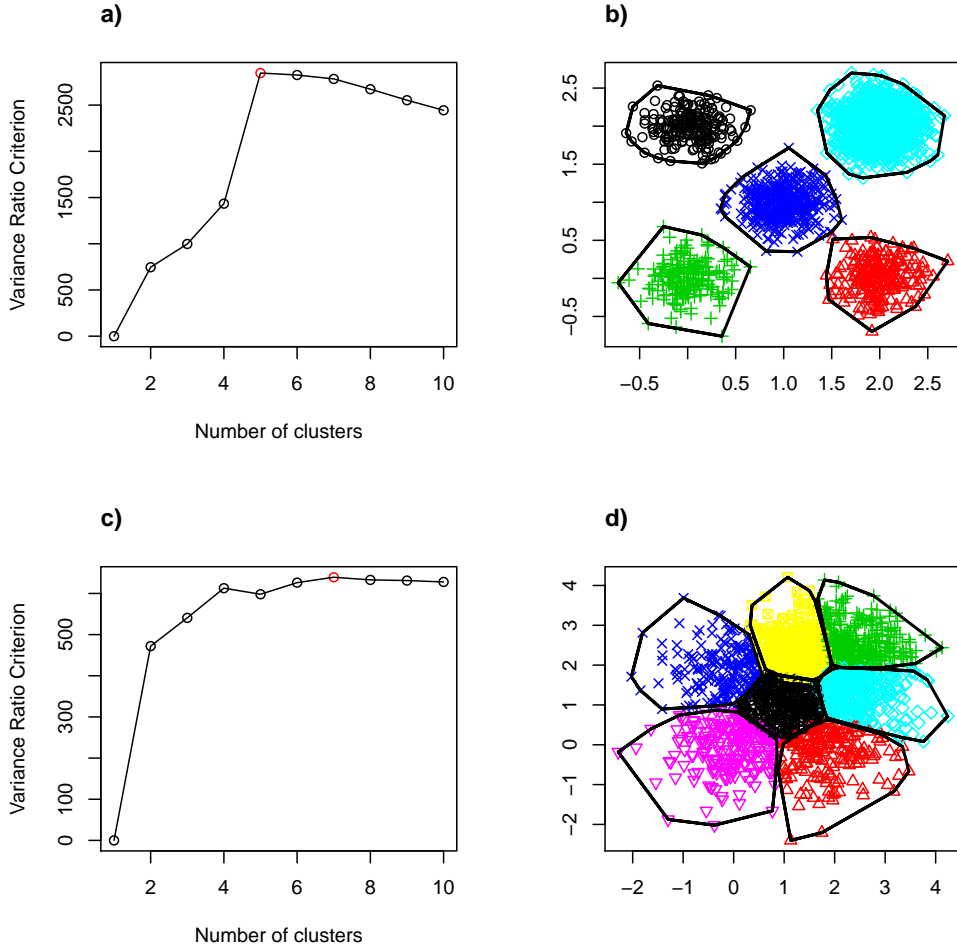


Figure 1.8. Variance ratio criterion used to estimate the number of clusters with K-means. Two simulated datasets are used to illustrate the variance criterion ratio on K-means. The first dataset (a and b) is simulated from a five component mixture of bivariate spherical Gaussians with covariance of 0.05, the second (c and d) is simulated from the same model but with the covariance scaled 10-fold to 0.5. While on the first dataset the optimal number of clusters according to the variance ratio criterion is correctly estimated as 5 (a), on the second dataset it is overestimated as 7 due to the increased noise (c). (b) and (d) depict the clustering resulting from K-means with $K = 5$ and $K = 7$ respectively.

Chapter 2

The influence of gating on reproducibility and association testing in flow cytometry

On va toujours, en fin de compte, vers
où l'on pè

2.1 Background

At least two SNPs that associate with T1D are located in the chromosome 10p15 region containing *IL2RA*, the interleukin-2 receptor subunit alpha gene (Lowe et al, 2007). *IL2RA* codes for CD25, the high affinity binding alpha chain of the trimeric IL-2 cytokine receptor. CD25 is found at varying quantities on the surface of numerous T lymphocyte subsets such as naive, memory and regulatory cells. CD25 is also upregulated upon activation in lymphocytes and monocytes, and is known to play a key role in immunoregulation and immune responsiveness (Brusko et al, 2009; Boyman and Sprent,

2012). SNPs in the *IL2RA* region have also been associated with other immune mediated diseases including multiple sclerosis (Beecham et al, 2013) and rheumatoid arthritis (Stahl et al, 2010).

To better study the downstream implications of three *IL2RA* SNPs, namely rs12722495, rs2104286 and rs11594656, on CD25 expressing T lymphocyte subsets, Dendrou et al analysed blood samples obtained from healthy donors from the CambridgeBioresource¹, selected by genotype at these SNPs, and matched by sex and age. The experiment consisted of a total of 180 individuals, fifteen of which were recalled for a second sample (Table 2.1). The distribution by age (20 to 50 years old) and sex was split evenly across genotype groups (Table 2.2).

After lysis of the red blood cells, the samples were stained with the antibody panel specified in Table 2.3. The running time of the whole experiment was seven months over which samples were analysed on 51 days, between one and six samples per day (Figure 2.1).

The cell phenotypes studied by Dendrou et al (2009b), were obtained using manual gating with the FlowJo software². Manual gating follows the current state of knowledge of immune cell lineages and the gating strategy followed by Dendrou et al (2009b) is described in Figure 2.3. Lymphocytes are distinguishable from more granular and larger cell types based on forward and side scatter (Figure 2.3a). The lymphocytes include, B cells and T cells, and the latter population includes cells expressing CD8 or CD4. Within the lymphocytes, the subset expressing CD4 are defined as T lymphocytes (Figure 2.3b). The CD4⁺ T lymphocyte subset can be further divided into regulatory and non-regulatory cells. Regulatory cells represent a low-frequency subset which has the highest CD25 expression compared to other resting cells, and which expresses no or very low level of CD127. Regulatory T cells can be defined more precisely by the intracellular

¹www.cambridgebioresource.org.uk

²www.flowjo.com

Individual	pch	number of days between visits
1	a	196
2	b	225
3	c	217
4	d	197
5	e	161
6	f	153
7	g	133
8	h	133
9	i	117
10	j	112
11	k	112
12	l	116
13	m	119
14	n	98
15	o	79

Table 2.1. Number of days till second visit for recalled individuals. Fifteen individuals recalled between 79 and 225 days later. pch is the plotting character used to refer to these individuals in plots later in this chapter.

rs12722495	rs2104286	rs11594656	F	M	mean age
AA	AA	AA	18	10	38.9
AA	AA	AT	12	12	38.2
AA	AA	TT	31	32	39
AA	AG	TT	10	6	37.7
AA	GG	TT	12	9	40.8
AG	AG	TT	12	10	41.5
GG	GG	TT	9	12	38.4

Table 2.2. Distribution of subjects in study, by genotype, age and sex.

Fluorochrome	Antibody target
Alexa-488	CD127
PE-Cy7	HLADR
APC	CD25
PE	CD101
Alexa-700	CD4
Pacific Blue	CD45RA

Table 2.3. The fluorochrome-antibody panels with six markers used in the IL2RA dataset.

32The influence of gating on reproducibility and association testing in flow cytometry

FOXP3 transcription factor, which is constitutively expressed only in regulatory T cells. Non-regulatory T cells represent a larger proportion of T lymphocytes, they express more CD127 and less CD25 than regulatory T cells (Figure 2.3c). Non-regulatory T cells can be further divided into naive and memory subsets (Figure 2.3d). Upon antigen presentation, naive cells are activated and differentiate into effector cells, some of which further differentiate into memory cells while the remainder die. As part of the transition process from naive to memory, the cell surface protein CD45RA is lost so that consequently naive cells have higher CD45RA expression than memory cells. A further difference between these subsets is that memory cells tend to have a higher CD25 expression than naive cells. Since CD25 expression on the naive cells is low, with only a subset of the cells expressing substantial levels of the molecule, Dendrou et al (2009b); Pekalski et al (2013) define a threshold above which naive cells are deemed positive for CD25.

Following this manual gating strategy, two T cell phenotypes, percent of CD25⁺ naive cells over total naive cell count and normalised fluorescence intensity of CD25 on memory cells, were found to be associated with rs2104286 and rs12722495 respectively. The percent of CD25⁺ naive cells and percent of memory cells, were found to be associated with age and marginally associated with sex. The repeatability was also tested thanks to the 15 recalled individuals. Repeatability is an important factor to take into consideration, because reduced within-individual variation increases the power to detect between-individual variation. The repeatability and association results, as reported by Dendrou et al (2009b), are summarised in Table 2.4.

Besides the genetic and environmental factors driving variation in these cell phenotypes, there are two important sources of technical variation which need to be controlled for as they can have some bearing on the repeatability and association statistics: instrument variation over time and the subjectivity of manual gating.

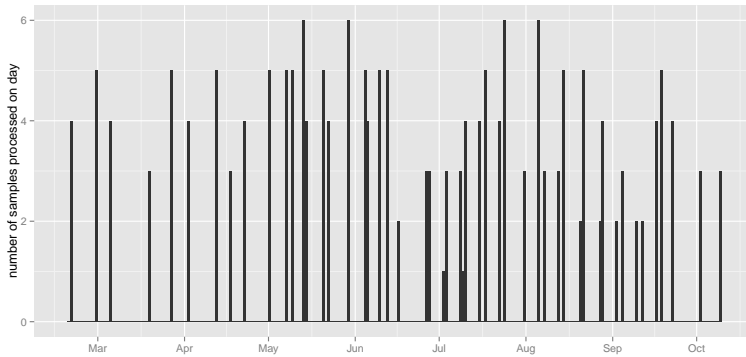


Figure 2.1. Number of samples analysed per day. A total of 195 (180 + 15 repeats) samples were analysed over seven months (from March to October). During that period, samples were analysed on 51 days, with between one and six samples analysed each day.

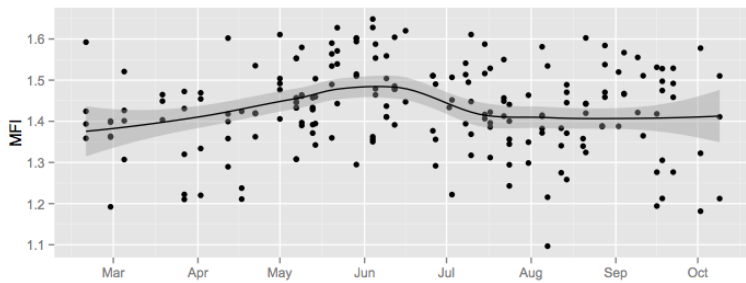


Figure 2.2. Effect of time on CD25 MFI in memory cells. CD25 MFI of memory cell population (manually gated) over time of experiment. The black line represents the loess regression line. Samples analysed after July tend to have a lower CD25 MFI than those analysed before.

CD4 ⁺ T Cell Subset	Phenotype	Repeatability (r^2)	Genetic Effect	Age Effect	Sex Effect
CD25 ⁺ Naive	Percentage	0.669	↓ rs2104286 $P = 4.25 \times 10^{-6}$	↑ $P = 2.22 \times 10^{-9}$	$P = 0.005$ M < F
Memory	CD25 MEF	0.997	↑ rs12722495 $P = 1.16 \times 10^{-10}$	None	None
	Percentage	0.862	None	↑ $P = 8.97 \times 10^{-5}$	None

Table 2.4. Repeatability and significance of effects of percentage of naive CD25⁺ CD25 MEF and percentage of memory cell phenotypes. Subset of results from Dendrou et al (2009b) for cell populations under re-analysis in this chapter. r^2 is the Pearson correlation squared.

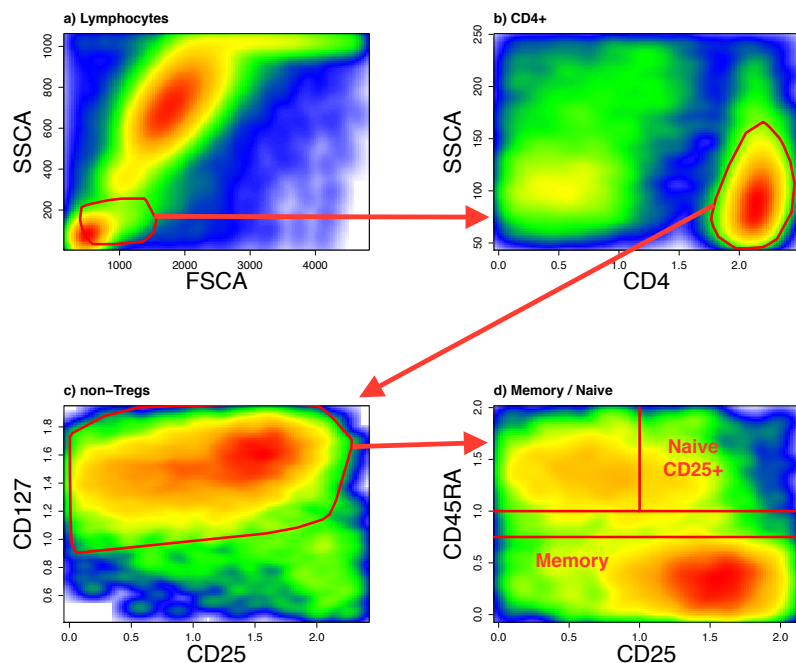


Figure 2.3. Manual gating strategy followed by Dendrou et al (2009b).
Manual gating strategy to extract memory T cells and CD25⁺ naive T cells (d). Note that the CD45RA gates in (d), excludes cells which are considered to be neither memory nor naive. The automated gating considered in this chapter, replaces the final stage of the manual gating on CD25 and CD45RA.

Over the seven month period of the experiment during which samples were collected and analysed, instrument variation is detectable in the CD25 Mean Fluorescence Intensity (MFI) of the memory cell population (Figure 2.2). The influence of this time effect on repeatability was first discussed by Dendrou et al (2009a). To correct for this, Dendrou et al (2009b) run fluorescent six-peak beads daily in order to define a normalisation transform from MFI to Molecules of Equivalent Fluorochrome (MEF). Concretely, the transformation is defined by a linear regression of the observed MFI of the six, manually gated, bead populations, against their expected MEF, as specified by the bead manufacturer. In the first section of the chapter, I will show that this process can be automated by computationally gating beads using my R package **flowBeads** (Pontikos, 2013).

Manual gating, besides being laborious on large datasets, is an inherently subjective task as it relies on the opinion of the gater and can lead to between gater variation (Maecker et al, 2005). Although there is considerable interest in standardising and automating the gating process (Aghaeepour et al, 2013), some customisation is often necessary since some gating steps remains experiment and context specific. For example, when deciding on the position of the $CD25^+$ gate on the naive cell subset (Figure 2.3d), the manual gater may rely on fluorescent bead information but also on external experimental information, such as an isotype control. Nonetheless, I will show, in the second section of this chapter, that bead data is sufficient in order to develop a computational method which can closely emulate the $CD25^+$ manual gating.

In the third section of this chapter, I will look at automating the univariate gating on CD45RA in order to identify memory cells. From this gate, we obtain the percentage of memory cells and the CD25 MFI of memory cells. As the CD45RA distribution is typically bimodal, the manual gating of CD45RA into negative (memory) and positive (naive) subsets, translates well into a clustering problem, which I will attempt to solve by fitting a two-component mixture model.

For both the CD25 and CD45RA gating, I will assess their performance in terms of their repeatability. Finally, in the fourth section of this chapter, I will test the association of the cell phenotypes, percentage of $CD25^+$ naive cells, percentage of memory cells and CD25 MEF of memory cells, obtained using these computational methods, in order to assess the influence of these automatic gating approaches on effect size estimation.

2.2 Univariate gating of bead data

In flow cytometry, a method of normalising fluorescence intensity to account for instrument variation, is to convert the MFI measured on a population to MEF (Schwartz et al, 1996; Dendrou et al, 2009a). In order to apply this conversion, specially designed beads of known and (assumed) constant fluorescence defined in terms of MEF, are used as a reference. The MEF property of these beads is deemed stable whereas the MFI of the bead population is dependent on the instrument and varies over time. The beads used here are specially manufactured so that they belong to six distinct populations of increasing MEF as shown in Table 2.5. Following the bead manufacturer's guidelines, plotting the $\log_{10}(MEF)$ of these six bead populations against the corresponding calculated $\log_{10}(MFI)$ from the gated bead populations, we fit the linear regression:

$$\log_{10}(MEF) = \beta \times \log_{10}(MFI) + \alpha \quad (2.1)$$

The MEF is in fact a power transform of the MFI (only defined for strictly positive MFI values):

$$MEF = 10^\alpha \times MFI^\beta$$

The original MEF transform used by Dendrou et al (2009a) assumes that $\beta = 1$, although I relax that assumption. In calculating the slope β and the intercept α pa-

rameters of the linear model, only the five brightest bead populations are used because the MEF of the blank beads is not specified by the manufacturer. However, as we will see in the next section, the blank beads can be used to define a threshold for positivity. Typically bead data are gated manually. Here, in order to obtain the parameters of the MEF transform, I will use an automatic process to gate the beads. Since all beads are manufactured to be of identical dimensions, we expect a single cluster in the scatter channels: the singlet bead population. Events which lie away from the singlet population are deemed to be beads clumped together or debris and so are discarded. Filtering of singlets can be achieved by fitting a bivariate normal distribution on forward and side scatter and only keeping points within the 95th percentile. Having gated the singlets, I subset the data and proceed to gate on the fluorescence channels to identify the six bead populations. Given that the number of bead populations is known, that the bead signal is sufficiently clear and that the number of events is small (in the order to 10,000), I use the K-medoids algorithm. The solution has been implemented in the R package `flowBeads` (Pontikos, 2013), available on BioConductor. Automatic gating shows near perfect agreement with manual gating (Figure 2.5). Applying the bead normalisation to the memory CD25 MFI from Figure 2.2, we improve on the repeatability of that cell phenotype from $r^2 = 0.972$ to $r^2 = 0.985$, where r^2 is the Pearson correlation squared (Figure 2.6).

Population	FITC	RPE	REP-Cy5	APC	PE-Texas Red
1	B	B	B	B	B
2	2,500	1,500	750	4,100	552
3	6,500	4,400	2,100	10,300	2,014
4	19,000	14,500	6900	25,500	6,975
5	55,000	43,800	22,100	67,300	20,685
6	150,000	131,200	77,100	139,100	71,888

Table 2.5. FluoroSpheres from DakoCytomation. The Molecules of Equivalent Fluorochromes (MEF) values for the six bead populations as provided by the manufacturer. B denote the blank beads which by design contain no fluorochrome. Of the six fluorochromes contained by each bead only APC is used in the experiment.

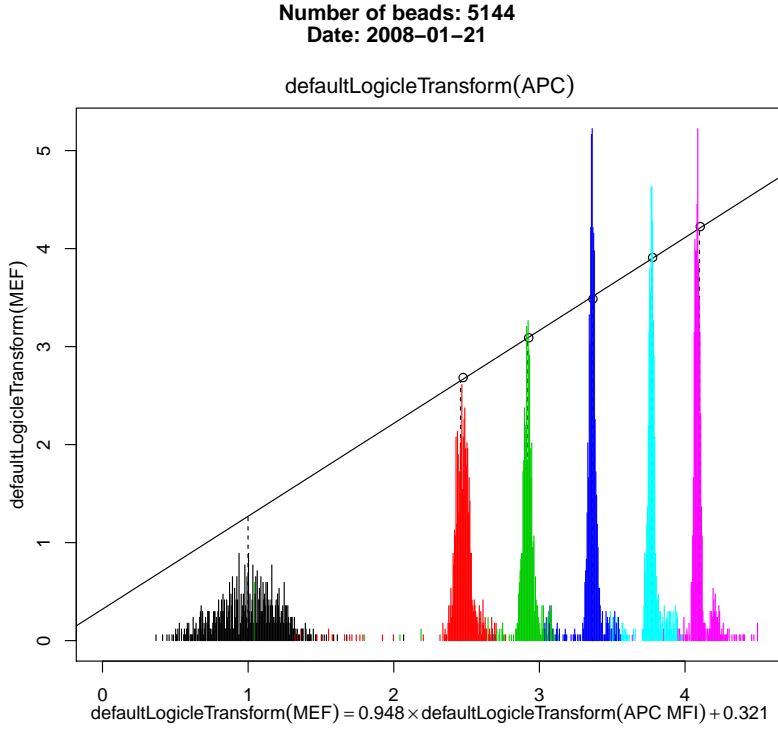


Figure 2.4. Linear regression of bead APC MEF against the APC MFI as defined in Table 2.5. The six peaks represent the six bead populations. These types of plots are generated automatically by the R package **flowBeads** (Pontikos, 2013).

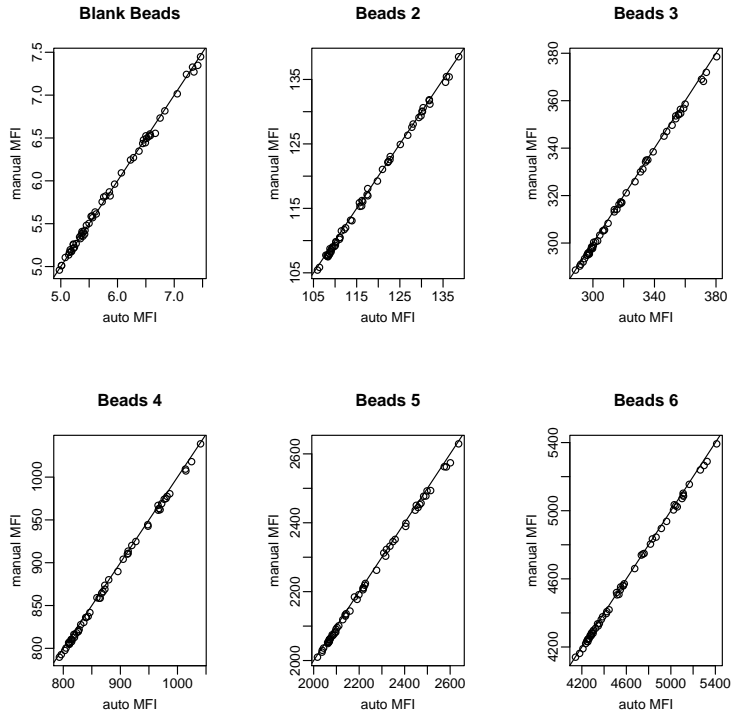


Figure 2.5. Comparison of bead population MFI using manual and **flowBeads** gating. There is near perfect agreement of the APC MFIs of the six bead populations identified with manual and using the automatic **flowBeads** approach.

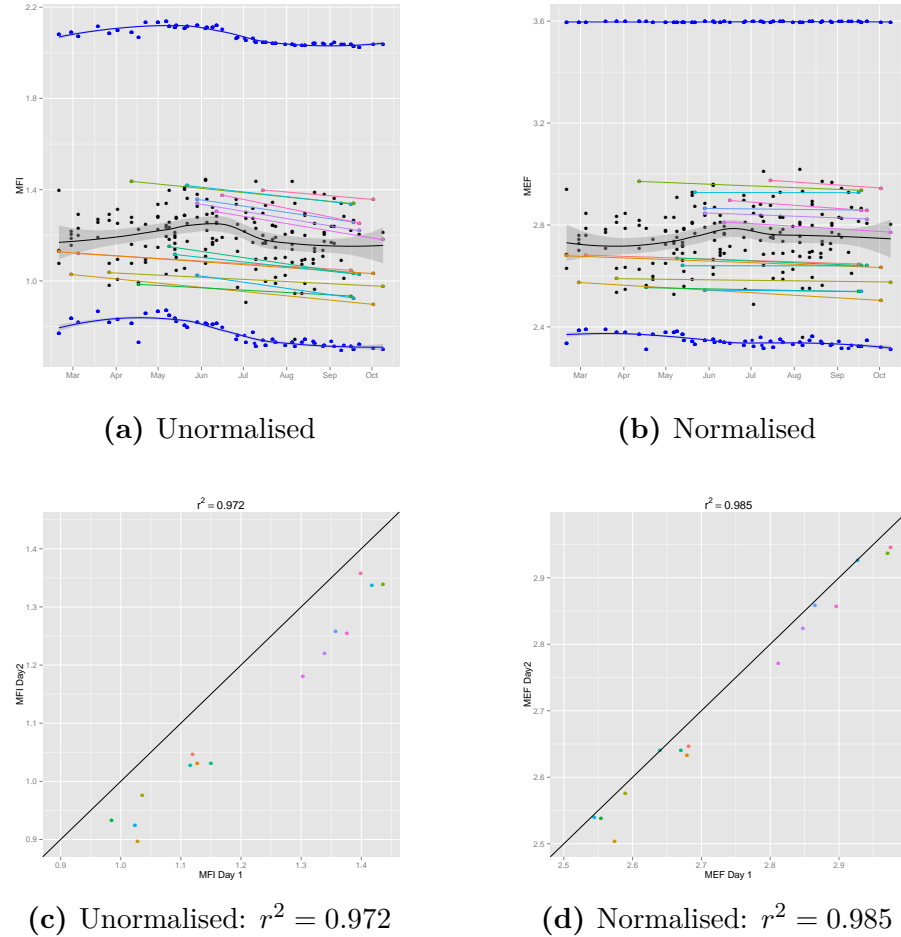


Figure 2.6. Bead normalisation partially corrects for long term time effect in CD25 MFI of the memory cell population. In (a) and (b), the blue points represent the CD25 MFIs of the two lowest bead populations, in black the CD25 MFIs of the memory cell populations. The dashed blue lines represent the overall mean of each the two bead populations. A loess regression is fitted to the MFIs of the beads and memory cells to illustrate the MFI variation over days. The points joined by lines are memory cell CD25 MFIs from the 15 recalled individuals (Table 2.1). The bead normalisation transform Equation (2.1) improves the repeatability of the MFI in recalled individuals from $r^2 = 0.972$ (c) to $r^2 = 0.985$ (d).

2.3 Univariate gating on CD25: defining a CD25⁺ threshold on naive cells

The approach adopted by the manual method is to define a threshold above which cells are considered positive for CD25. According to Dendrou et al (2009b) (and Calliope Dendrou personal communication), the CD25⁺ threshold is set manually using an ad-hoc process based on an isotype control, bead data and ultimately a judgement call by the manual gater. An isotype control is a sample stained with the same fluorochrome (APC) but conjugated to a non-specific antibody not designed to target the marker we are interested in quantifying. It is used as a technique for assessing background APC fluorescence not resulting from CD25 binding.

This manual approach to setting the threshold, leads to a different gate position per sample per day (Figure 2.7). We notice that on some days there is greater variability in the positions of the gates. Also, the gate position moves down with time, reflecting the same downwards time-trend in the position of the gates observed in Figure 2.2.

Drawbacks of the manual approach are its lack of consistency and its reliance on isotype controls. The gating criterion is subject to human judgement and so may not be consistent across samples. Isotype controls are costly since part of the sample and fluorochromes is consumed for control purposes, consequently they are not always analysed. Also they are not necessarily an accurate measure of background fluorescence since they are also a source of noise linked to differences in the constitution of the control sample, the behaviour of the staining and other sources of technical variation (O’Gorman and Thomas, 1999; Maecker and Trotter, 2006).

I wished to improve on this process by using a more consistent and economical approach, using only beads, which I called `beads.thresh`. Instead of using isotype data, my working hypothesis, was that blank beads would constitute a more stable reference,

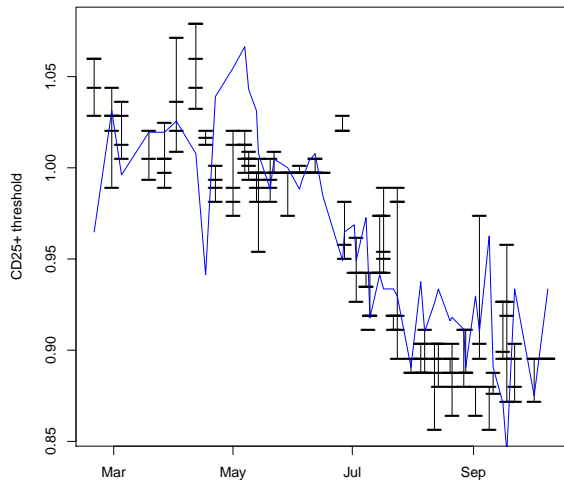


Figure 2.7. Position of the CD25⁺ gate over duration of experiment. The black horizontal dashes are the positions of the manual CD25⁺ gates for all 196 samples over the time course of the experiment (51 days). The vertical black lines represent the days and so define the range of the manual gate positions on a given day. The blue line represents our automatic CD25⁺ gate which corresponds to the 86th percentile of the blank bead population (see Figure 2.8).

which could be used to define an APC-CD25 threshold. To find a suitable bead-derived threshold, I first gated the blank beads using my R package **flowBeads** (Pontikos, 2013), then I searched for the APC percentile of the blank bead population which best agreed with the manual gate (Figure 2.8). I found that in this dataset, the 86th percentile of the blank bead population, best matched the manual gate position.

Hence the CD25⁺ threshold defined by my approach, **beads.thresh**, is set as the 86th percentile of the automatically gated blank bead population on that day. As we only have one bead set per day, we have a single fixed CD25 gate for all samples on that day (Figure 2.2).

The **beads.thresh** method for setting CD25 thresholds shows improved repeatability of the percentage of CD25⁺ naive T cell phenotype over manual (Figure 2.10).

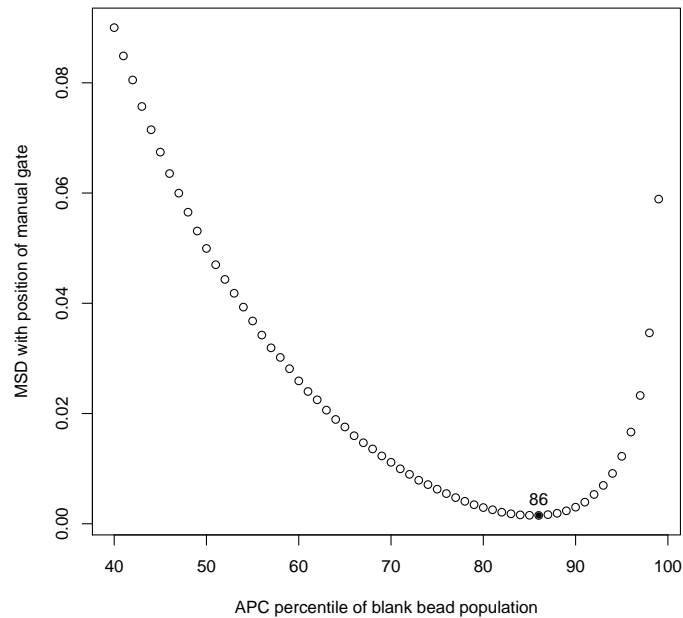


Figure 2.8. Mean square difference (MSD) of the position of the manual gate with that of beads.thresh. On the x axis, the APC-CD25 percentiles of the blank bead population from 40 to 99. On the y axis, the mean squared difference between the position of the manual gate and that of the bead-derived gate for that percentile threshold. The 86th percentile yields the lowest mean squared difference hence the best agreement with the manual gating. The automatic threshold selection method (beads.thresh) is therefore defined as the APC 86th percentile of the blank beads population.

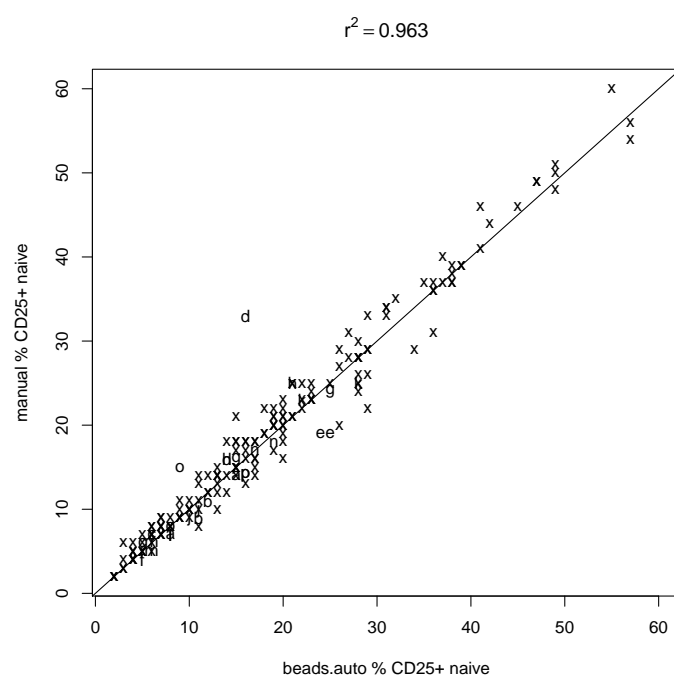


Figure 2.9. Agreement with manual of percentage of CD25⁺ naive cell phenotype. Except for individual d, the agreement of beads.thresh with manual for percentage of CD25⁺ naive cells is very good. r^2 is the Pearson correlation squared.

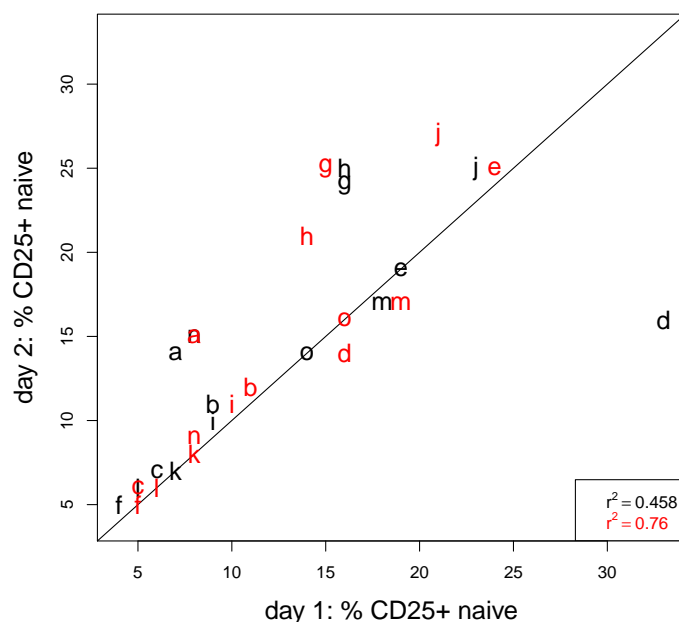


Figure 2.10. Repeatability of percentage of naive CD25⁺ with manual (black) and beads.thresh (red). Repeatability of the percentage of naive cells which are CD25⁺ from day one to day two. The overall repeatability of this cell phenotype was better with beads.thresh (red) than the manual (black). Letters are used to identify individuals, see Table 2.1. The Pearson correlation squared is $r^2 = 0.458$ for manual and $r^2 = 0.76$ for beads.thresh.

2.4 Univariate gating on CD45RA: fitting two-component mixtures on non-regulatory T cells

Non-regulatory CD4⁺ T cells appear bimodal with respect to CD45RA expression, because this marker is lost upon activation of naive cells (CD45RA⁺) to memory cells (CD45RA⁻). In this section, we will model the CD45RA distribution by fitting a two component mixture model. Although we model both populations, we will only gate the memory (CD45RA⁻) cell population, which corresponds to the first component, since the naive (CD45RA⁺) cell population, the second component, is not a terminal gate as it is further divided into CD25 negative and positive subsets (see previous section).

In order to model the bimodal CD45RA distribution, I use the R function `normalmixEM` function in the R package `mixtools` (Young et al, 2009), which provides an implementation of the EM algorithm (Dempster et al, 1977). The parameters, mean, variance and component weight, of the two-component Gaussian mixture model, are first initialised by the K-medoids algorithm. The parameter estimates are then obtained by running the EM algorithm until convergence. I call this method `mm`.

2.4.1 Using the mixing proportions of the mixture model

Since we are fitting a mixture model, instead of emulating manual gating by picking a threshold, I will first try a more statistically intuitive approach, using the mixing proportions obtained from `mm`. Additionally to the `mm` approach, I will also apply a more flexible mixture model of semi-parametric symmetric distributions (R function `spEMsymloc`) again from the R package `mixtools` (Young et al, 2009), which I will call `spmm`. Semiparametric symmetric distributions are kernel density estimates centered around a location parameter.

Comparing the percent of memory cell obtained using `mm` and `spmm` to those ob-

tained using manual (Figure 2.11), we see that although there is agreement between the methods, the automatic methods tend to underestimate the percentage of memory cells. Also with regards to repeatability, **mm** and **spmm**, yield worse repeatability than manual (Figure 2.12).

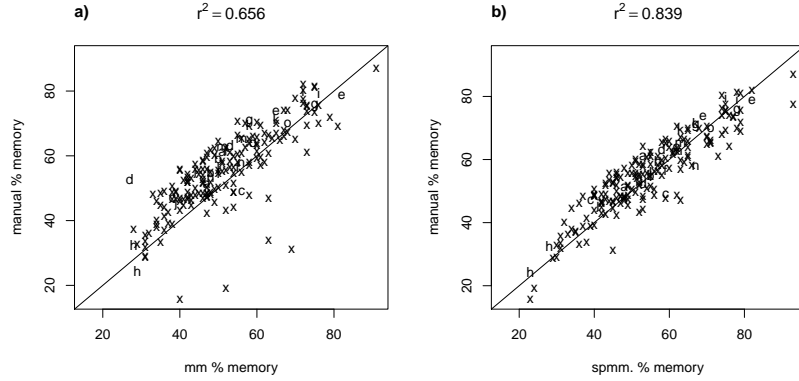


Figure 2.11. Agreement with manual of the percent memory cell phenotype obtained with **mm (a) and **spmm** (b).** The more flexible model, **spmm**, tends to agree better with percent memory cell phenotype returned by manual, than **mm**. Again we can see in (a), that **mm** underestimates the percentage of memory cells in individual d compared to manual. r^2 is the Pearson correlation squared.

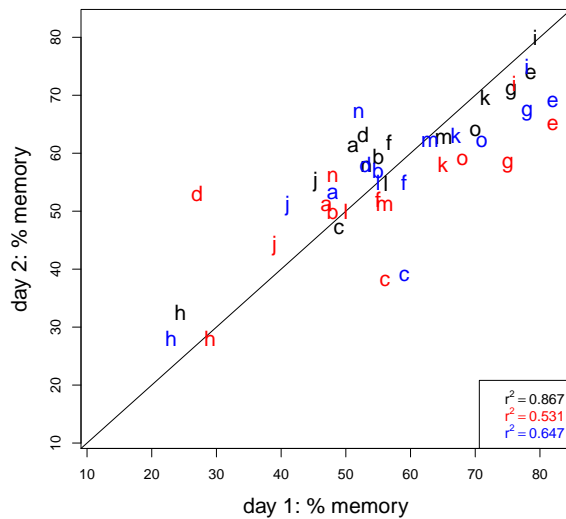


Figure 2.12. Repeatability of the percent memory cell phenotype with manual (black), **mm (red) and **spmm** (blue).** While manual still shows the best repeatability, the repeatability of the automatic methods is quite encouraging, given these have no knowledge of the manual gates and are based purely data driven. Also as seen using the thresholding methods, individual d is a clear outlier when gated with the **mm** method.

2.4.2 Emulating manual gating by picking a threshold

Although the previous approach makes sense from a statistical perspective, it does not exclude the transitional cell population which lie between the memory and naive cells. Instead in the manual gating, the memory cell subset is defined by a threshold on the bimodal CD45RA distribution, below which cells are regarded as CD45RA⁻. Here, I attempt to emulate manual gating by defining a threshold on the fitted two-component mixture model, `mm`. I consider two approaches of selecting a threshold, `pct.thresh` and `post.thresh`, both which are illustrated in Figure 2.13.

The first method, `pct.thresh`, closely replicates the manual CD45RA⁻ gating procedure, as explained to me by Linda Wicker. In this approach, only the shape of the first left-most, component of the mixture model defines the position of the CD45RA⁻ memory gate. In order to delineate the memory population, we first identify the first peak of the bimodal CD45RA distribution, which should correspond to the peak of the first component, after the two-component mixture has been fitted. Then, following the CD45RA density curve from the peak towards the left-hand-side, we record the CD45RA value after which the density curve drops below a certain given threshold. This CD45RA value is then mirrored to the right-hand-side of the peak in order to define the CD45RA-threshold. This technique is in fact equivalent to selecting a fixed percentile threshold for the first component to gate consistently across all samples.

The second method, `post.thresh`, considers the density ratio of both components in order to decide where to draw a threshold. Formally, `post.thresh` selects a threshold on the posterior probability of belonging to the first component, the memory population, across all samples. At a given point, the posterior probability of belonging to the first component is defined as the ratio of the density of the first component, over that of the total density. Concretely, given a two-component mixture model where, f_1 is the density of the first component and f_2 the density of the second, and a posterior threshold of p ,

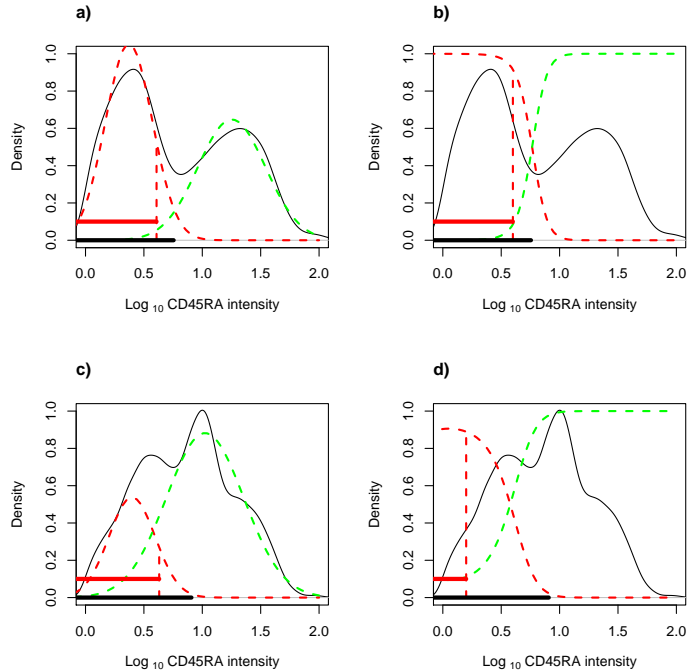


Figure 2.13. Example on individual d of the two approaches, `pct.thresh` (a and c) and `post.thresh` (b and d), of selecting a threshold. Individual d was chosen to illustrate `pct.thresh` and `post.thresh`, because the CD45RA distribution takes on a very different shape on day one (a and b) compared to day two (c and d). In (a) and (c), the `pct.thresh` method, places the gate at the 88th percentile of the first component. In (b) and (d), the `post.thresh` method, places the gate at the largest CD45RA value where the posterior of the first component reaches 89 percent. This poses a problem for `post.thresh` in (d) because the overlap of the components is such that the posterior is only reached close to zero which yields a much smaller gate and consequently a lower percent of memory cells (Figure 2.16d). On the other hand, while the two-component distribution is not a good fit to the data, this is less of an issue for `pct.thresh`, as can be seen in (c).

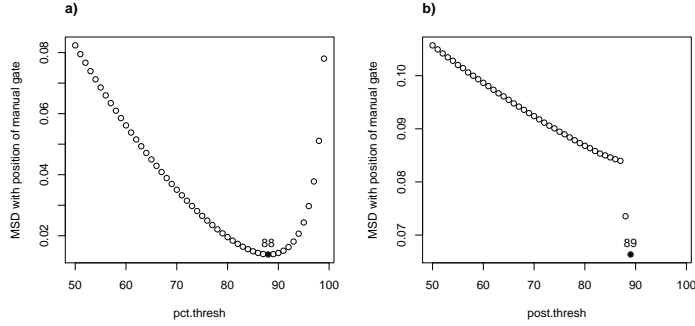


Figure 2.14. Mean square difference (MSD) of the position of the manual gate with that of `pct.thresh` (a) and `post.thresh` (b). The threshold which minimises the MSD is 88 for `pct.thresh` (a) and 89 for `post.thresh`. At that threshold, the `pct.thresh` (a) gate position matches better the manual than `post.thresh` (b). For `post.thresh`, the MSD is not defined for threshold larger than 89, because there are samples for which the posterior probability does not reach 89 percent (Figure 2.15e).

then a point x is assigned to component 1 provided that:

$$f_1(x) \geq f_2(x) \frac{p}{1-p}$$

For example, if the posterior probability threshold was $p = 95\%$, then for x to be assigned to the first component, $f_1(x)$ would need to be 19 times larger than $f_2(x)$.

Given these two thresholding approaches, I wish to select a threshold for `pct.thresh` and for `post.thresh`, which most closely matches the manual gating. To this purpose, I use the method described in the previous section (Figure 2.8), to find the threshold which minimises the mean square difference with the manual gate position. Applying this method, I find that the optimal threshold is the 88th percentile for `pct.thresh`, and 89% for `post.thresh` (Figure 2.14). Also, I notice that for `post.thresh`, in certain samples, the posterior probability of belonging to the first component does not exceed 89% (Figure 2.15). This is why in Figure 2.14, we do not obtain points beyond a threshold of 89, because gates are missing for certain samples. This can be due to

poor model fit (Figure 2.15a) or too much overlap between the memory and naive cell populations.

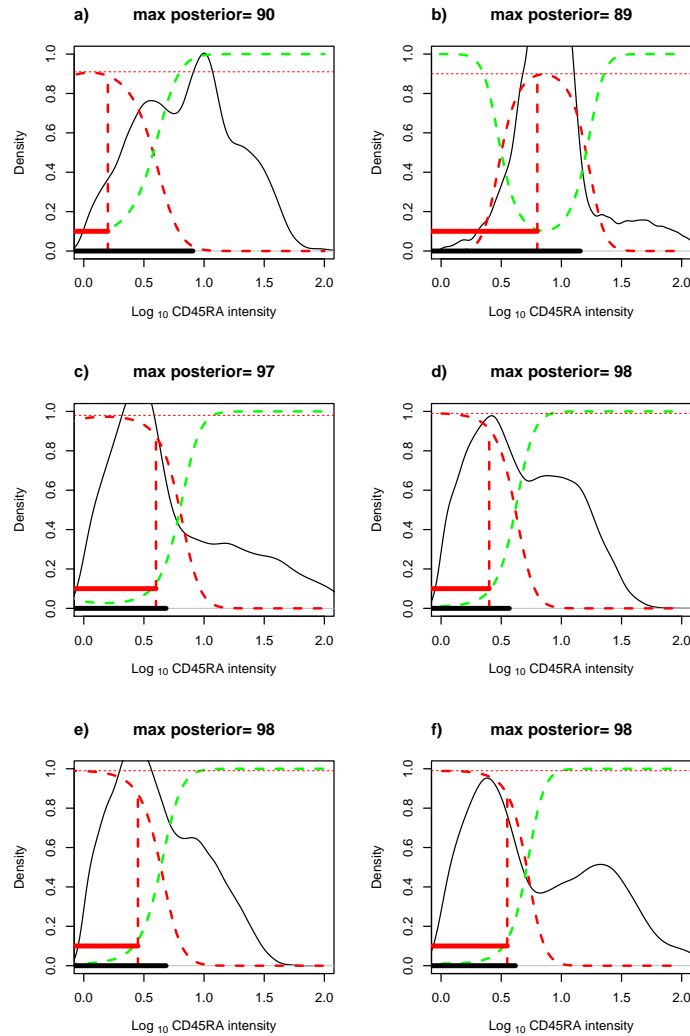


Figure 2.15. Samples for which the 99 maximum posterior probability is not reached. In black the manual gate. In red the post.thresh gate drawn at 89. The posterior probability does not reach 99 percent in these six samples. In a) this is because of poor model fit. In the others b), c) and d), this is due to the mixing of the two distributions. In b), the non-uniform decreasing posterior function, can be explained by the green distribution, component 2, being much wider than the red distribution.

Using either approach, there is good agreement between the CD25 MEF values obtained for the memory population when gated using either the automated or the manual

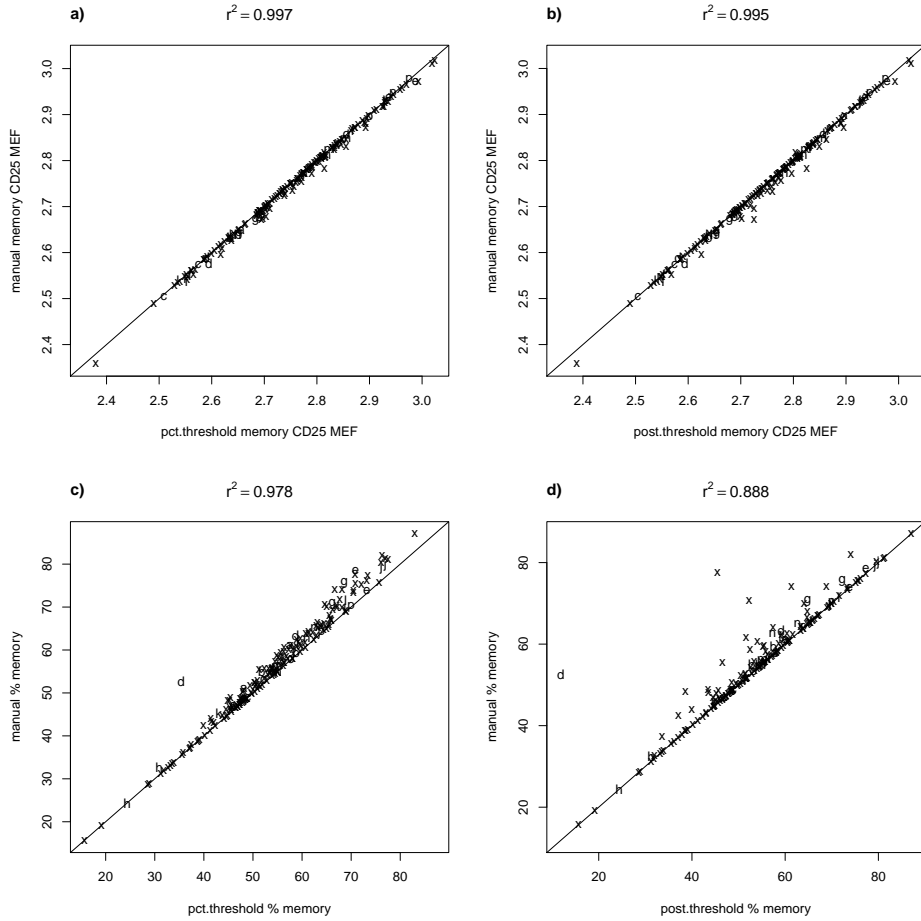


Figure 2.16. Agreement of memory CD25 MEF (a and b) and percentage of memory cells (c and d), obtained from `pct.thresh` and `post.thresh` with `manual`. The agreement of memory CD25 MEF is very close to manual (a and b) while the automatic methods tend to yield smaller memory cell percentages (c and d).

approach (Figure 2.16). This is to be expected as this cell phenotype is not very sensitive to the position of the CD45RA gate (Figure 2.17). Hence, for this phenotype, this translates to similar repeatability to that obtained with manual gating (Figure 2.18). On the other hand, the repeatability of the percentage of memory cells is very sensitive to the gate position.

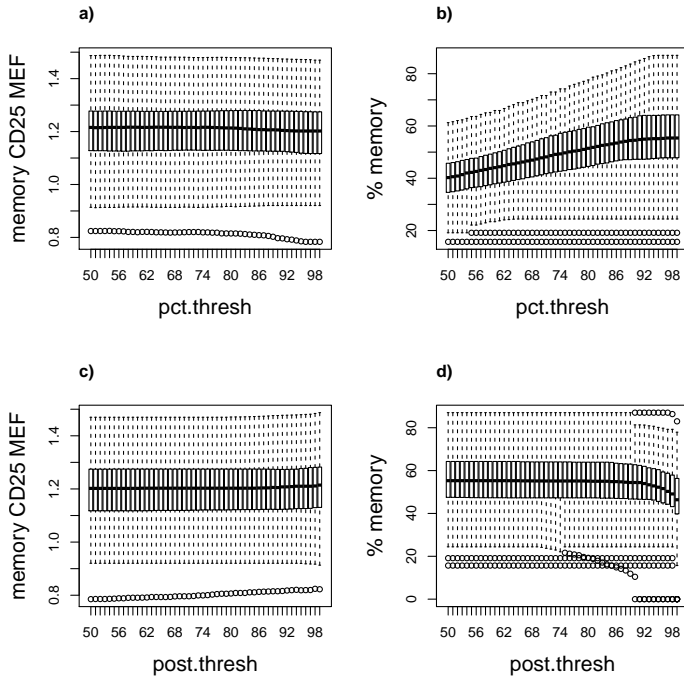


Figure 2.17. Influence of threshold for pct.thresh and post.thresh on distribution of memory CD25 MEF and percent memory cell phenotypes. Memory CD25 MEF is not sensitive to position of CD45RA gate (a and c) whereas percent memory is (b and d). On the other hand, the percent memory phenotype is more sensitive in particular when using the pct.thresh (c) method as opposed to the post.thresh (d).

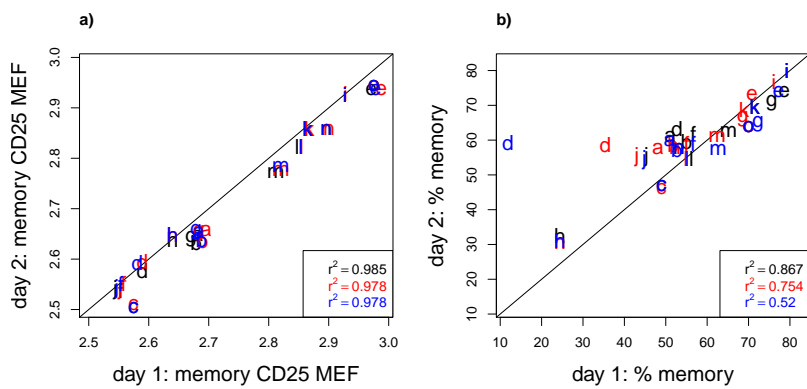


Figure 2.18. Repeatability of the memory cells phenotypes, CD25 MEF (a) and percentage (b), obtained from manual gating (black), pct.thresh (red) and post.thresh (blue). While the repeatability is very close for CD25 MEF ($r^2 = 0.985$ for manual, $r^2 = 0.978$ for pct.thresh and $r^2 = 0.978$ for post.thresh) it varies considerably for the percentage of memory cells ($r^2 = 0.867$ for manual, $r^2 = 0.754$ for pct.thresh and $r^2 = 0.52$ for post.thresh). Individual 'd' is a clear outlier when gated with the post.thresh method (b)

2.5 Association tests

Having obtained cell phenotypes by different gating strategies, I would like to assess how these influence our association test statistics. Since our dataset contains 15 repeated cell phenotypes from recalled individuals, I accounted for those in my association testing by applying a linear mixed effects model with random intercept to allow for per individual effect. To that purpose I used the R function `lme` from the R package `nlme` (Pinheiro et al, 2014). Each covariate, genotype, age and sex, was tested separately, with an additive recessive model assumed for the SNP effect.

Overall, the association test with the percent CD25⁺ naive cells phenotype yields similar effect sizes to manual (Table 2.6). A significant age and rs2104286 effect are reported using both manual and `beads.thresh` gating. However, the significance of the rs2104286 effect found with `beads.thresh`, is an order of magnitude less (10^{-4}) than with manual (10^{-5}). On the other hand, `beads.thresh` adds some evidence to the suggested association by Dendrou et al (2009b) of a sex effect on percentage of CD25⁺ naive cells, whereby males have a lower percentage of naive CD25⁺ than females, although the effect remains marginal.

Regarding the percentage memory cell phenotype, an age effect is also detected using automatic methods, `post.thresh` and `pct.thresh`, however the significance of the association is an order of magnitude less with `post.thresh` (pvalue 10^{-2}) than with manual and `pct.thresh` (pvalue 10^{-3}). This could be due to greater noise in the measurement as suggested by lower repeatability. Also, noteworthy, is that a marginally significant rs2104286 effect (pvalue=0.042322) is reported with `post.thresh`, which is not found with the other methods. However, on closer inspection, the association appears to be driven by the outlying sample from individual d (Figure 2.19).

For the memory CD25 MEF cell phenotype, the association results between manual and automatic are virtually identical (Table 2.7), which is to be expected, given this cell

54The influence of gating on reproducibility and association testing in flow cytometry

phenotype is largely unchanged by the CD45RA gate position (Figure 2.17).

	rs12722495	effect	95%CI	p-value
manual	-2.479	[-5.422;0.463]	0.098145	
beads.thresh	-1.509	[-4.453;1.435]	0.31326	
	rs2104286	effect	95%CI	p-value
manual	-4.714	[-6.894;-2.534]	3.2017e-05	
beads.thresh	-4.39	[-6.569;-2.212]	0.0001014	
	rs11594656	effect	95%CI	p-value
manual	-1.459	[-3.924;1.006]	0.2443	
beads.thresh	-1.328	[-3.774;1.118]	0.28531	
	Age	effect	95%CI	p-value
manual	0.475	[0.286;0.664]	1.6584e-06	
beads.thresh	0.457	[0.269;0.645]	3.514e-06	
	Sex	effect	95%CI	p-value
manual	-4.216	[-7.856;-0.575]	0.023475	
beads.thresh	-4.327	[-7.936;-0.718]	0.019046	

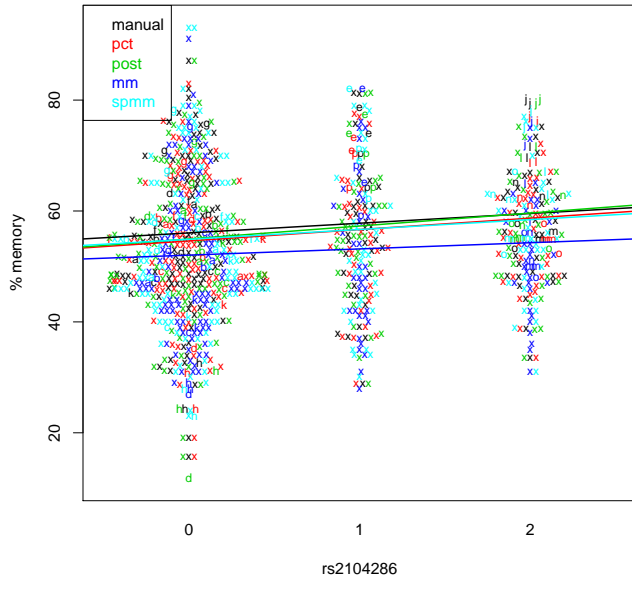
Table 2.6. Genotype, age and sex effect sizes on percentage of CD25⁺ cells.
Effect of rs12722495, rs2104286, rs11594656, age and sex, on the percentage of CD25⁺ naive cells.

	rs12722495	effect	95%CI	p-value
manual	0.062	[0.036;0.088]	4.7176e-06	
pct.thresh	0.06	[0.034;0.086]	9.0361e-06	
post.thresh	0.061	[0.035;0.087]	6.822e-06	
	rs2104286	effect	95%CI	p-value
manual	0.014	[-0.007;0.035]	0.18022	
pct.thresh	0.014	[-0.007;0.035]	0.19525	
post.thresh	0.014	[-0.007;0.035]	0.18634	
	rs11594656	effect	95%CI	p-value
manual	0.012	[-0.011;0.035]	0.29945	
pct.thresh	0.011	[-0.012;0.034]	0.34754	
post.thresh	0.011	[-0.012;0.033]	0.35147	
	Age	effect	95%CI	p-value
manual	0.001	[-0.001;0.003]	0.43937	
pct.thresh	0.001	[-0.001;0.003]	0.44201	
post.thresh	0.001	[-0.001;0.003]	0.38071	
	Sex	effect	95%CI	p-value
manual	0	[-0.034;0.034]	0.9983	
pct.thresh	0.001	[-0.033;0.035]	0.95584	
post.thresh	0.002	[-0.032;0.036]	0.89534	

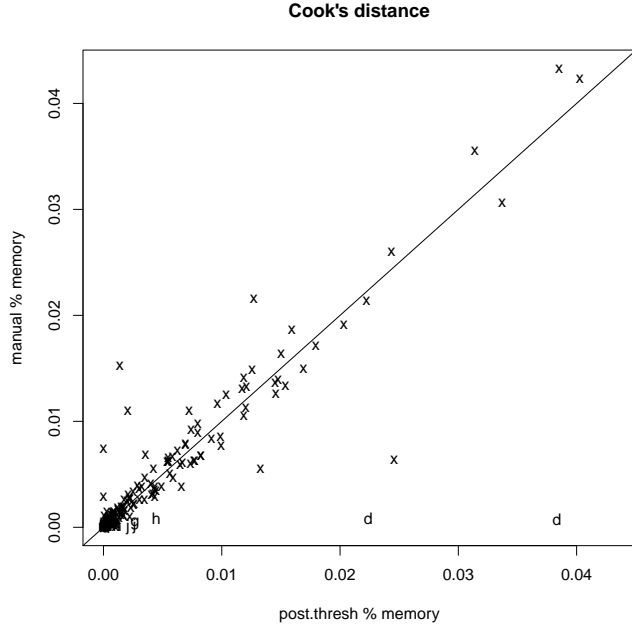
Table 2.7. Memory CD25 MEF effect sizes. Effect of rs12722495, rs2104286, rs11594656, sex and age on memory CD25 MEF.

	effect	95%CI	p-value
rs12722495			
manual	1.736	[-1.246; 4.718]	0.25209
pct.thresh	2.326	[-0.408; 5.06]	0.094952
post.thresh	2.624	[-0.26; 5.508]	0.074263
mm	1.131	[-1.84; 4.101]	0.45366
spmm	1.957	[-1.301; 5.214]	0.23746
rs2104286	effect	95%CI	p-value
manual	1.75	[-0.544; 4.045]	0.13399
pct.thresh	2.051	[-0.063; 4.165]	0.057164
post.thresh	2.337	[0.082; 4.593]	0.042322
mm	1.118	[-1.194; 3.431]	0.34129
spmm	1.775	[-0.744; 4.293]	0.16611
rs11594656	effect	95%CI	p-value
manual	-0.018	[-2.514; 2.479]	0.98884
pct.thresh	0.269	[-2.048; 2.585]	0.81927
post.thresh	0.402	[-2.092; 2.896]	0.75075
mm	1.253	[-1.265; 3.771]	0.32737
spmm	1.272	[-1.466; 4.01]	0.36044
Age	effect	95%CI	p-value
manual	0.387	[0.192; 0.582]	0.000127
pct.thresh	0.35	[0.169; 0.531]	0.00018575
post.thresh	0.316	[0.119; 0.513]	0.0018033
mm	0.431	[0.236; 0.625]	2.0985e-05
spmm	0.534	[0.326; 0.743]	1.0325e-06
Sex	effect	95%CI	p-value
manual	3.485	[-0.198; 7.168]	0.063526
pct.thresh	2.826	[-0.594; 6.246]	0.10471
post.thresh	2.811	[-0.86; 6.481]	0.1325
mm	2.793	[-0.925; 6.51]	0.13998
spmm	3.361	[-0.687; 7.408]	0.10308

Table 2.8. Memory percentage effect sizes. Effect of rs12722495, rs2104286, rs11594656, sex and age on memory cell percentage.



(a)



(b)

Figure 2.19. Effect of rs2104286 on percent memory gated by manual (black), post.thresh (green) and pct.thresh (red). In Table 2.8, marginally significant association is detected with rs2104286. This association is driven by the leverage of individual d which stands out as an outlier (b).

2.6 Discussion

In this chapter, I have shown that bead data is readily gated by automatic methods and that the results are comparable to manual gating. Automatic gating of bead data is fast and automates other related tasks such as MFI to MEF transformation, and threshold selection.

Gating of biological data is more difficult as we have little prior knowledge of the sample we are analysing and the data is far more noisy. So far, I have developed two automatic univariate gating strategies:

- a bead defined threshold method on CD25 to identify $CD25^+$ naive cells
- a two component mixture model on CD45RA to identify memory cells ($CD45RA^-$)

My CD25 univariate gating method (`beads.thresh`) relies on defining a threshold based on automatically gated bead data. The value of the threshold is selected as the percentile of the blank bead population which minimises the mean squared difference with manual gate positions. The percentage of naive $CD25^+$ cells phenotype identified with my approach showed better repeatability than manual (Figure 2.10). My approach defines one threshold for all samples gated on the same day, whereas the manual approach, relies on isotype controls and allows for different thresholds per day. Isotype controls should theoretically be an estimate of background but have been criticised for being an extra source of noise (O’Gorman and Thomas, 1999; Maecker and Trotter, 2006).

My CD45RA univariate gating method fits a specific model to the data: a mixture of two univariate distributions. The parameters of the model are estimated using an EM algorithm (Dempster et al, 1977) initialised with K-medoids.

In a first instance, I used the parameters estimated by the two-component mixture model. Specifically, I used the weight parameter of the first component as the percentage of memory cells phenotype. Although this seemed a sensible approach from the statistical

perspective of fitting a two-component mixture model, it does not match the biological perspective that transitional cells should be excluded.

Therefore, in the second instance, I attempted to emulate manual gating by defining a threshold. I tried two approaches of defining a threshold, `pct.thresh` which thresholds on the percentile of the first component of the fitted mixture model, and `post.thresh` which thresholds instead on the posterior probability of the first component. As with the `beads.thresh`, the value of the threshold is selected as the value which minimises the Mean Square Difference (MSD) with manual gate positions.

Two benchmarks were used to evaluate my univariate gating strategies: repeatability and comparison of the effects sizes obtained by Dendrou et al (2009b) using manual.

Repeatability is an independent measure which does not require comparison to other gating methods (such as manual). Unfortunately, given that in our data set only 15 samples are repeated, it is difficult to evaluate methods on such a small sample size. Moreover, good repeatability does not necessarily imply that the gating is unbiased but rather that the gating is consistent. Hence repeatability, needs to be complemented with some metric, in the form of manual gating or some prior biological knowledge, to assess whether the computed cell phenotypes are in a sensible range.

I have shown that the difference in the identification of cell phenotypes by different gating methods can influence the effect size estimates in association studies. In particular, outliers can have an important influence in relation to their leverage as seen in Figure 2.19. For example when testing association with age, outlier cell phenotypes from younger or older individuals have more leverage than ones closer to the mean. When testing for association with genotype, outlier cell phenotypes from rarer variants have more leverage than one from common variants.

Hence, if we are to deploy automatic gating techniques more generally, detection of outliers is crucial, to avoid false positive associations. In particular, we require outlier

detection metrics which do not only rely on the availability of repeated samples or manual gates. Already, we have seen that looking at the maximum posterior probability in a sample can give us some insight (Figure 2.15). Another metric of evaluating how well a model fits the data could be a cost function like the Mean Integrated Square Error (MISE).

When outliers have been detected, we may want to exclude or down-weight them, or extend the gating method to account for these. One simple way of modifying the method, could be to use the gate positions in non-outlier samples to influence that in outliers. This could motivate borrowing information from other samples, using for example a hierarchical Bayesian framework as was recently developed by Cron et al (2013), designed specifically to deal with rare cell populations which might not consistently be detectable across all samples.

However, one may argue that this approach, conceals rather than addresses the underlying problem of poor model fit. For example, as we see from the trimodal distribution in Figure 2.13, it may be more appropriate to fit a three component instead of a two component mixture model on this sample.

Chapter 3

Methods to assess cell response to ex-vivo stimulation in flow cytometry

*Mais la fleur n'en finissait pas de se
pré
chambre verte, elle choisissait avec soin
se*

Building on the work of the previous chapter, in which only two steps of the manual gating were replaced with an automatic algorithm, I will now consider a different dataset on which only preliminary manual analysis has been done. In this chapter, I will revisit the bead normalisation method as well as elaborate on further normalisation methods, and will this time, attempt to replace the entire manual gating with a computational process. In particular, I will develop approaches for discovering biologically relevant subsets not considered by the manual gating.

3.1 Background

Motivation Genomewide association studies have implicated the IL-2 signalling as an important aetiological pathway associated with the development of T1D. As seen in Chapter 2, the protective T1D associated *IL2RA* variant, at rs12722495 in healthy individuals, predicts an increase in the expression of CD25, the α chain of the trimeric IL-2 receptor, on memory CD4 $^{+}$ T lymphocytes (Dendrou and Wicker, 2008; Dendrou et al, 2009b). Garg et al (2012) found that regulatory and memory CD4 $^{+}$ T cells in healthy carriers of the T1D associated rs12722495 haplotype, also exhibit decreased sensitivity to IL-2. The decreased sensitiviy was measured in terms of lower MFI levels of phosphorylated STAT5 (pSTAT5). STAT5, the signal transducer and activator of transcription 5 protein, dimerises or tetramerises on phosphorylation and acts as a transcription factor that also induces the transcription of *FOXP3*, one of the transcription factors characteristic of regulatory T cells (Tregs) (Figure 3.1).

Long et al (2011) have reported that a T1D associated variant at rs1893217 of the protein tyrosine phosphatase N2 gene (*PTPN2*), a negative regulator of the IL-2 pathway, also correlates with lower pSTAT5. Furthermore, it is suspected that IL-2 production might be diminished in T1D, since disease associated *IL2RA* variants correlate with reduced CD25 levels and reduced IL-2 production on activated CD69 $^{+}$ CD4 $^{+}$ memory T cells after antigen stimulation (Dendrou et al, 2009b). Long-term reduced sensitivity to IL-2 also correlates with diminished maintenance of FOXP3 expression in the CD4 $^{+}$ CD25 $^{+}$ regulatory T cells of T1D subjects (Long et al, 2010). Hence, these findings appear to consolidate the hypothesis that type 1 diabetics tend to have a reduced ability to respond to IL-2 in part due to genetic differences in *PTPN2*, *IL2RA* and possibly other gene variants involved in the IL-2 signalling pathway (Long et al, 2010, 2011, 2012). These results are of great clinical relevance to us, since our lab is currently conducting

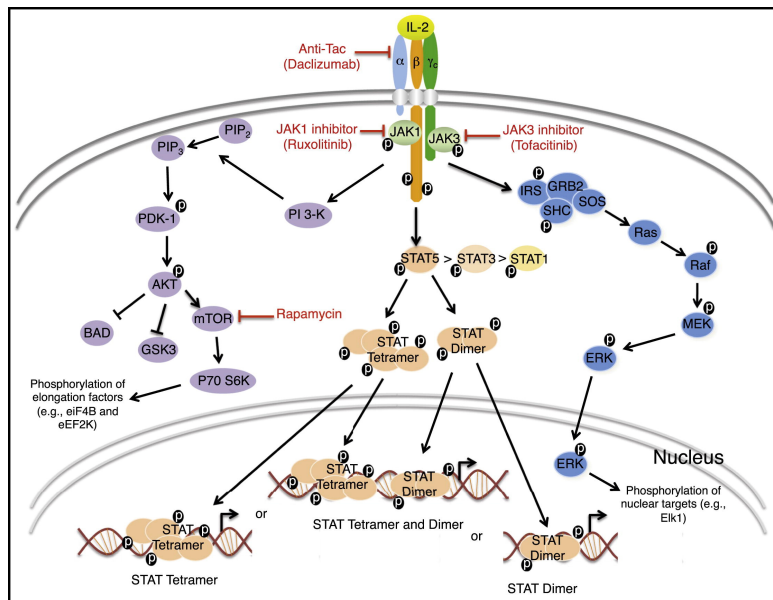


Figure 3.1. Schematic of major IL-2 signaling pathway. Figure from Liao et al (2013). The trimeric IL-2 receptor (IL2R) is constituted of: the α chain IL2RA (CD25), the β chain IL2RB (CD122) and the γ chain IL2RG (CD132). On binding of an IL-2 molecule to the receptor, a signalling cascade is initialised in which STAT5 is phosphorylated to pSTAT5, which then dimerises or tetramerises into a transcription factor. Only the β and γ chains have signalling motifs. The α chain supplies an increase in affinity but does not signal. Cells express variable proportions of each of the components of the trimeric receptor with CD132 being the most commonly expressed. The pSTAT5 response to IL-2 is correlated with the relative expression of the three subunits and there is generally strong correlation between the CD25 MFI and the pSTAT5 MFI.

an adaptive study of IL-2 dose on regulatory T cells in type 1 diabetes (DILT1D¹), and to all researchers interested in low-dose IL-2 therapy to autoimmune diseases (Koreth et al, 2011; Saadoun et al, 2011).

However some concerns have been raised with these studies. One concern was that the Tregs discrimination was not particularly thorough. Long et al (2010) define Tregs based only on two markers $CD4^+$ and $CD25^+$, whereas these cells are usually also defined on CD127 and FOXP3 expression. Another a notable omission by Long et al (2010) was the lack of repeated samples to assess the within-individual variance or reliability of the

¹<http://www.clinical-trials-type1-diabetes.com/>

assay. In order to assess the validity of these results, Tony Cutler, in our lab, set to find if he could replicate some of these findings in an independent cohort, using a more refined gating strategy by including the FOXP3 regulatory T cell marker. He also included the CD3 T cell marker, as well as more NK cell specific markers, CD8 and CD56, to discover other cell subsets which may potentially, also be sensitive to IL-2 (Table 3.2).

Samples and panels He selected 22 long-standing diabetics (6 males and 16 females, mean age 29) and 28 controls (mean age 27) from the Cambridge Biorepository, as well as 30 newly diagnosed (20 males and 9 females, mean age 11.7) and 15 unaffected siblings of type 1 diabetics (5 males and 12 females, mean age 12.3) from the Diabetes - Genes, Autoimmunity and Prevention (D-GAP) resource. These were matched on age and sex to 43 controls. In order to assess the reproducibility, ten individuals, five cases and five controls, were recalled for a second blood sample from the Cambridge Biorepository (Table 3.1).

Individual	status	pch	number of days between visits
1	control	a	98
2	case	b	140
3	control	c	167
4	control	d	98
5	case	e	167
6	case	f	112
7	control	g	112
8	case	h	98
9	case	i	120
10	control	j	140

Table 3.1. Ten individuals recalled between 98 and 168 days later to assess stability of the cell phenotypes. pch is the plotting character used to refer to these individuals in plots later in this chapter.

Blood samples were prepared and analysed by flow cytometry on day of collection. Each sample was split into four aliquots of 500 µl. The first aliquot was left unstimulated. The remaining three were stimulated ex-vivo for 30 minutes at three increasing doses of

proleukin, a recombinant IL-2 molecule, at 0.1, 10 and 1000 U ml⁻¹ respectively.

After the set stimulation time, the samples were fixed, permeabilised and stained, with different panels (Table 3.2), on a set of core markers, not expected to be affected by short-term proleukin stimulation, CD4, CD25, CD45RA and FOXP3. These were used to delineate different cell types, and the functional marker, pSTAT5, was used to measure proleukin response. In order to control for batch, age or sex, T1D samples were, when possible, run in parallel with an age and sex paired healthy control, although in practice, this was not always possible (Figure 3.2). Also for practical and financial reasons, not all samples were stained with every panel (Table 3.2). Hence the case-control statistical analysis was only conducted in samples stained with the CD4 T cell panel, which included all samples in the study.

Fluorochrome	T/NK cell panel	CD4 T cell panel
Alexa Fluor 488	pSTAT5	pSTAT5
Alexa Fluor 700	CD4	CD4
APC	CD25	CD25
Pacific Blue	CD56	CD45RA
PE YG	FOXP3	FOXP3
PE-Cy7 YG	CD45RA	
PerCP Cy5-5	CD3	
Qdot 605	CD8	
Number of samples	5	95

Table 3.2. Proleukin stimulation assay antibody-fluorochrome panels. The fluorochrome-antibody panels used in IL-2 stimulation. The panel used on the majority of samples was the CD4 T cell panel, used to discriminate effector and regulatory naive and memory T cells. The T/NK cell panel, which contains the most markers, was only run on a subset of 5 samples.

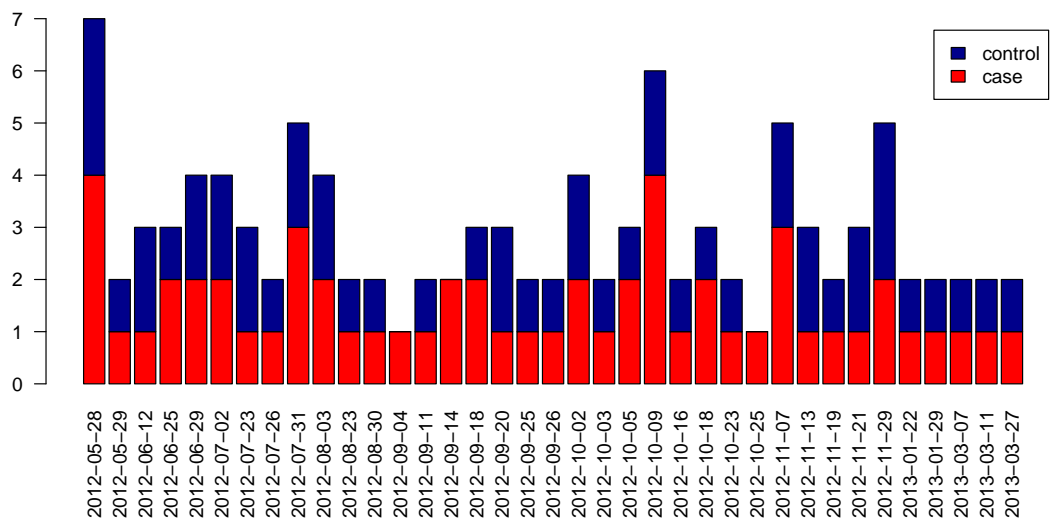


Figure 3.2. Number of cases and controls analysed per day in the 95 samples. To account for batch effects in the case-control association testing, Tony Cutler aimed to analyse, when possible, at least one healthy control sample and one type 1 diabetic sample per day. However, on two days, 2012-09-04 and 2012-10-25, no matching controls were run.

3.2 Preliminary analysis by Tony Cutler

In this section, I will describe the preliminary manual analysis using FlowJo that was conducted by Tony Cutler. Four CD4⁺ lymphocyte subsets (Figure 3.3) were gated manually using FlowJo:

- memory effector T cells (Teffs)
- memory regulatory T cells (Tregs)
- naive Teffs
- naive Tregs

Within each lymphocyte subset, the pSTAT5 distribution was measured, in each of the four samples stimulated at an increasing proleukin dose (Figure 3.4). As expected, the pSTAT5 distribution shifts progressively right for higher doses of proleukin, as more STAT5 is phosphorylated. Of the four subsets, the most sensitive cells to proleukin are the rarer memory and naive Treg subsets (Figure 3.4 b and d), then the memory Teffs (Figure 3.4 a) and finally the naive Teffs (Figure 3.4 c). This correlates with the level of CD25 expressed by these cells.

Next the repeatability of the pSTAT5 response was assessed by measuring the pSTAT5 MFI in each of the four subsets. This pSTAT5 response cell phenotype was poorly reproducible, since the location of the peaks was not stable across days as illustrated by the sample shown in Figure 3.5. This motivated a threshold approach to define the ratio of cells which are pSTAT5⁺. An idea similar to that applied in Chapter 2 to define naive cells as CD25⁺. However, here an internal threshold was used, namely the threshold was defined to be the 99th percentile of the pSTAT5 distribution in the resting cell subset per sample. Thus each sample and cell subset had its own pSTAT5⁺ threshold. Tony Cutler presented his results in six of the ten repeated individuals for the four stimulated cell subsets, memory Teffs (Figure 3.6), memory Tregs (Figure 3.7), naive Teffs (Figure 3.8) and naive Tregs (Figure 3.9). At the highest 1000 units proleukin dose,

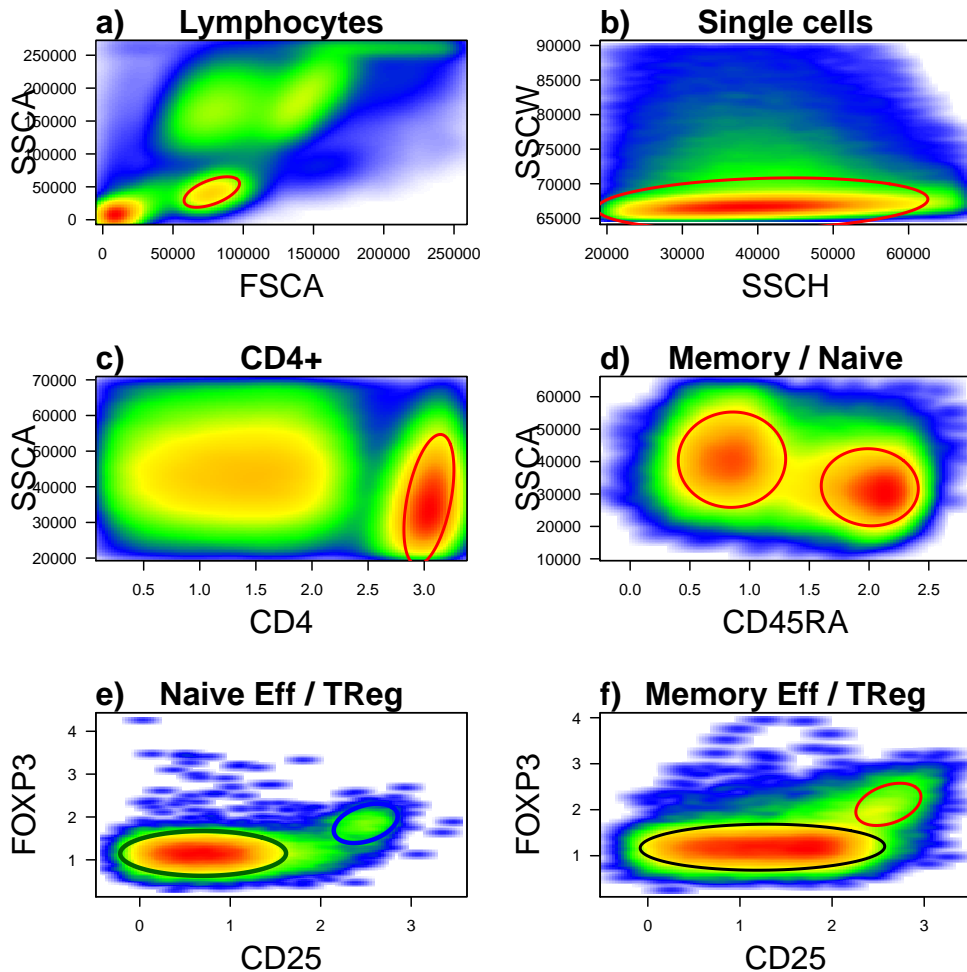


Figure 3.3. Gates applied across doses. Manual gating conducted using FlowJo by Tony Cutler to identify naive Teffs (green ellipse) and Tregs (blue ellipse) (e) and memory Teffs (black ellipse) and Tregs (red ellipse) (f).

most memory and naive Tregs are pSTAT5⁺, however, as these cell populations already show a significant response at the lowest 0.1 unit dose, the percentage of pSTAT5⁺ cells at the 0.1 units dose was selected to be the relevant cell phenotype for memory and naive Treg pSTAT5 cells (Figures 3.7 and 3.9). For the less responsive memory Teffs, 10 units was chosen as the representative dose, while for naive Teffs, the least responsive of the four cell subsets considered, the repeatability was assessed at the 1000 unit dose.

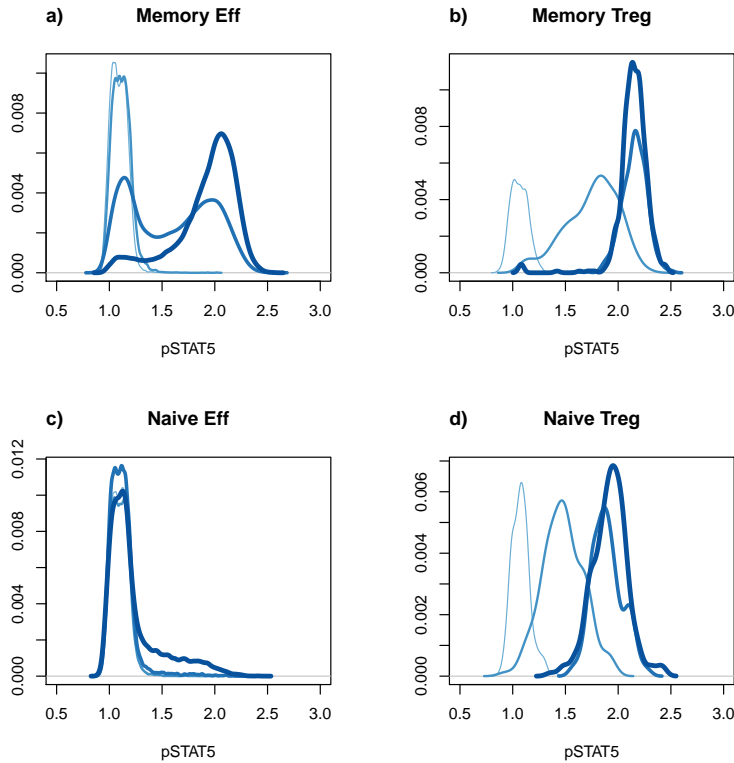


Figure 3.4. pSTAT5 distribution in the manually gated cell subsets from Figure 3.3. The thickness of the lines is representative of the four increasing doses of proleukin (0, 0.1, 10 and 1000 units). The dose-response is most striking in the smaller Treg subsets with higher CD25 (b and d).

The repeatability was assessed with the coefficient of determination:

$$R^2 = 1 - \frac{\sum_{i=1}^N (x_{i1} - x_{i2})^2}{\sum_{i=1}^N (x_{i1} - \bar{x}_1)^2}$$

where x_{i1} is the phenotype of i^{th} individual on the first day and x_{i2} is the phenotype of the i^{th} individual on the second day. The coefficient of determination can take negative values if the correlation between x_{i1} and x_{i2} is very low. Contrary to the Pearson correlation, used in the previous chapter, the coefficient of determination is sensitive to linear transforms. In Figure 3.10, even when using the percent of pSTAT5⁺ cell phenotype, the overall reproducibility across the four cell subsets was still poor, with the more

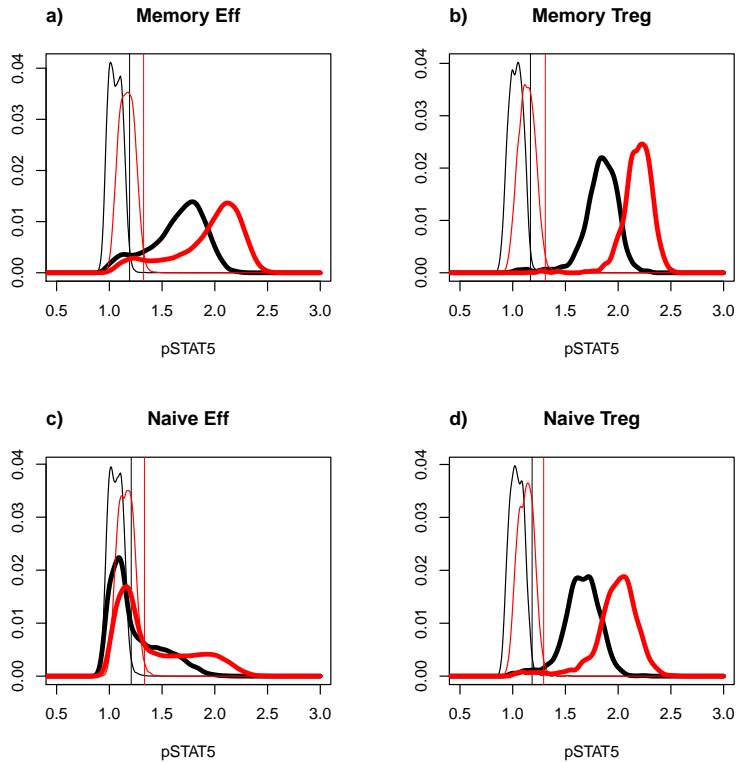


Figure 3.5. pSTAT5 distribution in an individual on visit one (black) and visit two (red). In black, the pSTAT5 distribution on visit one and in red, on visit two. The thinner lines are from the resting sample whereas the thicker lines are from the sample stimulated at 1000 units. The vertical lines represent the pSTAT5⁺ threshold set at the 99th percentile of the pSTAT5 distribution in the resting sample. This clearly shows that pSTAT5 distribution is not stable across days in the four cell subsets.

sensitive and smaller cell subsets, naive and memory Tregs showing the worst correlation ($R^2 = -0.16$ and $R^2 = -0.82$), memory Teffs showing slightly better correlation ($R^2 = 0.021$) and the less responsive naive Teffs showing good correlation ($R^2 = 0.7728$). The association with T1D was tested using a two-tailed paired t-test of 20 cases matched with 20 controls analysed on the same day (Figure 3.11). He also tested for association with *IL2RA* SNP rs12722495, and the *PTPN2* SNPs rs45450798 and rs478582 (plots not shown). No significant association was detected either with disease or with genotype.

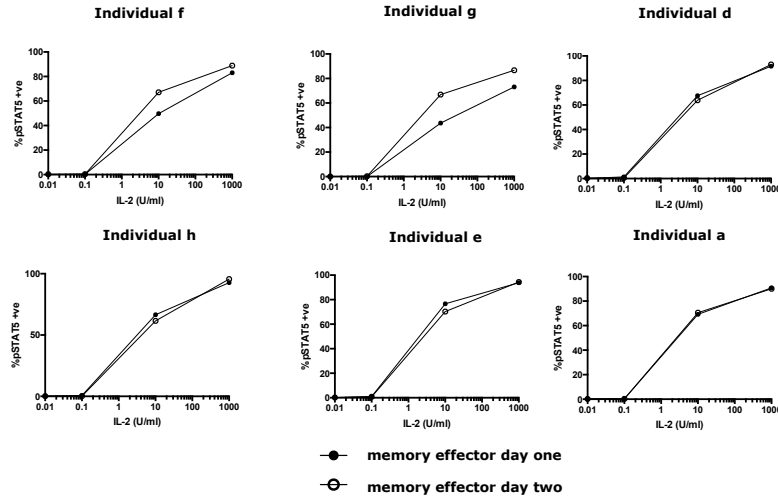


Figure 3.6. The percentage of pSTAT5⁺ cells increases with proleukin dose in memory Teffs. Plot produced by Tony Cutler. The percent of pSTAT5⁺ cells increases with proleukin dose in memory Teffs, but the measured response is not consistently repeatable (f, g).

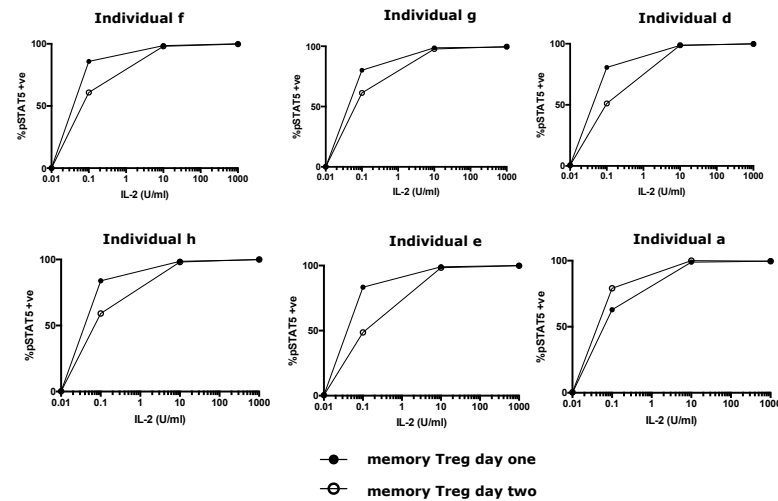


Figure 3.7. The percentage of pSTAT5⁺ cells increases with proleukin dose in memory Tregs. Plot produced by Tony Cutler. While at the highest proleukin dose of 10 and 1000 units, all memory tregs are consistently pSTAT5⁺, there is more discrepancy at the low dose of 0.1 units.

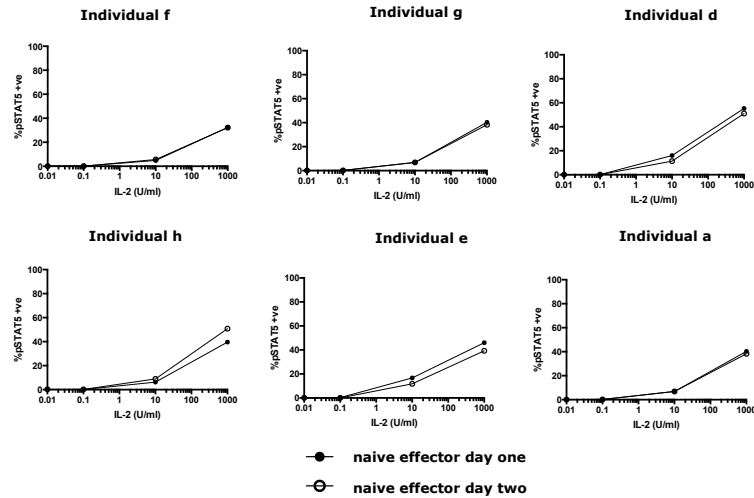


Figure 3.8. The percentage of pSTAT5⁺ cells increases with proleukin dose in naive Teffs. Plot produced by Tony Cutler. Only 40 % of the naive effector cells are pSTAT5⁺ even at the highest 1000 unit proleukin dose.

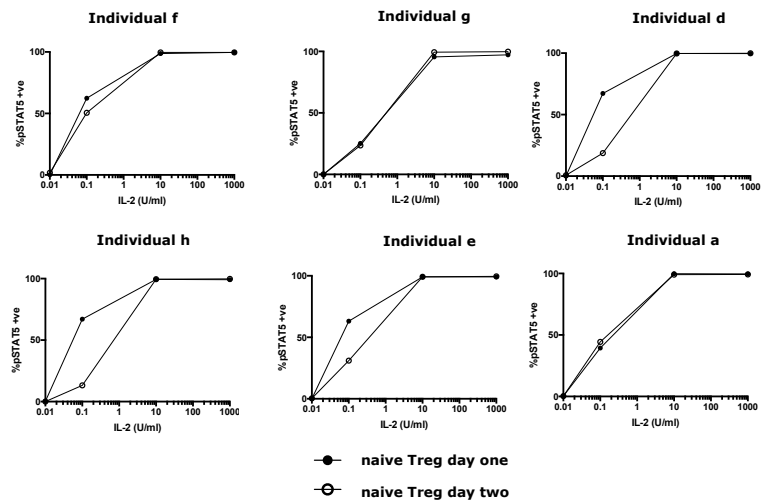


Figure 3.9. The percentage of pSTAT5⁺ cells increases with proleukin dose in naive Tregs. Plot produced by Tony Cutler. While at the highest proleukin doses of 10 and 1000 units, all naive tregs are consistently pSTAT5⁺, there is more discrepancy at the low dose of 0.1 units.

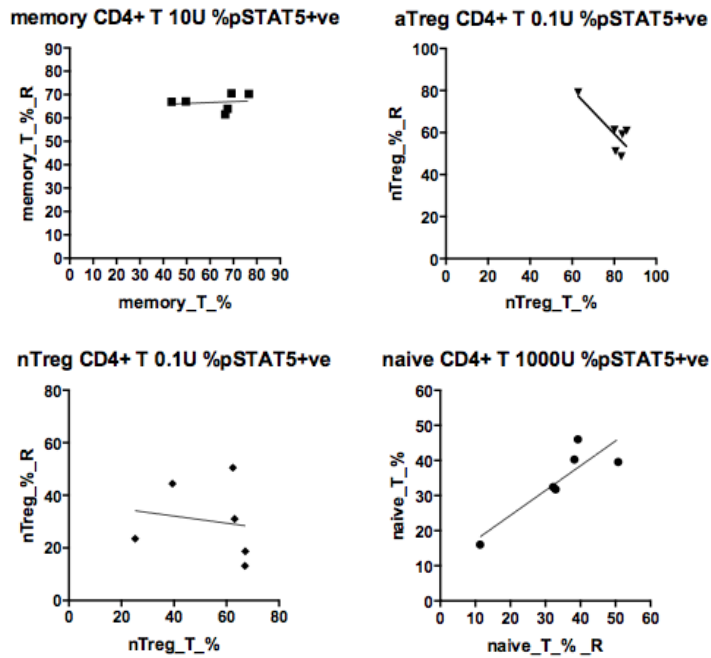


Figure 3.10. Repeatability of pSTAT5⁺ in six individuals in the four cell subsets. Plot produced by Tony Cutler. The repeatability of the percent of cells which are pSTAT5⁺ is assessed in effector memory and naive at the 10 units and 1000 units dose respectively, and in memory and naive Tregs at the 0.1 units dose. While the repeatability in the naive effector subset was good ($R^2 = 0.7728$), the repeatability in the other cell subsets is poor (memory Teffs $R^2 = 0.021$, naive tregs $R^2 = -0.16$ and memory tregs $R^2 = -0.82$).

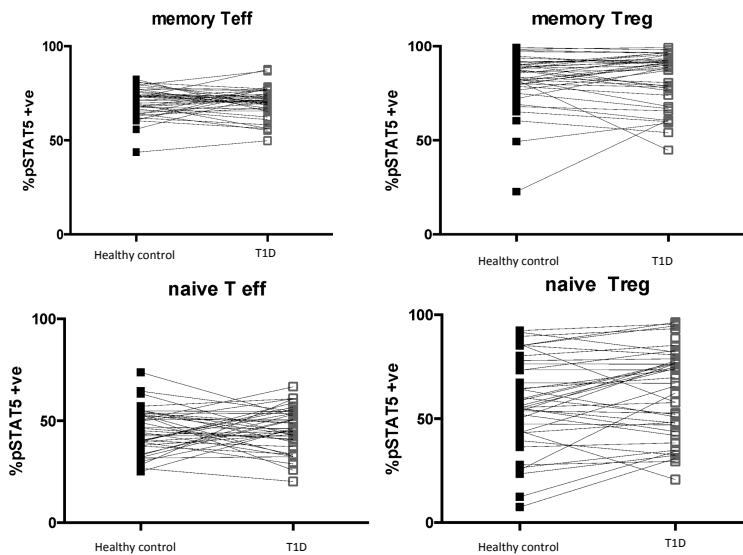


Figure 3.11. Association test of percent pSTAT5⁺ in the four cell subsets. Plot produced by Tony Cutler. The association with T1D of the percent of cells which are pSTAT5⁺ is assessed in effector memory and naive at the 10 units and 1000 units dose respectively, and in memory and naive Tregs at the 0.1 units dose. The association test is a two-tailed paired-t-test on 20 cases paired with 20 controls analysed on the same day (40 out of the available 96 individuals). No significant association is detected.

3.3 Reproducibility of pSTAT5 response within an individual

Tony Cutler's preliminary results in the six repeated individuals suggested that the pSTAT5 MFI and percent pSTAT5⁺ were poorly reproducible cell phenotypes using the methodology and approach described, which consequently would give us little power to detect an association with disease status or genetics. In Chapter 2, repeatability of CD25 MFI in memory cells was improved thanks to bead normalisation. This motivated me to see whether on this data, normalisation approaches would also improve the repeatability of these cell phenotypes.

3.3.1 Normalisation approaches

Bead normalisation In Chapter 2, I used beads to correct for day to day variation in the CD25 channel. However for these data, using beads in the Alexa-488 channel, the fluorochrome conjugated to pSTAT5 (Table 3.2), did not adequately capture the short term variation in pSTAT5 (Figure 3.12). This suggests that day to day variation in the instrument is unlikely to be the major cause of day to day variation in the data, and that bead normalisation cannot be usefully applied.

Correcting for baseline MFI in cell subsets One observation which can be drawn from Figure 3.5 is that the MFI of the pSTAT5 distribution in the resting sample is different across days. If a cell population had a higher resting pSTAT5 MFI due only to day to day variability, then one might expect that the pSTAT5 MFI in the stimulated population would also be higher. I first attempted to account for the difference in resting pSTAT5 by taking the ratio of the MFI of the stimulated populations over that of the MFI of the resting population, or equivalently by subtracting the log transformed MFIs.

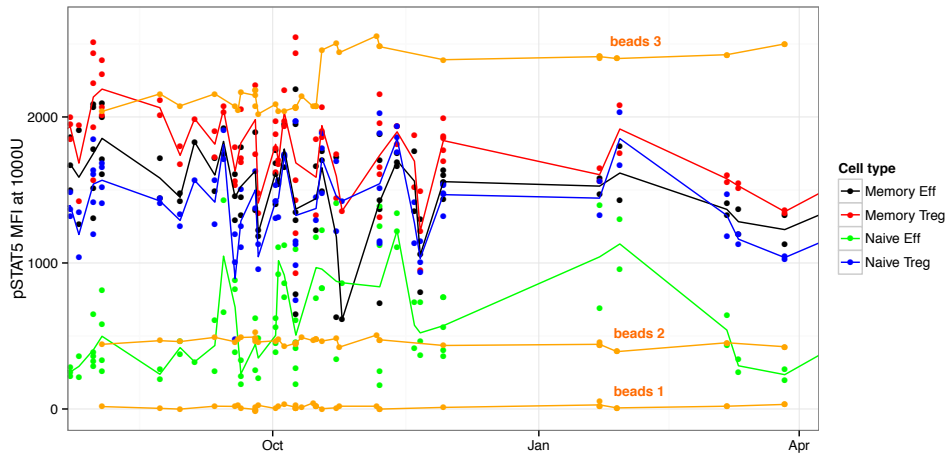


Figure 3.12. Variation in pSTAT5 MFI is not captured by variation in bead MFI. For the purpose of MFI normalisation, the fluorescence intensity of six-peak flow cytometry beads was measured in the Alexa 488 channel, the fluorochrome conjugated to the pSTAT5 marker. However, as illustrated by the loess lines, the MFI of the three dimmest populations of beads (orange) does not capture the pSTAT5 MFI time variation in the four cell subsets. The pSTAT5 MFIs are obtained from samples stimulated at 1000 units of proleukin.

Nearest-neighbour joining on whole sample One concern with adjusting by baseline MFI is that differences in cell counts across samples within the same batch stimulated at different doses, may influence the accuracy of the MFI estimate. Another concern is that since the pSTAT5 distribution is often bimodal in the cell populations considered, subtracting the MFI may not be ideal. Instead, a more correct approach would be to subtract the pSTAT5 fluorescence intensity for each resting cell. One way of emulating this is to match each cell to its closest neighbour in the unstimulated sample. This was accomplished by joining samples on their core markers using the Approximate-Nearest-Neighbour (ANN) to the resting sample (Jones et al, 2011) as implemented in the R package RANN (Arya et al, 2013). This created a dataset of the same number of cells as the resting dataset, but where each cell now had a total of four functional pSTAT5 markers, one for each stimulation dose. At each cell it is now possible to assess the difference in pSTAT5 response between resting and stimulated states. This is important

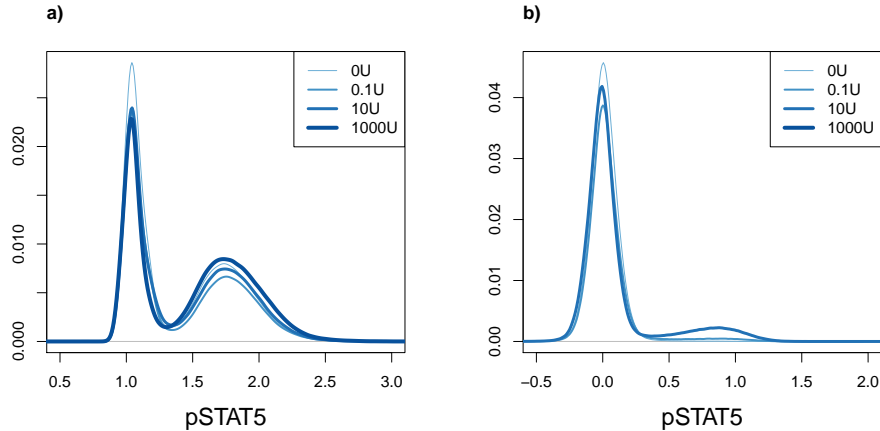


Figure 3.13. pSTAT5 intensity across the three proleukin doses, before (a) and after (b) per-cell baseline pSTAT5 subtraction in the ungated sample. An important proportion of cells are already saturated for pSTAT5 (high baseline) in the resting sample (a). Correcting for the per cell pSTAT5 baseline, shows the true proportion of cells which responds to proleukin within this sample (b).

because cells do not all have the same resting level of pSTAT5 (Figure 3.13). This approach presents a number of advantages. Firstly, only the sample to which the other samples are joined needs to be gated. Secondly, since the pSTAT5 response is relative to the baseline, it should be more robust to variation between days and consequently, more reproducible than pSTAT5 fluorescence intensity. Thirdly, since we have response at the cell-level, we can apply methods to do multivariate regression of pSTAT5 from core markers. This could help identify cells which would have been missed from only examining core markers.

3.3.2 Repeatability

The repeatability of the pSTAT5 MFI and percent pSTAT5⁺ across doses gives a different pattern depending on the cell type but at the highest dose it appears that the least responsive naive effector T cells (Teffs) yield the best repeatability (Figure 3.14 and (Figure 3.15)). On the other hand, the repeatability of the naive Treg phenotype is poor

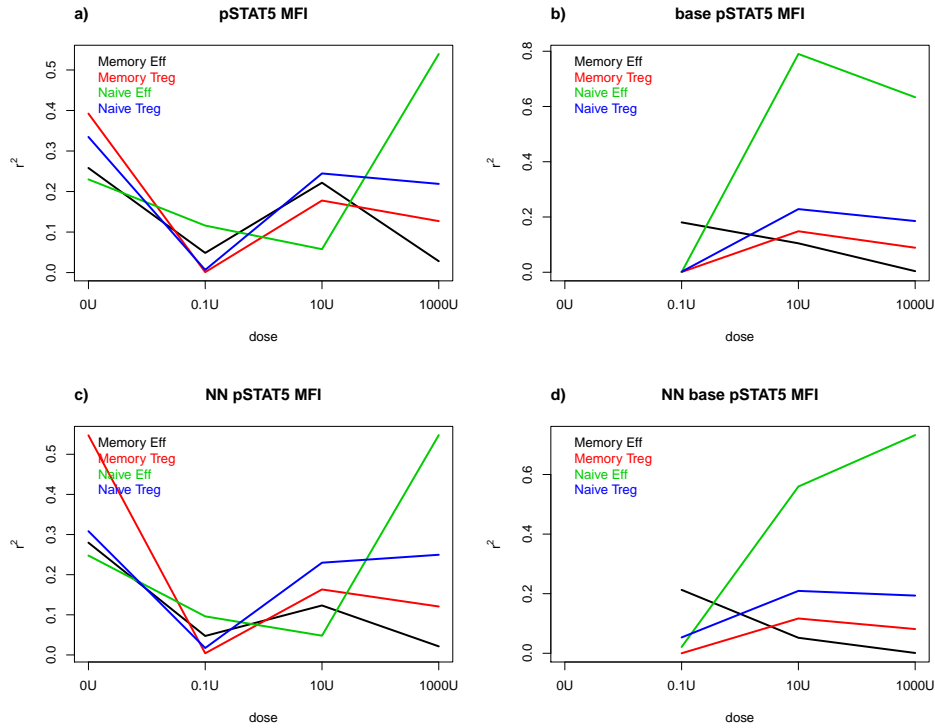


Figure 3.14. Repeatability of pSTAT5 MFI measured as Pearson correlation squared (r^2) per dose per cell type. For all ten repeated samples, the Pearson correlation squared r^2 of the MFI was assessed at the four increasing doses, in the four cell subsets, for the raw (a), baseline corrected (b), nearest-neighbour joined (c) and nearest-neighbour baseline corrected (d). On correcting for the baseline, the repeatability of the naive effector subset is improved but not in the other cell subsets.

at all doses. In summary, I concluded that the day to day variation must relate to some factor not directly captured in baseline samples, perhaps subtle differences in the titration of proleukin doses or in cell preparation.

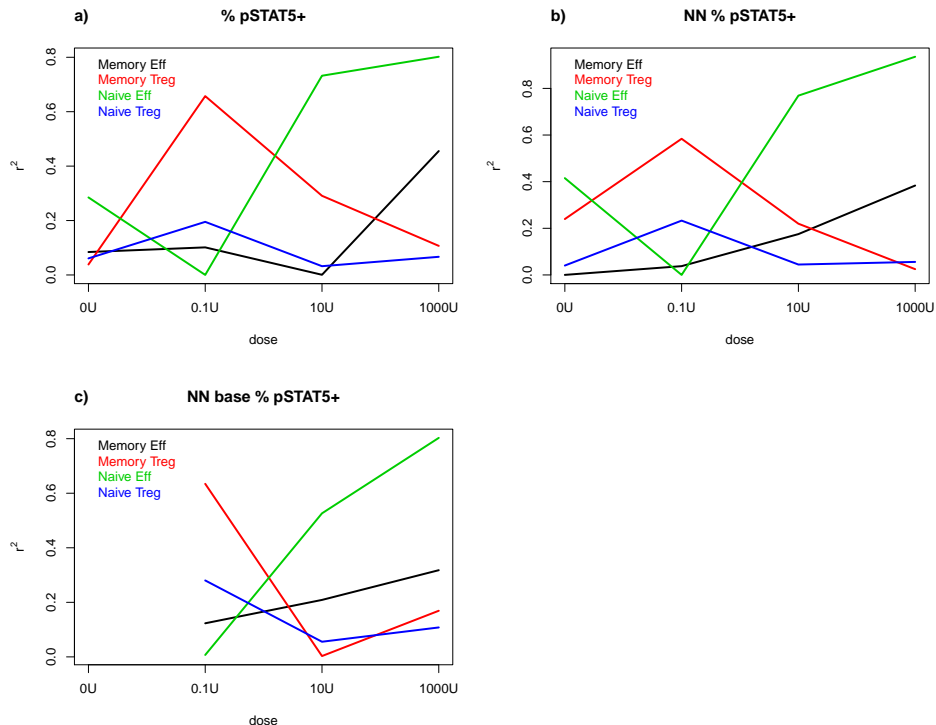


Figure 3.15. Repeatability of the percent of pSTAT5⁺ as Pearson correlation squared (r^2) per dose per cell type. Only the pSTAT5 in the naive effector subset stimulated at 1000 units shows good repeatability across all normalisation methods.

3.3.3 Association of pSTAT5 response with type 1 diabetes

Given the large within-individual variance, I was not expecting to find significant association in most of the cell subsets. However for the sake of completeness, I tested the association with T1D at each dose, as well as for the total response across all doses (area under the curve). I accounted for repeated individuals and day of analysis by including them as random effects in a linear mixed effects model as applied in Chapter 2. The figures are included in the Appendix Chapter B. No significant T1D association was detected with the pSTAT5 MFI (Appendix Figures B.1 and B.2) nor with the percent pSTAT5⁺ (Appendix Figures B.3 and B.4) cell phenotypes in the four cell subsets considered.

3.4 Response in the whole sample

Using the normalisation methods described in the previous section, I was unable to significantly improve the reproducibility of this assay. My view is that this dataset, as it stands, is not sufficiently reproducible to rigorously assess whether there is a difference in proleukin response between cases and controls in the cell subsets under study. However, it may still contain useful biological information. As described in Table 3.2, a subset of samples stained with a quite comprehensive panel, including CD3, CD56 and CD8, we can be used to address another clinically relevant question: beside the four manually gated cell subsets, are there other subsets which respond to proleukin within the Peripheral Blood Mononuclear Cells (PBMC)?

This question is extremely relevant for DILT1D² and other clinical trials of IL-2 which have mostly focused on lymphocytes. Biologists know that any cell which carries high levels of the three subcomponents of the IL-2 receptor, α (CD25), β (CD122) or

²<http://www.clinical-trials-type1-diabetes.com>

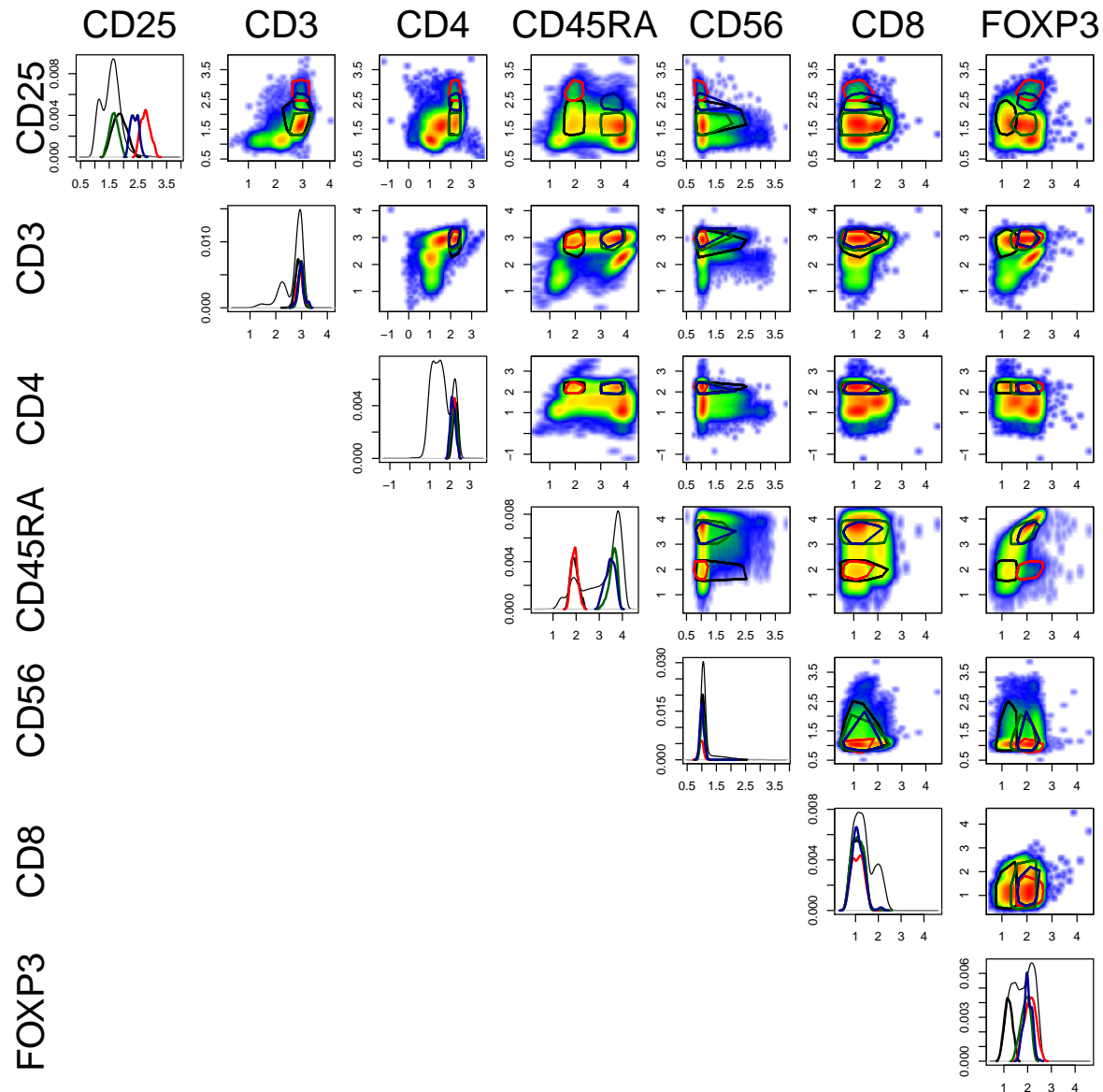


Figure 3.16. Manually gated lymphocyte subsets projected on all core markers. The manually identified subsets are naive Teffs (dark green) and Tregs (blue), memory Teffs (black) and Tregs (red). Although, CD8 and CD56 are not included in the gating (Figure 3.3), all the identified subsets are primarily $CD8^-$ and $CD56^-$. There is some spillover causing spurious correlation between CD45RA and FOXP3. The fluorescent dye used to tag CD45RA, PE Cy7 YG, has a significant spillover into the PE YG (tagging FOXP3) channel. This explains the spurious correlation between $CD45RA^+$ and $FOXP3^+$ cells making it impossible to discriminate the $CD45RA^+$ subsets, naive Teffs (green) from naive Tregs (blue), based on FOXP3.

γ (CD132), should respond to IL-2, but due to the limitation on the possible number of fluorochromes per tube, these are not all included as part of every flow experiment. This study of *ex vivo* stimulated whole blood offers the opportunity to identify other, potentially new, cell subsets also responsive to IL-2. In order to increase my chances of characterising these subsets, I only analysed samples stained with the most comprehensive marker panel we had available, the one containing the additional fluorochromes for CD3, CD8 and CD56 (Table 3.2). Unfortunately, the staining using this panel was of poor quality in many samples, due to the harsh nature of the permeabilisation protocol and to the larger number of markers used, which caused certain marker stains, such as CD56, to not work well across all batches. This made between-batch analysis infeasible so instead, I focused on the analysis of a single batch for which the staining had worked. Assessing the staining quality of a sample requires prior knowledge, and so Marcin Pekalski, an experienced flow cytometrist, assisted me in finding a batch with no obvious staining artefacts (Figure 3.16). This batch was then used for subsequent analysis in the rest of this chapter.

When assessing the dose-response to stimulation in a flow cytometry sample, the classic approach is to first gate cell populations in each sample based on their core markers, then to assess the response of the functional marker in the gated subset. Obviously, this approach is not exhaustive and consequently may miss other dose-responsive cell populations which are not included in the gating strategy. Here I first explored approaches to visualise the pSTAT5 dose-response in the whole sample in order to spot other potential dose-responsive cell subsets. I also considered more automated methods which use the pSTAT5 response to guide the identification of these cell subsets. One of the challenges faced in identifying new cell types is how to reconcile the two different kinds of flow cytometric data, scatter and fluorescence, since these represent quite different physical properties and are measured on a linear and logarithmic scale respectively. Typically

scatter gating takes precedence over fluorescence gating, and the standard protocol is to first use scatter to discriminate live cells from debris. In the next section, I followed this protocol, by first gating on side and forward scatter in order to distinguish lymphocytes from non-lymphocytes, then conducting separate analysis on the lymphocyte subset using fluorescent markers only, and to the non-lymphocyte subset, using both fluorescent and scatter markers.

3.4.1 SPADE: spanning-tree progression analysis of density-normalized events

Visualisation is a fundamental tool for exploring high dimensional datasets. In this instance, I am interested in visualising the pSTAT5 response in the whole sample as a function of proleukin dose and a total of nine core markers, seven fluorescent markers and two scatter markers. Dimensionality reduction methods can provide a two-dimensional representation of a higher dimensional data set from a distance matrix. These methods are particularly suited for datasets with less data points but more dimensions than in flow cytometry, as generated by mass cytometry technologies such as CyTOF. In mass cytometry datasets, more emphasis is given on uncovering cell lineages and progressions rather than discrete cell populations which share marker properties. Most of these methods, like multidimensional scaling (MDS), require computation of the complete pairwise distance matrix, but some like Principal Component Analysis (PCA) can use the covariance matrix instead to identify the components which accounts for most of the variation. However, the structure in the data may be poorly represented by the principal components since certain cell populations are unlikely to be linearly separable. Therefore, there is considerable interest in developing methods that capture both the local and global structure of the data, so that points which lie close in higher-dimensional space tend to lie close in two-dimensional space. In flow cytometry, one such method is Spanning-tree

Progression of Density-normalised Events (SPADE) which yields a Minimum Spanning Tree (MST) representation, where each node in the tree represent a multi-dimensional cluster in flow marker space (Qiu et al, 2011). The MST is defined as the shortest path that connects all points in a network. The computation of the MST requires the distance of every point to every other point to be known, hence the complete distance matrix must be calculated. However, it is too large to fit in computer memory for most ungated flow cytometry samples which can contain millions of data points. Hence SPADE first needs to reduce the number of data points by making use of downsampling and clustering. In order for all existing regions of the marker space to be equally represented in the reduced dataset, the density is normalised across the sample.

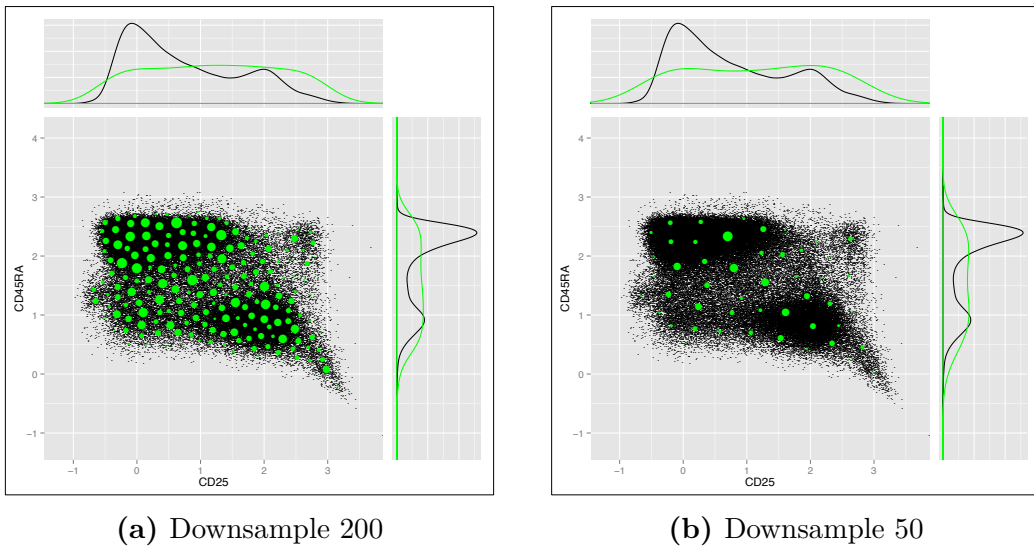


Figure 3.17. Example of density-dependent downsampling on bivariate 50,000 point dataset on CD45RA and CD25. Effect of density-dependent downsampling from 50,000 to 200 datapoints (a), and density-dependent downsampling to 50 datapoints (b). The size of the green points represent the density. The small top-right cloud of points is preserved after density dependent down-sampling.

At each data point, the multivariate density is estimated, then the number of points is reduced by preferentially removing points with high local density while preserving

lower density ones (Figure 3.17). Once the number of points has been reduced to some target number or by some factor, in each individual sample, the samples are pooled and agglomerative clustering is applied. The distance matrix is then calculated on the clusters and they are joined as nodes by the Minimum Spanning Tree (MST) algorithm for the purpose of visualisation. The points from each sample which were discarded in the density normalisation step, are then added back and assigned to their closest node in the tree. Hence the structure of the tree is the same across all samples but the size of the tree nodes is dependent on the number of data points assigned to each node per sample. The tree nodes can then be coloured according to the intensity of a functional marker, for example here pSTAT5, which was not used in its construction. Two steps of the algorithm require user specified parameters, the parameter that defines the downsampling, which can either be a target number of data points or a factor, and parameter that defines the number of desired clusters in the agglomerative clustering step.

Lymphocytes I first ran SPADE on the manually gated lymphocyte subset (excluding doublets), in the resting and stimulated samples from an individual. The algorithm was run on the core surface markers, CD25, CD3, CD4, CD45RA, CD56, CD8 and FOXP3, which are expected to be stable across within-batch stimulation doses. The number of events in each sample was reduced by a factor of 90 percent. The desired number of cluster in the agglomerative step was set to 1000. The layout of the resulting MST was determined by the R function `SPADE.layout.arch` which aims to orientate the longest branch of an MST along an arch with shorter offshoot branches hanging below. The nodes in the tree were then coloured according to the fold increase in median pSTAT5 compared to the same node in the resting sample (Figure 3.18). The initial pSTAT5 response to the lowest 0.1 units dose proleukin, clusters in two regions of the tree, as seen in Figure 3.18b. As the stimulation dose is increased to 10 units, the level of the response

increases in these two regions, and there are signs of response in further adjacent nodes of the tree (Figure 3.18c). Finally at the highest dose of 1000 units, the majority of the nodes show some level of response (Figure 3.18d).

In order to discover where the responsive cells lie on the tree in relation to the cells identified using manual gates, I mapped the cells labelled by manual gating as memory and naive, both Teffs and Tregs, cells onto their assigned tree nodes (Figure 3.19a). I found that the manually identified cell types tend to appear in neighbouring tree nodes with a few in other locations of the tree. Also, memory Teffs and Tregs lie closer to each other than naive Teffs and Tregs (Figure 3.19a). From visual inspection, the pattern of pSTAT5 response in the MST corresponds to the locations of the cell types with the memory and naive Tregs showing the first signs of response at 0.1 units, memory Teffs starting to show activation at 10 units, followed by naive Teffs at 1000 units.

In Figure 3.19b, a number of dose-responsive tree nodes which lie far on the main branch from the other studied subsets, were selected and the cells they contain were projected back to marker space. Thus, I could visualise where these cells lay in relation to the known subsets (Figure 3.20). These cells constitute approximately one percent of the cells in the lymphocyte subset. As depicted in Figure 3.20, some properties of these cells distinguishes them from naive and memory subsets. They are CD56^{hi}, CD3⁻, CD4⁻, CD8⁺ and express low levels of CD25. Since those cells are CD8⁺ CD56⁺ they are probably Natural Killer (NK) like cells, and may have cytotoxic properties. These cells constitute 1.14 percent of all lymphocytes. However they are only stimulated somewhere between 10 and 1000 units of proleukin so may not be influential at the low doses used in DILT1D.

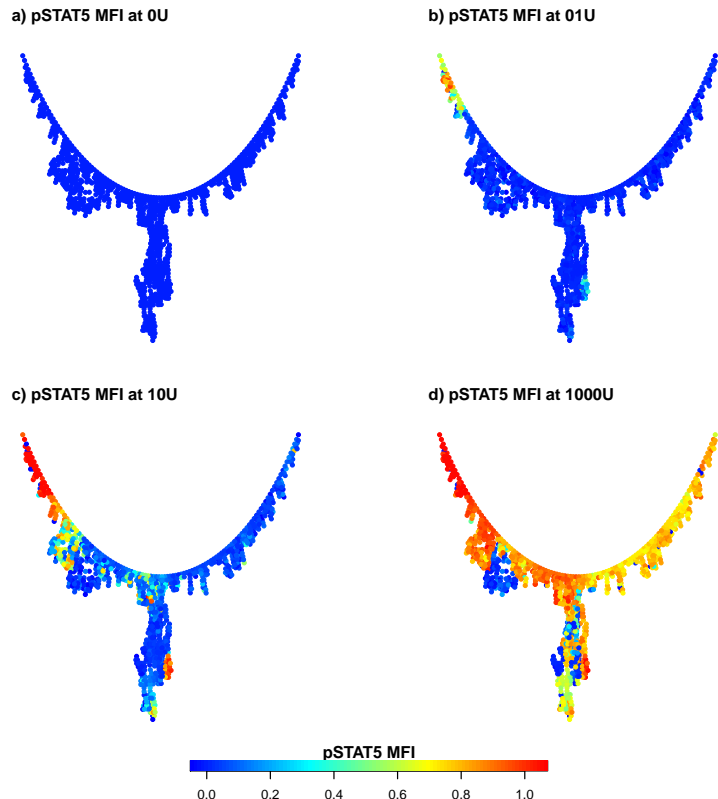


Figure 3.18. Lymphocytes: MST generated by applying SPADE. MST nodes are coloured by pSTAT5 MFI. The MST was constructed from running SPADE on the core surface markers, CD25, CD3, CD4, CD45RA, CD56, CD8 and FOXP3, in the manually gated lymphocyte subset (after double exclusion), pooled across the four stimulation doses in a sample from one individual. The required number of clusters in the agglomerative clustering step was set to $k=1000$. The colouring of the nodes from dark blue to bright red follows the pSTAT5 MFI fold increase. In samples where the proleukin dose is increased, more nodes in the tree are illuminated since the pSTAT5 MFI increases in various cell subsets. The size of the tree nodes are proportional to the number of cells in the data file which are assigned to that node.

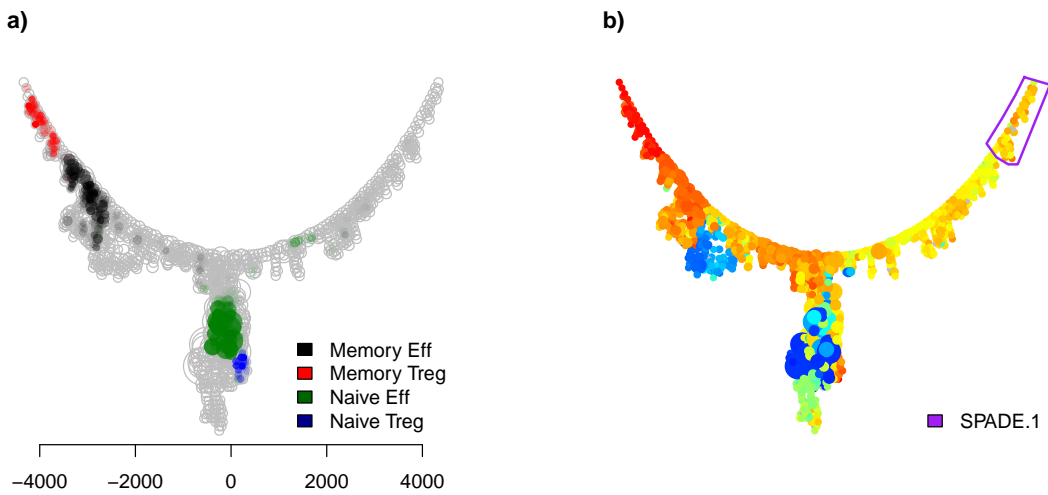


Figure 3.19. Lymphocytes: (a) Mapping of cell subsets defined by manual gates onto the MST obtained in Figure 3.18. (b) A manually identified subset of cells, SPADE.1 (purple). (a) The different manually gated cell types do not always segregate to different branches but can be spread across the tree. For example, naive Teffs appear in different regions of the tree. Furthermore, certain nodes of the tree can contain a mixture of cell types which complicates the interpretation. In order to guard against this, the number of clusters in the agglomerative clustering needs to be set to a high number. (b) Manually identified subset of cells, SPADE.1 (purple), which respond to 1000 units but lie far from the other manually gated cell subsets. The MST was generated on the lymphocytes stimulated at 1000 units and coloured by the pSTAT5 MFI fold increase.

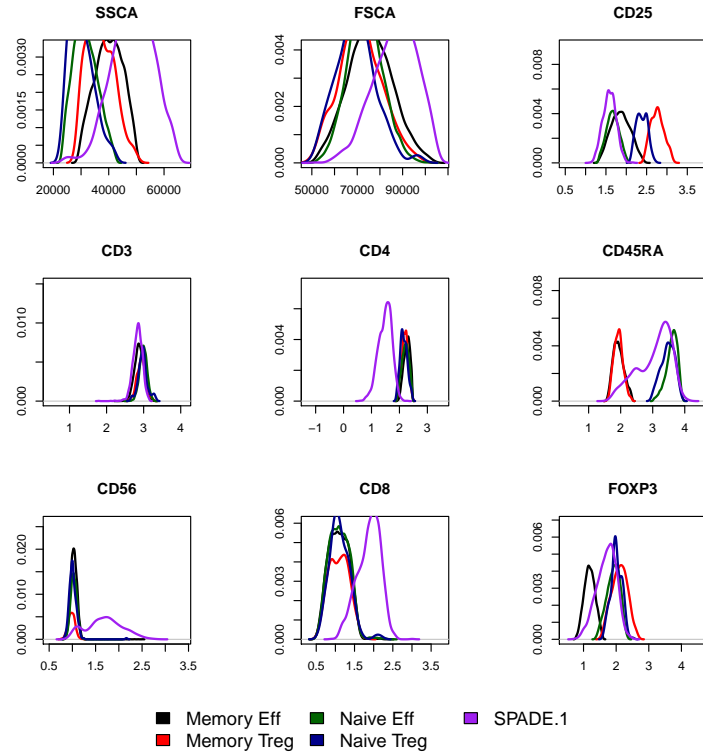


Figure 3.20. Lymphocytes core markers: SPADE.1. The subset of cells, SPADE.1 (purple), manually identified in Figure 3.19, is distinct from the manually gated cell subsets memory Teffs, memory Tregs, naive Teffs and naive Tregs. Its discriminating features are that it is CD4⁻, high for CD8 and CD56, while expressing low levels of CD25.

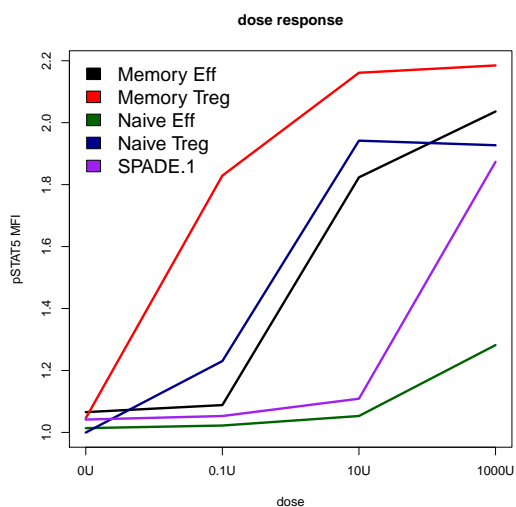


Figure 3.21. Lymphocytes pSTAT5 MFI dose-response: SPADE.1 In purple, the newly identified cell subset SPADE.1 in Figure 3.19 only shows response at 1000 units of proleukin.

Non-lymphocytes In order to see whether I could detect other cell subsets besides lymphocytes, which respond to proleukin, I reran SPADE on the same dataset, this time excluding cells lying within the lymphocyte scatter gate, but including forward and side scatter as markers in the clustering. While at 0.1 units little response was seen (Figure 3.22b), two small clusters showed response at 10 units, SPADE.1b (purple) and SPADE.3b (blue), and at 1000 units, a much larger cluster highlighted in SPADE.2b (pink) (Figure 3.22c and d).

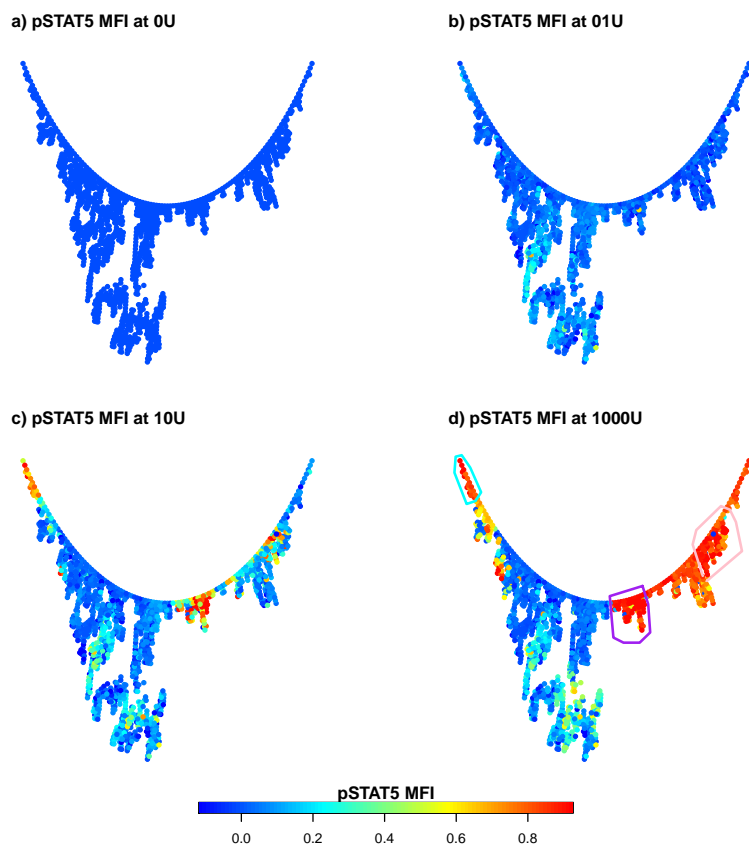


Figure 3.22. Non-lymphocytes: pSTAT5 MFI coloured MST generated by applying SPADE on cells which fall outside of the lymphocyte gate.
 Three subsets of cells are manually identified which show response to proleukin at 10 units, SPADE.1b and SPADE.3b (highlighted in purple and blue on d), and 1000 units, SPADE.2b (pink).

I manually selected these groups of nodes and projected them back to forward and

side scatter space to see where they lay in relation to the lymphocyte cluster (Figure 3.23). I found that these three groups (purple, pink and blue) cluster around the lymphocyte scatter gate which suggested that there are no detectable clusters of cells which fall within the other major scatter clusters which constitute physically larger and more granular cells such as monocytes or granulocytes (Figure 3.23). The cells responsive to the lower 10 unit dose of proleukin, SPADE.1b and SPADE.3b, cluster closer to the lymphocyte scatter (Figure 3.23a) than the large 1000 unit responsive subset of cells (in pink) (Figure 3.23b), suggesting that the former are more likely to be lymphocytes which were not included in the manual gate. While the larger population, SPADE.2b (pink), also tends to aggregate around the lymphocyte scatter, it further appears to aggregate in another potential, less well defined, scatter cluster, SPADE.1, delineated by the purple polygon in Figure 3.23b.

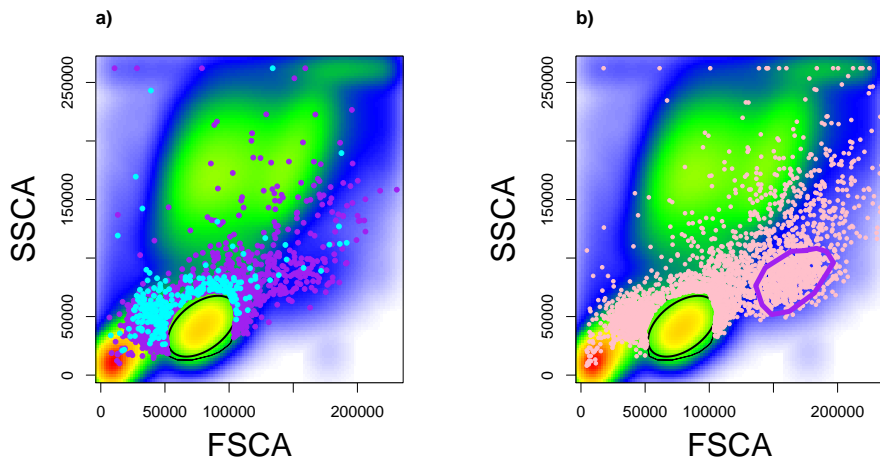


Figure 3.23. Non-lymphocytes: SPADE.1b (purple), SPADE.2b (pink) and SPADE.3b (blue) mapped back to forward and side scatter coordinates.

The three cell subsets, manually identified in the MST of Figure 3.22 are mapped back to scatter coordinates. The 10 unit responsive groups, blue and purple points in (a), and the 1000 units responsive group, pink points in (b), lie close to the lymphocyte cluster (black ellipse), but a potential secondary scatter cluster of 1000 unit responsive cells, delineated by the purple polygon in (b), are worthy of further investigation. This cell subset will be defined as SPADE.1.

Following further investigation of this subset of cells on other core markers in Figure 3.24, and after filtering of doublets on side scatter width and height, while they appeared mostly CD3⁺, CD4⁺ and CD56⁻ therefore likely to be T cells, they also contained a small fraction of CD3⁻ cells, hence likely to be a heterogeneous subset that may contain some monocytes or B cells.

As they are bigger on forward and side scatter than lymphocytes, they could be bigger T cell blasts, and as they are mostly CD45RA⁺, possibly activated T cells. However, they may well result from a technical artefact of the fixation protocol. Further markers, possibly B cell markers such as CD19, are needed to better define this cell type and ascertain its clinical relevance.

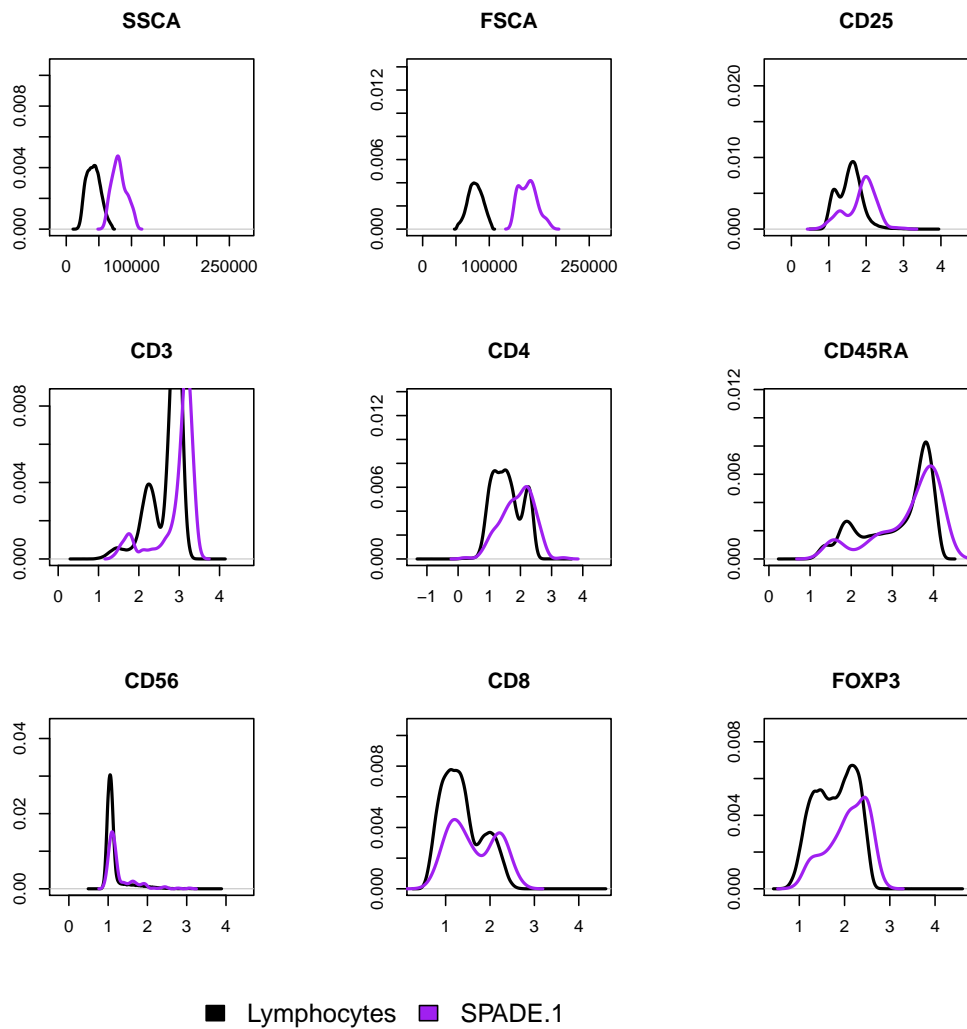


Figure 3.24. Non-lymphocytes core markers: SPADE.1. After filtering of doublets on the side scatter height, the SPADE.1 cluster defined on side and forward scatter in Figure 3.23 is displayed on the other core markers. The cluster appears to be quite heterogeneous is predominantly CD3⁺, CD4⁺ and high for CD25.

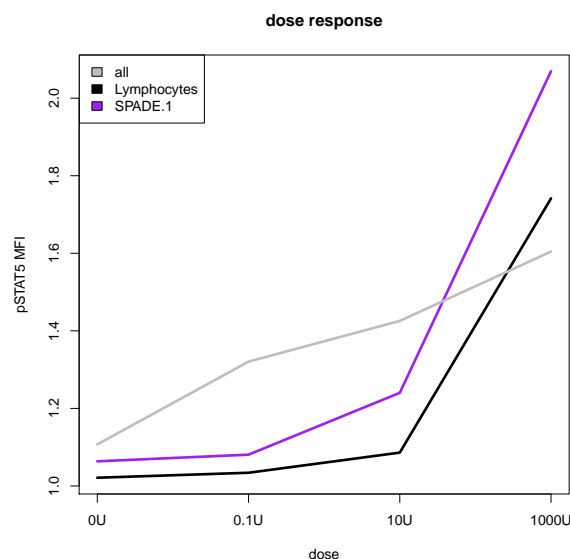


Figure 3.25. Non-lymphocytes pSTAT5 MFI dose-response: SPADE.1. The gray line represents the whole sample. The black line is the lymphocyte population and the purple line is the SPADE.1 subset identified in Figure 3.23.

3.4.2 RPART: recursive partitioning on core markers

The SPADE approach first clustered on the core markers across batches, then built the MST from these, allowing for visual identification of clusters with a high pSTAT5 response. The clustering was preceded by a downsampling step which aimed to make the density more uniform across the sample so that all points had an equal probability of being represented as part of a distinct cluster. An alternative to clustering across samples, is to use recursive partitioning instead to split the core marker space into bins containing roughly the same number of events across samples within the same batch. This can be achieved by recursively splitting on the median of each marker, so that at each split, half of the dataset is assigned to each of the two branches. The process is applied recursively to each bin until a minimum bin size or maximum number of recursive steps is reached. Typically, the order in which the markers are selected is guided by picking the marker with the largest variance or range at each split. Since each bin contains approximately the same proportion of events, this implies that the binning is finer in regions of high density and coarser in regions of low density. Provided that the number of bins is sufficiently large, this is conceptually another approach of reducing the number of events while preserving lower density regions, similar to the method of density-dependent downsampling. Recursive partitioning was first introduced to flow cytometry by Roederer et al (2001), under the name of “probability binning”, as a means of translating a multivariate distribution into a univariate one, in order to test statistical significant differences in event counts between individual bins or whole samples. The algorithm was later implemented in the R BioConductor package `flowFP` (Holyst and Rogers, 2009) as “flow cytometric fingerprinting” and has been applied to discriminate bins which differ significantly in proportion between healthy controls and Acute Myeloid Leukemia (AML) patients (Rogers et al, 2008; Rogers and Holyst, 2009).

For the purpose of visualisation, I first illustrate the recursive partitioning algorithm

on side and forward scatter using 128 bins (Figure 3.26). The binning was defined by pooling all four samples on side and forward scatter. Since each bin should contain approximately $\frac{1}{128^{th}}$ of the events, finer binning is applied to higher density regions and coarser binning to sparser regions.

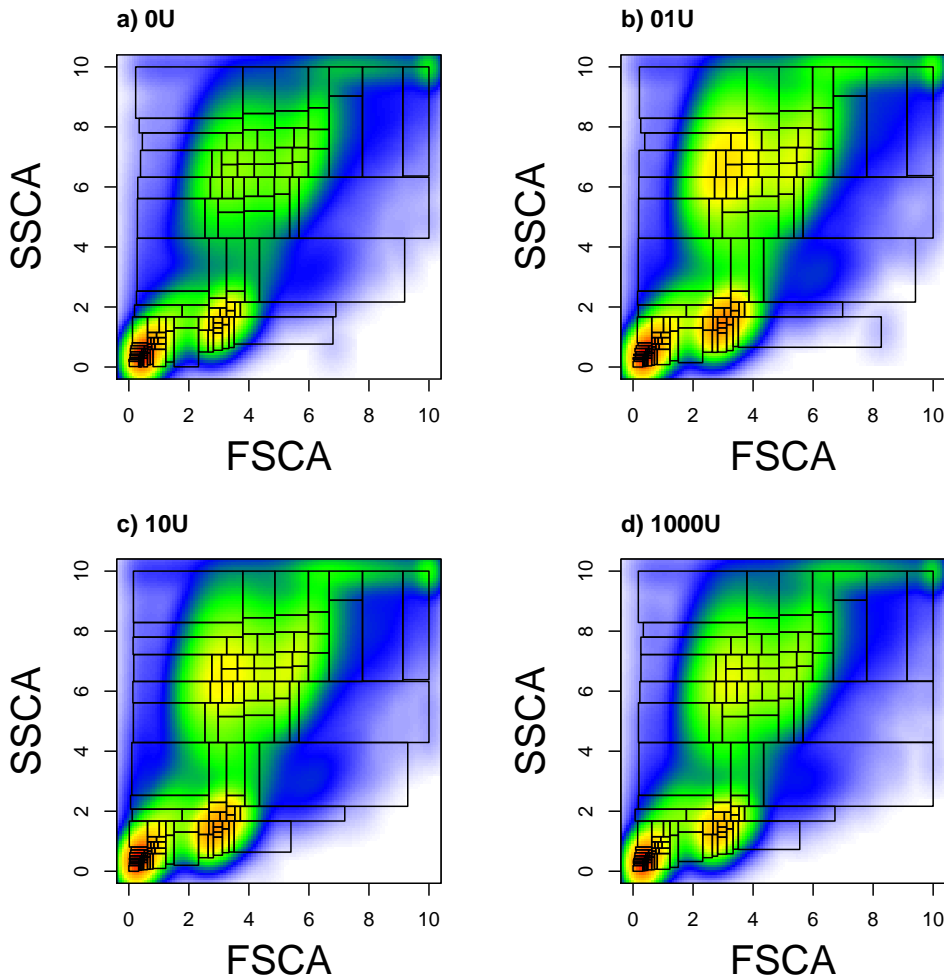


Figure 3.26. Sample recursively partitioned into 128 bins on side and forward scatter. The binning is determined in the resting sample (a) and then the same binning is applied across all samples (b, c and d). While each each bin contains the same number of events in the resting sample (a), this does not necessarily hold in the other samples (b, c and d).

Applying the same binning across the four samples, the relative proportion of events assigned to each bin varies between samples (Figure 3.27). If the number of bins is

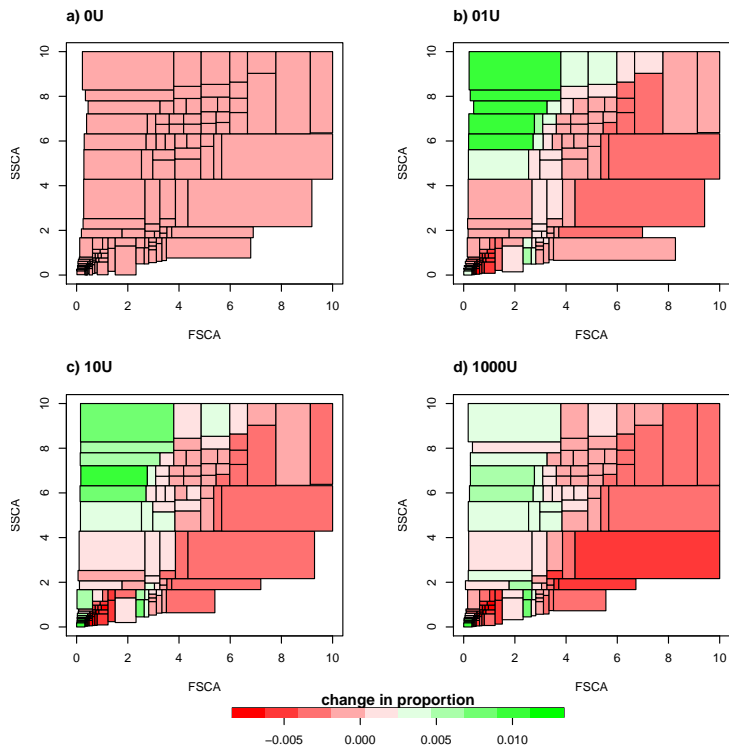


Figure 3.27. Each sample is recursively partitioned using 128 bins. The colour indicates whether the proportion of events increases (green) or decreases (red) relative to the mean in each bin across all samples.

increased each bin represents a smaller proportion of the sample so consequently the variations between samples should also become smaller.

The pSTAT5 response on side and forward scatter is visualised in Figure 3.28 by colouring each bin by its median pSTAT5 response. No pSTAT5 is visible in any of the 128 bins at 0.1 or 10 units (Figure 3.28b and c) which suggest that the proportion of 0.1 unit and 10 unit responsive cells is too small within each bin to influence the pSTAT5 median. However at 1000 units, bins which overlap with the lymphocyte cluster show clear response as well as the bin which overlaps with the uncharacterised cells, SPADE.2b delineated in pink in Figure 3.23b.

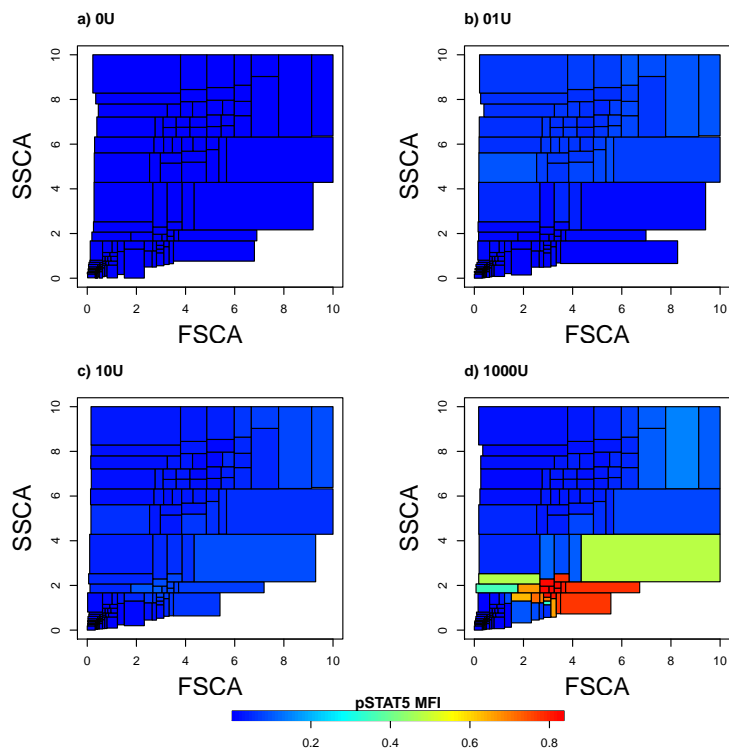


Figure 3.28. pSTAT5 response in sample recursively partitioned into 128 bins on side and forward scatter. No pSTAT5 response is visible in any of the bins at 0.1 (b) or 10 (c) units. However at 1000 units (d), the bins which overlap with the location of the lymphocytes on side and foward scatter show strong response. Also the bin which coincides with the location of the cluster in Figure 3.23 shows some moderate response confirming that there is likely to be some responsive cells lying within that cluster.

Lymphocytes Extending recursive partitioning to all core markers, I aimed to identify dose-responsive cells not assigned to any manual gate within the lymphocyte subset. The number of bins was increased to 1024 and the recursive partitioning was run on the core markers CD25, CD3, CD4, CD45RA, CD56, CD8 and FOXP3, on the lymphocyte subset, after excluding doublets. I also excluded cells which were assigned to the manually gated subsets, both memory and naive, Teffs and Tregs, in order to focus on potentially unidentified cell subsets. Since for any two dimensional projection of the data, many bins overlap, I used the same MST visualisation as described in the previous section, where each node this time represents the core marker median of one of the 1024 bins (Figure 3.29). Using the MST visualisation, I was able to identify a cluster of cells which responded to 1000 units. From the MST, I visually identified two responsive cell subsets, a 1000 unit responsive one, RPART.1 (purple), and a 10 unit responsive cluster, RPART.2 (pink). Selecting the tree nodes manually and projecting the corresponding bins back to marker space, I plotted these two cell subsets in relation to the manually gated subsets, memory Teffs (black), memory Tregs (red), naive Teffs (green) and naive Tregs (blue) (Figure 3.30). The cell subset RPART.2 (pink) constitutes around 4 percent of the lymphocytes. This cell subset contains moderate levels of CD25 similar to a memory Teffs and is CD3⁺, CD4⁺, CD8⁻, CD45RA⁻ and FOXP3⁻. It is likely to represent the transitional cell population between memory Teffs and Tregs which was not included in the manual gating. On the other hand, the cell subset RPART.1 (purple) appeared to be CD3⁻, CD4⁻, CD8⁻ and high for CD56. These cells were also low in CD25, with the same level of expression as naive Teffs, which explains their limited response at lower doses. They constitute around 1.66 percent of the total lymphocyte population within this sample. These CD56 bright cells include CD3⁻ cells so could belong to a cell subset currently under investigation by Charlie Bell in our lab using RNAseq, which are known to express high levels of CD122, the beta chain of the IL-2 receptor.

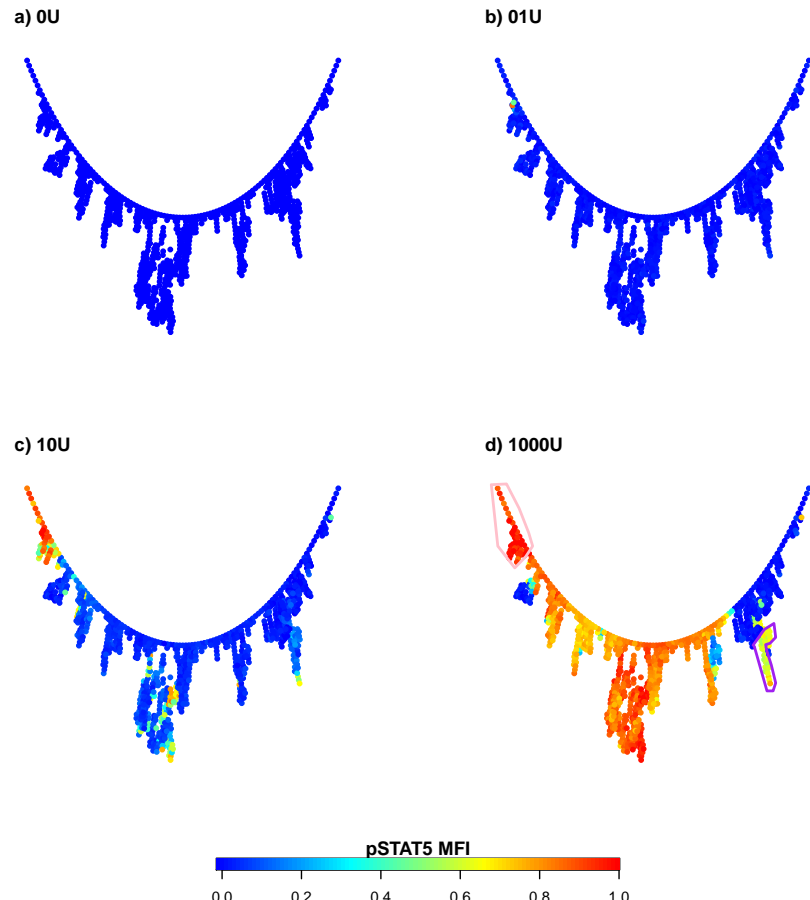


Figure 3.29. Lymphocytes: MST built using the 1024 bins obtained from recursive partitioning on the lymphocytes core markers. A subset of cells delineated in purple, RPART.1, shows pSTAT5 response at 1000 units, and a subset of cells delineated in pink, RPART.2, shows pSTAT5 response at 10 units. RPART.1 lies in a different part of the MST from the remainder of the dose-responsive cells.

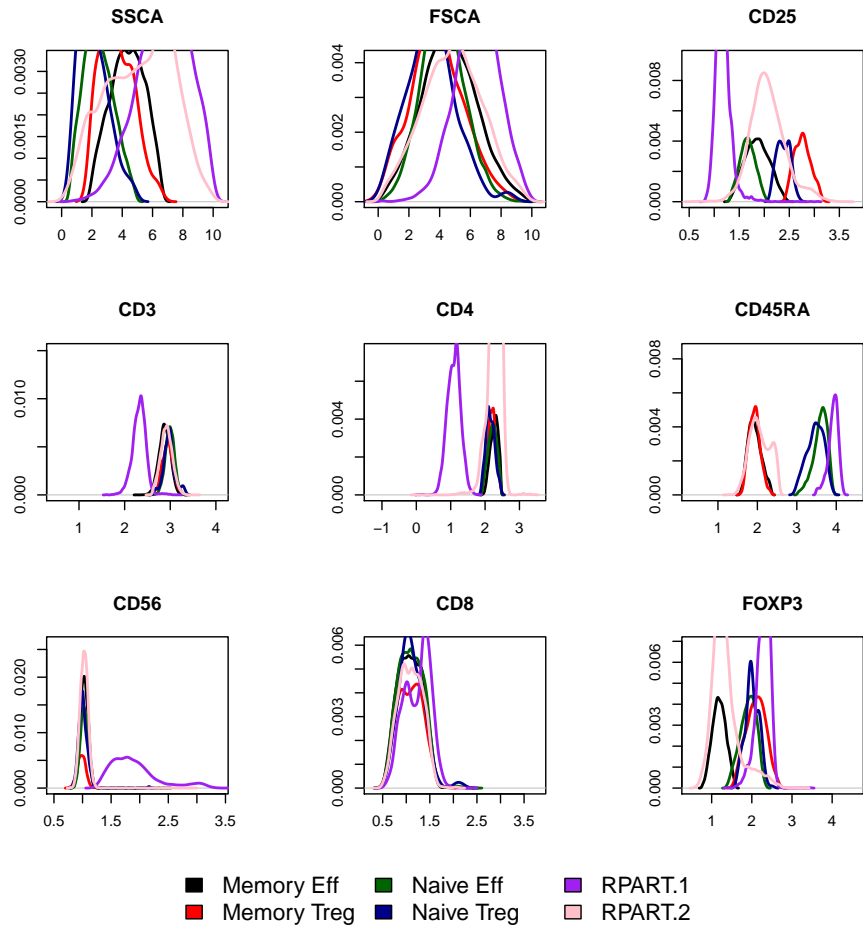


Figure 3.30. Lymphocytes core markers: RPART.1 and RPART.2. Two subset of cells, a 10 unit responsive subset, RPART.2, and a 1000 unit responsive subset, RPART.1, manually identified in the MST of Figure 3.29, which are distinct from the manually gated cell subsets memory Teffs (black), memory Tregs (red), naive Teffs (green) and naive Tregs (dark blue), are projected back to core marker space. RPART.2 overlaps with the manually identified cell subsets. The discriminating features of RPART.1 are that it is CD3⁻, CD4⁻ and high in CD56, while expressing low levels of CD25.

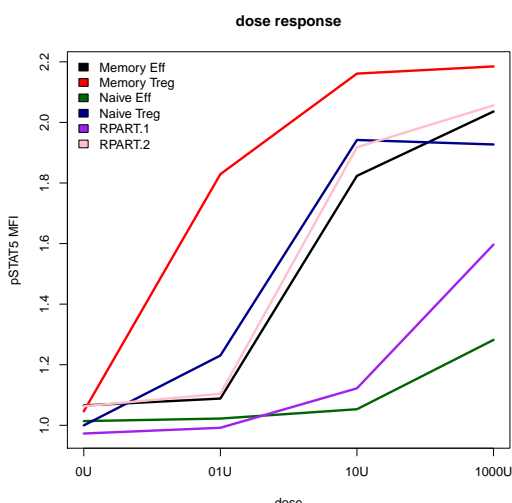


Figure 3.31.
Lymphocytes pSTAT5
MFI dose-response:
RPART.1 and RPART.2.

Non-lymphocytes Recursive partitioning was next applied to non-lymphocytes, in order to detect potentially new responsive subsets. As side and forward scatter need to be included in the recursive partitioning of non-lymphocytes, I scaled the scatter so as to have a similar range to the fluorescent markers. I again used 1024 bins although this number could have been increased because we are dealing with larger number of cell. The recursive partitioning was run on the same markers but this time also included the side and forward scatter. Once more, the MST was used to visualise the response across the whole sample (Figure 3.32). At 0.1 units, no clear response is visible (Figure 3.32b) but at 10 units (Figure 3.32c) certain nodes show moderate response within a branch of the MST which later become part of cluster (delineated in purple) which shows strong response at 1000 units (Figure 3.32d). Projecting the cells contained within this cluster back to marker space (Figure 3.33), they seem to lie close to the lymphocyte cluster (black) on side and forward scatter and also appear to contain both CD4⁻ and CD4⁺ cells. They also overlap on side and forward scatter with the cluster identified in Figure 3.23.

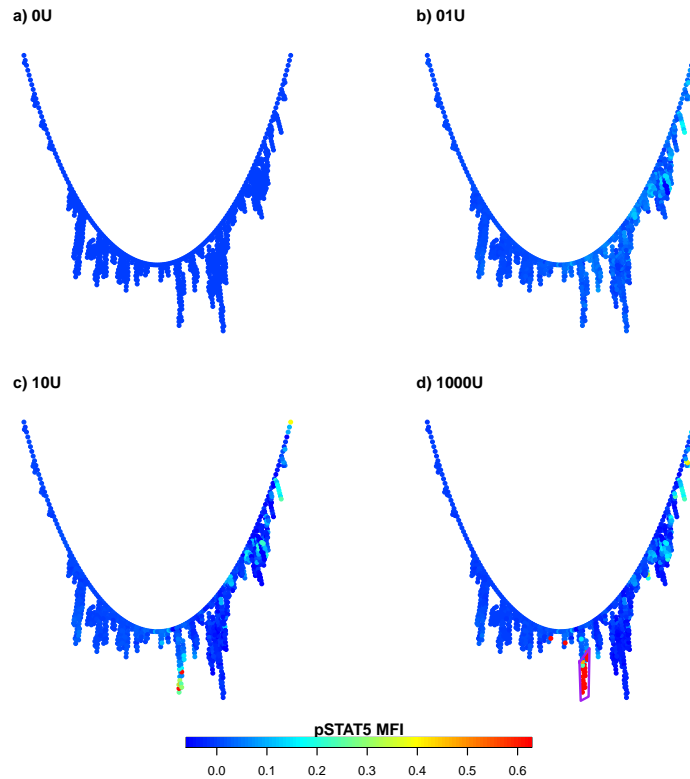


Figure 3.32. Non-lymphocytes: MST built on the 1024 bins obtained from RPART on non-lymphocytes. A cluster of cells, RPART.1 (purple), stands out that shows pSTAT5 response at 1000 units.

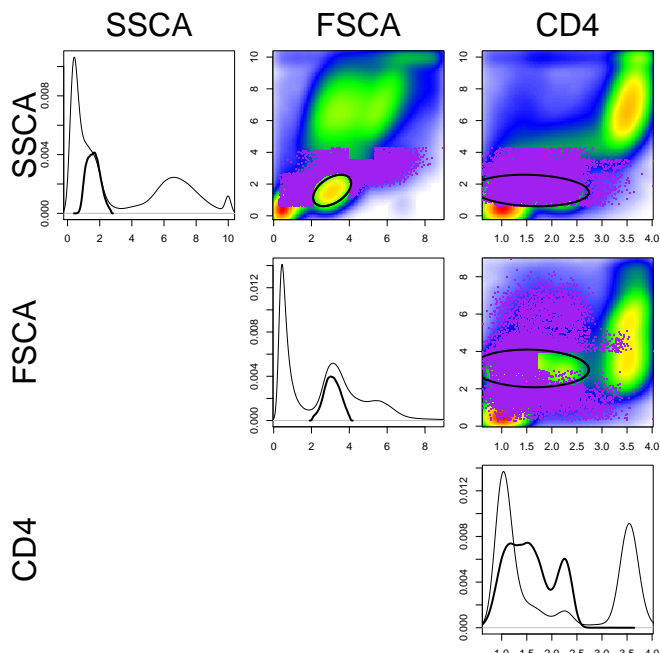


Figure 3.33.
Non-lymphocytes:
RPART.1 (purple) does
not belong to the
lymphocytes
population (black).
In order to visualise
where the subset
RPART.1, manually
identified in Figure 3.32,
lies in relation to the rest
of the sample it is
overlaid on top of the
whole sample (including
lymphocytes).

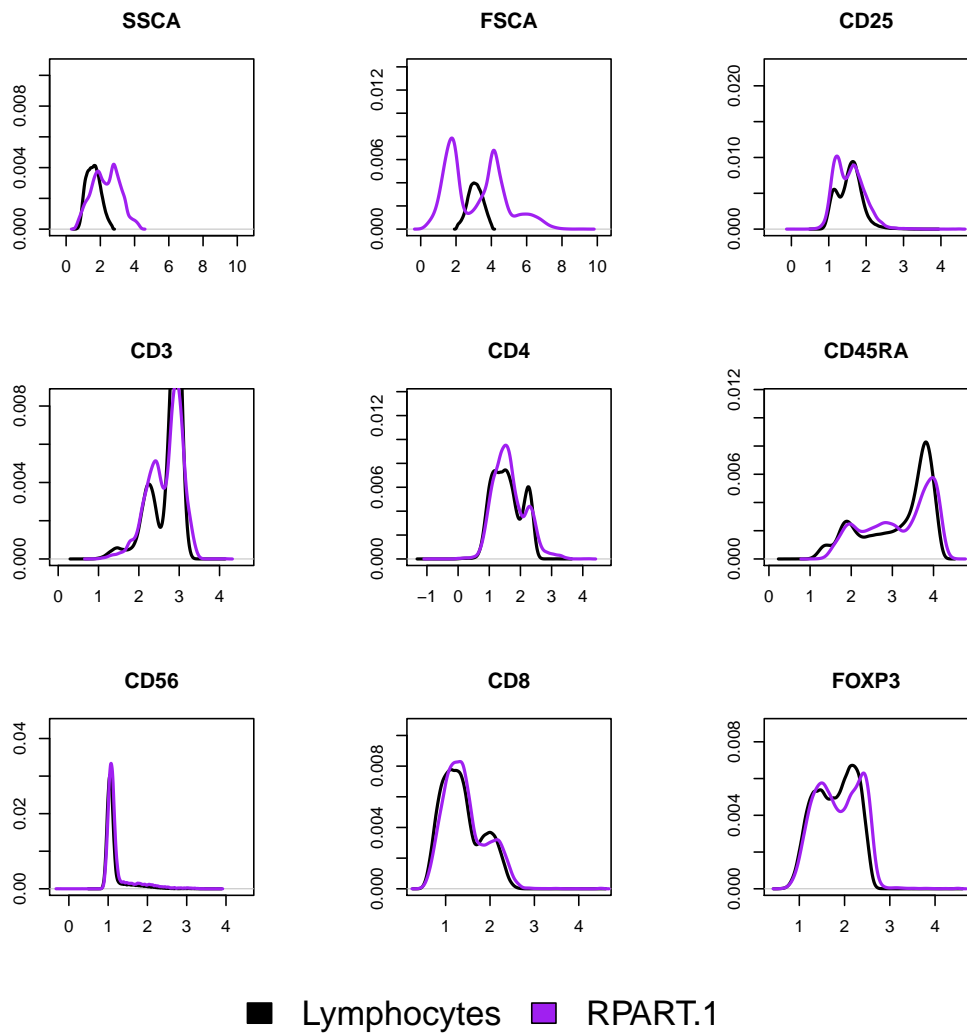


Figure 3.34. Non-lymphocytes core markers: RPART.1. A 1000 unit responsive cell subset, RPART.1, in purple, is identified which does not belong to the manually defined lymphocyte population, in black.

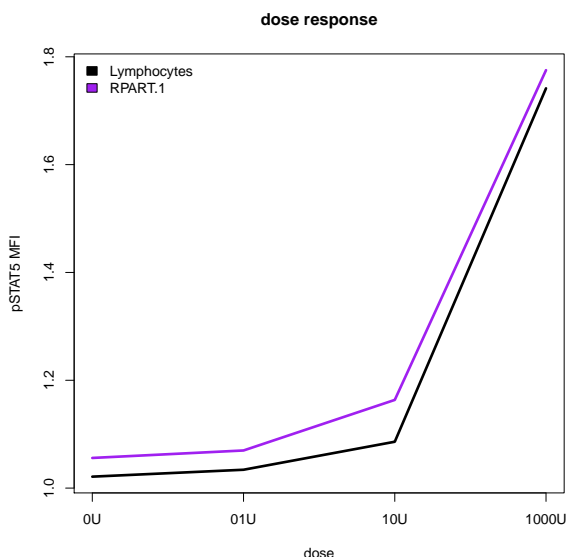


Figure 3.35. Non-lymphocytes dose-response: RPART.1. A 1000 unit responsive cell subset, RPART.1 (purple), is identified which does not belong to the manually defined lymphocytes population (black).

3.4.3 PLSR: partial least squares regression

So far, the only visualisation I have explored is the MST, a non-linear projection of a multivariate dataset. However, no information about the pSTAT5 response is captured in the layout of the tree, instead, I used colour to visually identify clusters with increased pSTAT5 MFI response. An alternative may be to include the pSTAT5 in the linear projection using a technique known as Partial Least Squares (PLS). PLS is based on the well established PCA method which decomposes the covariance matrix into orthogonal linear combinations of the variables, known as principal components, where each principal component successively captures most of the residual variation in the sample. However while in PCA all variables are treated the same, in PLS, variables can be specified as response variable \mathbf{Y} or predictors \mathbf{X} . The general underlying model of the multivariate PLS is then:

$$\mathbf{X} = \mathbf{T}\mathbf{P}^\top + \mathbf{E}$$

$$\mathbf{Y} = \mathbf{U}\mathbf{Q}^\top + \mathbf{F}$$

where \mathbf{X} is an $n \times m$ matrix of predictors and \mathbf{Y} is an $n \times p$ matrix of responses. \mathbf{T} and \mathbf{U} are $n \times l$ orthogonal matrices that are, respectively, projections of \mathbf{X} and projections of \mathbf{Y} . The matrices \mathbf{P} and \mathbf{Q} are, respectively, $m \times l$ and $p \times l$ orthogonal loading matrices. The matrices \mathbf{E} and \mathbf{F} are the error terms, assumed to be independent and identically distributed random normal variables. The decompositions of \mathbf{X} and \mathbf{Y} are made so as to maximise the covariance between \mathbf{T} and \mathbf{U} .

I applied partial least squares regression, using the R function `plsr` implementation in the R package `pls` (Mevik et al, 2013), to both the lymphocytes and non-lymphocytes.

Lymphocytes I ran the PLS regression of the pSTAT5 response at each dose, within the manually gated lymphocyte subset (Figure 3.36). I found that manually gated subsets generally project to distinct clusters. However the naive Teffs and naive Tregs

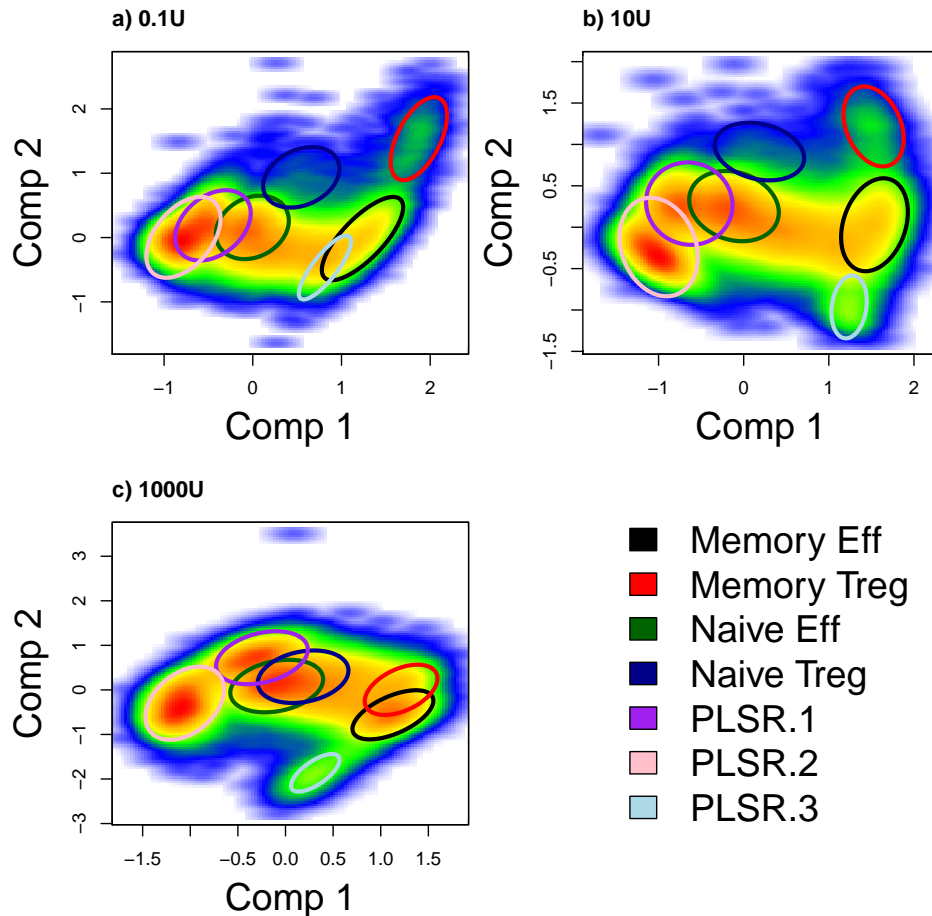


Figure 3.36. Lymphocytes: First two components of PLS projection using pSTAT5 as response. Three new clusters, PLSR.1, PLSR.2 and PLSR.3, newly identified using PLS, in relation to known manually gated subsets within lymphocytes. The known manually gated cell populations are naive Teffs (dark green), naive Tregs (dark blue), memory Teffs (black) and memory Tregs (red). Three other clusters have been identified manually in light blue, pink and purple.

greatly overlap and that may be due to spurious correlation created by spillover between CD45RA and FOXP3, which makes the naive Teffs look abnormally high in FOXP3, as is apparent in the FOXP3 channel in Figure 3.37. Based on the PLS projections at 1000 units, three additional clusters, delineated in purple, pink and light-blue, were manually identified (Figure 3.37). These clusters were then plotted across all doses (Figure 3.38). As can be appreciated in Figure 3.36, the known cell populations are better distinguishable at 0.1 units and 10 units, while the three new clusters are better

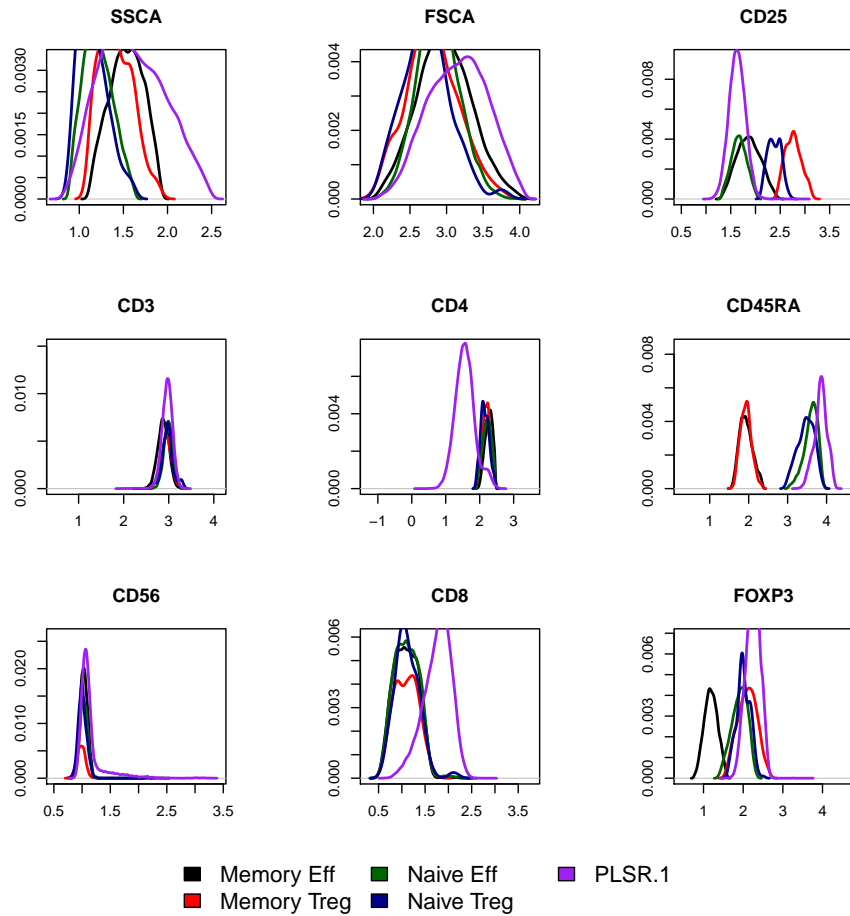


Figure 3.37. Lymphocytes core markers: PLSR.1. The density of the PLSR.1 cluster (purple), identified using PLS projection in Figure 3.36, plotted on all core markers, in relation to known manually gated ones within the lymphocytes. I only included the PLSR.1 cluster since PLSR.2 and PLSR.3 do not show response to proleukin, as per Figure 3.38. A distinctive property of PLSR.1 is that it is high for CD8 and low for CD4. It constitutes approximately 16 percent of the lymphocyte cells in this sample.

separated at 1000 units. This is likely the consequence of the pSTAT5 response reaching saturation at 1000 units. Plotting the dose response in Figure 3.38 shows that of the three new subsets, only PLSR.1 (purple) is responsive at 1000 units while PLSR.2 (pink) and PLSR.3 (light-blue) conserve baseline pSTAT5 even at the highest dose. PLSR.2 and PLSR.3 are therefore not of interest here and so only PLSR.1 is considered for further study. In Figure 3.37, PLSR.1 is plotted in relation to the known subset on all core

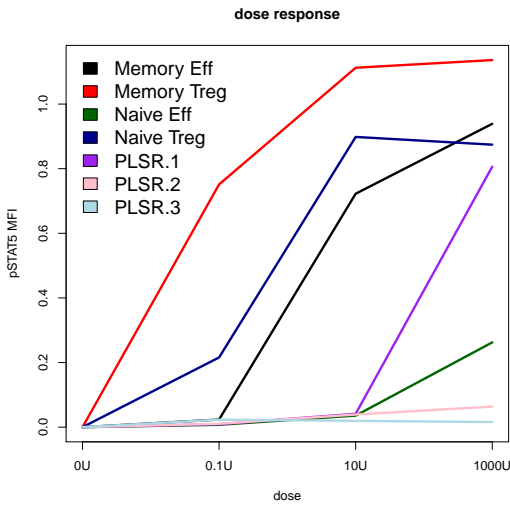


Figure 3.38. Lymphocytes pSTAT5 MFI dose response: PLSR.1, PLSR.2 and PLSR.3. The MFI of the pSTAT5 at each dose is shown, in the known cell subsets, memory Teffs, memory Tregs, naive Teffs and naive Tregs, as well as the three newly identified cell subsets in (Figure 3.36). Of the newly identified cells subsets, only PLSR.1 shows signs of response. PLSR.2 and PLSR.3 do not respond even at the highest dose of 1000 units.

markers. Its main distinguishing features are that it is CD8⁺ and CD4⁻. It is also CD45RA⁺ indicating that it could include naive CD8 T cells. It constitutes a total of 16 percent of the lymphocytes in this sample.

Non-lymphocytes I repeated the same analysis on the non-lymphocytes, this time including side and forward scatter as predictors in PLS. From the first two components of the PLS projections, I visually identified three distinct subsets, PLSR.1, PLSR.2 and PLSR.3, in addition to the known lymphocyte cluster (black), which were discernible in at least one of the three different stimulation doses. I further identified two less discernible cell populations, a subset of the lymphocytes, PLSR.4 (orange), and a low-density cluster most visible at 10 units, PLSR.5 (yellow). As can be seen in Figure 3.41, of the newly identified cell subsets, only PLSR.4 and PLSR.5 show response from 10 units.

While this is to be expected of PLSR.4 as it constitutes a subset of the lymphocytes,

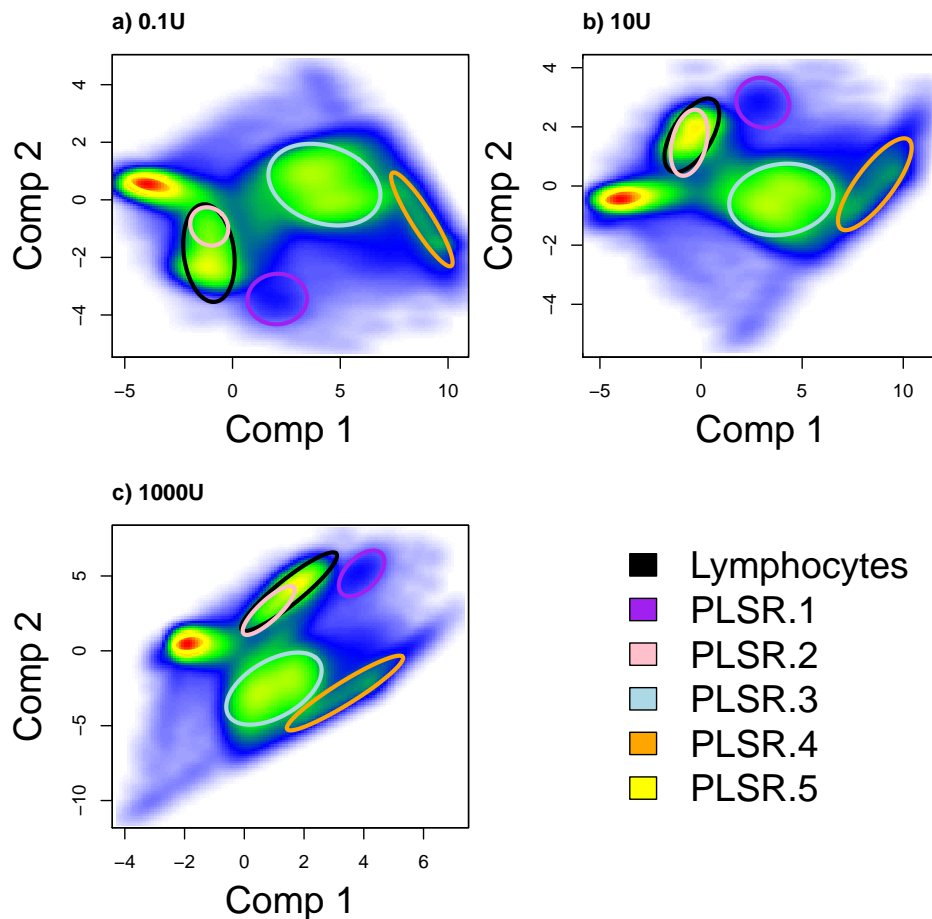


Figure 3.39. Non-lymphocytes: First two components of PLS projection using pSTAT5 as response. Clusters newly identified using PLS in relation to lymphocytes.

PLSR.5 when plotted along with the lymphocytes in Figure 3.40, has higher side and forward scatter which suggests it constitutes an artefact or possibly another type of dose-responsive T cell, since it is CD3⁺. The PLSR.5 cell subset however makes up a very small proportion of the whole sample at less than 1 percent, compared to the lymphocytes at 16 percent.

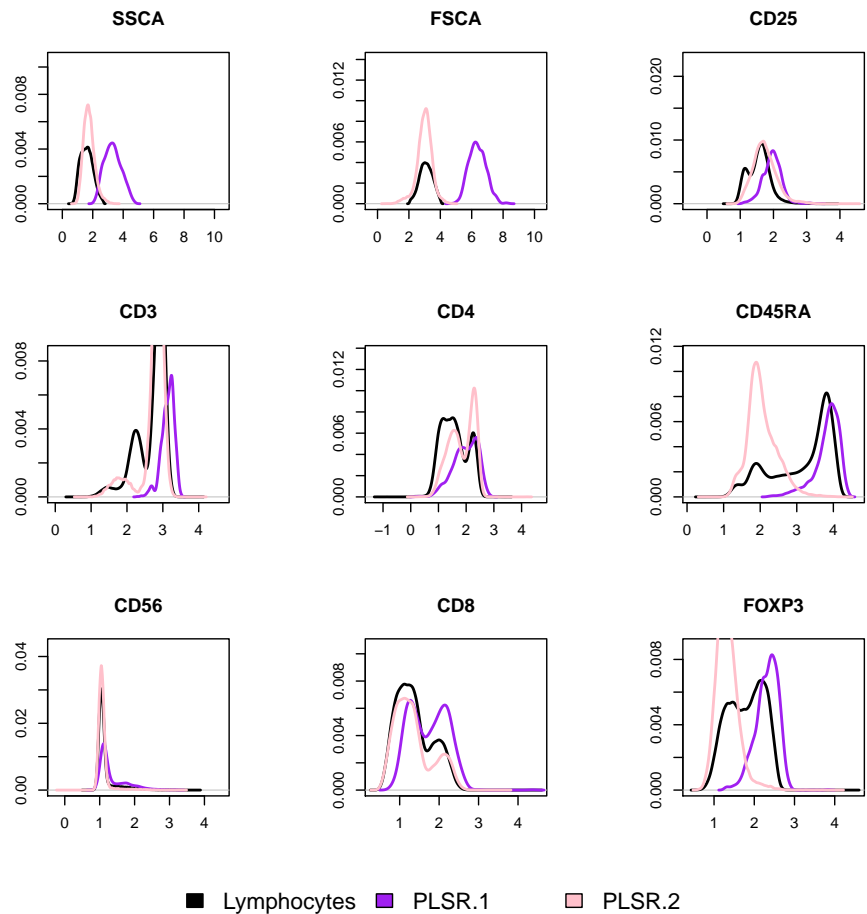


Figure 3.40. Non-lymphocytes core markers: PLSR.1 and PLSR.2. Clusters newly identified using PLS within non-lymphocytes, PLSR.1 and PLSR.2, in relation to lymphocytes.

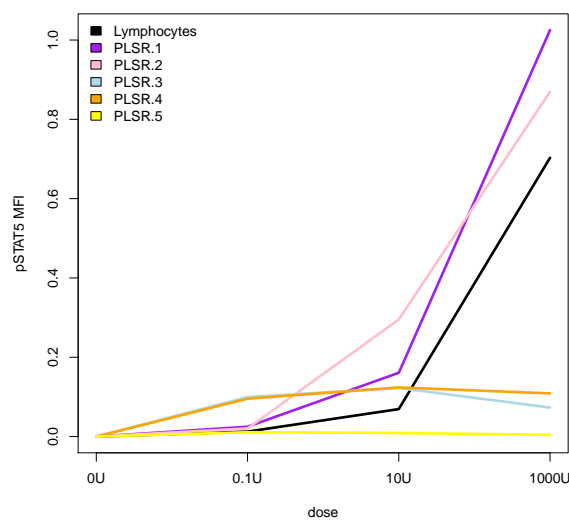


Figure 3.41. Non-lymphocytes dose-response: PLSR.1, PLSR.2, PLSR.3, PLSR.4, PLSR.4 and PLSR.5. Subsets identified with PLS in relation to lymphocytes. Of the five newly identified cells and lymphocytes (black), only the lymphocytes, PLSR.1 and PLSR.2 show response at 10 units.

3.4.4 CART: binary recursive partitioning using regression tree on pSTAT5

The SPADE and recursive partitioning methods described in the previous sections have proceeded by first reducing the number of events through clustering or binning on the core markers across stimulation doses, then visually identifying clusters or bins which show pSTAT5 response using a two-dimensional MST projection of the reduced dataset. The clusters or bins are then projected back to core marker space to examine their MFI and relative size.

However since the objective is to identify dose responsive cell subsets, a logical extension to the methods described previously would be to include the pSTAT5 response in the clustering of these datasets. One way this can be achieved is to build on the recursive partitioning approach from the previous section, by applying the Classification And Regression Tree (CART) method to the pSTAT5 response. Instead of using the variance of the core markers, the Classification And Regression Tree (CART) uses the variance of the pSTAT5 response to guide the recursive partitioning. This approach however requires the pSTAT5 response to be known at each point in the dataset. Such a dataset can be constructed by using the ANN algorithm to join samples from the same batch on their core markers as was explained in Section 3.3.1. In fact, the ANN algorithm uses the recursive partitioning technique covered in the previous section, on the core markers to build a K dimensional tree (KD-tree) data structure. A KD-tree serves as an indexing data structure, allowing faster retrieval of data points based on their coordinates by refining the search to the bin within which the point is likely to lie. This indexing is exploited to efficiently find the approximate nearest neighbour between datasets.

The CART, as implemented in the R package `tree` (Ripley, 2014), proceeds by considering each core marker coordinate as a potential splitting point. The splitting point

which minimises the sum of the within branch variance of the response variable, is selected and the data is split between the left and the right branch. Note that contrary to the recursive partitioning scheme defined in the previous section, since the split point does not usually correspond with the median, the tree is not balanced. This splitting is applied recursively until some minimum leaf node size is reached or the reduction in variance from splitting reaches some threshold (the default is 0.01 of the total variance). A leaf node represents a partition obtained by applying the cuts defined along the branch. In order to reduce the number of partitions, the tree can be pruned to minimise the cost-complexity for a desired number of leaf nodes. On the same ungated sample as was used in the previous section, partitioning only on side and forward scatter using pSTAT5 response at 1000 units and pruning the tree to the best three subsets, I obtained the clustering in Figure 3.42. This confirms that based on forward and side scatter alone, the lymphocyte cluster is the most responsive cluster to proleukin. However, if the pSTAT5 of the sample stimulated at 0.1 or even 10 units is used as the response, then the CART algorithm does not consistently partition the data, since few cells within the lymphocytes respond at these doses of proleukin and so the reduction in the total variance is not sufficient to justify a split.

Lymphocytes I first ran CART on lymphocytes, excluding all manually gated CD4⁺ cells, in order to see if any dose-responsive non-manually gated cell subsets were identified. The CART was run without pruning on the ANN joined dataset using the pSTAT5 response at each of the stimulation doses. In Figure 3.43 are the trees obtained from 0.1 (a), 10 (b) and 1000 units (c).

At 0.1 units, only two subsets can be distinguished based on CD25. At 10 units, four clusters are distinguishable based on CD45RA, CD56, CD25 and CD4. However, at 1000 units, only three subsets are discernible. This may be because there is more homogeneity in the response as an important proportion of the lymphocyte subset will have reached

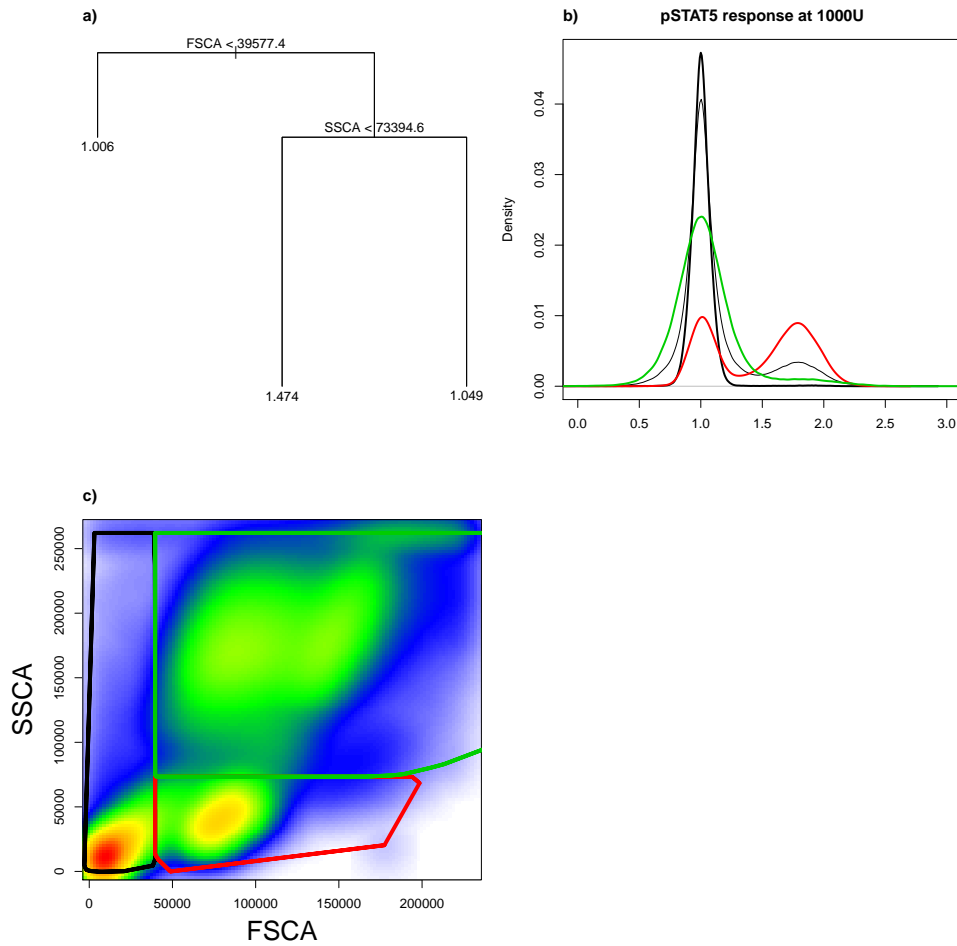


Figure 3.42. CART of 1000 unit response against side and forward scatter identifies three subsets. The CART obtained from recursive partitioning of side (SSCA) and forward (FSCA) scatter against the pSTAT5 response at 1000 units, after pruning on the best three subsets (a). The values at the terminal nodes are the expected pSTAT5 response within each subset. According to this regression tree, most of the pSTAT5 response comes from the lymphocyte cluster (red) whereas the black and green clusters are less responsive (b).

saturation at that dose. Furthermore CD25 does not feature in the regression tree, which may be because once the response is saturated, CD25 adds little predictive value. Since these regression trees include only a few of the available markers, their utility is rather limited in identifying cell subsets. Nonetheless, some information can be extracted. For example, the inclusion of the CD56 marker at 10 and 1000 units suggests that it becomes a relevant predictor of the pSTAT5 response. In particular at 10 units, where

the CD45RA⁻ CD25⁺ subset shows the strongest response, the CD45RA⁺ CD56^{hi} subset shows the second strongest response. At 1000 units, the highest response is in the CD3⁺ subset, but the CD3⁻ CD56⁺ subset is the second highest. This points to the same CD3⁻ CD56⁺ subset that was identified from the MST in Figure 3.30 at 1000 units of stimulation.

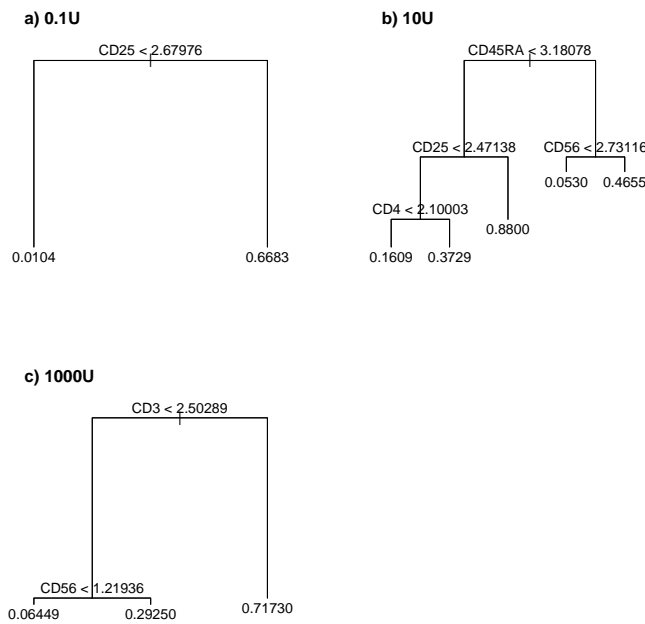


Figure 3.43.
Lymphocytes: Recursive partitioning tree obtained for the pSTAT5 at 0.1 units (a), 10 units (b) and 1000 units (c) in the lymphocytes which do not belong to any manually identified cell subset.
Each non-leaf node of the tree represents a split point where the dataset is partitioned along the left or the right branch according to the inequality. The numbers at the bottom of each leaf represent the mean pSTAT5 response within that partition of the data. The markers which are selected as split points differ depending on the doses. The height of each branch is proportional to the reduction in variance which results from that split.

Non-lymphocytes Next, I repeated the analysis, including side and forward scatter, on non-lymphocytes (Figure 3.44). Side and forward scatter were scaled so as to have a comparable variance to the other parameters. At 1000 units, the strongest response comes from the subset with low side scatter, high CD25 and high CD3. This subset

includes lymphocytes and the cells identified in Figure 3.33. Since the cells are high in CD3, they are also likely to include T cells which would overlap with the pink and purple cell subsets defined in Figure 3.22.

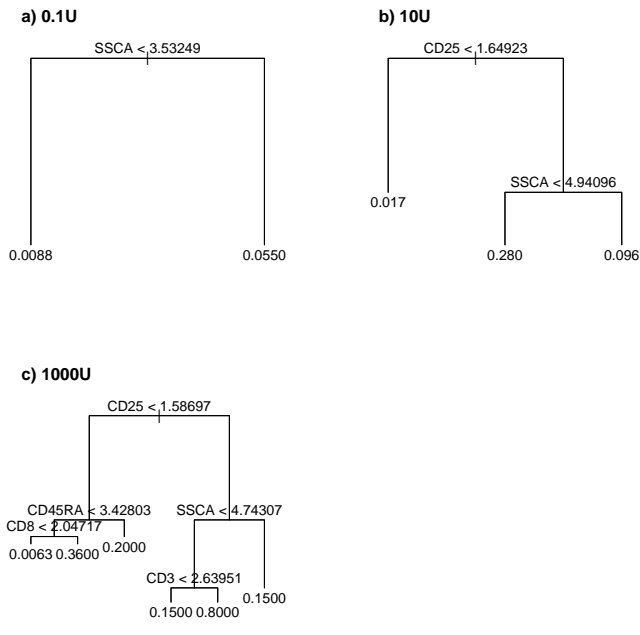


Figure 3.44.
Non-lymphocytes:
Recursive partitioning
tree obtained for the
pSTAT5 at 0.1 units (a),
10 units (b) and 1000
units (c) in the
non-lymphocyte cells.

The numbers at the bottom of the tree represent the mean pSTAT5 response within that partition of the data. The height of each branch is proportional to the reduction in variance which results from that split.

3.4.5 MMPART: identification of low-dose sensitive cells by recursive application of a two component mixture model on pSTAT5

The CART approach, described previously, seeks the core marker split point which minimises the deviance of the response variable. This approach successfully discriminates, based on side and forward scatter, the lymphocytes as the most responsive cluster when stimulated at the 1000 unit dose of proleukin. Unfortunately, it is not sufficiently sensitive to detect the small proportion of cells which are responsive to lower doses of proleukin.

In order to address this issue, I developed an approach based on the idea that by

recursively splitting cells into pSTAT5 high and pSTAT5 low subsets, at decreasing doses of proleukin, it should be possible to identify cells which respond to the lowest proleukin dose. The algorithm, as illustrated in Figure 3.45, proceeds by first dividing cells as low responders (red) and high responders (green) on pSTAT5 response at 1000 units by fitting a two-component univariate GMM. The responder population (in green) is then further divided into low and high subsets by fitting the GMM on the pSTAT5 response at 10 units. This process is finally repeated in the pSTAT5 response stimulated at the lowest doses of 0.1 units. Cells which consistently appear in the high group are the most sensitive. This hierarchical approach draws some similarity to the recursive partitioning using CART except that the splitting decision depends only on applying a two-component GMM to the pSTAT5 distribution rather than selecting a core marker value on which to do the split. The process is entirely driven by the bimodality of the pSTAT5 distribution at each dose. As subsets are recursively split into low and high at decreasing doses of proleukin, the objective is to identify cells responsive to the lowest dose of proleukin.

Lymphocytes I applied this algorithm within the lymphocyte subset, keeping the manually gated cell subsets so as to improve the two-component GMM fit and only removed them at the end once the new subsets, **MMPART.1**, **MMPART.2** and **MMPART.3**, were identified (Figure 3.45). These three new subsets constituted respectively, 0.21, 2.26 and 0.96 percent of the total cells in the sample. The three subsets have different response profiles with **MMPART.1** responding to 0.1 units of proleukin, **MMPART.2** responding at 10 units and **MMPART.3** responding at 1000 units (Figure 3.47). This difference in response can be partially explained by their ranking of CD25 expression (Figure 3.46). However, the subtle difference in CD25 MFI in the lower intensity subsets, **MMPART.1**, **MMPART.2**, memory Teffs and Tregs, does lead to surprisingly different response profiles (Figure 3.47). The three newly identified cell subsets are not homogeneous for the other core markers

but MMPART.2 and MMPART.3 appear to be enriched for CD4⁻ and CD8⁺ cells. MMPART.2 appears mostly CD45RA⁻ whereas MMPART.3 appears mostly CD45RA⁺.

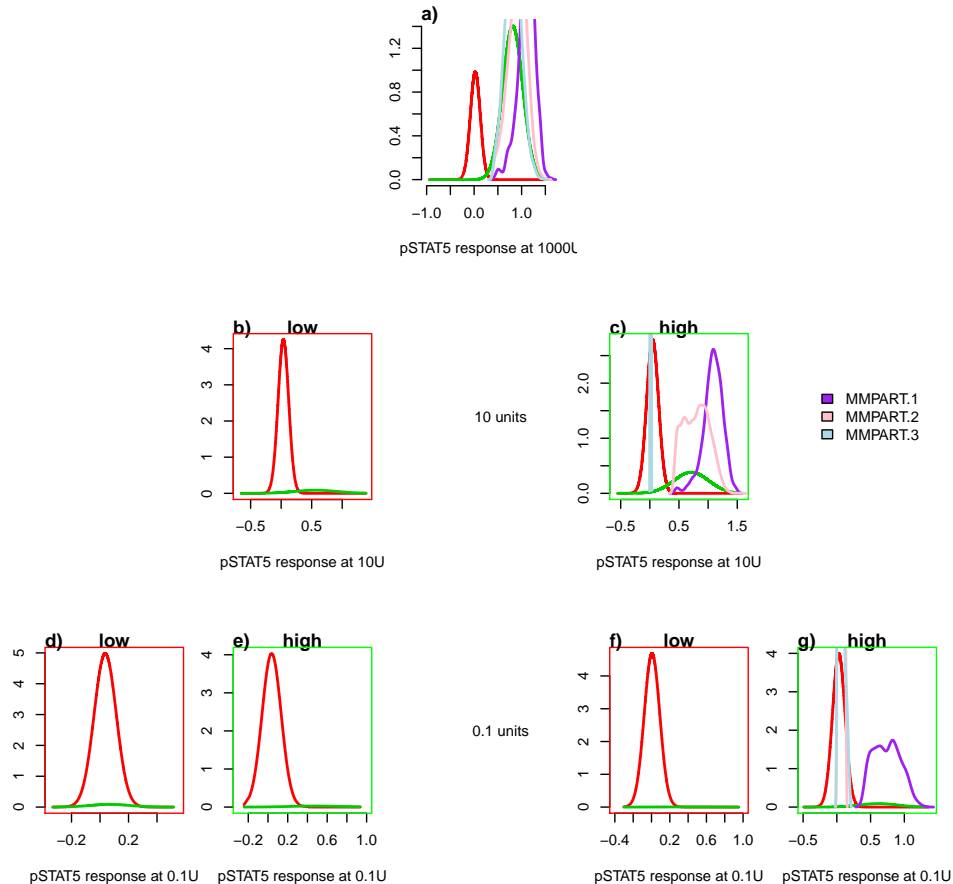


Figure 3.45. Lymphocytes: Recursive partitioning of pSTAT5 response into low (red) and high (green) subsets. In the top plot (a), the 1000 units pSTAT5 distribution is divided into negative (red) and positive (green) subsets by fitting a two-component GMM. The low and high subsets from (a) are then further subdivided in (b) and (c) respectively, by again fitting a two-component GMMs, but this time to the 10 units pSTAT5 distribution. This process is recursively applied to the low and high subsets obtained from (b) and (c) by fitting two-component GMMs to the 0.1 units pSTAT5 distribution, in order to obtain (d) and (e), and (f) and (g). The plots with green borders represent the positive subsets (c, e, and g) whereas the plots with red borders represent the negative subsets (b, d and f). Three subsets are identified, MMPART.1, MMPART.2 and MMPART.3, which respond at 0.1 units (g), 10 units (c) and 1000 units (a) respectively.

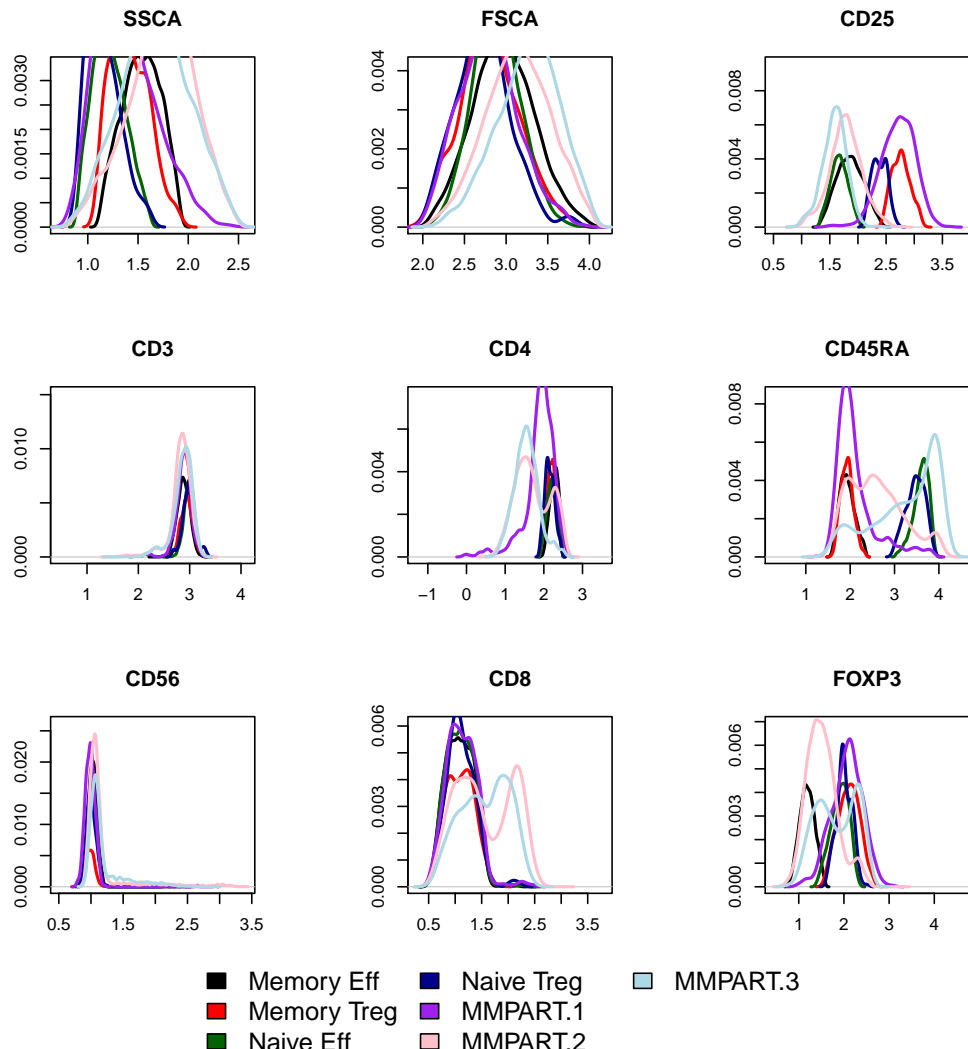


Figure 3.46. Lymphocytes core markers: MMPART.1, MMPART.2 and MMPART.3. MMPART.2 and MMPART.3 are enriched for CD4⁻ CD8⁺ cells.

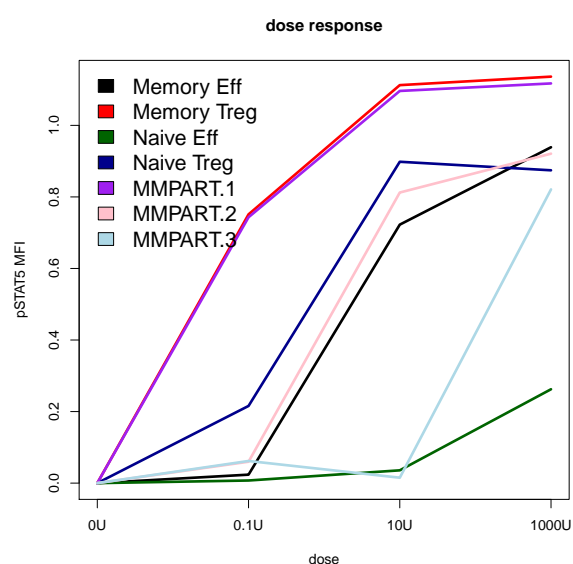


Figure 3.47. Lymphocytes pSTAT5 MFI dose-response: MMPART.1, MMPART.2 and MMPART.3.

Non-lymphocytes I applied the same algorithm to the non-lymphocyte subset (Figure 3.48). Again I left the lymphocytes in until the end to improve the model fit. At the lowest dose certain subsets could not be further subdivided further into two components (d and f).

I identified two subsets of cells **MMPART.1** and **MMPART.2** responsive at 0.1 and 10 units respectfully (Figure 3.48). Looking at the core markers (Figure 3.49), the forward and side scatter of these subsets appears similar to the lymphocyte population. However, **MMPART.1** also contains a subset of cells at the top of the scatter range which are likely to be debris. Both **MMPART.1** and **MMPART.2** appear to be $CD3^+$, thus T cells. They also appear primarily $CD45RA^-$, so naive.

Successive univariate clustering on response is not an obvious approach to multi-variate data analysis but can be useful in identifying potentially interesting cells. One drawback of this approach is that since the scatter and core markers don't influence the gating, some filtering of the reported cells is required to eliminate debris and doublets. This approach also relies on being able to fit a two-component GMM which becomes increasingly difficult as the responsive population becomes smaller and wider spread than the non-responding population.

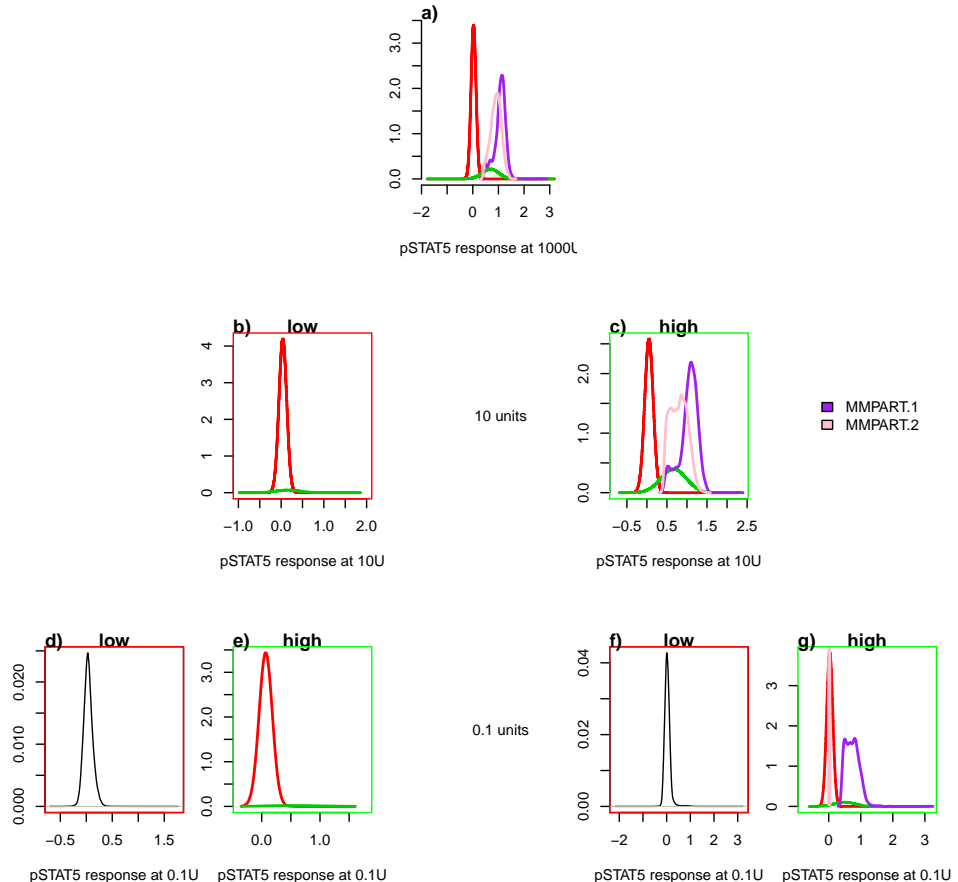


Figure 3.48. Non-lymphocytes: recursive partitioning of pSTAT5 response into low (red) and high (green) subsets. In the top plot (a), the 1000 units pSTAT5 distribution is divided into negative (red) and positive (green) subsets by fitting a two-component GMM. The low and high subsets from (a) are then further subdivided in (b) and (c) respectively, by again fitting a two-component GMMs, but this time to the 10 units pSTAT5 distribution. This process is recursively applied to the low and high subsets obtained from (b) and (c) by fitting two-component GMMs to the 0.1 units pSTAT5 distribution, in order to obtain (d) and (e), and (f) and (g). The plots with green borders represent the positive subsets (c, e, and g) whereas the plots with red borders represent the negative subsets (b, d and f). Two subsets are identified, MMPART.1 and MMPART.2, which respond at 0.1 units (g) and 10 units (c).

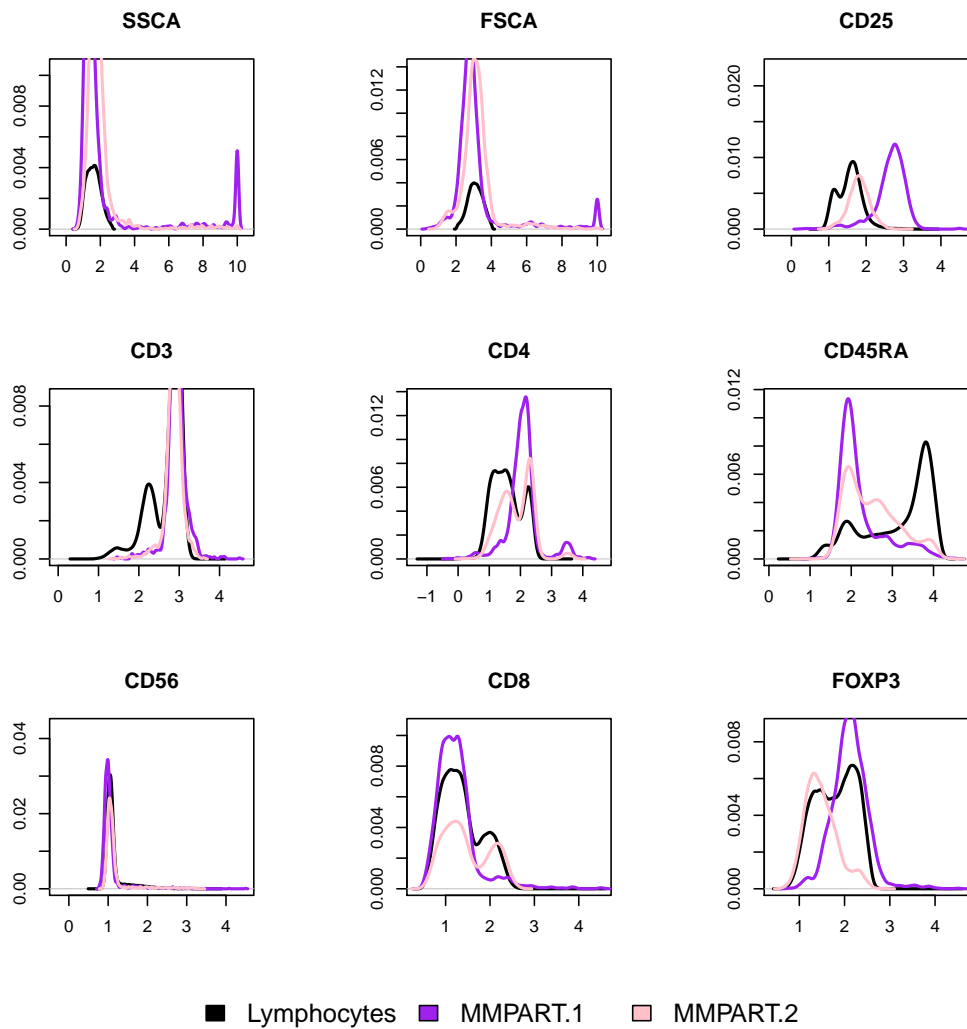


Figure 3.49. Non-lymphocytes core markers: MMPART.1 and MMPART.2. MMPART.1 and MMPART.2 both have similar forward and side scatter profiles to the lymphocytes. However MMPART.1 also includes a peak at the top end of the side and forward scatter which is likely to include debris.

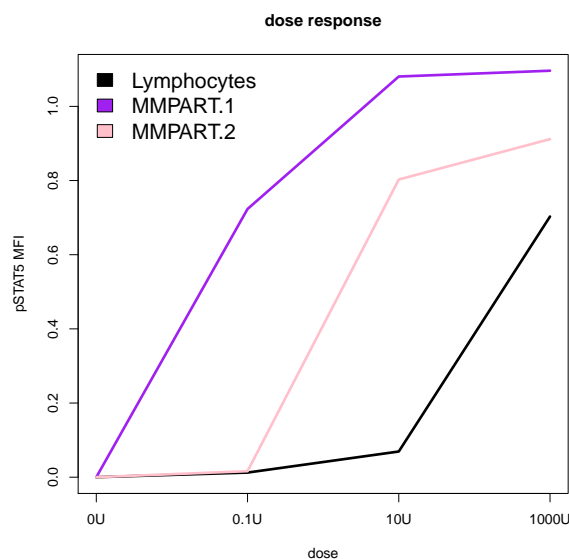


Figure 3.50.
Non-lymphocytes
pSTAT5 MFI
dose-response:
MMPART.1 and
MMPART.2.

3.5 Discussion

3.5.1 Association of pSTAT5 with T1D

Comparison with previous studies The Long et al (2010) study was in a relatively small number of individuals, a total of 66 cases and 125 controls, and the reproducibility of the phenotypes was not assessed. Although Tony Cutler's experiment was on an even smaller number of individuals, the reproducibility was assessed more thoroughly. Both Tony and I found that the response of the fluorescence intensity of pSTAT5 to stimulation was poorly reproducible in the various cell subsets examined. Although I attempted to improve on the reproducibility of the fluorescence intensity by various approaches, I was unable to do so. One reason why I believe the pSTAT5 MFI is not reproducible in memory Teffs cells, is because the pSTAT5 distribution is not unimodal. In naive and memory Treg cells, the pSTAT5 distribution is unimodal but the peak shift on stimulation is not reproducible. Tony Cutler suggests that this is because of technical aspects of performing the proleukin stimulation experiment. Since the proleukin must be stored at a very high concentration to maintain its stability, each experiment requires that the IL-2 stock be extensively diluted on the day of the experiment. Additional variation is caused by the varying efficiency of intracellular staining. Instead of using MFI, this motivated counting the percent of cells whose pSTAT5 fluorescence is greater than the 99th percentile of the pSTAT5 distribution in the unstimulated sample. Since this phenotype was found to be slightly more reproducible, it was used to test the association with T1D in the four cell subsets, memory, naive, Teffs and Tregs.

Another concern we had with the Long et al (2010) study was that the dose was too high for the studied cell subsets. Our doses are 0.1, 10 and 1000 U/ml, whereas theirs was 100 U/ml. We found that pSTAT5 Tregs are maximally stimulated by 10 U/ml and near maximum at 0.1 U/ml, which is in contrast to Long et al (2010) where

maximum stimulation was not achieved at 100 U/ml. One possible explanation is that they used frozen PBMC, while we used fresh blood. Dendrou et al (2009b) showed that frozen samples generally had lower CD25 and this difference may explain the difference in response between the two studies.

Normalisation of pSTAT5 Several normalisation methods were attempted to make the pSTAT5 dose-response phenotype more reproducible:

- bead normalisation
- correcting for baseline MFI
- nearest-neighbour joining

However none were able to substantially improve the repeatability. From my limited success, I can only conclude that the noise in this dataset is substantial and not systematic, which makes normalisation very challenging. Unsurprisingly, given the small dataset and the poor repeatability, no significant association was detectable with dose-response and disease status. Given that this assay was not sufficiently reproducible for across-batch analysis, this brought me instead to focus on within-batch analysis.

3.5.2 Methods for identifying dose-responsive cell populations

In this chapter, I attempted a total of five different methods for identifying dose-responsive cell populations visually or semi-automatically:

- SPADE
- RPART
- CART
- PLSR
- MMPART

The first two methods, density normalisation with SPADE and recursive partitioning with RPART, used only the core markers in order to pool across samples within a batch.

The other two methods, PLSR and CART, included the response variable pSTAT5 alongside with the core markers, and the final method, MMPART, used only information about the response variable.

I have also tried the two main approaches of combining data across samples using either pooling or by joining. Given the large number of events per sample in flow cytometry, the total number of events needs to be reduced for pooling, and I have looked at two ways of achieving this, first with density-dependent downsampling, as done in SPADE, and then with binning using recursive partitioning, as implemented in RPART. Both methods aim to achieve a uniform sampling of the core marker space, the first by thinning the data, the second by dividing the space into regions containing approximately the same number of points, which were then used instead of the data points in the downstream analysis. On the other hand, the joining does not aim to reduce the number of events but instead to normalise the number of events across samples. The joining was implemented using the nearest neighbour approximation in each sample, in order to obtain a sample containing the same number of events as in the base sample.

From the pooled data, I was able to calculate multidimensional scaled representations such as the MST. Colour coding the MST by pSTAT5 response, I then identified new dose-responsive clusters of cells within lymphocytes and non-lymphocyte cell populations, ignored by the manual gating. The value of SPADE here, lies in the downsampling and agglomerative clustering steps which allow for probing of the entire marker space by reducing the number of data points while preserving the structure of the data. Although SPADE suggests the MST as a visualisation tool, it is not necessarily the most useful representation of the data since it can be hard to interpret. The mapping of the manual gates to the MST may not be intuitive, as seen in Figure 3.19, where the manually gated cell types are spread across several branches of the tree and certain nodes contain more than one cell type (Figure 3.19). Hence the MST requires some

manual annotation in order to understand where the different cell types lie. One way of visualising the relationship between the value and location of a node in the tree is to colour the tree according to each marker individually. However this approach is not practical for a large number of markers, nor does it yield an overview of the relationship between the various markers. Instead, a more useful alternative could be to plot the tree node coordinates against the core marker node MFI, as illustrated in Figure 3.51. This approach not only provides some insight into the marker progression, at least along the main branch of the tree where the different cell types lie, but also into the relationship between the markers in the sample. Potentially, this approach could be repeated along each branch in the MST to identify the different types of cells progression in the sample. This would rely on the definition of a root node, an idea which needs to be explored further. Sometimes from the MST it may be difficult to delineate the cluster of cells which are responsive as they do not cluster in distinct sections of the tree.

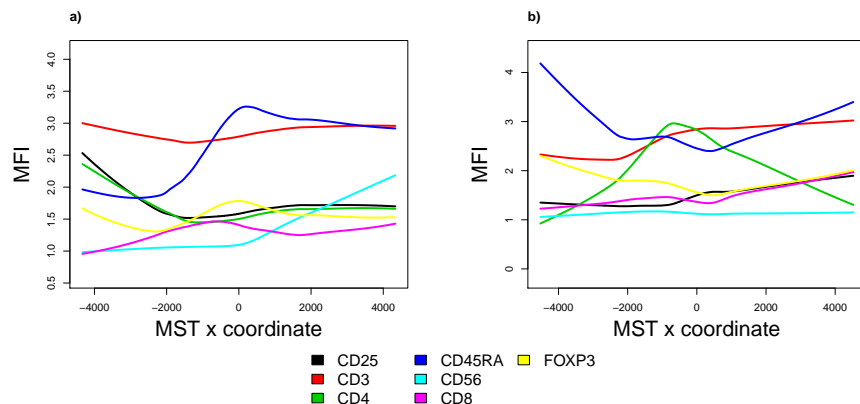


Figure 3.51. The progression of the marker MFI along the horizontal coordinate of the MST nodes in lymphocytes (a) and non-lymphocytes (b). The LOWESS(Cleveland, 1981) progression of the marker MFI along the horizontal coordinate of the MST. For the MST constructed on the lymphocytes (a), the markers which show the clearest progression are markers, CD45RA CD56 which increase from left to right, and markers CD4 and CD25 which decrease. For the MST constructed on the non-lymphocytes (b), the progression of the markers is not monotonic.

In fact, the downsampled data used to create the MST visualisation can been used to represent the data in a number of ways using established for example PLS with pSTAT5 as the response variable, as I have shown earlier, or other MDS style methods which rely on the distance matrix computation.

From the joined data, I have explored methods which use the pSTAT5 response to guide the binary recursive partitioning of the core marker space using CART or the estimation of the principal components using PLS. Applying CART to side and forward scatter, the lymphocyte population was consistently identified as the most responsive cell population in all samples stimulated at 1000 units. However, I found that applying this method on all markers simultaneously across all samples yielded different partitioning schemes per sample. It is a known drawback that recursive partitioning techniques are prone to overfitting and consequently very sensitive to batch effects. As illustrated in Figure 3.52, when the same algorithm is applied to the lymphocyte subset in another sample, the returned partitioning is very different.

Another issue with the regression tree approach is that it doesn't exploit the bimodality of the pSTAT5 distribution at higher doses of proleukin. This motivated the next approach, **MMPART**, which aimed to identify highly sensitive dose-responsive cells by using the bimodality of the pSTAT5 response rather than the variance for the partitioning. By recursively splitting the bimodal pSTAT5 distribution in a sample at decreasing doses of proleukin, my hope was to isolate the subset of cells which respond to the lowest dose of proleukin. The subset of cells which was identified using this method, overlapped with the lymphocyte gate based on side and forward scatter. However, as expected, these cells constituted quite a heterogeneous cell population, since core markers are not included in the splitting decisions. Ideally, some further clustering would be required on this subset, but in practice, the number of events are too few for this to be feasible.

There are other possible extensions to the regression tree methods covered in the "Elements of Statistical Learning" textbook (Hastie et al, 2009). These extensions allow for a linear combination of more than one marker at each split, or for more than one split at each level. Multivariate Adaptive Regression Splines (MARS) for example uses multiple additive regression splines as a generalisation of stepwise linear regression or a modification of the CART method to improve its performance in the regression setting. MARS foregoes the tree structure and instead of approximating each bin by the pSTAT5 mean, the pSTAT5 function is approximated by a piecewise linear function with knots at core markers points. Unfortunately, I found the existing R package `earth` (Milborrow, 2014) to be too slow to run on my datasets. Another extension is the Patient Rule Induction Method (PRIM) also known as the "bump hunting" algorithm introduced by Friedman and Fisher (1999). PRIM searches for a bounding boxes in the marker space in which the average response is high. Since there is no binary constraint this reduces the number of splits. The main box construction method in PRIM works from the top down, starting with a box containing all the data. The box is compressed along one face by a small amount, and the observations that fall outside the box are filtered out. The face chosen for compression is the one resulting in the largest box mean, after the compression is performed. Then the process is repeated, stopping when the box contains some minimum amount of points. After the top-down sequence is computed, PRIM reverses the process expanding along any edge, if such an expansion increases the box mean. Since the top-down procedure is greedy at each step such an expansion is often possible. The result of these steps is a sequence of boxes, with a different number of observations per box. An advantage of PRIM over CART is its patience, since CART tends to fragment the data rather quickly, but this comes at the cost of performance and I found the R package `prim` (Duong, 2014) implementation of this method too slow to run on my dataset. Another alternative to regression trees which avoids overfitting is

Random Forests (RF) but requires reduction of the number of splits to be interpretable. Although recursive partitioning schemes are very sensitive to even small changes in the data and suffers from the biases of tree like data structures in which errors propagate because of the dependency of the splits on previous splits, I found them to be a useful non-parametric method of exploring a dataset, in line with the tree like nature of the manual gating approach.

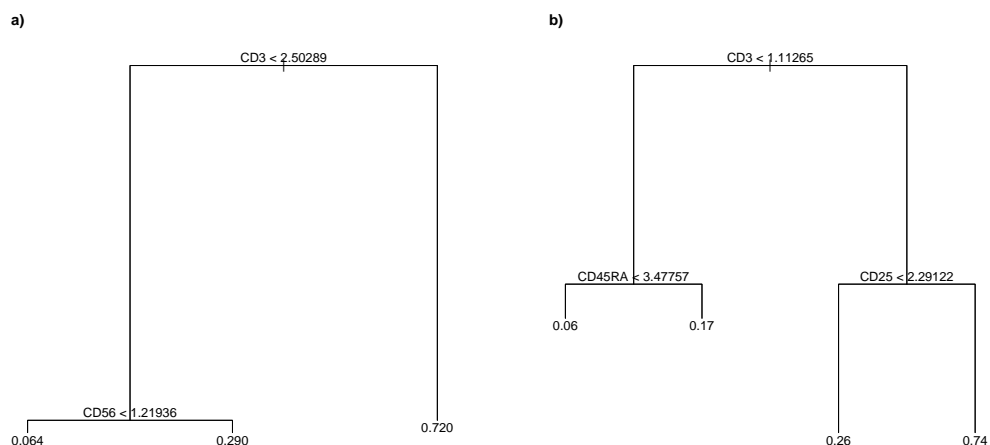


Figure 3.52. Lymphocytes: Partition tree obtained in two different sample from running CART on all core markers against pSTAT5 response at 1000 units. While both trees agree on the initial partitioning on CD25 and further partitioning on CD45RA in the first branch, the partitioning in the second branch is done on different markers and so not comparable.

3.6 Dose responsive populations identified

Finally, I will now go over some of the subsets which were discovered with the various methods described in this chapter, in lymphocytes and non-lymphocytes subsets.

Lymphocytes The marker intensities and frequencies of the cell subsets identified with these methods are summarised in Table 3.3. In Figure 3.53, the lymphocyte cell populations are presented on all core markers, and their response is presented in Figure 3.54.

The SPADE.1 and the PLSR.1 population, constituting 1.14 and 15.08 percent of the lymphocytes, appear to have similar dose-response profiles. However, the PLSR.1 population is CD56⁻ and has slightly higher CD45RA (and so higher FOXP3 because of the spillover). The SPADE.1 subset is CD3⁺ CD4⁻ CD8⁺ CD45RA⁺ CD56⁺ whilst the PLSR.1 subset is CD3⁺ CD4⁻ CD8⁺ CD45RA^{hi} CD56⁻. The PRPART.2 subset which constitutes 4.05 percent of the lymphocytes is CD3⁺ CD4^{hi} CD25^{hi} CD8⁻ CD45RA⁻ CD56⁻, appears to be a combination of the memory CD4⁺ Treg and Teff populations. Interestingly, the RPART.1 population, which constitutes 3.36 percent of the lymphocytes, has the lowest CD25 but is more sensitive than the PLSR.1 and SPADE.1 populations to proleukin. This RPART.1 subset is CD3⁻ CD4⁻ CD8⁻ CD45RA⁺ CD56⁺.

These cells are likely to be NK cells, although, CD16 would need to be measured to confirm that these cells are CD16⁺. Ortaldo et al (1992) report that these CD3⁻ CD56⁺ cells are producers of the pro-inflammatory cytokine, interferon gamma, on stimulation with IL-2. Also CD56⁺ cells can induce elevated levels of granzyme B which is implicated in T1D (Thomas et al, 2010). These pro-inflammatory molecules could be problematic for IL-2 treatment, however it would appear that these cells are relatively low responders in comparison with the memory and naive T cell subsets. The properties and function of this CD3⁻ CD8⁻ CD45RA⁺ CD56⁺ cell subset will be further investigated in our lab

by Charlie Bell using RNAseq.

	FSCA	SSCA	CD25	CD3	CD4	CD45RA	CD56	CD8	FOXP3	freq
Memory Eff	2.96	1.54	1.86	2.88	2.27	1.92	1.03	1.08	1.19	5.03
Memory Treg	2.8	1.39	2.76	2.95	2.2	1.93	0.98	1.1	2.11	0.22
Naive Eff	2.87	1.2	1.67	2.99	2.22	3.62	1.03	1.09	1.92	9.76
Naive Treg	2.71	1.13	2.38	2.98	2.14	3.48	1	1.09	1.99	0.13
SPADE.1	3.41	1.88	1.59	2.85	1.51	3.19	1.69	1.92	1.73	1.14
RPART.1	3.35	1.95	1.16	2.33	1.1	3.94	1.82	1.29	2.31	3.36
RPART.2	3.02	1.71	2.04	2.92	2.31	2.04	1.03	1.09	1.27	4.05
PLSR.1	3.19	1.61	1.62	2.96	1.53	3.86	1.08	1.82	2.27	15.08
MMPART.1	3.01	1.58	1.89	2.88	2.18	2.77	1.04	1.09	1.39	0.32
MMPART.2	3.11	1.72	1.8	2.86	1.68	2.49	1.07	1.42	1.5	12.69

Table 3.3. Lymphocytes: Cell phenotypes of identified subsets. The frequencies of the subsets (%) are relative to the lymphocytes.

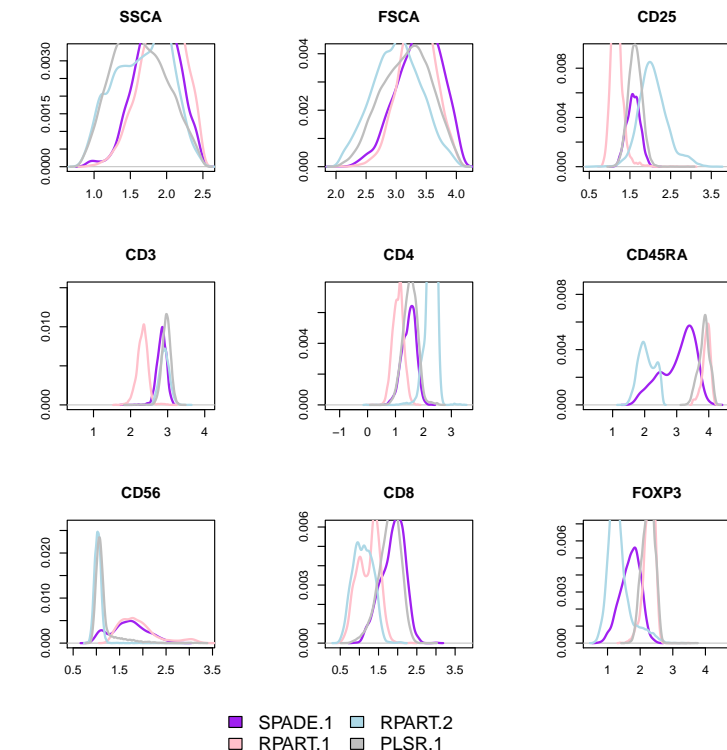


Figure 3.53. Lymphocytes core markers: SPADE.1, RPART.1, RPART.2 and PLSR.1. None of the cell subsets completely overlap across all markers.

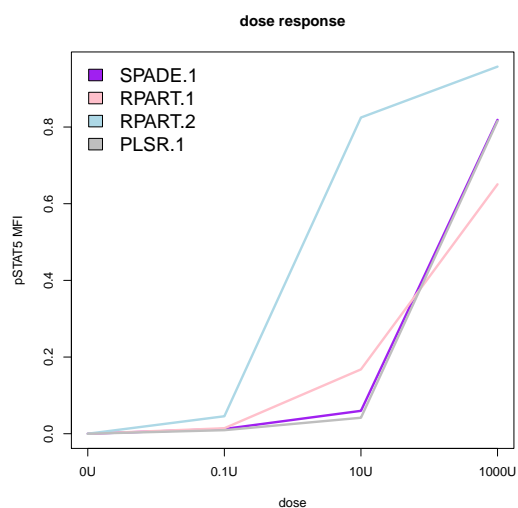


Figure 3.54.
Lymphocytes pSTAT5
MFI dose-response:
SPADE.1, RPART.1,
RPART.2 and PLSR.1.
The PLSR.1 and SPADE.1
subsets have similar
dose-response profiles.

Non lymphocytes Outside of the lymphocytes, no strong response was visible in any of the clusters based on side and forward scatter. However, smaller clusters were identified, SPADE.1 (Figure 3.23) and PLSR.1 (Figure 3.39), with larger side scatter than the lymphocytes. The SPADE.1 cluster, containing 0.21 percent and the PLSR.1 cluster containing 0.14 percent of the total number of events, were found to be heterogeneous clusters on the core markers. This SPADE.1/PLSR.1 subset contains mostly CD3⁺ CD4⁺ CD45RA⁺ cells (Figure 3.55), thus could be activated CD4 T cells, but, as suggested by experienced flow cytometrists, Marcin Pekalski and Tony Cutler, could also be an artefact of the permeabilisation and staining protocol.

	FSCA	SSCA	CD25	CD3	CD4	CD45RA	CD56	CD8	FOXP3	freq
Lymphocytes	3.09	1.59	1.58	2.84	1.53	3.46	1.07	1.29	1.83	16.97
SPADE.1	6.1	3.25	1.9	3.1	1.97	3.79	1.15	1.53	2.23	0.21
RPART.1	3.24	2.36	1.53	2.77	1.57	3.33	1.1	1.35	1.86	1.66
PLSR.1	6.33	3.29	1.97	3.16	2.01	3.91	1.17	1.75	2.35	0.14
MMPART.1	4.62	6.61	2.4	3.1	2.35	2.74	1.15	1.51	2.23	0.03
MMPART.2	4.07	2.74	1.84	3	2.21	2.76	1.13	1.47	1.7	0.57

Table 3.4. Non-lymphocytes: Cell phenotypes. The frequency of the subsets (%) is relative to the whole sample (including debris).

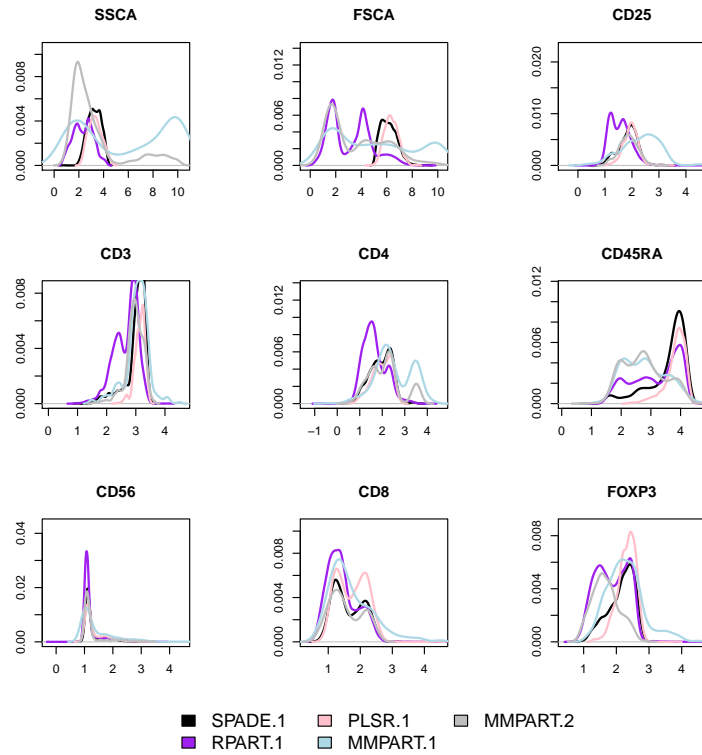


Figure 3.55. Non-lymphocytes core markers: SPADE.1, RPART.1, PLSR.1, MMPART.1 and MMPART.2. The PLSR.1 and SPADE.1 subsets show the most overlap. The other identified subsets do not appear unimodal both on side and forward scatter.

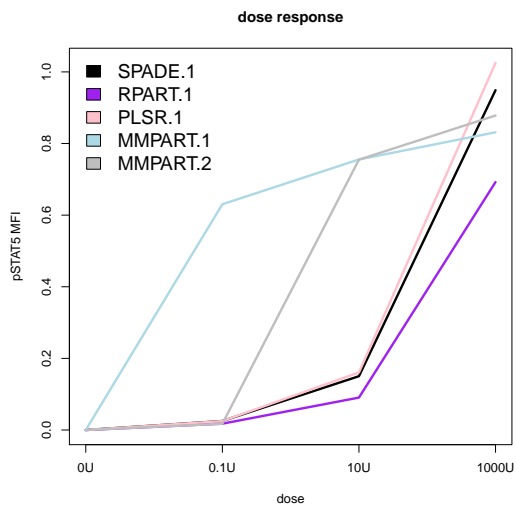


Figure 3.56.
Non-lymphocytes
pSTAT5 MFI
dose-response:
SPADE.1, RPART.1,
PLSR.1, MMPART.1 and
MMPART.2. The PLSR.1
and SPADE.1 subsets have
similar responses.

3.6.1 Are these cells present in other samples?

In order to assess whether these identified subsets were real and not artefacts of a single batch, I attempted to identify them in the other five samples analysed with the same panel.

Lymphocytes In the lymphocytes, I tried to identify the $CD3^- CD4^- CD25^- CD56^+$ subset, also known as the CD56 bright subset, corresponding to the RPART.1 population in Figure 3.53. I again applied the recursive partitioning method discussed in Section 3.4.2 to obtain 1024 bins containing approximately the same number of events which cover the marker space. However, instead of using the MST visualisation, I used the parallel plot representation, where dimensions are represented as parallel axes and each point is represented by a line segment between dimensions (Figure 3.57). This representation is easier to interpret than the MST representation to highlight a known subset. Each line in the parallel plot represents one of the 1024 bins and is colour coded by pSTAT5 MFI. The width of the lines is also increased for cells with a CD56 MFI higher than 1.2 to better highlight the CD56 bright cells. While, as expected, the majority of lymphocytes are CD56 low, the CD56 bright populations clearly stand out and in particular, one line/bin shows particularly high activation. This cell population is consistently identified in four additional samples, stained with the same panel and analysed on different days, suggesting that this is likely to be a real population and not only the consequence of a batch effect (Figure 3.58).

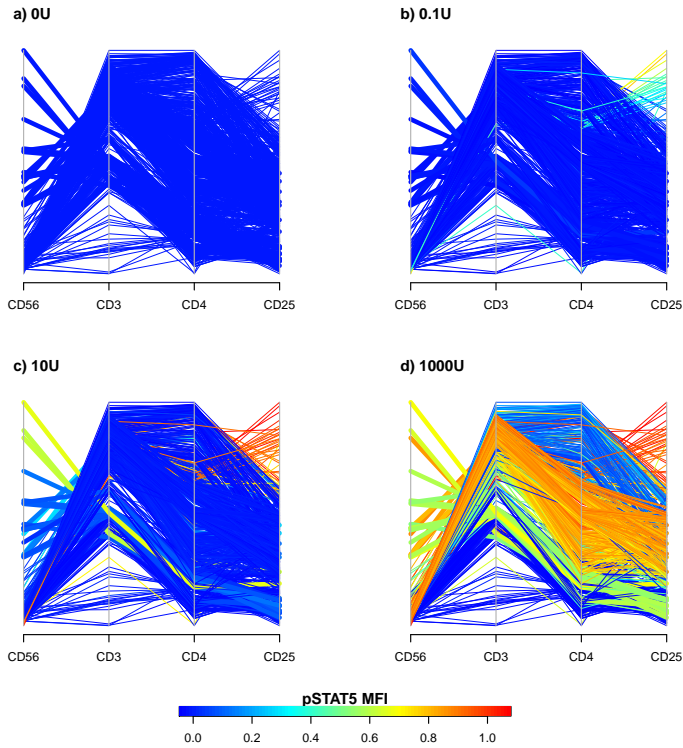


Figure 3.57. Lymphocytes: $CD56^{hi}$ cells within single batch show increased pSTAT5 MFI at 10 units. Parallel plot of the 1024 bins obtained by using RPART on CD56, CD3, CD4 and CD25. At 10 units (c), pSTAT5 MFI is already saturated in the $CD25^{hi}$ bins, but a $CD56^{hi}$ bin already shows moderate levels of pSTAT5 MFI. At 1000 units (d), most bins have high levels of pSTAT5 MFI and all $CD56^+$ bins show moderate pSTAT5 MFI.

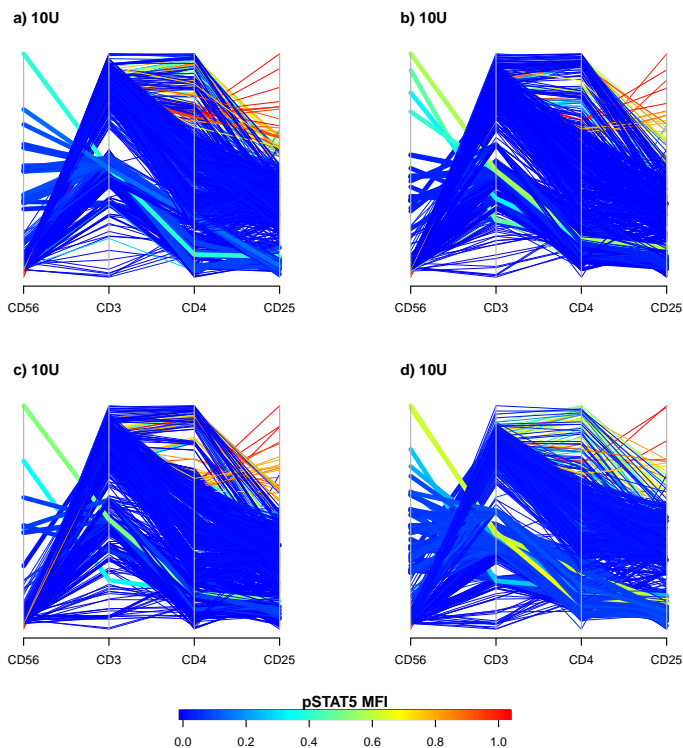


Figure 3.58. Lymphocytes: $CD56^{hi}$ cells at 10 units in four additional samples. Parallel plot showing bins obtained by using RPART on CD56, CD3, CD4 and CD25. The subset of $CD56^{hi}$ cells appears to exist in these additional samples and shows response at 10 units.

Non-lymphocytes Outside of the lymphocyte cluster, I attempted to identify the subset of cells with slightly larger forward scatter, that I reported as the SPADE.1 subset in Figure 3.55. Since I am now interested in visualising the pSTAT5 MFI response in two dimensions, forward and side scatter, instead of using RPART as in Figure 3.28 or SPADE to reduce the number of events, I resorted to a fixed width two-dimensional grid on forward and side scatter. Data points were then assigned to their closest grid coordinate and the pSTAT5 MFI at each grid coordinate was calculated per dose. In samples from a single batch, the subset identified previously is delineated in purple and shows response at 1000 units (Figure 3.59). This subset appears consistently in the four additional batches stained with the same panel, as well as in a further 49 batches stained with the CD4 T cell panel (Table 3.2). All plots can be viewed at <http://goo.gl/eeRYkE>.

Upon closer investigation, this cell population contained doublets which were excluded by using side-scatter width and height. After this filtering, the remaining cells which responded to proleukin were primarily CD4⁺ CD3⁺, hence T cells, and CD45RA⁺, hence naive, as can be seen in the parallel plot representation in Figure 3.60. Whether these cells are actually a distinct cell population of larger naive T cells or simply an artefact of the protocol it still not entirely clear. On one hand, this cell population does appear consistently in most samples stained for pSTAT5, but on the other it is not as clearly distinguishable, based on side and forward scatter in samples which did not undergo permeabilisation for pSTAT5 staining, as can be seen in Figure 2.3.

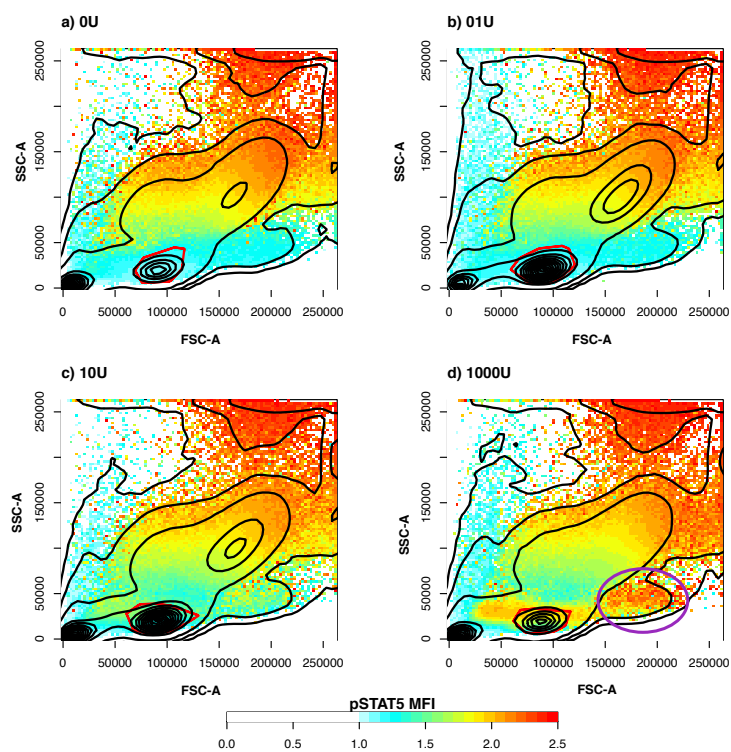


Figure 3.59.
Non-lymphocytes:
pSTAT5 MFI on side
and forward scatter
within a single batch.
The same grid is applied
within the batch and
points are assigned to
their closest grid point.
At each grid point the
pSTAT5 MFI is
calculated. The colour
code for the pSTAT5 MFI
at each grid point. The
contour lines delineate
regions of similar density.
The red polygon
represents the
lymphocyte gate on side
and forward scatter. The
purple ellipse delineates
the newly identified
subset which shows
response at 1000 units.

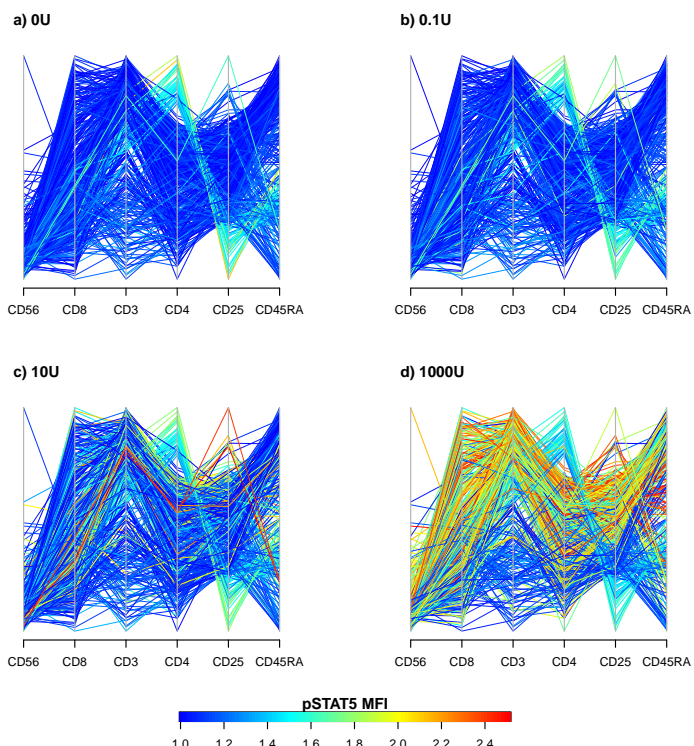


Figure 3.60. **New**
non-lymphocyte
subset on core
markers after doublet
exclusion. Each line
represents a single cell
from the subset identified
in Figure 3.59 after
doublet-exclusion. The
number of cells has been
normalised using the
ANN method described in
Section 3.3.1. At 1000
units, the cells which
respond are primarily
 $CD3^+ CD4^+$, hence T
cells, and $CD45RA^+$,
hence naive.

3.6.2 Conclusion

Using the methods described in this chapter on the most complete staining panel at my disposal for these PBMC samples, it would appear that, although other cell types carriers of IL-2 receptors are potential responders, the majority of the response comes from within the conventional lymphocyte subset, with a smaller secondary response coming from the SPADE.1/PLSR.1 cluster at 1000 units of proleukin. Another observation is that, within the lymphocytes, at the lowest 0.1 units proleukin dose, CD25 explains a significant proportion of the pSTAT5 response, however at higher, 10 and 1000 units doses, the beta receptor, CD122, and common gamma receptor, CD132, are likely to become more influential (Pekalski et al, 2013). For example, the CD56^{hi} subset shows response at 10 units in spite of having relatively low CD25 (Figure 3.53).

From a methodological perspective, I have also discovered the benefits of methods which make the density more uniform so that more importance is attached to the separation between clusters rather than uniquely their weight. Once the density is homogenised and the data appropriately thinned, simpler computationally efficient methods which assume the same cluster sizes can be used. The challenge then lies in the thinning which can boost artefacts as well as rare cell populations. The only way around this is to either optimise the experimental protocol to minimise artefacts or to increase the number of samples, which can be hard to achieve in flow experiments.

Chapter 4

***KIR3DL1/KIR3DS1* copy number variation in type 1 diabetes**

*Le de
chapeau. Il re
qui digérait un élé*

In Chapter 2 and Chapter 3, I have identified and analysed cell populations in flow cytometry using normalisation and clustering methods. Of the clustering methods I have applied, mixture-model clustering proved to be particularly useful in dealing with noise. As discussed, one of the benefits of mixture-model approach are the posterior probabilities which can be used in downstream statistical analysis. So far, I have not made full use of this feature in the association tests, partly because the number of cells is large and the fraction of cells which lie clearly within one cluster is an adequate measure for association testing. However, as one deals with smaller datasets, the uncertainty in clustering can have an important impact on association statistics. In this chapter, I will apply normalisation and mixture model clustering to a much smaller genetic dataset, and account for the clustering uncertainty in testing association with disease.

4.1 Background

4.1.1 Killer immunoglobulin receptors and their interaction with human leukocyte antigen molecules

The KIR region, a 150 kb cluster of 17 identified genes located within the 1 Mb Leukocyte Receptor Complex on chr19q13.4, is an interesting candidate region in HLA-associated autoimmune diseases such as T1D, due to the interaction between KIR and HLA molecules. KIRs are transmembrane glycoproteins, expressed by NK cells and subsets of T cells, which bind to the peptide presenting HLA class I molecules on the surface of target cells.

It is thought that the interaction of these two loci plays an important part in immunity and, as a result, these regions have co-evolved (Parham and Moffett, 2013), leading to much diversity in the allelic frequency of HLA and KIR genes between populations. However, while the polymorphism of the HLA region is primarily due to allelic diversity, the alleles of the KIR region also vary in copy number. The copy number variation of these genes is thought to correlate with the level of expression of KIRs and to bear some influence on disease outcome. KIRs are named according to their number of extracellular immunoglobulin domains (2D and 3D) and whether their cytoplasmic tail is short (S) or long (L). Generally, KIR proteins with the long cytoplasmic domain transduce inhibitory signals upon ligand binding via an Immune Tyrosine-based Inhibitory Motif (ITIM), whereas KIRs with the short cytoplasmic domain, do not contain the ITIM motif and instead transduce an activating signal upon ligand binding. The fate of the target cell then depends on the composite signal generated by the combination of inhibiting/activating KIRs in the presence of their HLA class 1 ligands (Bashirova et al, 2006). The longer KIR genes tend to have greater allelic diversity, whereas the shorter KIRs tend to vary more in copy number. The polymorphic and highly homologous na-

ture of these genes leads to very extensive haplotype and copy number diversity in the KIR region (Jiang et al, 2012).

Despite the important biological function of KIRs, no GWAS hits have been reported in the KIR region. This could well be due to the shortcomings of GWAS in detecting trait-associated sequence polymorphism in more complex, poorly mapped regions of the genome. The technology primarily used in GWAS is the SNP array. SNP arrays assay the polymorphism in single nucleotides positions across the genome by the means of SNP probes of typically 20 base pairs in length. Depending on the region of the genome and the array used, the SNP probe coverage varies greatly. In certain regions, the SNP probe coverage is insufficient to capture the underlying genetic complexity. Also, SNP probes are template based, they are designed based on reference sequences. They are not designed to discover new sequences, only the distribution of known alleles. Consequently, SNP probes targeting regions which are more polymorphic than anticipated, such as regions of allelic specific copy number variation like KIR, may lead to signals which cannot be clustered into the expected three genotypes (e.g AA, AT, TT) of bi-allelic SNPs. Instead the signal returned by these probes can return a variable number of clusters which requires more careful analysis using flexible genotype calling algorithms (Kumasaka et al, 2011). Additionally, KIR is poorly mapped in the human reference genome (build36/hg18) and does not contain all KIR genes. Thus, KIR has been mostly overlooked by GWAS, which makes it worthy of further investigation and characterisation.

4.1.2 *KIR3DL1* and *KIR3DS1*: two strong candidates for T1D association

Two genes in the KIR complex, *KIR3DL1* and *KIR3DS1*, are particularly interesting candidates for T1D association due to their interaction with T1D-associated HLA class

I molecules. The KIR3DL1 protein is known to interact with the HLA class I allotypes that contain the HLA-Bw4 serological epitope (Gumperz et al, 1997; Vivian et al, 2011), whereas the protein encoded by *KIR3DS1*, which shares 97 % sequence similarity to *KIR3DL1*, is thought to bind the more restrictive HLA-Bw4-80I epitope subset (Martin et al, 2007).

The grouping of HLA-A and HLA-B alleles according to HLA-Bw4 serological epitope (Martin et al, 2002) is given in Table 4.1 and includes several HLA class I alleles that are associated with T1D risk after conditioning on the major HLA class II effects (Nejentsev et al, 2007; Howson et al, 2009).

Copy number variation in the *KIR3DS1* gene is thought to be implicated in viral diseases, such as HIV-1 (Martin et al, 2002; Pelak et al, 2011), and certain autoimmune diseases, but there is no substantial evidence of association with T1D (Körner and Altfeld, 2012). However, studies to date have been small, and evidence for its association has not yet been addressed in large, well powered studies.

Epitope	Residues (77-83)	HLA-B	HLA-A
HLA-Bw4 80I	NLR I ALR	B*1516 B*1517 B*1524 B*2702 B*3801 B*4901 B*5101 B*5108 B*5201 B*5301 B*5302 B*5701 B*5702 B*5801	A*2301 A*2402 A*2403 A*2407 A*2501 A*3201
HLA-Bw4 80T	D LRT T LLR S LRT T LLR N LRT A LR	B*1302 B*2701 B*2704 B*2705 B*3701 B*3802 B*4402 B*4403 B*4404 B*4405 B*4414 B*4417 B*4429 B*4435 B*4701	
HLA-Bw6	SLR N LRG	B*702 B*703 B*705 B*706 B*708 B*710 B*716 B*726 B*801 B*1401 B*1402 B*1501 B*1503 B*1504 B*1505 B*1507 B*1508 B*1509 B*1510 B*1514 B*1515 B*1518 B*1539 B*1801 B*3501 B*3502 B*3503 B*3508 B*3901 B*3906 B*3928 B*4001 B*4002 B*4006 B*4011 B*4023 B*4101 B*4102 B*4202 B*4501 B*4601 B*4801 B*5001 B*5002 B*5501 B*5601	

Table 4.1. Grouping of HLA alleles by HLA-Bw4 epitope. *HLA-A* and *HLA-B* alleles which carry the serological epitope HLA-Bw4 can be further subdivided as HLA-Bw4-80I or HLA-Bw4-80T, depending on whether the amino acid at position 80 in the heavy alpha chain of the HLA class I protein is an isoleucine (I) or a threonine (T) (Gumperz et al, 1997; Martin et al, 2002).

4.2 Samples and genotyping assays

4.2.1 Samples

Our study involved 12,106 individuals: 6,744 cases (age at diagnosis less than 17 years) from the Genetic Resource Investigating Diabetes (GRID) cohort, and 5,362 controls from the British 1958 Birth Cohort (1958BC). All subjects were of white European ancestry (as confirmed by PCA of earlier GWAS data in these samples (Barrett et al, 2009)) with written informed consent and Ethics Committee/Institutional Review Board approval. The DNA for the cases and controls was prepared using the same protocols in Cambridge and in Bristol respectively, and all samples were cell-line derived.

4.2.2 HLA and SNP Genotyping

HLA Epitope	Cases	Controls	Total
N/A	3822 (11)	2681 (70)	6503 (81)
HLA-Bw6	1175 (308)	753 (199)	1928 (507)
HLA-Bw4-80T	651 (162)	754 (174)	1405 (336)
HLA-Bw4-80I	1096 (266)	1174 (284)	2270 (550)
HLA total	2922 (736)	2681 (657)	5603 (1393)

Table 4.2. Classification of subjects in study by HLA epitope (as defined in Table 4.1). In parentheses, number of subjects analysed with qPCR post QC. No HLA typing was done for the N/A category. The HLA epitopes are defined in Table 4.1. An individual is assigned to an HLA epitope group if he is a carrier of at least one allele of that group. So that each individual only belongs to a single HLA epitope group, the assignment priority is first HLA-Bw4-80I, then HLA-Bw4-80T and finally HLA-Bw6 allele if no HLA-Bw4 alleles were found.

HLA genotypes were available on a subset of 5,603 individuals, 2,922 cases and 2,681 controls. HLA-A and HLA-B genes were typed at four-digit allele resolution using Dynal RELI SSO assays (Invitrogen, Paisley, U.K.) (Table 4.2). The epitope classification of HLA-A and HLA-B alleles is given in Table 4.1.

All 12,106 samples were genotyped using the ImmunoChip SNP array, according to the manufacturer's protocol, and processed at the University of Virginia in Charlottesville, USA. ImmunoChip is a custom Illumina 200K Infinium high-density SNP array (Nikula et al, 2005), which contains 100 SNPs in the LILR complex, 30 of which fall in the 14 kb *KIR3DL1* region (Table 4.4).

4.2.3 qPCR experimental protocol

Jiang et al (2012) have designed qPCR assays to study copy number variations in KIR, which have led to the discovery of many rare haplotypes. In collaboration with Jiang et al (2012), Deborah Smyth developed multiplexed qPCR 384-well assays, designed to determine copy numbers in most known alleles of *KIR3DL1* and *KIR3DS1*. The gene *STAT6*, known to always be present in two copies, was used as a reference. The forward/reverse primers and probe sequences for *KIR3DL1*, *KIR3DS1* and *STAT6* are summarised in Table 4.3.

Nonetheless, qPCR assays remain expensive (£12 per sample) and labour intensive compared to SNP arrays, and thus qPCR was only performed on a subset of 1629 samples, 816 cases and 813 controls by Deborah Smyth.

The qPCR platform used was the LightCycler 480 Real-Time PCR Instrument. For each qPCR reaction, 2 µl of DNA at 5 ng µl⁻¹ were used with 5 µl of Quantifast Multiplex PCR mastermix (0.25 µl primer mix, 0.045 µl probe mix and 4.705 µl of water). qPCR conditions were 95 °C for 5 min, followed by 40 cycles at 95 °C for 15 s and 66 °C for 50 s. Data was collected at 66 °C. The samples were tagged with three different dyes, Fam for *KIR3DS1*, Cy5 for *KIR3DL1* and DFO for *STAT6*, and amplified on eighteen 384-well plates. On all plates, samples were replicated across four wells. So that each plate contained a maximum of 96 samples. Four calibrator samples of known *KIR3DL1*/*KIR3DS1* copy number and one water sample were included on all but one

plate. Cases and controls were distributed evenly across all plates. Four plates were analysed in duplicate.

Gene	Oligos	Sequence (5'-3')
<i>KIR3DS1</i>	Forward Primer	CATCGGTTCCATGATGCG
	Reverse Primer	GGGAGCTGACAACGTGATAGG
	Probe	AACAGAACCGTAGCATCTGTAGGTCCCT
<i>KIR3DL1</i>	Forward Primer	CACAGTTGGATCACTGCGT
	Reverse Primer	CCGTGTACAAGATGGTATCTGTA
	Probe	CCCTTCTCAGAGGCCAAGACAC
<i>STAT6</i>	Forward Primer	CCAGATGCCTACCATGGTG
	Reverse Primer	CCATCTGCACAGACCCTCC
	Probe	CTGATTCCCTCATGAGCATGCAGCTT

Table 4.3. The qPCR probes and primers. The qPCR probes and primers used in our assay, these were originally designed by Jiang et al (2012).

4.3 Data Analysis

4.3.1 Quality control and normalisation of qPCR data

The experiment files exported from the LightCycler gave us the crossingpoint (Ct) value for each dye-DNA conjugate. By subtracting from the Ct value of the reference dye-DNA conjugate, DFO-STAT6, I obtained the baseline relative ΔCt value for Fam-KIR3DL1 and Cy5-KIR3DS1. Since *STAT6* is known to have two copies, negative values of ΔCt should indicate two copies or less, and positive values, two copies or more. However, due to qPCR differences in efficiency this threshold does not necessarily hold in practice as shown in Figure 4.1, which is why it is more correct to cluster when calling copy number. As part of the quality control (QC), I excluded 64 samples that did not yield a DFO-STAT6 Ct reading in all four well replicates. All remaining samples were summarised by the ΔCt median of the four well replicates.

The individual distributions of *KIR3DS1* and *KIR3DL1* ΔCt differed between plates

(Figure 4.1.a.b) which prevented clustering all samples together. Visual inspection of the data distributions by plate led us to drop plate 22 because it appeared excessively noisy (Figure 4.1.a.b). To normalise the ΔCt values across the remaining plates, I first applied the k-medoids algorithm within plates for *KIR3DL1* and *KIR3DS1* separately to identify the location of the most distinguishable copy number groups, one and two copies, then normalised across plates by a linear transformation so that the median ΔCt of the two groups were aligned across all seventeen plates. Samples repeated across different plates were summarised by the median of their repeated value. Following QC, 1474 unique individuals, 747 cases and 727 controls, were available for analysis.

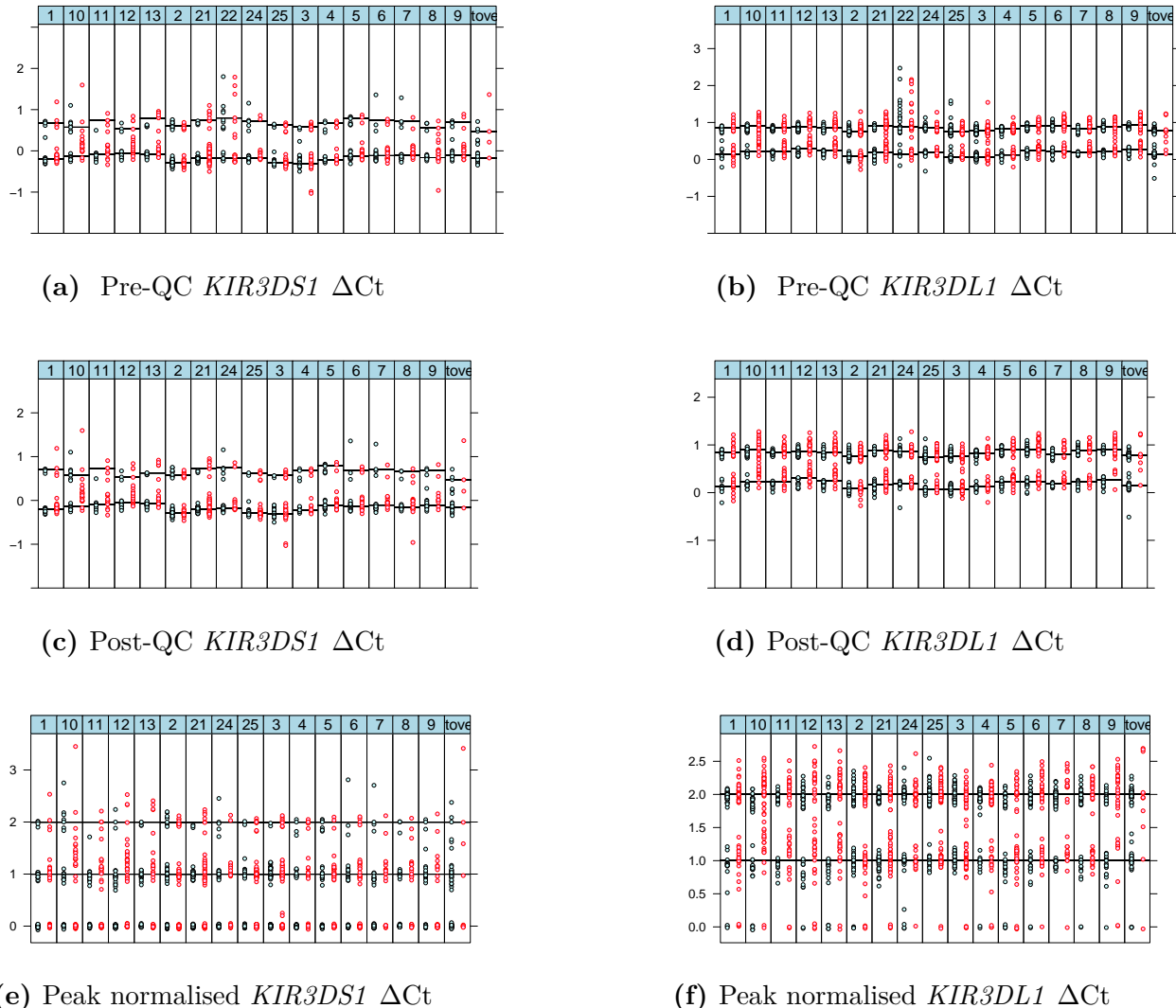


Figure 4.1. *KIR3DS1* and *KIR3DL1* ΔCt values for cases (red) and controls (blue) per qPCR plate. Plate 22 stands out as the noisiest for both *KIR3DL1* (a) and *KIR3DS1* (b), and so is subsequently dropped as part of the QC (c and d). Negative ΔCt are not displayed for pre and post QC so as to better visualise the one and two copy number groups. Normalisation consists a linear transform which maps the medians of the one and two copy groups from each plate to 1 and 2 (e and f). After normalisation, negative ΔCts values are assigned to zero.

4.3.2 Bivariate clustering: copy number calling in qPCR data

Samples which yielded one or less Ct reading for Fam-KIR3DL1 or Cy5-KIR3DS1, but all four Ct readings for the reference DFO-STAT6, were assumed to contain zero copies

of *KIR3DL1* or *KIR3DS1*. For the remainder of the samples, I called copy number groups by fitting a mixture of bivariate Gaussian distributions to the two dimensional normalised ΔCt values, allowing for eight *KIR3DS1/KIR3DL1* copy number groups: three common groups of two copy numbers (0-2, 1-1, 2-0) and five rarer groups of lower or higher copy numbers (Figure 4.2). The mixture was fitted using an EM algorithm (Young et al, 2009) with initial parameters calculated from the clusters returned by k-means with centers set to the eight expected locations of the copy number groups. After fitting the mixture model each sample was assigned a posterior probability of belonging to each of the eight copy number groups which allows for uncertainty in copy number calling. These posterior probabilities were taken into account in downstream statistical analysis via multiple imputation.

Raw median ΔCt distributions varied across plates which prevented simple visual copy number assignment (Figure 4.1). After normalisation, samples repeated across different plates showed good reproducibility (Figure 4.4) and two dimensional clustering enabled 1474 samples to be confidently assigned to a single copy number group, including all samples with known copy number which were assigned to the correct cluster.

Jointly clustering on *KIR3DL1* and *KIR3DS1*, has the advantage of exploiting the correlation between the ΔCt values. For example, this can be seen in plate 10, where noisy cases (Figure 4.1.f) are difficult to assign as one or two copies based solely on their *KIR3DL1* ΔCt , but are much more clearly distinguishable when I also consider their *KIR3DS1* ΔCt value (Figure 4.3).

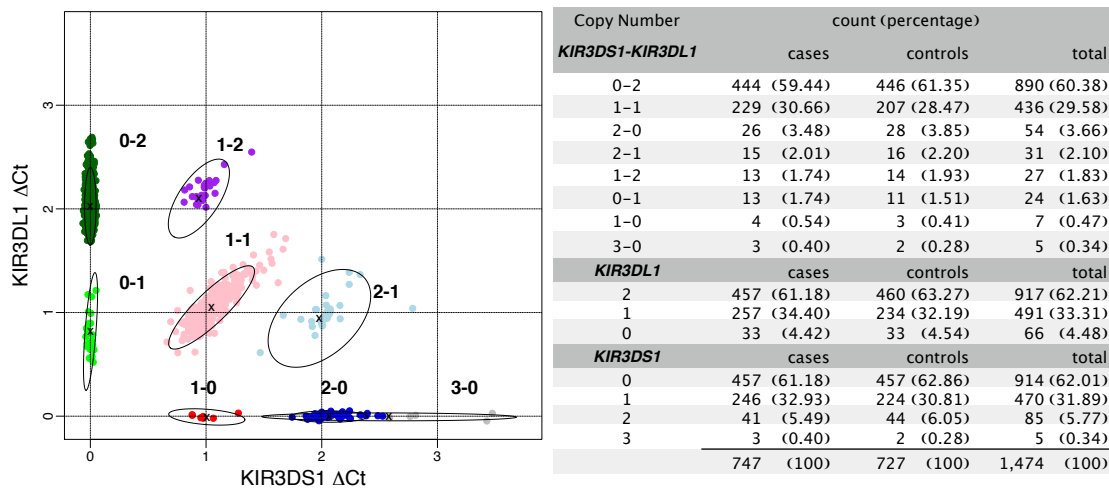


Figure 4.2. Copy number calling of *KIR3DL1*/*KIR3DS1* from qPCR ΔCt . On the left, the median normalised ΔCt values for *KIR3DS1* and *KIR3DL1* are shown with the results of clustering into the eight copy number groups coloured according to the group with the highest posterior probability. The three most common copy number groups are the ones with a total copy number of two: *KIR3DL1* 0-2 (dark green), *KIR3DL1*/*KIR3DS1* 1-1 (pink) and *KIR3DS1* 2-0 (dark blue). The ellipses delimit the 95th percentile. On the right, the counts of the most probable copy number state are shown for cases and controls.

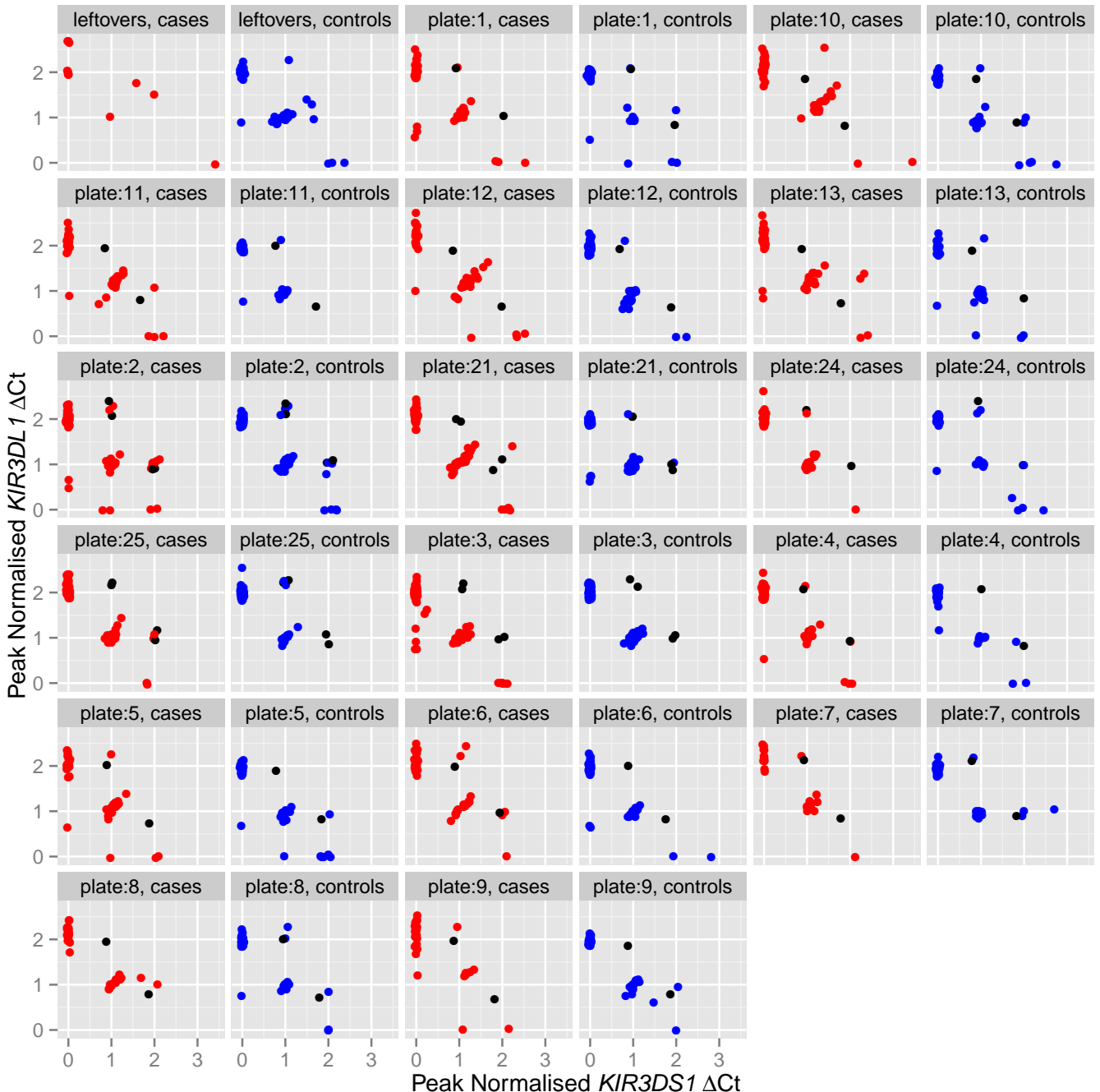


Figure 4.3. Post-QC cases (red) and controls (blue) are plotted separately for each qPCR plate. The samples with known *KIR3DL1*/*KIR3DS1* copy number are plotted in black. I can see that there is a larger spread in cases than in controls which is especially clear in the 1-1 copy number group. Also, it is apparent that the ΔCt of *KIR3DL1* and *KIR3DS1* are correlated in the 1-1, 2-1 and 1-2 groups. I exploited this correlation in the copy number calling by doing bivariate clustering.

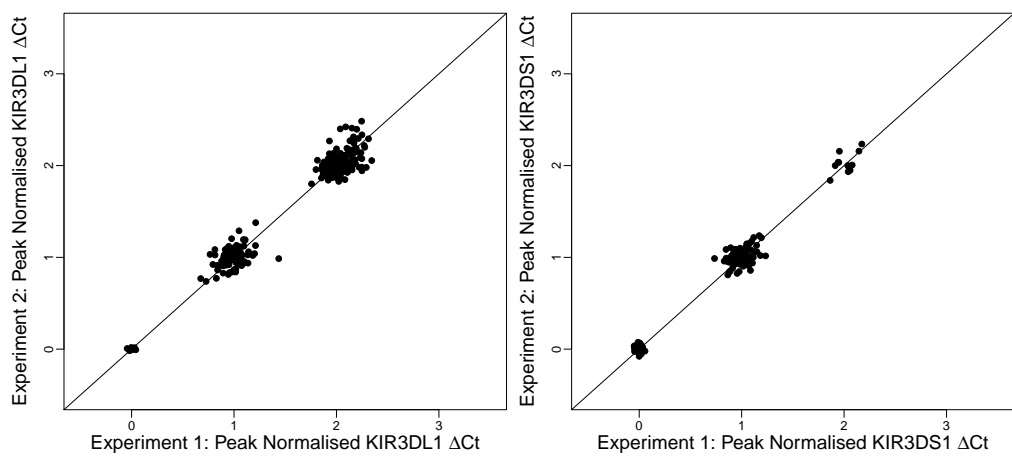


Figure 4.4. Repeatability of qPCR assay. In order to assess the reliability of the qPCR assay 310 samples were re-analysed. I found very high reproducibility of the ΔCt values ($r^2 > 0.96$) confirming the reliability of our qPCR assay. r^2 is the Pearson correlation squared.

4.3.3 KNN classification: copy number imputation into the SNP data

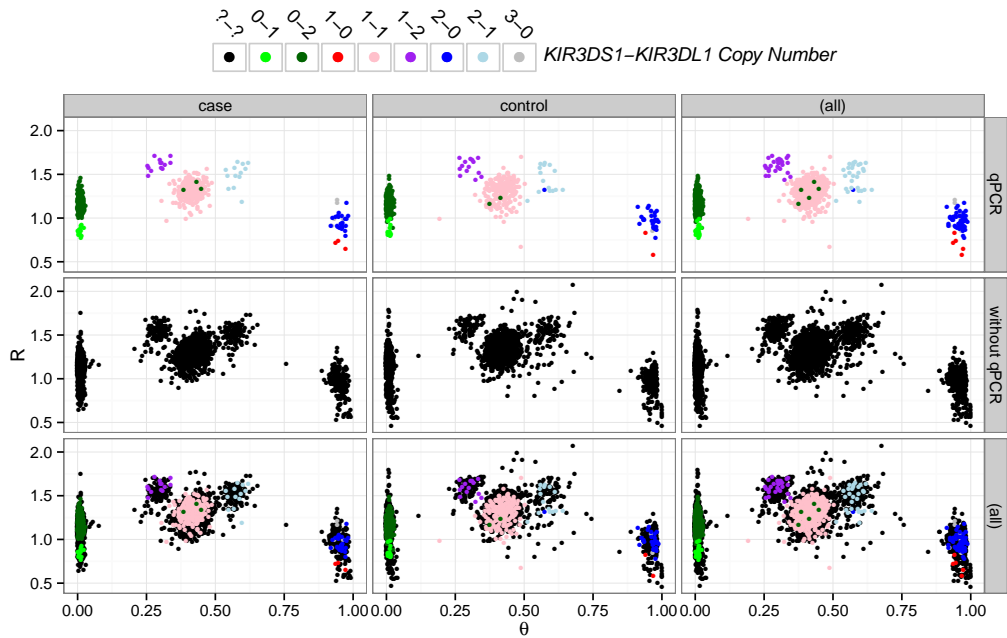


Figure 4.5. Overlay of ImmunoChip and qPCR samples for R and θ at SNP rs592645. Samples are coloured by the most likely *KIR3DS1*-*KIR3DL1* copy number group according to the qPCR analysis (see Figure 4.2). The first and second row split the samples on the availability of qPCR data, and the third row is the overlay of the samples from the first and second row. The first and second column split the samples by case-control status and the third column is the overlay of the samples from the first and second column.

I extended our sample size by using the subset of samples common between the qPCR and SNP datasets, 747 cases and 727 controls, to train a k-nearest neighbour (KNN) classifier to predict *KIR3DL1*/*KIR3DS1* copy number using the R and θ signals from ImmunoChip SNPs.

Each of 30 SNPs lying within the *KIR3DL1* (since *KIR3DS1* is not on the reference genome) region were assessed for association with either *KIR3DL1* or *KIR3DS1* copy number in individual linear regression of copy number against R and θ (Table 4.4).

SNP signals, R and θ , showed good association with copy numbers of *KIR3DL1* and of *KIR3DS1* for 19 of 30 SNPs in the *KIR3DL1* region (Table 4.4). The best example is shown in Figure 4.5, in which seven clusters for SNP rs592645 can be discerned that correspond closely with qPCR derived *KIR3DL1*/*KIR3DS1* copy numbers. This is also visually apparent in Figure 4.6 where SNP rs592645 shows the best clustering of copy number out of those 30 SNPs. Figure 4.5 also illustrates a number of important points about using SNP signals for imputation. First, θ corresponds to the ratio of copies of *KIR3DL1* to *KIR3DS1*, while R corresponds to the total copy number. Second, some clusters overlap; without the qPCR data, the number of clusters and their boundaries would be difficult to define, particularly along the R axis. Finally, the clusters are in slightly different positions in cases and controls, reflecting the known sensitivity of genotyping chips to subtle differences in DNA preparation and storage conditions. This has two implications: probabilistic clustering of the SNP data alone is likely to be poor in the combined sample, while unsupervised clustering of cases and controls separately when clusters are not clearly separated risks increasing type 1 error rates (Plagnol et al, 2007). Instead, I used the qPCR copy numbers as training data to perform supervised clustering of the SNP signals.

I first explored the validity of our imputation approach by means of leave-one-out cross-validation (LOOCV) in the samples with qPCR data. I examined using all nineteen predictive SNPs, or various subsets, and found optimal KNN imputation was achieved with the single most predictive SNP, rs592645 with $k = 8$, which minimised the mean LOOCV error rate to 2.0 % across ten multiply imputed qPCR datasets (Figure 4.7).

I also explored the effect of varying the size of the training data set by setting KIR gene copy numbers to missing for a randomly chosen subset of samples and imputing them in the remaining samples. I suggest that only 295 samples are required to achieve LOOCV error rates < 5 % and 590 for error rates < 2.5 % (Figure 4.8).

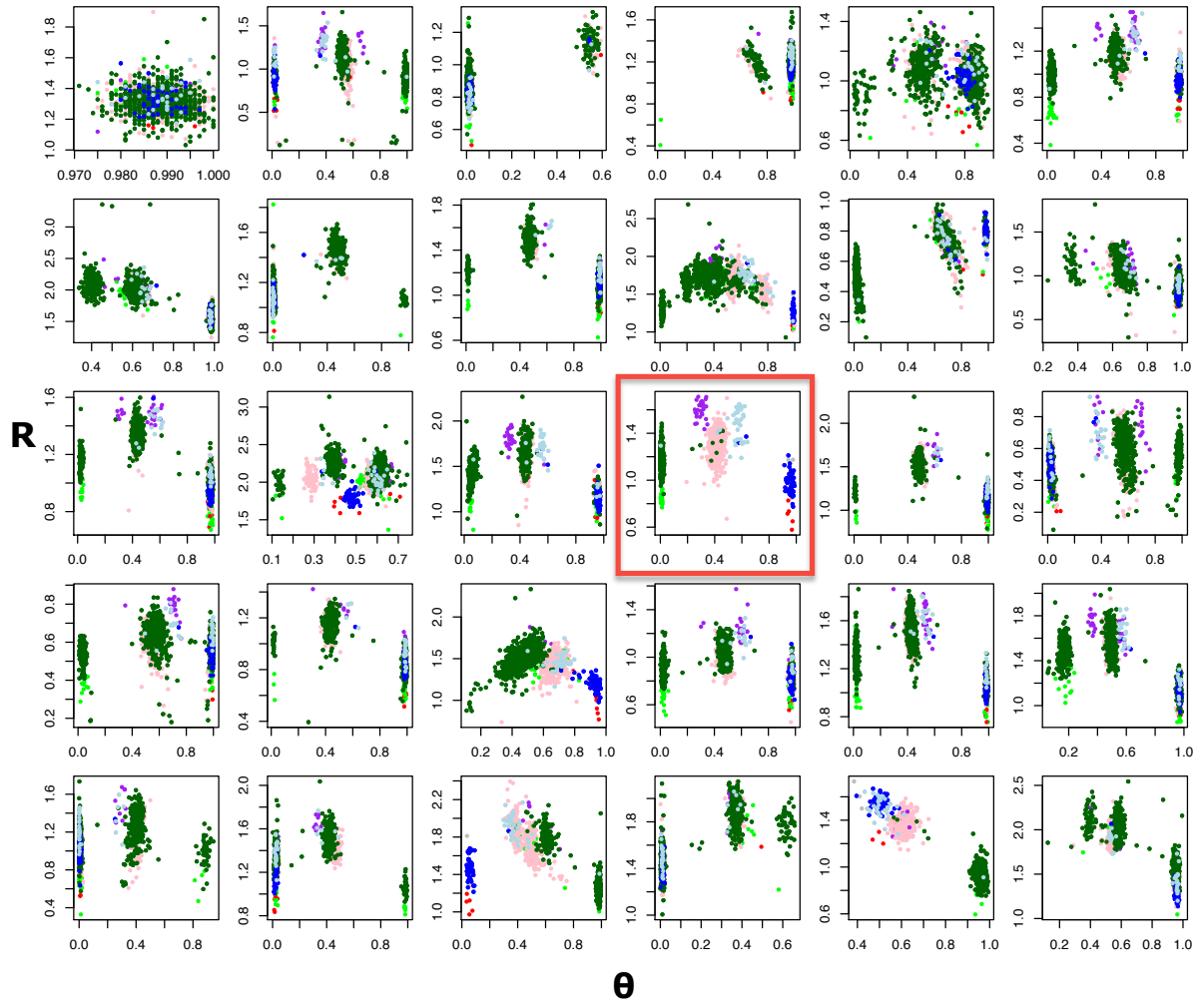


Figure 4.6. Signal plots of ImmunoChip SNPs which fall in the *KIR3DL1* region. Each of the 30 ImmunoChip SNPs from Table 4.4, coloured by *KIR3DL1*/*KIR3DS1* copy number (see Figure 4.5 for legend). SNP rs592645 (red square) shows the best clustering by copy number.

	Name	Position	SNP	GenCall QC	p-value θ	p-value R	
	seq-rs597598	60007252	[A/G]	ok	3.19E-03	7.81E-01	
	seq-rs598452	60007428	[A/G]	ok	6.53E-01	2.62E-01	
	seq-t1d-19-60007809-C-G	60007809	[G/C]	ok	3.64E-02	6.27E-06	
	seq-rs55761930	60008141	[T/C]	ok	6.33E-01	6.12E-01	
	seq-rs10500318	60012591	[A/G]	ok	7.59E-11	1.31E-13	
	seq-rs592645	60012739	[A/T]	ok	8.85E-01	3.38E-09	
	seq-rs604077	60013208	[A/G]	ok	4.82E-03	1.20E-01	
	seq-rs604999	60013409	[A/G]	ok	1.77E-15	9.99E-04	
	seq-t1d-19-60014013-A-C	60014013	[T/G]	lowcallrate	8.74E-01	3.15E-08	
		rs3865507	[T/G]	ok	8.62E-03	6.93E-17	
		seq-rs3865510	[A/C]	ok	2.23E-10	2.04E-10	
		seq-rs648689	[A/G]	ok	2.31E-01	1.03E-02	
		seq-rs649216	[T/C]	ok	2.85E-02	1.04E-13	
		rs581623	[A/G]	ok	3.76E-02	2.06E-13	
		seq-rs4806568	[A/G]	lowcallrate	1.44E-20	2.93E-01	
		seq-rs674268	[T/C]	lowcallrate	1.43E-02	2.90E-01	
		rs12461010	[A/G]	ok	4.72E-01	1.72E-01	
		seq-rs2295805	[T/C]	lowcallrate	9.55E-08	8.40E-04	
		seq-rs12976350	[T/C]	lowcallrate	1.70E-05	5.07E-01	
		seq-t1d-19-60034052-C-T	[A/G]	hwe	3.27E-02	4.07E-01	
			rs4806585	[T/G]	hwe	2.20E-11	2.42E-02
			seq-rs62122181	[T/C]	lowcallrate	2.40E-13	2.26E-01
			rs10422740	[T/C]	monomorph	7.78E-01	8.49E-02
			rs640345	[A/G]	ok	3.61E-07	6.83E-02
			seq-t1d-19-60054973-T-C	[A/G]	ok	2.92E-01	2.28E-04
			seq-t1d-19-60056605-A-T	[A/T]	ok	3.99E-01	1.48E-16
			seq-t1d-19-60056721-C-T	[A/G]	ok	9.02E-01	2.04E-09
			seq-rs10407958	[T/A]	ok	1.06E-02	5.45E-10
			seq-rs1654644	[T/G]	ok	7.94E-14	5.21E-12
			rs3826878	[A/G]	ok	2.63E-05	3.55E-06

Table 4.4. ImmunoChip SNPs which fall in *KIR3DL1*. The 30 ImmunoChip SNPs which fall in the *KIR3DL1* region according to build36/hg18, nineteen of which are significantly associated with *KIR3DL1*/*KIR3DS1* copy number (highlighted in blue). *KIR3DS1* is missing from build36/hg18. SNP rs592645 which has shown to be highly predictive of *KIR3DL1*/*KIR3DS1* copy number is highlighted in light red. The QC column reports the GenCall quality control diagnosis: ok, low call rate, failure to meet Hardy Weinberg equilibrium (hwe) or monomorphic SNP.

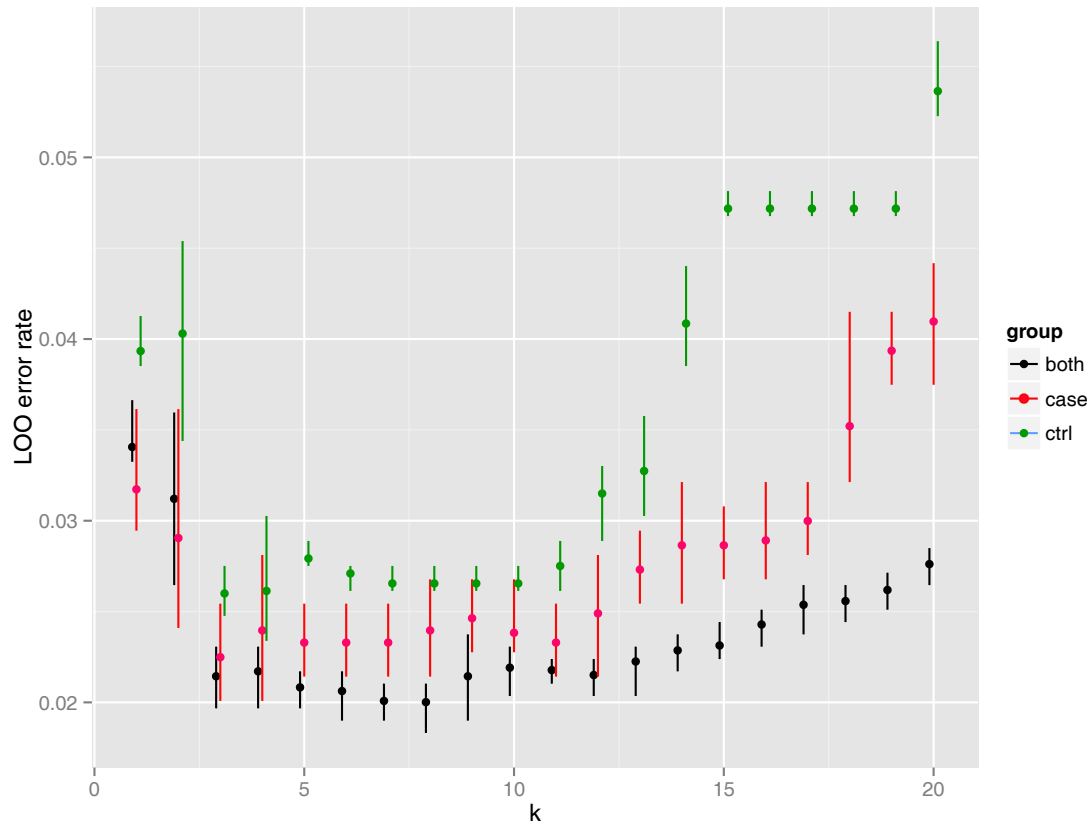


Figure 4.7. Leave-one-out crossvalidation error rate for k-nearest neighbour (KNN) prediction. Leave-one-out cross validation error rates obtained from KNN prediction of *KIR3DL1/KIR3DS1* copy numbers from the R and θ signals of SNP rs592645. Each point shows the proportion of samples for which the KNN predicted copy number did not match the qPCR call, averaged over ten multiply imputed qPCR call datasets (using the posterior probabilities from Figure 4.2). Error bars show the minimum and maximum error rates over the ten multiply imputed datasets. KNN was run in parallel for cases only, controls only and on all samples together. The minimum error rate is achieved for $k = 8$ when the prediction uses both cases and controls.

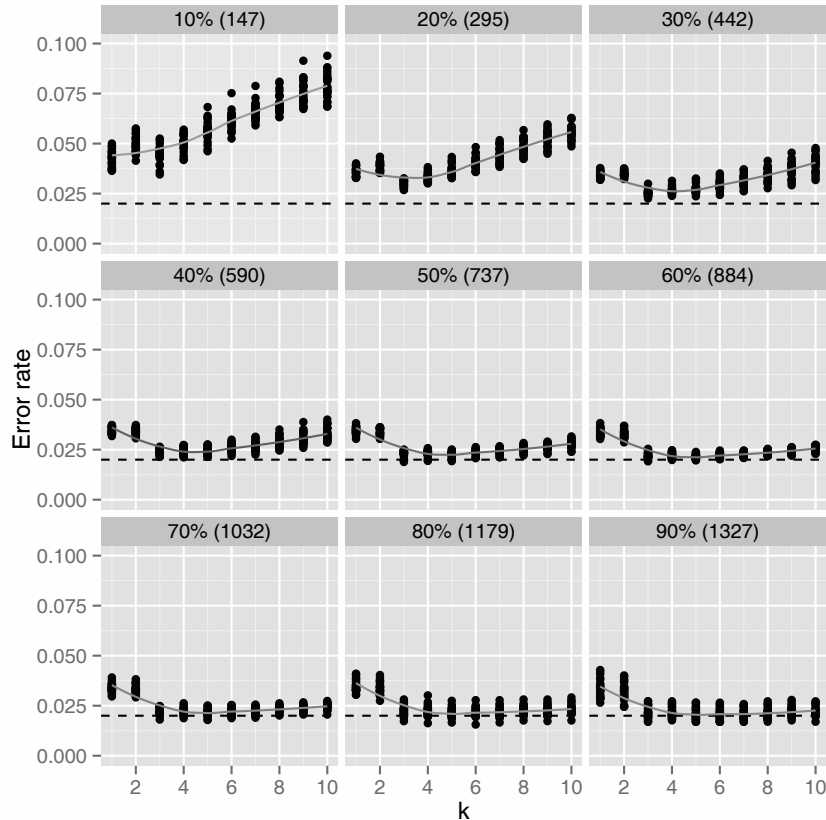


Figure 4.8. Error rate of k-nearest neighbour (KNN) prediction from R and θ of SNP rs592645 in random subset of samples. Each panel shows the LOOCV error rates of *KIR3DL1/KIR3DS1* copy number prediction from R and θ of rs592645 in the remaining unlabeled samples when using a different size subset of the training data. The percentage of the complete training data set and the size of the subset is given in the title of each panel. Each point represents the LOOCV error rate averaged over ten multiply imputed qPCR call datasets (using the posterior probabilities from Figure 4.2). Smoothing lines show the average over 25 independent random subsets of training data. The black dashed line represent the observed error rate in the complete sample. As the size of the training dataset increases the error rate becomes less sensitive to the choice of the parameter k . Only 295 samples are required to achieve LOOCV error rates $< 5\%$ and 590 for error rates $< 2.5\%$.

4.4 Association testing of *KIR3DL1*/*KIR3DS1* copy number with T1D

In calling copy number states from qPCR data, rare amplifications of three or more copies are harder to classify with certainty than more common copy number states such as zero, one, or two copies. This is mainly because copy numbers higher than two are rare but also because the ΔCt difference between successive higher copy numbers shrinks logarithmically. However dropping samples which can not be classified with certainty can lead to bias. A less biased approach is to allow for uncertainty by using posterior probabilities in the association tests (Plagnol et al, 2007).

I tested for association of T1D with the predicted copy numbers from the qPCR and SNP datasets using logistic regression. I allowed for uncertainty in the copy number call when estimating individual odds ratios by using ten multiply imputed datasets (Cordell, 2006), and averaging results over those using the R package `mitools` (Lumley, 2012).

I allowed for statistical interaction with HLA-Bw4 by repeating the association test in the subsets of carriers of the target ligand HLA-Bw4 epitopes, HLA-Bw4 for *KIR3DL1* and the putative ligand HLA-Bw4-80I for *KIR3DS1*. I directly tested for interaction with a more powerful case-only χ^2 test (Yang et al, 1999; Cordell, 2009).

Finally, I attempted to correlate *KIR3DL1*/*KIR3DS1* copy number with T1D status. I performed an ANOVA χ^2 test on the logistic model using the most likely copy number group, which yielded a p-value of 0.9776 in the qPCR and 0.1739 in the SNP dataset, thus showing no overall association. I also used multiple imputation to assess the effect of individual copy number groups while allowing for the uncertainty in copy number calling. I found no significant evidence for association, in the qPCR data (747 cases and 727 controls) nor in the extended SNP data (6744 cases and 5362 controls) (Table 4.5). By expanding to these large samples, which would be infeasible to genotype directly

with qPCR, I am able to exclude odds ratios outside of the range [.92; 1.08] for the common copy number groups with 95 % certainty.

I also repeated the association tests in the subset of individuals carriers of the HLA-Bw4 epitope, and again detected no significant association (Table 4.6). A disadvantage of subsetting by HLA-Bw4 is that power is lost by greatly reducing the sample size. A more powerful test for interaction between unlinked genes is a case-only test (Yang et al, 1999). If there were an interaction effect between *KIR3DL1*/*KIR3DS1* and HLA-Bw4 then this should be detectable as a difference in *KIR3DL1*/*KIR3DS1* copy number frequencies across HLA-Bw4 strata in the cases. However, I found no significant difference in either the qPCR or SNP data sets, before or after reducing the degrees of freedom by collapsing the KIR copy number to present/absent to increase power (Table 4.7).

a)	<i>KIR3DS1-KIR3DL1</i>	qPCR					SNP				
		case:control	total	OR	95%CI	p-value	case:control	total	OR	95%CI	p-value
	0-2	444:446	890	1.00			4094:3222	7316	1		
	1-1	229:207	436	1.11	0.88-1.40	0.3673	2050:1628	3678	0.99	0.92-1.07	0.8349
	2-0	26:28	54	0.92	0.52-1.61	0.7713	229:225	454	0.79	0.65-0.96	0.0193
	2-1	15:16	31	0.94	0.46-1.93	0.8695	121:101	222	0.92	0.7-1.2	0.5246
	1-2	13:14	27	0.93	0.43-2.01	0.8587	98:74	172	1.04	0.77-1.42	0.7822
	0-1	13:11	24	1.19	0.53-2.68	0.6794	116:77	193	1.19	0.89-1.59	0.2535
	1-0	4:3	7	1.34	0.30-6.02	0.7031	25:21	46	0.94	0.52-1.68	0.8255
	3-0	3:2	5	1.52	0.27-8.62	0.6369	11:14	25	0.74	0.3-1.82	0.518
Overall		747:727	1474			0.9842	6744:5362	12106			0.3552

b)	<i>KIR3DL1</i>	qPCR					SNP				
		case:control	total	OR	95%CI	p-value	case:control	total	OR	95%CI	p-value
	2	457:460	917	1.00			4192:3296	7488	1		
	1	257:234	491	1.11	0.89-1.38	0.3702	2287:1806	4093	0.99	0.92-1.07	0.8883
	0	33:33	66	1.01	0.61-1.66	0.9795	265:260	525	0.8	0.67-0.96	0.0151
Overall		747:727	1474			0.6651	6744:5362	12106			0.0506

c)	<i>KIR3DS1</i>	qPCR					SNP				
		case:control	total	OR	95%CI	p-value	case:control	total	OR	95%CI	p-value
	0	457:457	914	1.00			4210:3299	7509	1		
	1	246:224	470	1.10	0.88-1.37	0.4096	2173:1723	3896	0.99	0.91-1.07	0.7785
	2	41:44	85	0.94	0.60-1.47	0.7787	350:326	676	0.83	0.71-0.97	0.0212
	3	3:2	5	1.24	0.21-7.28	0.8084	11:14	25	0.74	0.3-1.82	0.5119
Overall		747:727	1474			0.8044	6744:5362	12106			0.1494

Table 4.5. Association test of *KIR3DS1-KIR3DL1* copy number with T1D. Association with T1D tested for the joint *KIR3DS1-KIR3DL1* (a), marginal *KIR3DL1* (b) and *KIR3DS1* (c) copy number group. No evidence of a significant, joint or marginal, effect detected in the qPCR dataset, 747 cases and 727 controls, nor in the SNP dataset, 6744 cases and 5362 controls. Case-control counts shown are derived from the most likely copy number assignment across the 10 multiply imputed qPCR and SNP datasets. Statistical inference for association is derived from the multiply imputed datasets using the R package *mitools* (Lumley, 2012). The last row of each table contains the pooled p-value for each association test using the R package *mice* (van Buuren and Groothuis-Oudshoorn, 2011).

	<i>KIR3DS1-KIR3DL1</i>	qPCR					SNP				
		case:control	total	OR	95%CI	p-value	case:control	total	OR	95%CI	p-value
a) HLA-Bw4 subset	0-2	259:286	545	1.00			1025:1156	2181	1.00		
	1-1	123:128	251	1.06	0.79-1.43	0.6976	556:583	1139	1.08	0.93-1.24	0.3194
	2-0	16:15	31	1.22	0.58-2.57	0.5985	61:87	148	0.79	0.56-1.11	0.1733
	2-1	7:13	20	0.59	0.23-1.51	0.2754	32:40	72	0.90	0.56-1.45	0.6695
	1-2	8:8	16	1.10	0.41-2.98	0.8450	27:32	59	0.95	0.57-1.60	0.8513
	0-1	10:7	17	1.58	0.59-4.20	0.3621	36:26	62	1.56	0.94-2.60	0.0876
	1-0	2:1	3	2.21	0.20-24.50	0.5187	7:3	10	2.63	0.68-10.19	0.1614
	3-0	3:0	3				3:1	4	3.38	0.35-32.51	0.2910
		428:458	886				1747:1928	3675			
b) HLA-Bw4 subset	<i>KIR3DL1</i>	qPCR					SNP				
	2	case:control	total	OR	95%CI	p-value	case:control	total	OR	95%CI	p-value
	2	267:294	561	1.00			1052:1188	2240	1.00		
	1	140:148	288	1.04	0.78-1.38	0.7787	624:649	1273	1.09	0.95-1.25	0.2414
	0	21:16	37	1.45	0.74-2.83	0.2822	71:91	162	0.88	0.64-1.21	0.4399
		428:458	886				1747:1928	3675			
c) HLA-Bw4-80I subset	<i>KIR3DS1</i>	qPCR					SNP				
	0	case:control	total	OR	95%CI	p-value	case:control	total	OR	95%CI	p-value
	0	159:187	346	1.00			650:734	1384	1.00		
	1	93:83	176	1.32	0.92-1.90	0.1370	384:365	749	1.19	0.99-1.42	0.0578
	2	12:14	26	1.01	0.45-2.24	0.9842	61:75	136	0.92	0.64-1.31	0.6376
	3	2:0	2				1:0	1			
		266:284	550				1096:1174	2270			

Table 4.6. Association test of *KIR3DS1-KIR3DL1* copy number with T1D, conditional on HLA-Bw4. In order to test whether *KIR3DL1/KIR3DS1* is associated with T1D risk conditional on the presence of the respective the HLA-Bw4 epitope, association with T1D is tested in the subset of individuals carriers of an HLA-Bw4 epitope for the joint *KIR3DS1/KIR3DL1* (a) and marginal *KIR3DL1* (b) copy number groups and, also tested in the subset of individuals carriers of HLA-Bw4-80I for the marginal *KIR3DS1* (c) copy number group.

		qPCR		SNP	
		HLA-Bw4-	HLA-Bw4+	HLA-Bw4-	HLA-Bw4+
KIR3DS1-	KIR3DL1+	183	269	739	1063
KIR3DS1+	KIR3DL1-	12	21	40	71
KIR3DS1+	KIR3DL1+	113	138	396	613
		p-value = 0.4094		p-value = 0.4235	
b)		qPCR		SNP	
		HLA-Bw4-	HLA-Bw4+	HLA-Bw4-	HLA-Bw4+
KIR3DL1-		12	21	40	71
KIR3DL1+		296	407	1135	1676
		p-value = 0.5144		p-value = 0.3609	
c)		qPCR		SNP	
		HLA-Bw4-80I-	HLA-Bw4-80I+	HLA-Bw4-80I-	HLA-Bw4-80I+
KIR3DS1-		293	159	1153	649
KIR3DS1+		159	107	673	447
		p-value = 0.4922		p-value = 0.0353	

Table 4.7. Case-only χ^2 test for interaction between *KIR3DS1*-*KIR3DL1* copy number and HLA-Bw4, across the ten multiply imputed qPCR and SNP datasets. Counts in each contingency table are derived from the most likely copy number assignment across the multiply imputed datasets. To reduce the degrees of freedom and improve power, I summarise copy numbers higher or equal to one by presence (+) and zero by absence (-). The pooled p-value of each χ^2 test, across the multiply imputed datasets, is given in the last row of each contingency table. I find no significant association with HLA-Bw4, within cases, in either the joint (a) or the marginal (b)(c) *KIR3DS1*-*KIR3DL1* distributions.

4.5 Discussion

4.5.1 Previous association studies of KIR genes with T1D

So far, case-control studies using PCR in different ethnicities have looked at whether the presence or absence of KIR genes but not the copy number are associated with T1D (van der Slik et al, 2003, 2007; Nikitina-Zake et al, 2004; Santin et al, 2006; Middleton et al, 2006; Park et al, 2006; Mogami et al, 2007; Shastry et al, 2008; Jobim et al, 2010; Zhi et al, 2011). These, however, represent an incomplete version of the KIR genotype because, as shown by Jiang et al (2012), a considerable portion of the diversity in the KIR haplotypes arises from copy number variation. Although presence/absence might have a stronger effect than copy number variation.

From the studies I know of, as summarised in Tables 4.8 and 4.9, only two have reported individual KIR genes to be associated with T1D independently of HLA. First Nikitina-Zake et al (2004), reported that *KIR2DS2*/*KIR2DL2* were both more frequent in cases ($n = 98$) than in controls ($n = 100$) in the Latvian population. Then Park et al (2006), reported that *KIR2DS2* and *KIR2DL5* were both significantly associated in the South Korean population, but that the *KIR2DS2* was instead less present in cases than in controls. They also found that *KIR2DL5* was significantly more frequent in cases than in controls. In an independent study, Ramos-Lopez et al (2009) attempted to confirm the association of *KIR2DL2* in German and Belgian families, by a transmission test of rs2756923, a SNP in exon 8 of the *KIR2DL2* gene. They found that there was over-transmission of the G allele of rs2756923 in T1D.

However, a number of issues surrounding these studies cast some doubt on the results. Firstly, as pointed out by Middleton et al (2006), the difference in frequency between *KIR2DS2* and *KIR2DL2*, two genes which are normally in high linkage disequilibrium (Single et al, 2007), is suspiciously large in both the Latvian study, 53% vs 81%, and in

the South Korean study, 20% vs 46% (Table 4.8). Secondly, in the Ramos-Lopez et al (2009) German/Belgian study, rs2756923 is not in Hardy-Weinberg Equilibrium (HWE). Both these issues are possibly linked to genotyping errors due to differences in primer sequences. Thirdly, rs2756923 has since disappeared from the current genome build, which leads us to think that rs2756923 may not in fact tag *KIR2DL2* or at least not all isoforms of that gene. Finally, this KIR association has not been replicated in other populations including Dutch (van der Slik et al, 2003), Finnish (Middleton et al, 2006), Basque (Santin et al, 2006), Japanese (Mogami et al, 2007), South Brazilian (Jobim et al, 2010) and Chinese Han (Zhi et al, 2011) (Tables 4.8 and 4.9).

	Study	Pop	cases	controls			
1	van der Slik et al (2003)	Dutch	149	207			
2	Nikitina-Zake et al (2004)	Latvian	98	100			
3	Middleton et al (2006)	Finnish	137	101			
4	Santin et al (2006)	Basque	76	71			
5	Park et al (2006)	South Korean	139	132			
6	Mogami et al (2007)	Japanese	204	240			
7	van der Slik et al (2007)	Dutch	275	215			
8	Shastry et al (2008)	Latvian	98	70			
9	Ramos-Lopez et al (2009)	Belgian	394	401			
10	Ramos-Lopez et al (2009)	German	380	315			
11	Jobim et al (2010)	South Brazilian	248	250			
12	Zhi et al (2011)	Chinese Han	259	262			
13	Mehers et al (2011)	British	551	168			
14	Pontikos et al (2014)	British	6744	5362			
Study	2DL1	2DL2	2DL3	2DL4	2DL5	2DS1	2DS2
1	94.6:97.6	55.7:48.4	91.9:92.3		50.3:46.9	36.2:35.7	55.7:47.8
2	95:98	81:32	86:91	98:100	65:55	43:27	53:25
3	97.1:100	35:41.6	94.9:96		46:55.4	43.1:48.5	38.7:41.6
4	97:98	52:62	93:95		49:66	48:54	52:63
5	99.3:100	46:34.8	98.6:98.5	97.8:97.7	42.4:84.1	33.8:43.9	20.1:47
6	98.8:98.5	15.4:13.7	98.8:99	100:100	40.8:34.8	40.8:35.8	15.4:13.7
7						41.1:35.8	53.5:48.8
8		82.65:32			66.32:55	43.87:27	54.08:25
11	95.6:97.6	49.2:54.4	87.9:86.4	99.2:100	56:49.6	46.4:36.4	52.8:53.6
12	93.82:96.56	28.19:32.44	98.46:99.62		40.15:42.37	37.84:37.4	28.96:30.92
13	97.9:100	52.8:53.6	94.2:90.5		54.1:56.5	42.9:41.7	52.8:53.6
14							
Study	2DS3	2DS4	2DS5	3DL1	3DL2	3DL3	3DS1
1	24.8:27.1	40.9:42	32.9:27.1	96:96.1			38.9:33.3
2	35:19	94:92	29:22	92:94	98:100	98:100	40:27
3	18.2:23.8	92.7:94.1		92.7:93.1			40.1:49.5
4	24:25	80:85	35:43	89:90			53:63
5	10.1:9.8	96.4:96.2	22.3:33.3	96.4:96.2	97.8:98.5	96.4:99.2	36:37.1
6	9.6:9.8	87.1:85.3	34.6:30.8	99.6:100	99.6:99.5	100:100	44.1:36.8
7							40.4:34
8	35.71:19						40.81:27
11	33.9:33.2	85.2:95.2	37.1:34	95.2:97.6	100:100	100:100	47.6:42.4
12	11.58:12.98	92.66:93.13	27.03:27.1	93.05:95.42			36.29:35.5
13	30.5:33.3	95.7:94.6	34.5:34.5	96.4:95.2		100:100	44.9:44
14				96.07:95.15			37.6:38.47

Table 4.8. Proportion of cases to controls in all known KIR studies in T1D. Study 14 is the study presented in this chapter. Table cells highlighted in gray are the ones which report a significant association.

Study	Pop	cases	controls	2DL1	2DL2	2DL3	2DL4	2DL5	2DS1	2DS2	2DS3	2DS4	2DS5	3DL1	3DL2	3DL3	3DS1
1 van der Slik et al (2003)	Dutch	149	207	0.97	1.15	1	1.07	1.01	1.17	0.92	0.97	1.21	1	1.17			
2 Nikitina-Zake et al (2004)	Larvian	98	100	0.97	2.53	0.95	0.98	1.18	1.59	2.12	0.84	1.02	1.32	0.98	0.98	1.48	
3 Middleton et al (2006)	Finnish	137	101	0.97	0.84	0.99	0.83	0.89	0.93	0.76	0.96	0.94	1			0.81	
4 Saatin et al (2006)	Basque	76	71	0.99	0.84	0.98	0.74	0.89	0.83	0.96	0.94	0.81	0.99			0.84	
5 Park et al (2006)	South Korean	139	132	0.99	1.32	1	1	0.5	0.77	0.43	1.03	1	0.67	1	0.99	0.97	0.97
6 Mogami et al (2007)	Japanese	204	240	1	1.12	1	1	1.17	1.12	0.98	1.02	1.12	1	1	1	1	1.2
7 van der Slik et al (2007)	Dutch	275	215		2.58				1.15	1.1							1.19
8 Shastry et al (2008)	Larvian	98	70	0.98	0.9	1.02	0.99	1.21	1.62	2.16	1.88						1.51
9 Jobim et al (2010)	South Brazilian	248	250	0.98	0.97	0.99	0.99	1.13	1.27	0.99	1.02	0.89	1.09	0.98	1	1	1.12
10 Zhi et al (2011)	Chinese Han	259	262	0.97	0.87	0.99	0.95	1.01	0.94	0.89	0.99	1	0.98				1.02
11 Mehers et al (2011)	British	551	168	0.98	0.99	1.04	0.96	1.03	0.99	0.92	1.01	1	1.01	1	1	1	1.02
12 Pontikos et al (2014)	British	6744	5362														0.98

Table 4.9. Case-control ratio in all known KIR studies in T1D. KIR studies in T1D. Study 14 is the study presented in this chapter. The case-control ratio is given per KIR gene. Table cells highlighted in gray are the ones which report a significant association.

Nonetheless, some of these KIR studies do report conditional association when they conduct subset analysis by grouping by age, HLA genotype or by grouping into activating or inhibiting composite KIR-HLA genotypes (Carrington et al, 2005; van der Slik et al, 2007). For example, van der Slik et al (2003) report association with *KIR2DS2* in the HLA-C1, *HLA-DQ2/HLA-DQ8* (high risk) subset of the Dutch cohort. Jobim et al (2010) report association with *KIR2DL1* in the HLA-C2 subset of the South Brazilian cohort. In the Chinese Han cohort, Zhi et al (2011) report association with *KIR2DL3* in the HLA-C1 subset. In the Japanese cohort, Mogami et al (2007) find association in the adult-onset diabetes subset (age of onset older than 35 years) after assignment into three KIR-HLA activation groups as defined by Carrington et al (2005). Mehers et al (2011) find association with *KIR2DS2/KIR2DL2* and *KIR2DL3* in the early-onset (less than 5 years old), HLA-C1 subset of the UK cohort.

Of concern in these analyses is that, as the starting samples are small (no more than 300 individuals), further subsetting and testing for multiple hypotheses (presence/absence of up to seventeen KIR genes) is likely to lead to false positives (Wittes, 2009).

Also since the HLA region is known to be associated with T1D it is difficult to tell whether the KIR-HLA interaction is significant, independently of HLA. In fact, these studies only control for HLA Class II and have not checked whether the effect is actually driven by other HLA Class I risk factors. Furthermore, it is unclear whether the established biological interaction between KIR and HLA should translate into the statistical KIR-HLA interaction claimed in those studies. As HLA-C is significantly associated with T1D before controlling for HLA Class II and HLA-B (Nejentsev et al, 2007; Howson et al, 2009), careful interaction analysis such as case-only tests (Yang et al, 1999; Cordell, 2009) are required to assess whether there is a significant epistatic KIR-HLA effect or if the reported associations to T1D are only driven by HLA-C or some other latent HLA risk factor.

4.5.2 My approach

As discussed, regions with great allelic and copy number variation are difficult to properly assess using genome-wide SNP arrays. While these arrays are typically cost effective ways to assay common genetic variation, very polymorphic regions can make the design of SNP probes difficult or impossible, which has contributed to low SNP coverage in the KIR region on most kinds of SNP arrays. The SNPs that do exist on arrays, such as ImmunoChip, are often discarded during the QC phase of any GWAS because they do not exhibit the expected three clusters. In contrast, assaying individual genes by other methods can prove expensive. For example, the qPCR assays used here to target *KIR3DL1* and *KIR3DS1* cost £12 per sample.

Our hybrid approach, the key steps of which are summarised in Figure 4.9, allowed us to perform the largest study (twenty-fold) of *KIR3DL1*/*KIR3DS1* copy number in T1D to date. In 12,106 samples, I found no association of *KIR3DS1*-*KIR3DL1* copy number with T1D, alone or conditional on presence of the HLA-Bw4 epitope. Our results suggest that, despite the association of certain HLA-A and HLA-B alleles with T1D and the established biological interaction between HLA-Bw4 and *KIR3DL1*, copy number variation in *KIR3DL1*/*KIR3DS1* is unlikely to have a significant effect on the risk of developing T1D.

Other KIR genes that are in high Linkage Disequilibrium (LD) with *KIR3DL1* and *KIR3DS1* are also unlikely to be associated. According to the Allele Frequency Net database (Gonzalez-Galarza et al, 2011), these include *KIR2DS4* (97 %) and *KIR2DL3* (86 %), for *KIR3DL1* and, *KIR2DL5* (81 %), *KIR2DS5* (84 %) and *KIR2DS1* (92 %), for *KIR3DS1* (<http://www.allelefrequencies.net/kir6010a.asp>). Thus, copy number variation in *KIR3DL1*/*KIR3DS1* or neighbouring genes is unlikely to be an important risk factor in T1D.

In order to better understand why rs592645 is the best available SNP for predicting

copy number variation in *KIR3DL1*/*KIR3DS1*, I used BLAT (Kent, 2002) to match the probe sequences of rs592645 on ImmunoChip against the allelic sequences of all KIR genes available from the Immuno Polymorphism Database (Robinson et al, 2010). Interestingly, I found that the SNP probes do not target *KIR3DL1*/*KIR3DS1* but instead bind uniquely to *KIR2DL4*, a neighbouring framework gene. Examining the *KIR2DL4* alleles matched by the rs592645 probes, I discovered, thanks to James Traherne, that the SNP probes are in fact picking up copy number variation of *KIR2DL4*005*, an allele of *KIR2DL4* that undergoes copy number variation along with *KIR3DL1*/*KIR3DS1* (Gómez-Lozano et al, 2005). This explains the small but persistent misclassification error rate of 2 % since our imputation is based on linkage disequilibrium between rs592645 and *KIR3DL1*/*KIR3DS1* rather than on perfect discrimination between our target genes.

4.5.3 Future work

I expect that, eventually, fully sequenced KIR haplotypes will be available in a large number of individuals. In order to improve our chances of correct assembly, long reads will be required to deal with the great sequence similarity in this region. According to a collaborator James Traherne, sequencing would require amplification of the polymorphic exons using locus-specific primers and sequencing of the barcoded products. This would necessitate read lengths of at least 300 base pairs to span the exons. The cost of this using Roche 454 has been estimated to be of approximately £30 per sample.

Until KIR sequencing becomes sufficiently cheap, hybrid methods combining allele typing techniques such as qPCR in a subset of samples, with SNP typing in a larger cohort, are likely to remain the most cost-effective approach for large scale analysis. This method could also be applied to other allele typing techniques such as pyrosequencing (Norman et al, 2009) or sequence-specific oligo hybridisation (Martin et al, 2007). Another alternative to using raw SNP signal would be to use tagging SNP as has been done

in HLA imputation by Leslie et al (2008) and Dilthey et al (2013) at Oxford University. In this approach, copy number is correlated with the genotype of flanking SNPs instead of raw SNP signals, as in my approach. However, from a seminar I attended on the 1st of November 2014, the speaker, the same Stephen Leslie of Leslie et al (2008) now at the Murdoch Childrens Research Institute in Australia, stated that the tagging approach, built on a Hidden Markov Model with positional information, that has successfully been applied to HLA imputation, performs poorly for KIR imputation. The reason for this, claimed Stephen Leslie, is due to the unreliable positional information and unknown patterns of SNP LD in the region. Instead, Stephen Leslie and Damjan Vukcevic, found that training a Random Forests (RF) algorithm, which does not use positional information, on 300 SNPs taken on either side of the KIR region, performs better in the prediction of common KIR gene copy numbers. However, performance remains poor for rarer copy numbers or KIR alleles for which there is insufficient training data available. Furthermore, because of the high degree of homology between certain KIR genes, the ambiguity in their definition can lead to mislabelling of the training data in the reference panel. However Stephen Leslie did mention that my approach of using signal intensities instead of genotype calls could improve on performance, given that the genotype calls are often highly unreliable, most failing HWE. They intend to submit a manuscript in the coming months.

As discussed, hybrid qPCR/SNP approaches are particularly suited to the large case-control cohorts genotyped on ImmunoChip, since the platform contains numerous SNPs in the KIR region (Nikula et al, 2005). In fact in our dataset, I have observed other SNPs in KIR with more than three clusters which may correlate with copy number of other KIR genes and, given the availability of qPCR data, could be imputable in a similar manner. One possible improvement to my method, in order to achieve better prediction rate at smaller samples sizes (as suggested in Figure 4.8), would be to preferentially select

samples to qPCR from smaller SNP clouds, since these are more likely to correlate with rarer copy number groups (for example the 3-0 group in Figure 4.5).

I would recommend that this approach be adopted in KIR association studies which have so far been hindered by small sample sizes (Table 4.9). But it could also be applied more generally to other genes in non-genotypable chromosome regions of similar common copy number variation and sequence complexity as KIR, in order to leverage existing SNP datasets.

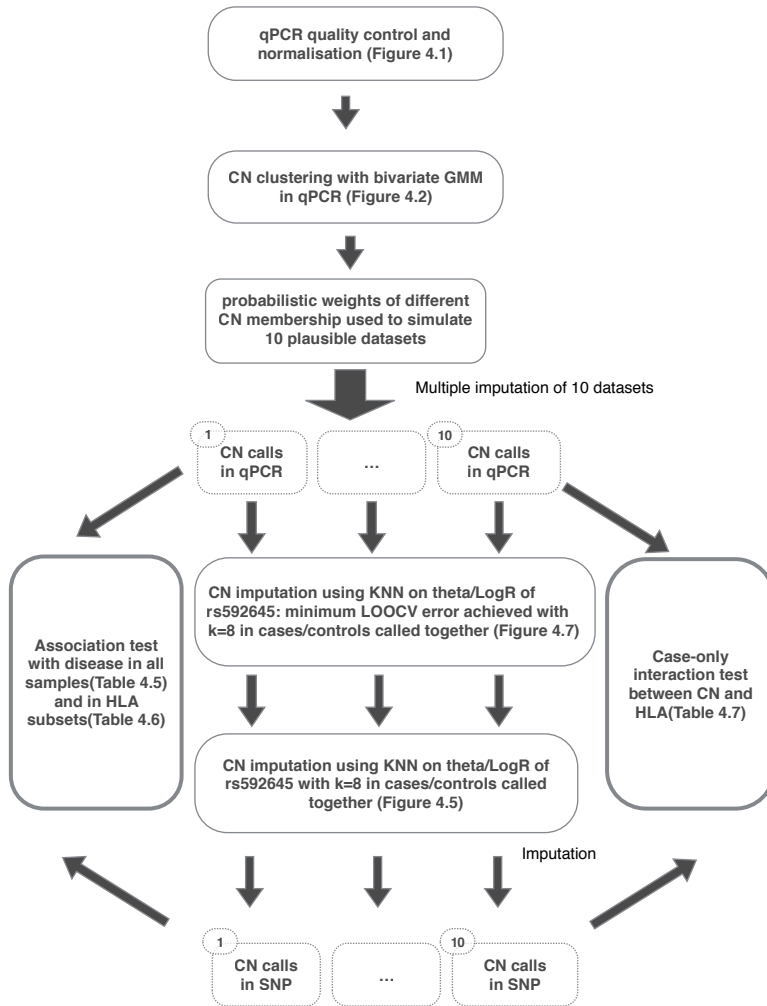


Figure 4.9. Flow chart summarising the key steps involved in the KNN imputation of *KIR3DL1*/*KIR3DS1* copy number in SNP data (R and θ signal) from qPCR copy number predictions obtained from GMM clustering. GMMs clustering of the qPCR data assigns to each sample a posterior probability of belonging to each Copy Number (CN) group. Using these probabilities I can allow for the uncertainty of the CN calling when testing for association with disease by using multiple imputation. Multiple imputation involves the simulation of datasets (in this case, ten) from the probabilities returned by the GMM. I find that the SNP rs592645 and $k=8$ minimises the LOOCV error rate. Association tests are conducted on each imputed dataset and inference combined using methods in the R package mice (van Buuren and Groothuis-Oudshoorn, 2011).

Chapter 5

Discussion

*L'avenir n'e
mettre en ordre, tu n'as pas à le
prévoir, mais à le rendre po*

Throughout my thesis I have considered, normalisation and clustering methods for computationally analysing flow cytometry and genetic datasets in order to characterise the immune cell types and the genetic variants which could influence T1D risk. These methods have the potential to be more efficient, formal, consistent, objective and generally better at dealing with uncertainty than manual analysis. Consequently they could lead to more powerful statistical association testing.

5.1 Challenges in automation of flow gating

The methods discussed in this thesis suggest that there are many scenarios in which flow cytometry analysis can be automated. There are, however, a number of outstanding challenges, some technical, some methodological and some even philosophical, in applying these methods.

5.1.1 Performance: compute time and memory usage

While the applications that have been studied in this thesis do not require real-time analysis, there are still practical limitations on the amount of memory and compute time demands. It is well known in computer science that these resources can be interchangeable. For clustering, methods which rely on global knowledge of the data, such as computation of the complete pairwise distance matrix, have a large initial memory footprint (data matrix of size $\frac{N \times (N-1)}{2}$), but only require one pass of the data. A solution to the clustering solution is reached within just a few computational steps, by for instance, selecting a distance cut threshold on the dendrogram, built from hierarchical clustering, in order to define K clusters. On the other hand, methods like K-means necessitate a much smaller memory footprint since they only compute the distance of every point to the K cluster means (data matrix of size $N \times K$, where typically $K \ll N$), however, several updates of the matrix are required until the cluster centers are fixed. The choice of which method to apply is very much dependent on the dataset. For ungated flow cytometry, data matrices contain over a million rows, so the complete pairwise distance matrix is too large to fit in memory. I found that for the default R implementation, the maximum allocatable vector size is 1672.4 Gb, hence the distance matrix computation was only feasible in subsets of the order of 10000, such as the CD4⁺ lymphocyte subset, or data downsampled using the SPADE or RPART approaches in Chapter 3. The data downsampling performed by SPADE, relies on first estimating the local density at each point and then preferentially thinning the data in regions of high density in order to even out the density across the whole sample. The local density estimation step is itself computationally intensive since it needs to consider the distance from a single point to all other points in the sample to find the number of points lying within a certain radius. I found this step could be greatly sped up with Approximate-Nearest-Neighbour (ANN) which uses the K dimensional trees (KD tree) lookup method. KD-trees are a space-

partitioning data structure for organising points in a k-dimensional space, making for an efficient way of storing a high-dimensional dataset to lookup proximal datapoints. In theory, this approach could also be used to reduce the number of datapoints considered when applying mixture models to large datasets (McLachlan and Peel, 2004).

5.1.2 Consistency

Consistency can be defined as the variation in a method's output in relation to its input. If a clustering algorithm is consistent, one would expect that small perturbations to the data would lead to small changes in the clustering outcome. However, algorithms which rely on initialisation using random starting positions, such as K-means, can reach different clustering solutions, even when rerun on the same data. To guard against this when running K-means, initial cluster centers can be specified or the algorithm can be run with multiple restarts in order to increase the chances of finding a globally optimal solution. As I will discuss later, a relatively small number of outlier events which occur commonly within a flow cytometry experiment, due to cells clumping together or debris, can also be detrimental to consistency; it follows that automated gating algorithms need to be robust to these.

5.1.3 Accuracy

When labelled data is available, the accuracy of a method is defined based on how frequently a method assigns the correct label. Estimating accuracy relies on the existence of a test dataset, typically labelled using manual analysis or some other method. In Chapter 2, I assessed accuracy by comparing the cluster proportions and means with those obtained from manual gating. In Chapter 4, I used qPCR labelled data to assess the prediction accuracy of the KNN classifier. However, labelled data may not always be available, especially in the case of flow cytometry data. In addition, in the context

of flow cytometry, even when labelled data is available, this approach may not always be ideal, as it is merely comparing the relative agreement between methods rather than the objective truth. A more useful alternative may be instead to assess the prediction accuracy with clinical outcome, case-control status or genotype, or to maximise reproducibility in repeated independent samples from the same individual under the same conditions.

5.1.4 Interpretability

While an automated method might be accurate and consistent, it may be difficult to interpret the results. Improving the accuracy of a model by adding parameters can obfuscate the relationship between the input parameters and the clustering output. Random Forests (RF) and neural networks are examples of methods from which it is difficult to extract an interpretable model to justify the result. This is an issue because as part of the iterative process of knowledge discovery, it is important to understand which combination of features make objects distinguishable.

5.1.5 Choice of transformation

Flow cytometry, and fluorescence data in general, tend to be highly positively skewed. This is problematic because most clustering algorithms assume constant variance across the data range. While the skewness can be reduced by the means of transforms based on the logarithm function, care needs to be taken as these influence the modality of lower intensity populations, especially those which overlap into the negative range, as illustrated in Figure 1.5. Certain flow cytometry packages, such as the R package `curvHDR` (Luta et al, 2011) erroneously apply an arcinsh transform, however such a function introduces a split in the data density around zero, giving rise to spurious cell populations. In FlowJo, the transform can be customised visually by the manual gater, given the

knowledge of what cell populations to expect. The only existing automated methods of optimally selecting a transform that I am aware of are the R packages `flowTrans` and `flowClust` (Finak et al, 2010a; Lo et al, 2009). `flowTrans` assumes an underlying Gaussian distribution and uses Maximum Likelihood (ML) to estimate the optimal transform parameter. `flowClust` applies a Box-Cox transform for which the lambda parameter, the exponent of the transform, is estimated using ML. Nonetheless, as I discussed in Chapter 1 and showed in Figure 1.5, it is not always clear what transform to apply and, I would argue, aiming for a Gaussian distribution is a suboptimal criterion given the multimodality of the data. When the number of populations is unknown, one approach could be to estimate the transformation parameter as part of the clustering process.

5.1.6 Visualisation of higher dimensional datasets

Visual inspection is a fundamental tool for quality control, discovery of data features like skewness or symmetry, looking for patterns, gene lists appearing in pathways, confirming clustering results, spotting outliers. While visualisation works well for up to three dimensional data, information is lost when higher dimensional datasets are decomposed into a series of two-dimensional projections. Clusters which exist in higher dimensions do not necessarily map to clusters in two dimensions.

Open repositories such as Cytobank¹ and FlowRepository² (Spidlen et al, 2012) are encouraging researchers to share their annotated flow cytometry experiments along with their publications. By combining data across experiments, both the number of samples and parameters measured are increasing, although care must be taken to avoid confounding by batch effects. Also an upcoming biotechnology, time of flight cytometry (CyTOF), which combines mass spectrometry with cytometry, will push the number of markers which can be measured by experiment up to 34 and potentially higher. At the Gary

¹<https://www.cytobank.org/>

²<http://flowrepository.org/>

Nolan lab in Stanford, and the Cancer Research Institute in the UK, mass cytometry is being adopted to analyse cell heterogeneity in cancer. The analysis of datasets generated by this technology benefits greatly from the multidimensional visualisation techniques such as SPADE (Qiu et al, 2011) and visual Stochastic Neighbour Embedding (viSNE) (Amir et al, 2013). In Chapter 3, I presented one of these approaches, SPADE, which relies on a network visualisation of a dataset using a minimum spanning tree. viSNE is a more probabilistic approach which uses stochastic neighbour embedding. Visualising high-dimensional data using network representations is only informative if the number of datapoints is relatively small. In flow cytometry, some clustering or binning of the data is applied to reduce the number of points.

5.1.7 Ascertaining the number of clusters

Certain transformations can facilitate the clustering task, however the challenge remains to determine the number of clusters, K , in a particular dataset. This is an unsolved statistical problem, although a variety of approaches exist.

In univariate data, a sliding window approach can be used to estimate the number of modes/peaks. The number of peaks returned is influenced by the span of the sliding window. A large window span will tend to oversmooth the data, leading to fewer peaks while with a smaller window the number of peaks called will increase, but so will the chances of picking up spurious peaks. The number of clusters is controlled by the window span parameter, however the exact relationship between this parameter and the number of clusters returned is data dependent.

One approach to estimating K is to start with an upper bound for K and then merge clusters together, as can be done with R package `flowMerge` (Finak and Gottardo, 2011). Another approach would be to select a K that gave consistent clustering results across samples. However, finding such a K across clusters is not always possible due to sampling

variation. In particular, rare clusters may only be visible when a sample is sufficiently large, and so may not be consistently identifiable across all samples. In genetics for example, when genotyping low minor allele frequency variants, large samples sizes are required for homozygous individuals to be included. In order to distinguish such rare subsets from noise, strong supporting evidence is required. As illustrated in Chapter 4 on qPCR data, prior evidence from Jiang et al (2012) supports the existence of the rare 3-0 *KIR3DS1-KIR3DL1* copy number group at that sample size. In hindsight, the expected copy number group frequencies obtained from Jiang et al (2012) could have been used as prior group frequencies for all copy number groups in the clustering of the qPCR data. The prior information obtained from the qPCR dataset, was then used as training data in the next step of the analysis, in order to identify clusters predictive of *KIR3DS1-KIR3DL1* copy number in the SNP dataset.

However, prior evidence yields information about a cluster's expected proportion but little about its exact position and shape, which are usually experiment specific. This can be due to the reliability of the instrumentation and sample preparation, but also due to the stability of the biological sample; DNA variation changes can be seen over many human generations, while variations in cell protein expression and cell populations fluctuate at a much shorter time scale.

Generally, in order for clusters to emerge, the number of events collected should be increased when possible, but this may also increase the within sample noise.

5.1.8 Within sample noise

In flow cytometry, scatter channels for example, include many spurious events due to debris and cells clumping together creating doublets. In fact, there are many technical and biological artefacts, in flow cytometry, which can lead to spurious clusters or outliers. This is a problem because any clustering method or statistical test which relies on

estimating a mean is potentially sensitive to outliers.

The approach taken in top-down hierarchical manual gating is to filter out these datapoints. Automatic filtering of outliers usually relies on density estimation in order to exclude low density points from belonging to any cluster, as implemented in methods such as SPADE (Qiu et al, 2011).

An alternative solution, which does not rely on filtering, is to define, one or more background clusters to account for data points which are not part of the study. Certain model-based methods do this already by defining a background mixture with a covariance defined on the entire sample which essentially "mops up" all points which are not assigned with high posterior weight to any of the known components. The R package **mclust** (Chris Fraley and Scrucca, 2012), allows one to define a noise component with an expected frequency.

Another approach to filtering outliers, as adopted by the R package **flowClust** (Lo et al, 2009), is to downweight the effect of outliers on the parameter estimation of the mixture model by defining an "outlyingness" parameter which is inversely proportional to the Mahalanobis distance from a point to a cluster centre. Since the Mahalanobis distance from a point to a group of points is scaled by the covariance matrix, the distance is smaller to wider clusters than to tighter clusters:

$$(\mathbf{x}_i - \boldsymbol{\mu})^\top \boldsymbol{\Sigma}^{-1} (\mathbf{x}_i - \boldsymbol{\mu}) \quad (5.1)$$

where \mathbf{x}_i is the datapoint, $\boldsymbol{\mu}$ is the cluster mean and $\boldsymbol{\Sigma}$ is the cluster covariance.

It is worth noting that one issue with the Mahalanobis distance metric in detecting outliers, is that outliers influence and may greatly inflate the covariance matrix which is itself used in calculating the Mahalanobis distance. To address this circular dependency, packages such as the R package **robustbase** (Rousseeuw et al, 2015), use leave-one-out (LOO) methods to identify outliers which have high leverage on the covariance estima-

tion. Another outlier metric, commonly used in linear regression is Cook's distance, which returns the leverage of every data point i on the estimation of \hat{Y} when the point is left out:

$$D_i = \frac{\sum_{j=1}^n (\hat{Y}_j - \hat{Y}_{j(i)})^2}{p \text{ MSE}}$$

where p is the number of parameters in the model, n is the number of datapoints, MSE is overall mean square error in the model, \hat{Y}_j is the predicted value for datapoint j and $\hat{Y}_{j(i)}$ is the predicted value when datapoint i is excluded.

In higher dimensions, outliers are harder to identify as data tends to be sparse, but also because they can be outliers without being outliers in any single dimension. Reducing the dimensionality, using for instance PCA or viSNE, and increasing the sample size can facilitate outlier detection.

5.1.9 Between sample noise

Reproducibility is a big challenge in flow cytometry and biology in general. As seen in Chapter 2, within-individual variation, as ascertained from biological replicates, greatly compromises statistical power in detecting between-individual effects. In flow cytometry, differences in cell treatment can lead to very different scatter patterns, as illustrated when comparing the scatter profile of the sample in Figure 2.3 in Chapter 2 to that of Figure 3.3 in Chapter 3. However, even when experimental conditions are kept constant, the shape and location of clusters across experiments can change. We attempt to correct for these batch effects using normalisation.

Normalisation involves first matching certain features of the data across samples, and then transforming the data such that samples are comparable in a biologically meaningful way. When identifying a fixed number of features across samples, such as modes in the density function, the first part of normalisation can rely on clustering algorithms such as K-means, K-medoids, GMM or sliding window approaches. K-medoids was

used successfully in Chapter 2 when gating bead data from different days, and again in Chapter 4 to qPCR data for pooling data across different plates.

In Chapter 2, the linear transform applied to align the peaks of the bead data was later applied to the identified clusters in the biological data, in order to make Mean Fluorescence Intensitys (MFIs) comparable across batches processed months apart.

In Chapter 4, I applied between sample normalisation to qPCR datasets to enable pooling, followed by joint calling. I first identified the copy number peaks in the ΔCt of qPCR plates of the two most common groups. The peaks were then aligned with a linear transform across plates. Pooling permitted the identification of the 3-0 group in Figure 4.2. In genotyping, normalisation is greatly facilitated by having matching probes across samples or spike-ins.

In flow cytometry, there is a much larger number of cells than markers per sample, so clustering is typically done within each sample independently, followed by matching of clusters across samples. However, normalisation using peak alignment can also be done to align samples before the clustering, so that the same gating can be applied to all normalised samples. This allows for pooling of samples, to aid the identification of rarer cell populations (Hahne et al, 2009).

Stability of stains is a big challenge and biologists often have an intuition of which markers are stable, and objectively, it does appear that certain stains are much more stable than others, be it due to the antibody specificity, the chemical stability of the fluorochrome, the staining protocol or the thoroughness of the lab technician. In Chapter 2, I was able to improve the repeatability of the CD25 MFI by correcting long-term fluctuations thanks to bead normalisation. In Chapter 3, the variation in pSTAT5 MFI was not adequately captured by beads, possibly due to titration issues, so I had to resort to various other normalisation approaches, none of which performed particularly well.

In the context of flow cytometry data, the manual gate hierarchy contributes prior

information about the expected relative frequency of the different types of cells and their relative marker expression, but their absolute marker expression is generally not readily comparable across samples and requires normalisation as shown in Chapter 2.

From my experience, normalisation of raw flow cytometry data using peak identification is as hard a problem as clustering due to the multimodality and the level of noise in these data. Also this type of univariate clustering of each flow marker independently does not exploit the correlation which exists between markers. Finally, mismatching of peaks in the alignment is more detrimental to repeatability than no normalisation, as the wrong clusters will be aligned.

While in genetic data, the number of probes across arrays is constant and identifiable, flow cytometry data can contain very different number of events between samples and the distinction between cell populations is often blurry. Normalisation methods applied to flow cytometry data must thus account for the sampling variation as well as staining discrepancies. Distinguishing between staining noise and actual differences in cell biology requires a certain level of prior knowledge which is context dependent and difficult to implement algorithmically.

5.1.10 Small number of samples

Typically, immunostaining flow cytometry experiments contain much smaller numbers of samples than case-control genetic experiments since blood and PBMC samples are a limited resource and sample preparation and running tubes on the flow cytometer are an expensive and time-consuming process. Also, experiments undertaken in flow cytometry are often pilot experiments or tubes run to test and optimise panels, and therefore often not complete datasets. These pilot experiments may be implemented with varying degrees of thoroughness and hence are generally poorly comparable.

When dealing with the relatively small numbers of samples available in flow cytome-

try, I believe data quality is more influential than the methods used to process the data: sophisticated methods are no replacement for good data. In order to be able to make the judgment call between "good" and "bad" data, understanding of the experimental context and the underlying biology is required; for example which cell populations to expect and their relative position and frequency. In genotyping, calling a genotype based on only a few samples is sometimes possible, since the absolute position of the signal clouds can be estimated due to the stability of the DNA molecule, the standardisation of DNA preparation protocols and of SNP arrays (Di et al, 2005; Giannoulatou et al, 2008). On the other hand, in flow cytometry, the average protein expression of cell populations, as measured by the MFI, is generally not directly comparable across experiments, so it is difficult to predict where a cell population will fall. Instead, as is done when sorting cells, a few events need to be collected first in order to estimate where to draw gates. Also, the frequency of cell populations can differ widely between individuals, and the ratio of cell populations, for example naive to memory, may change in the course of an individual's lifetime with exposure to environment. However, clusters can be defined in relation to one another, for example memory cells are lower for CD45RA and higher for CD25 than naive cells (Chapter 2).

This prior knowledge is acquired through the experience of having seen a large number of samples and is difficult to encode in an automated method. Processing in larger batches, or perhaps reducing the human involvement in flow cytometry, could be a first step towards automation. This will become a necessity as the number of samples grows.

However there are larger facilities, like for example at the Vaccine Research Center at the National Institute of Allergy and Infectious Diseases, where these processes have been automated with robotics and can consequently process hundreds of samples a day. Automatic methods are more pervasive in those labs since manual analysis is no longer a viable option. Presently there are few flow datasets sufficiently well-powered to detect

the effect sizes expected in complex diseases.

5.2 Moving from manual gating to automatic gating

Despite the clear advantages that automatic gating promises over manual gating, fully automated gating may not always perform as well as expected due to the level of noise and the small sample sizes in flow cytometry experiments. Realistically, the move to automation is likely to be incremental, for example by replacing the sequence of univariate or bivariate gating steps in the process, by automatic methods. As was seen in Chapter 2, the one-dimensional sequential top-down gating strategy can easily be implemented as an algorithm using mixture models or bead-derived thresholds. Perhaps the immediate goal of automatic gating shouldn't be to supersede manual gating but rather to complement it. Until the number of samples is sufficiently large, these methods can benefit from the prior knowledge that manual analysis contributes, while providing more objective analysis.

My analysis of flow cytometry data has brought to light many issues surrounding the division of skill and the difference in thinking between data generation and data analysis. Here I will present steps to be taken towards adopting these more targeted approaches routinely.

5.2.1 Agreeing on standards

While people generally agree that standards are key to improving reproducibility, there is often disagreement about which to adhere to. However, inconsistencies as trivial as naming conventions may waste precious man-hours for the person analysing the data, if they were not involved in the data generation. This is partly because the Flow Cytometry Standard (FCS) does not contain sufficient metadata to understand the context of the

experiment. Instead the name of the FCS file is typically used to map the sample back to the donor in order to retrieve covariates such as disease status, age, sex or genotype. However, when the naming and documentation is incomplete, this makes it very hard to automate the analysis of these data. Some guidelines have been set out by Lee et al (2008) in an attempt to define the minimum information to be provided for a flow cytometry experiment (MIFlowCyt):

- The experiment overview, which includes the purpose of the experiment, the experiment variables, conclusions and the quality control.
- Information about the sample such as the source, the material used, the treatment of the cells and the reagents.
- Instrument configuration details.

Human errors such as typographical errors or inconsistencies in the naming of FCS files, fluorochromes and antibodies across experiments, are, in my experience, very time-consuming and distracting from the analysis. Even when the FCS file does contain metadata such as the date of the experiment, it does not always match what is given in the name of the file.

I believe part of the solution is to involve the person generating the data in the analysis, so that they can appreciate the implications of naming inconsistencies. Another part of the solution is to encourage automation of these more tedious tasks, as is being done in certain labs which use robots to feed the flow cytometer and barcoding to name the samples. At the same time, the data analyst also needs to have an appreciation of the quality of the data and the purpose of the experiment. For instance, in flow cytometry, it is important to remember that a large number of events are debris of no biological interest and can be excluded based on side and forward scatter. Likewise artefacts can arise from staining, sample preparation (permeabilisation) or correlation of flow markers due to spillover.

While these observations are not specific to flow cytometry analysis, I would argue that these issues are more striking because of the flexibility flow cytometry offers both in terms of generation and analysis, and how little is known of the underlying cell populations. In flow cytometry, the standardisation of reagents and operating procedures between laboratories is of crucial importance (Maecker et al, 2012).

5.2.2 Extending manual analysis

In order to encourage the adoption of more rigorous computational gating methods, these tools need to be made more accessible to non-programmers. One way to achieve this is by building on the FlowJo manual analysis.

A first step could be to use the manual gates as a template but automatically adjust them per sample. FlowJo already provides a basic version of this feature, known as "magnetic gate", that moves gates to accommodate the maximum number of events. X-Cyt (Hu et al, 2013) takes this approach further by using the mean and the covariance of the manually gated populations as initial starting parameters to a clustering algorithm, and then applying an EM algorithm to refine the parameters to better fit the data. I also tried a similar approach in Chapter 3 since manual gates were not available for all samples. First, I let the mean of the ellipse be influenced by the data while the covariance was set as fixed. I then obtained a classification by defining a threshold on the Mahalanobis distance (Equation (5.1)) above which points were excluded. This worked reasonably well unless there was too much overlap with another cluster, in which case the gate was pulled towards the wrong cluster.

Implementing this approach relies on extracting gate coordinates from FlowJo workspaces files. Unfortunately, parsing FlowJo workspaces was not straightforward, since the format is poorly documented and not stable between releases. Although there are several BioConductor packages designed to import and parse FlowJo workspaces, `flowUtils`,

`gatingML`, `flowJo`, `flowWorkspace`, I have generally found that the R/FlowJo interface was not very reliable: for example `flowWorkspace` parsed the workspace without errors but the calculated statistics might not match the ones returned by FlowJo. An alternative would be to develop a bespoke XML parser to extract gates from FlowJo workspace files, but this approach is laborious as it requires in-depth knowledge of the FlowJo XML schema, which changes on each new release.

In the end, a simpler solution may be to use the CLR files which are simply the classification results from FlowJo. Unfortunately, the current FlowJo implementation exports these files as text, which results in very large files, making the exporting impractical. In fact, FlowJo crashed or hanged on numerous occasions when trying to accomplish this simple task. In the end, I had to resort to exporting only a few CLR files, from which I could estimate the gate coordinates. One method of approximating gate coordinates is to calculate the mean and covariance of a CLR cluster and to use the Mahalanobis distance, hence approximating the cluster with an ellipse. It is worth noting that a column naming standard is needed for the CLR format so that the position of the gate in the hierarchy, as well as its dimensions, can be retrieved.

Another interesting application of manual gates is to use them to define priors. Specifically, when several samples have been manually gated, the mean and covariance of the gate across samples can be used to define the mean and covariance hyper parameters of the priors in the mixture model to guide the parameter estimation, as implemented in the R package `flowClust` (Lo et al, 2009). I found this approach gave good agreement with manual gating for CD4⁺ lymphocytes on forward, side scatter and CD4 on the dataset from Chapter 2.

When FlowJo manual gating is not available, an alternative using R is to draw polygons on the R display using the R function `locator` and then using the R function `in.polygon` to extract points which fall within the polygon. This is an approach that I

used in Chapter 3 to emulate Tony Cutler's gating. There also exist some commercial alternatives to FlowJo such as **ADICyt**³ and **Infinicyt**⁴, but, at the time of writing, these are not nearly as widely used as FlowJo. Even though commercial alternatives exist, I still believe there remains a gap in the market for a new open source and extensible piece of software which reconciles manual, supervised and unsupervised flow cytometry analysis, and provides further multidimensional visualisation techniques. At the time of writing, a promising candidate is the R package **openCyto** (Finak, Greg et al, 2014) which integrates various other R packages, such as **flowClust** and **flowDensity**, in order to offer access to a core library of automated gating approaches. Although some programming knowledge is required for creating user-defined extensions, much of the programming requirements are removed by using spreadsheets to define the sequential gating process, known as gating templates. Once gating has been completed, summary statistics and plots are easily obtained, and the raw fluorescence measurements can also be extracted for further analysis. While the number of studies that have adopted **openCyto** is low at the time of writing, I envisage a large increase in its use in the near future.

5.3 Conclusion

Larger datasets have allowed us to see finer biological variation, both in genetics and cell subsets, than previously possible. Also, increasing the number of dimensions, by combining different kind of experiments, for example qPCR coupled with genotyping (Chapter 4), have helped uncover patterns which might not have been visible even at larger sample sizes. These large datasets lend themselves to more sophisticated analytical methods, as was illustrated in Chapter 3, where unsupervised clustering on pSTAT5 dose-response, helped uncover previously overlooked responsive cell subsets. In theory,

³<http://www.adinis.sk/en/products/bioinformatics-and-data-processing/adicyt.html>

⁴<http://www.infinicyt.com/>

these large datasets can be analysed using sophisticated models with a large number of parameters to account for all the intricacies of the data, as they are less prone to overfitting, but often in practise, simpler methods yield similar performance and are much more efficient. Such methods can also be combined to reach a consensus, and this popular machine learning approach, known as boosting, increases performance at the expense of interpretability.

Interpretability is one of the important issues preventing biologists of making better use of these computational methods. For example, while mixture modelling approaches are conceptually close to manual gating, probabilistic cell types may not be intuitive to biologists, so their true power is not fully exploited as hard cut-offs are applied early in the analysis process (see Chapter 2). Biologists prefer manual gating as it gives them the freedom to draw exclusive gates whose contours can be made arbitrarily complex. This freedom, however, exacerbates the disagreement in standards and definitions in immunology, and reproducibility of results. Discrepancies in gate positions are unlikely to make much of an impact on the MFI and relative proportion of common cell populations, but these can make a big difference on rarer cell populations, such as regulatory T cells, where the effects are much smaller.

While, in my opinion, automated clustering ought to be applied more widely to flow cytometry data, the use of manual analysis is likely to continue where the number of samples and parameters permits it. However, as the number of samples and parameters continue to grow, and new single-cell biotechnologies such as CyTOF (Becher et al, 2014) and Drop-seq (Macosko et al, 2015) become widespread, biologists will have to relinquish more control to the computer.

The automatic gating community is growing stronger, with a number of contributions to BioConductor, and the GenePattern web interface maintained by the Broad Institute (Kvistborg et al, 2015). In particular, two labs, Raphael Gottardo at the Fred

Hutchinson Cancer Research Center in the USA and Ryan Brinkman at the Terry Fox Laboratory in Canada, have been central in developing automatic gating software and bring together the automatic gating flow cytometry community as part of the FlowCAP challenge every year (Aghaeepour et al, 2013). One of the key questions that this community is addressing is how we should benchmark these methods. If our benchmark is comparison to manual gating then clearly no method can ever outperform it. Independent benchmarks such as repeatability are fairer, but perhaps a more general benchmark could be the utility of the clustering outcome, for example, whether it is predictive for diagnosis or if it correlates strongly with genetic variation or some other covariate under study. Of course, we will need to account for multiple testing, given the large numbers of cell populations and phenotypes which will be tested with this method, and their correlation, given the interdependency between cell phenotypes (Roederer et al, 2015).

Finally, my view is, that in the context of flow cytometry, we will only reap the true fruits of automated analysis once the number of samples has grown considerably, although this may require earlier steps in the pipeline, such as sample processing, to be further standardised and automated, so that the signal may rise above the noise.

Appendix A

Flow markers

CD3 Found on all T cells.

CD8 Marker of cytotoxic T cells or killer cells.

CD4 Found on a subset of T lymphocytes and helper cells.

CD31 Largely present on naive CD4 T cells. Lost on maturation of naive cell after leaving the thymus.

CD45RA Isoform of CD45 lost on activation of naive CD4⁺ and CD8⁺ T cells. Can be used to distinguish CD45RA high naive cells from CD45RA low memory cells.

CD127 The alpha chain of the IL-7 receptor. The IL-7 receptor is expressed on various cell types, including naive and memory T cells, and usually expressed at higher levels on T effector and regulatory T cells.

CD25 Better known as the IL2RA, the alpha chain of the heterotrimeric IL-2 receptor. High affinity binding of IL-2 requires all three chains of the receptor.

CD122 The beta chain of the IL-2 receptor, also known as IL2RB.

CD132 The gamma chain of the IL-2 receptor, also known as IL2RG.

CD56 NK cell marker.

CD19 Found on the surface of B-cells. Expressed on follicular dendritic cells and B cells. Also a lineage marker which is lost on maturation to plasma cells.

CD69 A protein induced by the activation of T lymphocytes and Natural Killer cells. Involved in lymphocyte proliferation and functions as a signal-transmitting receptor in lymphocytes.

Appendix B

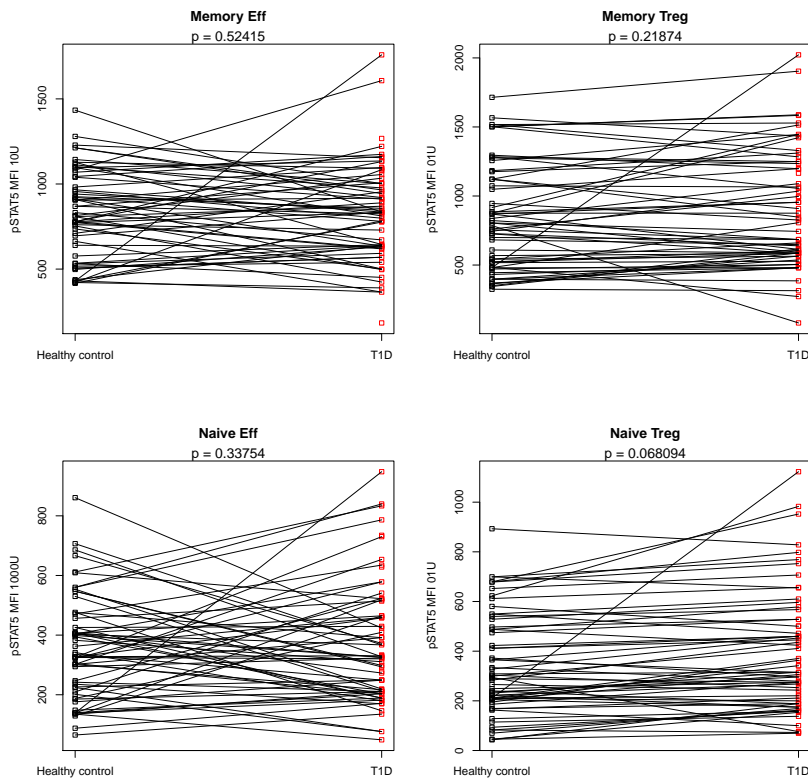


Figure B.1. Association test of pSTAT5 MFI with T1D. Samples are paired by day of analysis. Since there are nine more cases than controls, certain cases are not paired.

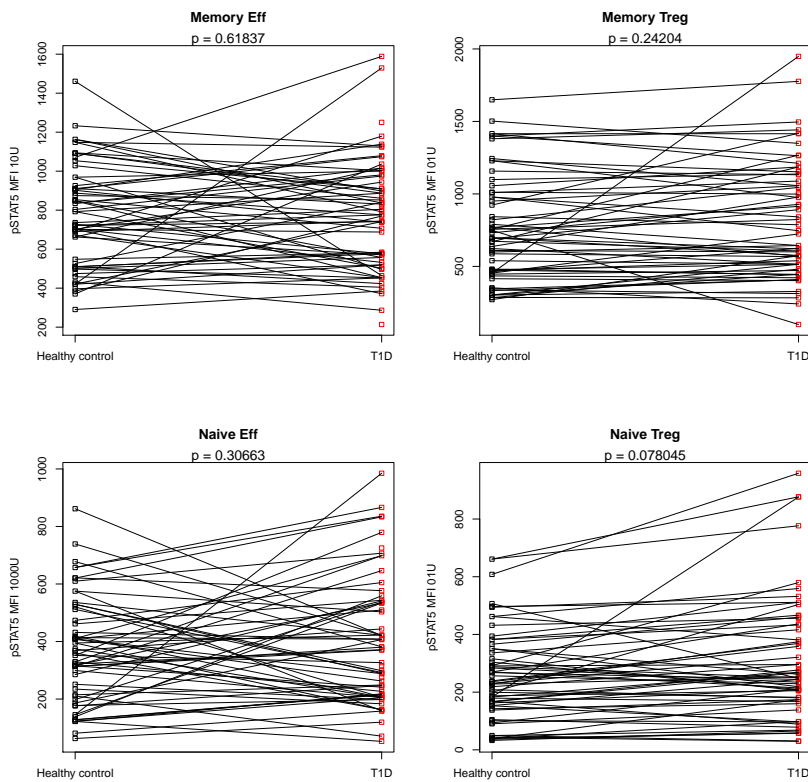


Figure B.2. Association test of pSTAT5 MFI, after nearest-neighbour normalisation, with T1D.

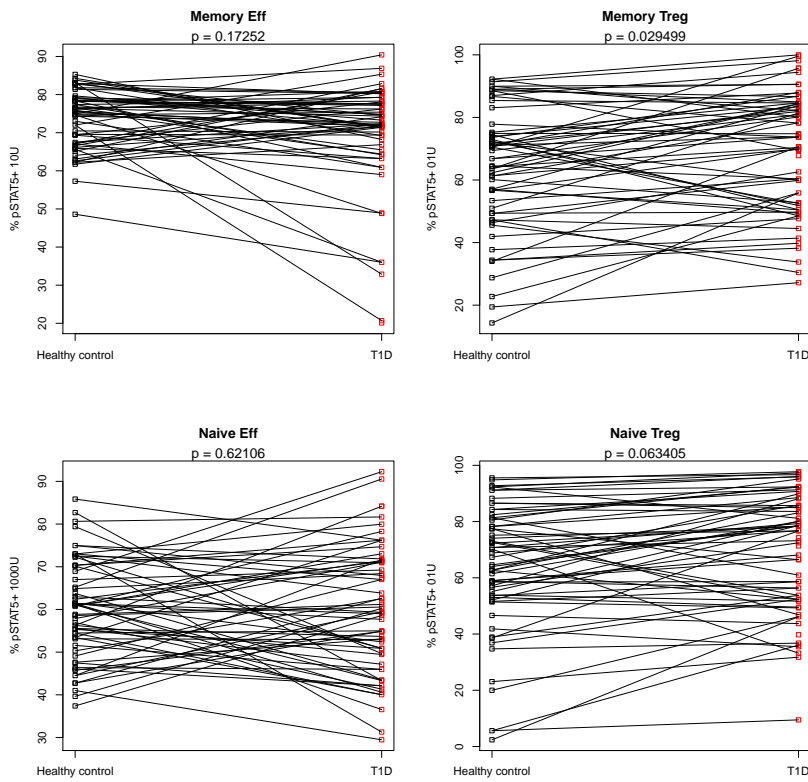


Figure B.3. Association test of percent pSTAT5⁺ with T1D.

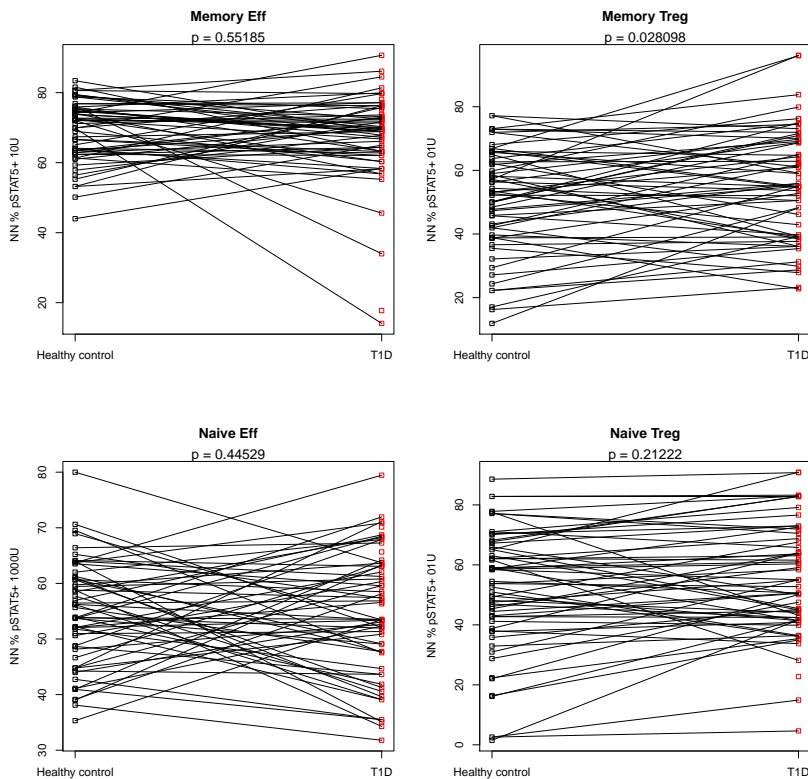


Figure B.4. Association test of percent pSTAT5⁺, after nearest-neighbour normalisation, with T1D.

Bibliography

- Aghaeepour N, Chattopadhyay PK, Ganesan A, O'Neill K, Zare H, Jalali A, Hoos HH, Roederer M, and Brinkman RR. 2012. Early immunologic correlates of HIV protection can be identified from computational analysis of complex multivariate T-cell flow cytometry assays. *Bioinformatics* **28**: 1009–1016.
- Aghaeepour N, Finak G, FlowCAP Consortium, Dougall D, Khodabakhshi AH, Mah P, Obermoser G, Spidlen J, Taylor I, Wuensch SA, et al. 2013. Critical assessment of automated flow cytometry data analysis techniques. *Nature Methods* **10**: 228–238.
- Aghaeepour N, Nikolic R, Hoos HH, and Brinkman RR. 2010. Rapid cell population identification in flow cytometry data. *Cytometry Part A* **79A**: 6–13.
- Amir EaD, Davis KL, Tadmor MD, Simonds EF, Levine JH, Bendall SC, Shenfeld DK, Krishnaswamy S, Nolan GP, and Pe'er D. 2013. viSNE enables visualization of high dimensional single-cell data and reveals phenotypic heterogeneity of leukemia. *Nature Publishing Group* **31**: 545–552.
- Arya S, Mount D, Kemp SE, and Jefferis G. 2013. *RANN: Fast Nearest Neighbour Search (wraps Arya and Mount's ANN library)*. R package version 2.3.0.
- Bagwell C. 2005. HyperLog - A flexible log-like transform for negative, zero, and positive valued data. *Cytometry Part A* **64A**: 34–42.
- Barrett JC, Clayton DG, Concannon P, Akolkar B, Cooper JD, Erlich HA, Julier C, Morahan G, Nerup J, Nierras C, et al. 2009. Genome-wide association study and meta-analysis find that over 40 loci affect risk of type 1 diabetes. *Nature Genetics* **41**: 703–707.
- Bashashati A and Brinkman RR. 2009. A Survey of Flow Cytometry Data Analysis Methods. *Advances in Bioinformatics* **2009**: 1–19.
- Bashirova AA, Martin MP, McVicar DW, and Carrington M. 2006. The killer immunoglobulin-like receptor gene cluster: tuning the genome for defense. *Annual Review of Genomics and Human Genetics* **7**: 277–300.
- Becher B, Schlitzer A, Chen J, Mair F, Sumatoh HR, Teng KWW, Low D, Ruedl C, Riccardi-Castagnoli P, Poidinger M, et al. 2014. High-dimensional analysis of the murine myeloid cell system. *Nature Immunology* **15**: 1181–1189.
- Beecham AH, Patsopoulos NA, Xifara DK, Davis MF, Kemppinen A, Cotsapas C, Shah TS, Spencer C, Booth D, Goris A, et al. 2013. Analysis of immune-related loci identifies 48 new susceptibility variants for multiple sclerosis. *Nature Genetics* **45**: 1353–1360.
- Bell GI, Horita S, and Karam JH. 1984. A polymorphic locus near the human insulin gene is associated with insulin-dependent diabetes mellitus. *Diabetes* **33**: 176–183.

- Bolstad BM, Irizarry RA, Astrand M, and Speed TP. 2003. A comparison of normalization methods for high density oligonucleotide array data based on variance and bias. *Bioinformatics* **19**: 185–193.
- Boyman O and Sprent J. 2012. The role of interleukin-2 during homeostasis and activation of the immune system. *Nature Reviews Immunology* **12**: 180–190.
- Brusko TM, Wasserfall CH, Hulme MA, Cabrera R, Schatz D, and Atkinson MA. 2009. Influence of membrane CD25 stability on T lymphocyte activity: implications for immunoregulation. *PLOS One* **4**: e7980.
- Calinski T and Harabasz J. 1974. A dendrite method for cluster analysis. *Communications in Statistics - Theory and Methods* **3**: 1–27.
- Carrington M, Wang S, Martin MP, Gao X, Schiffman M, Cheng J, Herrero R, Rodriguez AC, Kurman R, Mortel R, et al. 2005. Hierarchy of resistance to cervical neoplasia mediated by combinations of killer immunoglobulin-like receptor and human leukocyte antigen loci. *The Journal of Experimental Medicine* **201**: 1069–1075.
- Chan C, Feng F, Ottinger J, Foster D, West M, and Kepler TB. 2008. Statistical mixture modeling for cell subtype identification in flow cytometry. *Cytometry Part A* **73A**: 693–701.
- Chris Fraley Adrian E Raftery BTM and Scrucca L. 2012. mclust version 4 for R: Normal mixture modeling for model-based clustering, classification, and density estimation. Technical Report 597, Department of Statistics, University of Washington.
- Clayton DG. 2009. Prediction and interaction in complex disease genetics: experience in type 1 diabetes. *PLOS Genetics* **5**: e1000540.
- Cleveland WS. 1981. Lowess: A program for smoothing scatterplots by robust locally weighted regression. *The American Statistician* **35**.
- Cordell HJ. 2006. Estimation and testing of genotype and haplotype effects in case-control studies: comparison of weighted regression and multiple imputation procedures. *Genetic Epidemiology* **30**: 259–275.
- Cordell HJ. 2009. Detecting gene–gene interactions that underlie human diseases. *Nature Reviews Genetics* **10**: 392–404.
- Cron A, Gouttefangeas C, Frelinger J, Lin L, Singh SK, Britten CM, Welters MJP, van der Burg SH, West M, and Chan C. 2013. Hierarchical Modeling for Rare Event Detection and Cell Subset Alignment across Flow Cytometry Samples. *PLOS Computational Biology* **9**: e1003130.
- Cudworth AG and Woodrow JC. 1974. Letter: HL-A antigens and diabetes mellitus. *The Lancet* **2**: 1153.
- Davies JL, Kawaguchi Y, Bennett ST, Copeman JB, CORDELL HJ, Pritchard LE, Reed PW, Gough SC, Jenkins SC, and Palmer SM. 1994. A genome-wide search for human type 1 diabetes susceptibility genes. *Nature* **371**: 130–136.
- Dean PN, Bagwell CB, Lindmo T, Murphy RF, and Salzman GC. 1990. Data file standard for flow cytometry. *Cytometry Part A* **11**: 323–332.
- Dempster AP, Laird NM, and Rubin DB. 1977. Maximum Likelihood from Incomplete Data via the EM Algorithm. *Journal of the Royal Statistical Society Series B-Methodological* **39**: 1–38.

- Dendrou CA, Fung E, Esposito L, Todd JA, Wicker LS, and Plagnol V. 2009a. Fluorescence Intensity Normalisation: Correcting for Time Effects in Large-Scale Flow Cytometric Analysis. *Advances in Bioinformatics* **2009**: 1–6.
- Dendrou CA, Plagnol V, Fung E, Yang JHM, Downes K, Cooper JD, Nutland S, Coleman G, Himsworth M, Hardy M, et al. 2009b. Cell-specific protein phenotypes for the autoimmune locus IL2RA using a genotype-selectable human bioresource. *Nature Genetics* **41**: 1011–1015.
- Dendrou CA and Wicker LS. 2008. The IL-2/CD25 pathway determines susceptibility to T1D in humans and NOD mice. *Journal of clinical immunology* **28**: 685–696.
- Di X, Matsuzaki H, Webster TA, Hubbell E, Liu G, Dong S, Bartell D, Huang J, Chiles R, and Yang G. 2005. Dynamic model based algorithms for screening and genotyping over 100K SNPs on oligonucleotide microarrays. *Bioinformatics* **21**: 1958–1963.
- Dilthey A, Leslie S, Moutsianas L, Shen J, Cox C, Nelson MR, and McVean G. 2013. Multi-Population Classical HLA Type Imputation. *PLOS Computational Biology* **9**: e1002877.
- Duong T. 2014. *prim: Patient Rule Induction Method (PRIM)*. R package version 1.0.14.
- Duong T, Cowling A, Koch I, and Wand MP. 2008. Feature significance for multivariate kernel density estimation. *Computational Statistics & Data Analysis* **52**: 4225–4242.
- Durbin BP, Hardin JS, Hawkins DM, and Rocke DM. 2002. A variance-stabilizing transformation for gene-expression microarray data. *Bioinformatics* **18 Suppl 1**: S105–10.
- Finak G, Bashashati A, Brinkman R, and Gottardo R. 2009. Merging Mixture Components for Cell Population Identification in Flow Cytometry. *Advances in Bioinformatics* **2009**: 1–12.
- Finak G and Gottardo R. 2011. *flowMerge: Cluster Merging for Flow Cytometry Data*. R package version 2.8.0.
- Finak G, Manuel-Perez J, and Gottardo R. 2010a. *flowTrans: Parameter Optimization for Flow Cytometry Data Transformation*. R package version 1.18.0.
- Finak G, Perez JM, Weng A, and Gottardo R. 2010b. Optimizing transformations for automated, high throughput analysis of flow cytometry data. *BMC Bioinformatics* **11**: 546.
- Finak, Greg, Frelinger, Jacob, Jiang, Wenxin, Newell, Evan W, Ramey, John, Davis, Mark M, Kalams, Spyros A, De Rosa, Stephen C, and Gottardo, Raphael. 2014. Opencyto: An open source infrastructure for scalable, robust, reproducible, and automated, end-to-end flow cytometry data analysis. *PLOS Computational Biology* **10**: e1003806.
- Friedman JH and Fisher NI. 1999. Bump hunting in high-dimensional data. *Statistics and Computing* **9**: 123–143.
- Garg G, Tyler JR, Yang JHM, Cutler AJ, Downes K, Pekalski M, Bell GL, Nutland S, Peakman M, Todd JA, et al. 2012. Type 1 diabetes-associated IL2RA variation lowers IL-2 signaling and contributes to diminished CD4+CD25+ regulatory T cell function. *The Journal of Immunology* **188**: 4644–4653.
- Giannoulatou E, Yau C, Colella S, Ragoussis J, and Holmes CC. 2008. GenoSNP: a variational Bayes within-sample SNP genotyping algorithm that does not require a reference population. *Bioinformatics* **24**: 2209–2214.

- Gómez-Lozano N, Estefanía E, Williams F, Halfpenny I, Middleton D, Solís R, and Vilches C. 2005. The silent KIR3DP1 gene (CD158c) is transcribed and might encode a secreted receptor in a minority of humans, in whom the KIR3DP1, KIR2DL4 and KIR3DL1/KIR3DS1 genes are duplicated. *European journal of immunology* **35**: 16–24.
- Gonzalez-Galarza FF, Christmas S, Middleton D, and Jones AR. 2011. Allele frequency net: a database and online repository for immune gene frequencies in worldwide populations. *Nucleic acids research* **39**: D913–9.
- Gumperz JE, Barber LD, Valiante NM, Percival L, Phillips JH, Lanier LL, and Parham P. 1997. Conserved and variable residues within the Bw4 motif of HLA-B make separable contributions to recognition by the NKB1 killer cell-inhibitory receptor. *The Journal of Immunology* **158**: 5237–5241.
- Hahne F, Gopalakrishnan N, Khodabakhshi AH, Wong CJ, and Lee K. 2013. *flowStats: Statistical methods for the analysis of flow cytometry data*. R package version 3.20.3.
- Hahne F, Khodabakhshi AH, Bashashati A, Wong CJ, Gascoyne RD, Weng AP, Seyfert-Margolis V, Bourcier K, Asare A, Lumley T, et al. 2009. Per-channel basis normalization methods for flow cytometry data. *Cytometry Part A* **77**: 121–131.
- Hastie T, Tibshirani R, and Friedman J. 2009. *The Elements of Statistical Learning*. Data Mining, Inference, and Prediction, Second Edition. Springer.
- Herzenberg LA, Tung J, Moore WA, Herzenberg LA, and Parks DR. 2006. Interpreting flow cytometry data: a guide for the perplexed. *Nature Immunology* **7**: 681–685.
- Holyst H and Rogers W. 2009. *flowFP: Fingerprinting for Flow Cytometry*. R package version 1.18.0.
- Howson JMM, Walker NM, Clayton D, Todd JA, and Diabetes Genetics Consortium. 2009. Confirmation of HLA class II independent type 1 diabetes associations in the major histocompatibility complex including HLA-B and HLA-A. *Diabetes, Obesity and Metabolism* **11**: 31–45.
- Hu X, Kim H, Brennan PJ, Han B, Baecher-Allan CM, De Jager PL, Brenner MB, and Raychaudhuri S. 2013. Application of user-guided automated cytometric data analysis to large-scale immunoprofiling of invariant natural killer T cells. *PNAS* **110**: 19030–19035.
- Jiang W, Johnson C, Jayaraman J, Simecek N, Noble J, Moffatt MF, Cookson WO, Trowsdale J, and Traherne JA. 2012. Copy number variation leads to considerable diversity for B but not A haplotypes of the human KIR genes encoding NK cell receptors. *Genome Research* **22**: 1845–1854.
- Jing J, Koch I, and Naito K. 2009. Polynomial histograms for multivariate density and mode estimation. *Scandinavian Journal of Statistics* **39**: 75–96.
- Jobim M, Chagastelles P, Salim PH, Portela P, Wilson TJ, Curti AG, Jobim MR, João DA, Nardi NB, Tschiedel B, et al. 2010. Association of killer cell immunoglobulin-like receptors and human leukocyte antigen-C genotypes in South Brazilian with type 1 diabetes. *Human Immunology* **71**: 799–803.
- Jones PW, Osipov A, and Rokhlin V. 2011. Randomized approximate nearest neighbors algorithm. *PNAS* **108**: 15679–15686.
- Kent WJ. 2002. BLAT—the BLAST-like alignment tool. *Genome Research* **12**: 656–664.
- Koreth J, Matsuoka Ki, Kim HT, McDonough SM, Bindra B, Alyea III EP, Armand P, Cutler C, Ho VT, Treister NS, et al. 2011. Interleukin-2 and Regulatory T Cells in Graft-versus-Host Disease. *New England Journal of Medicine* **365**: 2055–2066.

- Körner C and Altfeld M. 2012. Role of KIR3DS1 in human diseases. *Frontiers in Immunology* **3**: 326.
- Kumasaka N, Fujisawa H, Hosono N, Okada Y, Takahashi A, Nakamura Y, Kubo M, and Kamatani N. 2011. PlatinumCNV: A Bayesian Gaussian mixture model for genotyping copy number polymorphisms using SNP array signal intensity data. *Genetic Epidemiology* **35**: 831–844.
- Kvistborg P, Gouttefangeas C, Aghaeepour N, Cazaly A, Chattopadhyay PK, Chan C, Eckl J, Finak G, Hadrup SR, Maecker HT, et al. 2015. Thinking outside the gate: Single-cell assessments in multiple dimensions. *Immunity* **42**: 591–592.
- Lee JA, Spidlen J, Boyce K, Cai J, Crosbie N, Dolphin M, Furlong J, Gasparetto M, Goldberg M, Goralczyk EM, et al. 2008. MIFlowCyt: The minimum information about a flow cytometry experiment. *Cytometry Part A* **73A**: 926–930.
- Leslie S, Donnelly P, and McVean G. 2008. A statistical method for predicting classical HLA alleles from SNP data. *American Journal of Human Genetics* **82**: 48–56.
- Liao W, Lin JX, and Leonard WJ. 2013. Interleukin-2 at the crossroads of effector responses, tolerance, and immunotherapy. *Immunity* **38**: 13–25.
- Lo K, Brinkman RR, and Gottardo R. 2008. Automated gating of flow cytometry data via robust model-based clustering. *Cytometry Part A* **73**: 321–332.
- Lo K, Hahne F, Brinkman RR, and Gottardo R. 2009. flowClust: a Bioconductor package for automated gating of flow cytometry data. *BMC Bioinformatics* **10**: 145.
- Long SA, Cerosaletti K, Bollyky PL, Tatum M, Shilling H, Zhang S, Zhang ZY, Pihoker C, Sanda S, Greenbaum C, et al. 2010. Defects in IL-2R Signaling Contribute to Diminished Maintenance of FOXP3 Expression in CD4+CD25+ Regulatory T-Cells of Type 1 Diabetic Subjects. *Diabetes* **59**: 407–415.
- Long SA, Cerosaletti K, Wan JY, Ho JC, Tatum M, Wei S, Shilling HG, and Buckner JH. 2011. An autoimmune-associated variant in PTPN2 reveals an impairment of IL-2R signaling in CD4(+) T cells. *Genes and immunity* **12**: 116–125.
- Long SA, Rieck M, Sanda S, Bollyky JB, Samuels PL, Goland R, Ahmann A, Rabinovitch A, Aggarwal S, Phippard D, et al. 2012. Rapamycin/IL-2 combination therapy in patients with type 1 diabetes augments Tregs yet transiently impairs β -cell function. *Diabetes* **61**: 2340–2348.
- Lowe CE, Cooper JD, Brusko T, Walker NM, Smyth DJ, Bailey R, Bourget K, Plagnol V, Field S, Atkinson M, et al. 2007. Large-scale genetic fine mapping and genotype-phenotype associations implicate polymorphism in the IL2RA region in type 1 diabetes. *Nature Genetics* **39**: 1074–1082.
- Lugli E, Roederer M, and Cossarizza A. 2010. Data analysis in flow cytometry: The future just started. *Cytometry Part A* **77A**: 705–713.
- Lumley T. 2012. *mitools: Tools for multiple imputation of missing data*. R package version 2.1.
- Luta G, Naumann U, and Wand M. 2011. *curvHDR: curvHDR filtering of flow cytometry samples*. R package version 1.0-3.
- Macosko EZ, Basu A, Satija R, Nemesh J, Shekhar K, Goldman M, Tirosh I, Bialas AR, Kamitaki N, Martersteck EM, et al. 2015. Highly Parallel Genome-wide Expression Profiling of Individual Cells Using Nanoliter Droplets. *Cell* **161**: 1202–1214.

- MacQueen J. 1967. Some methods for classification and analysis of multivariate observations. In *Proc. Fifth Berkeley Sympos. Math. Statist. and Probability (Berkeley, Calif., 1965/66)*, pp. Vol. I: Statistics, pp. 281–297. Univ. California Press, Berkeley, Calif.
- Maechler M, Rousseeuw P, Struyf A, Hubert M, and Hornik K. 2014. *cluster: Cluster Analysis Basics and Extensions*. R package version 1.15.2.
- Maecker HT, McCoy JP, FOCIS Human Immunophenotyping Consortium, Amos M, Elliott J, Gaigalas A, Wang L, Aranda R, Banchereau J, Boshoff C, et al. 2010. A model for harmonizing flow cytometry in clinical trials. *Nature Immunology* **11**: 975–978.
- Maecker HT, McCoy JP, and Nussenblatt R. 2012. Standardizing immunophenotyping for the Human Immunology Project. *Nature Reviews Immunology* **12**: 191–200.
- Maecker HT, Rinfret A, D’Souza P, Darden J, Roig E, Landry C, Hayes P, Birungi J, Anzala O, Garcia M, et al. 2005. Standardization of cytokine flow cytometry assays. *BMC Immunology* **6**: 13.
- Maecker HT and Trotter J. 2006. Flow cytometry controls, instrument setup, and the determination of positivity. *Cytometry Part A* **69**: 1037–1042.
- Martin MP, Gao X, Lee JH, Nelson GW, Detels R, Goedert JJ, Buchbinder S, Hoots K, Vlahov D, Trowsdale J, et al. 2002. Epistatic interaction between KIR3DS1 and HLA-B delays the progression to AIDS. *Nature Genetics* **31**: 429–434.
- Martin MP, Qi Y, Gao X, Yamada E, Martin JN, Pereyra F, Colombo S, Brown EE, Shupert WL, Phair J, et al. 2007. Innate partnership of HLA-B and KIR3DL1 subtypes against HIV-1. *Nature Genetics* **39**: 733–740.
- McLachlan G and Peel D. 2004. *Finite Mixture Models*. John Wiley & Sons.
- Mehers KL, Long AE, van der Slik AR, Aitken RJ, Nathwani V, Wong FS, Bain S, Gill G, Roep BO, Bingley PJ, et al. 2011. An increased frequency of NK cell receptor and HLA-C group 1 combinations in early-onset type 1 diabetes. *Diabetologia* **54**: 3062–3070.
- Mevik BH, Wehrens R, and Liland KH. 2013. *pls: Partial Least Squares and Principal Component regression*. R package version 2.4-3.
- Middleton D, Halfpenny I, Meenagh A, Williams F, Sivula J, and Tuomilehto-Wolf E. 2006. Investigation of KIR Gene Frequencies in Type 1 Diabetes Mellitus. *Human Immunology* **67**: 986–990.
- Milborrow S. 2014. *earth: Multivariate Adaptive Regression Spline Models*. R package version 3.2-7.
- Mogami S, Hasegawa G, Nakayama I, Asano M, Hosoda H, Kadono M, Fukui M, Kitagawa Y, Nakano K, Ohta M, et al. 2007. Killer cell immunoglobulin-like receptor genotypes in Japanese patients with type 1 diabetes. *Tissue Antigens* **70**: 506–510.
- Murphy RF and Chused TM. 1984. A proposal for a flow cytometric data file standard. *Cytometry Part A* **5**: 553–555.
- Naumann U, Luta G, and Wand MP. 2010. The curvHDR method for gating flow cytometry samples. *BMC Bioinformatics* **11**: 44.
- Nejentsev S, Howson JMM, Walker NM, Szeszko J, Field SF, Stevens HE, Reynolds P, Hardy M, King E, Masters J, et al. 2007. Localization of type 1 diabetes susceptibility to the MHC class I genes HLA-B and HLA-A. *Nature* **450**: 887–892.

- Nerup J, Platz P, Andersen OO, Christy M, Lyngsoe J, Poulsen JE, Ryder LP, Nielsen LS, Thomsen M, and Svejgaard A. 1974. HL-A antigens and diabetes mellitus. *The Lancet* **2**: 864–866.
- Nikitina-Zake L, Rajalingham R, Rumba I, and Sanjeevi CB. 2004. Killer cell immunoglobulin-like receptor genes in Latvian patients with type 1 diabetes mellitus and healthy controls. *Annals of the New York Academy of Sciences* **1037**: 161–169.
- Nikula T, West A, Katajamäa M, Lonnberg T, Sara R, Aittokallio T, Nevalainen O, and Lahesmaa R. 2005. A human ImmunoChip cDNA microarray provides a comprehensive tool to study immune responses. *Journal of Immunological Methods* **303**: 122–134.
- Norman PJ, Abi-Rached L, Gendzekhadze K, Hammond JA, Moesta AK, Sharma D, Graef T, McQueen KL, Guethlein LA, Carrington CVF, et al. 2009. Meiotic recombination generates rich diversity in NK cell receptor genes, alleles, and haplotypes. *Genome Research* **19**: 757–769.
- O’Gorman MRG and Thomas J. 1999. Isotype controls - time to let go? *Cytometry Part A* **38**: 78–80.
- Ortaldo JR, Winkler-Pickett R, Kopp W, Kawasaki A, Nagashima K, Okumura K, Yagita H, and Bach FH. 1992. Relationship of large and small CD3- CD56+ lymphocytes mediating NK-associated activities. *Journal of Leukocyte Biology* **52**: 287–295.
- Parham P and Moffett A. 2013. Variable NK cell receptors and their MHC class I ligands in immunity, reproduction and human evolution. *Nature Reviews Immunology* **13**: 133–144.
- Park Y, Choi H, Park H, Park S, Yoo EK, Kim D, and Sanjeevi CB. 2006. Predominance of the group A killer Ig-like receptor haplotypes in Korean patients with T1D. *Annals of the New York Academy of Sciences* **1079**: 240–250.
- Parks DR, Roederer M, and Moore WA. 2006. A new "Logicle" display method avoids deceptive effects of logarithmic scaling for low signals and compensated data. *Cytometry Part A* **69**: 541–551.
- Patterson CC, Dahlquist GG, Gyürüs E, Green A, and Soltész G. 2009. Incidence trends for childhood type 1 diabetes in Europe during 1989–2003 and predicted new cases 2005–20: a multicentre prospective registration study. *The Lancet* **373**: 2027–2033.
- Pekalski ML, Ferreira RC, Coulson RMR, Cutler AJ, Guo H, Smyth DJ, Downes K, Dendrou CA, Castro Dopico X, Esposito L, et al. 2013. Postthymic expansion in human CD4 naïve T cells defined by expression of functional high-affinity IL-2 receptors. *The Journal of Immunology* **190**: 2554–2566.
- Pelak K, Need AC, Fellay J, Shianna KV, Feng S, Urban TJ, Ge D, De Luca A, Martinez-Picado J, Wolinsky SM, et al. 2011. Copy Number Variation of KIR Genes Influences HIV-1 Control. *PLOS Biology* **9**: e1001208.
- Perfetto SP, Chattopadhyay PK, and Roederer M. 2004. Innovation: Seventeen-colour flow cytometry: unravelling the immune system. *Nature Reviews Immunology* **4**: 648–655.
- Permutt MA, Chirgwin J, Rotwein P, and Giddings S. 1984. Insulin gene structure and function: a review of studies using recombinant DNA methodology. *Diabetes Care* **7**: 386–394.
- Pinheiro J, Bates D, DebRoy S, Sarkar D, and R Core Team. 2014. *nlme: Linear and Nonlinear Mixed Effects Models*. R package version 3.1-117.
- Plagnol V, Cooper JD, Todd JA, and Clayton DG. 2007. A Method to Address Differential Bias in Genotyping in Large-Scale Association Studies. *PLOS Genetics* **3**: e74.
- Pontikos N. 2013. *flowBeads: Analysis of flow bead data*. R package version 1.0.0.

- Pontikos N, Smyth DJ, Schuilenburg H, Howson JMM, Walker NM, Burren OS, Guo H, Onengut-Gumuscu S, Chen WM, Concannon P, et al. 2014. A hybrid qPCR/SNP array approach allows cost efficient assessment of KIR gene copy numbers in large samples. *BMC Genomics* **15**: 274.
- Poretsky L. 2010. *Principles of Diabetes Mellitus*. Springer.
- Pyne S, Hu X, Wang K, Rossin E, Lin TI, Maier LM, Baecher-Allan C, McLachlan GJ, Tamayo P, Hafler DA, et al. 2009. Automated high-dimensional flow cytometric data analysis. *PNAS* **106**: 8519–8524.
- Qian Y, Wei C, Eun-Hyung Lee F, Campbell J, Halliley J, Lee JA, Cai J, Kong YM, Sadat E, Thomson E, et al. 2010. Elucidation of seventeen human peripheral blood B-cell subsets and quantification of the tetanus response using a density-based method for the automated identification of cell populations in multidimensional flow cytometry data. *Cytometry Part A* **78B**: S69–S82.
- Qiu P, Simonds EF, Bendall SC, Gibbs KD, Bruggner RV, Linderman MD, Sachs K, Nolan GP, and Plevritis SK. 2011. Extracting a cellular hierarchy from high-dimensional cytometry data with SPADE. *Nature Biotechnology* **29**: 886–891.
- Ramos-Lopez E, Scholten F, Aminkeng F, Wild C, Kalhes H, Seidl C, Tonn T, Van der Auwera B, and Badenhoop K. 2009. Association of KIR2DL2 polymorphism rs2756923 with type 1 diabetes and preliminary evidence for lack of inhibition through HLA-C1 ligand binding. *Tissue Antigens* **73**: 599–603.
- Ripley B. 2014. *tree: Classification and regression trees*. R package version 1.0-35.
- Risch N. 1987. Assessing the role of HLA-linked and unlinked determinants of disease. *American Journal of Human Genetics* **40**: 1–14.
- Robinson J, Mistry K, McWilliam H, Lopez R, and Marsh SGE. 2010. IPD—the Immuno Polymorphism Database. *Nucleic acids research* **38**: D863–9.
- Roederer M. 2001. Spectral compensation for flow cytometry: visualization artifacts, limitations, and caveats. *Cytometry Part A* **45**: 194–205.
- Roederer M, Moore W, Treister A, Hardy RR, and Herzenberg LA. 2001. Probability binning comparison: a metric for quantitating multivariate distribution differences. *Cytometry Part A* **45**: 47–55.
- Roederer M, Quaye L, Mangino M, Beddall MH, Mahnke Y, Chattopadhyay P, Tosi I, Napolitano L, Terranova Barberio M, Menni C, et al. 2015. The Genetic Architecture of the Human Immune System: A Bioresource for Autoimmunity and Disease Pathogenesis. *Cell* **161**: 387–403.
- Rogers WT and Holyst HA. 2009. FlowFP: A Bioconductor Package for Fingerprinting Flow Cytometric Data. *Advances in Bioinformatics* pp. 1–11.
- Rogers WT, Moser AR, Holyst HA, Bantly A, Mohler ER, Scangas G, and Moore JS. 2008. Cytometric fingerprinting: Quantitative characterization of multivariate distributions . *Cytometry Part A* **73**: 430–441.
- Rousseeuw P, Croux C, Todorov V, Ruckstuhl A, Salibian-Barrera M, Verbeke T, Koller M, and Maechler M. 2015. *robustbase: Basic Robust Statistics*. R package version 0.92-3.
- Saadoun D, Rosenzwajg M, Joly F, Six A, Carrat F, Thibault V, Sene D, Cacoub P, and Klatzmann D. 2011. Regulatory T-Cell Responses to Low-Dose Interleukin-2 in HCV-Induced Vasculitis. *New England Journal of Medicine* **365**: 2067–2077.

- Santin I, de Nanclares GP, Calvo B, Gaafar A, Castaño L, and Bilbao JR. 2006. Killer Cell Immunoglobulin-Like Receptor (KIR) Genes in the Basque Population: Association Study of KIR Gene Contents With Type 1 Diabetes Mellitus. *Human Immunology* **67**: 118–124.
- Schwartz A, Repollet E, Vogt R, and Gratama J. 1996. Standardizing flow cytometry: Construction of a standardized fluorescence calibration plot using matching spectral calibrators. *Cytometry Part A* **26**: 22–31.
- Seamer LC, Bagwell CB, Barden L, Redelman D, Salzman GC, Wood J, and Murphy RF. 1997. Proposed new data file standard for flow cytometry, version FCS 3.0. *Cytometry Part A* **28**: 118–122.
- Shapiro HM. 2003. *Practical flow cytometry*. John Wiley and Sons.
- Shastry A, Sedimbi SK, Rajalingam R, Nikitina-Zake L, Rumba I, Wigzell H, and Sanjeevi CB. 2008. Combination of KIR 2DL2 and HLA-C1 (Asn 80) confers susceptibility to type 1 diabetes in Latvians. *International Journal of Immunogenetics* **35**: 439–446.
- Siebert JC, Wang L, Haley DP, Romer A, Zheng B, Munsil W, Gregory KW, and Walker EB. 2010. Exhaustive expansion: A novel technique for analyzing complex data generated by higher-order polychromatic flow cytometry experiments. *Journal of Translational Medicine* **8**: 106.
- Singal DP and Blajchman MA. 1973. Histocompatibility (HL-A) Antigens, Lymphocytotoxic Antibodies and Tissue Antibodies in Patients with Diabetes-Mellitus. *Diabetes* **22**: 429–432.
- Single RM, Martin MP, Gao X, Meyer D, Yeager M, Kidd JR, Kidd KK, and Carrington M. 2007. Global diversity and evidence for coevolution of KIR and HLA. *Nature Genetics* **39**: 1114–1119.
- van der Slik AR, Alizadeh BZ, Koeleman B, Roep BO, and Giphart MJ. 2007. Modelling KIR–HLA genotype disparities in type 1 diabetes. *Tissue Antigens* **69**: 101–105.
- van der Slik AR, Koeleman BPC, Verduijn W, Bruining GJ, Roep BO, and Giphart MJ. 2003. KIR in Type 1 Diabetes: Disparate Distribution of Activating and Inhibitory Natural Killer Cell Receptors in Patients Versus HLA-Matched Control Subjects. *Diabetes* **52**: 2639–2642.
- Smyth DJ, Cooper JD, Bailey R, Field S, Burren O, Smink LJ, Guja C, Ionescu-Tîrgoviște C, Widmer B, Dunger DB, et al. 2006. A genome-wide association study of nonsynonymous SNPs identifies a type 1 diabetes locus in the interferon-induced helicase (IFIH1) region. *Nature Genetics* **38**: 617–619.
- Smyth GK and Speed T. 2003. Normalization of cDNA microarray data. *Methods* **31**: 265–273.
- Snow C. 2004. Flow cytometer electronics. *Cytometry Part A* **57**: 63–69.
- Spidlen J, Breuer K, Rosenberg C, Kotecha N, and Brinkman RR. 2012. FlowRepository: A resource of annotated flow cytometry datasets associated with peer-reviewed publications. *Cytometry Part A* **81A**: 727–731.
- Stahl EA, Raychaudhuri S, Remmers EF, Xie G, Eyre S, Thomson BP, Li Y, Kurreeman FAS, Zhernakova A, Hinks A, et al. 2010. Genome-wide association study meta-analysis identifies seven new rheumatoid arthritis risk loci. *Nature Genetics* **42**: 508–514.
- Sugár IP and Sealfon SC. 2010. Misty Mountain clustering: application to fast unsupervised flow cytometry gating. *BMC Bioinformatics* **11**: 502.
- Thomas HE, Trapani JA, and Kay TWH. 2010. The role of perforin and granzymes in diabetes. *Cell Death & Differentiation* **17**: 577–585.

- Tibshirani R, Walther G, and Hastie T. 2001. Estimating the number of clusters in a data set via the gap statistic. *Journal of the Royal Statistical Society: Series B (Statistical Methodology)* **63**: 411–423.
- Todd JA. 2010. Etiology of type 1 diabetes. *Immunity* **32**: 457–467.
- van Buuren S and Groothuis-Oudshoorn K. 2011. mice: Multivariate imputation by chained equations in R. *Journal of Statistical Software* **45**: 1–67.
- Vivian JP, Duncan RC, Berry R, O'Connor GM, Reid HH, Beddoe T, Gras S, Saunders PM, Olshina MA, Widjaja JML, et al. 2011. Killer cell immunoglobulin-like receptor 3DL1-mediated recognition of human leukocyte antigen B. *Nature* **479**: 401–405.
- Walther G, Zimmerman N, Moore W, Parks D, Meehan S, Belitskaya I, Pan J, and Herzenberg L. 2009. Automatic Clustering of Flow Cytometry Data with Density-Based Merging. *Advances in Bioinformatics* **2009**: 1–7.
- Wellcome Trust Case Control Consortium. 2007. Genome-wide association study of 14,000 cases of seven common diseases and 3,000 shared controls. *Nature* **447**: 661–678.
- Wittes J. 2009. On looking at subgroups. *Circulation* **119**: 912–915.
- Yang Q, Khoury MJ, Sun F, and Flanders WD. 1999. Case-only design to measure gene-gene interaction. *Epidemiology* **10**: 167–170.
- Young D, Hunter D, Chauveau D, and Benaglia T. 2009. mixtools: An R Package for Analyzing Mixture Models. *Journal of Statistical Software* **32**: 1–29.
- Zare H, Shooshtari P, Gupta A, and Brinkman RR. 2010. Data reduction for spectral clustering to analyze high throughput flow cytometry data. *BMC Bioinformatics* **11**: 403.
- Zhi D, Sun C, Sedimbi SK, Luo F, Shen S, and Sanjeevi CB. 2011. Killer cell immunoglobulin-like receptor along with HLA-C ligand genes are associated with type 1 diabetes in Chinese Han population. *Diabetes/Metabolism Research and Reviews* **27**: 872–877.